Characterization of Natural Hazards in the Great Lakes:

Remote Monitoring and Deep Learning

By

Wei Wang

A dissertation submitted in partial fulfillment of the requirements for the degree of

Doctor of Philosophy

(Civil and Environmental Engineering)

At the

UNIVERSITY OF WISCONSIN - MADISON

2025

Date of final oral examination: 08/28/2025

The dissertation is approved by the following members of the Final Oral Committee:

Paul Block, Associate Professor, Civil and Environmental Engineering (Advisor)

Daniel Wright, Associate Professor, Civil and Environmental Engineering

Steven Loheide, Professor, Civil and Environmental Engineering

Min Chen, Assistant Professor, Forest and Wildlife Ecology

Acknowledgements

I would like to express my deepest gratitude to the professors in the Water Resources group for creating a stimulating and supportive academic environment. I am especially grateful to my committee members—Dr. Paul Block, Dr. Daniel Wright, and Dr. Steven Loheide—for their invaluable guidance, constructive feedback, and encouragement throughout my Ph.D. journey. I also thank Dr. Chin Wu and Dr. Nimish Pujara for their insightful discussions and generous support that greatly enriched my research. In addition, I am grateful to Dr. Min Chen and Dr. Song Gao, committee members from other departments, for their support and thoughtful suggestions.

I would like to thank Michael Miller from the Wisconsin Department of Natural Resources for his generous support of our field surveys in Black Earth Creek. I would also like to thank Dr. Yuli Liu, a former Ph.D. student in the Water Resources group, for her essential help in deploying the web-cam system in Lake Michigan.

I am fortunate to have had the friendship and encouragement of my groupmates, particularly Boyuan Lu and Dr. Sarah Peterson, whose support has been a constant source of strength. I am also deeply thankful to my wife, Xiuling Zhang, for her unwavering love, patience, and emotional support, which sustained me through the many challenges of graduate school.

I am especially grateful to Dr. Kelvin Santiago for providing me with teaching assistantship funding over the years. His support not only eased my academic journey but also gave me the opportunity to grow as an educator and mentor.

Finally, I thank all of my colleagues, friends, and family who, in different ways, contributed to this work and made this achievement possible.

Table of Contents

Acknowledgementsi		
List of Figures	vi	
List of Tables	XV	
Abstract	xvi	
Chapter 1: Introduction	1	
1.1 Background	1	
1.1.1 Natural hazards in the Great Lakes region	1	
1.1.2 Monitoring	4	
1.1.3 Detection	5	
1.1.4 Characterization	7	
1.2 Research questions and objectives	8	
1.3 Outline of proposed chapters	9	
Chapter 2: Characterization of stream habitat quality usin	ng UAV-based toolkit 11	
2.1 Introduction	11	
2.2 Objectives and research goals	14	
2.3 Study site	14	
2.4 Methods	16	
2.4.1 Flight route design	17	
2.4.2 Image processing	19	
2.4.3 Stream habitat quality assessment	21	
2.4.4 Field measurements	23	
2.5 Results	25	

	2.5.1 Performance of flight routes	25
	2.5.2 Ortho-terrain map	26
	2.5.3 Stream habitat parameters	28
	2.5.4 Multi-metric indices (MMIs) assessment	31
	2.6 Discussion	34
	2.6.1 Flying parameters	34
	2.6.2 Potential errors	35
	2.6.3 Alternative depth measurements	37
	2.6.4 Cost-effectiveness of UAV-based toolkits	38
	2.6.5 Toolkit limitation and future generalization	39
	2.7 Conclusions	41
C	Chapter 3: Loss and resilience of stream habitat due to flooding	43
	3.1 Introduction	43
	3.2 Objectives and research goals	46
	3.3 Study Site	47
	3.4 Methods	49
	3.4.1 UAV observation and MMI assessment	49
	3.4.2 Loss and resilience assessment for MMIs	50
	3.4.3 Loss and resilience characterization for MMIs	52
		0 2
	3.5 Results	
	3.5 Results	53
		53 53
	3.5.1 Orthophotos of flood damage and recovery	53 53

3.5.5 Loss and resilience of stream habitat quality	60
3.5.6 Loss-Resilience Types	66
3.6 Discussion	68
3.6.1 Limitation and future improvements	68
3.6.2 Variations among transects	70
3.6.3 Potential generalization	72
3.7 Conclusion	73
Chapter 4: Detection and characterization of flash rips in Lake N learning framework	
4.1 Introduction	74
4.2 Objectives and Research Goals	77
4.3 Materials and Methods	78
4.3.1 Study site and data sources	78
4.3.2 Flash rip detection	80
4.3.3 Identification and classification of flash rip events	85
4.3.4 Flash rip characterization	88
4.4 Results	88
4.4.1 Detection performance	88
4.4.2 Flash rip occurrence and associated environmental con	ditions91
4.4.3 Flash rip characteristics	93
4.5 Discussion	97
4.5.1 Sensitivity Analysis	97
4.5.2 Co-occurrence patterns of flash rip features	100
4.5.3 Suggestions for future improvements	101

4.6 Conclusions	102
Chapter 5: Shoreline Change Estimation Toolkit (SCET): A D Framework for Detecting and Characterizing Coastal Erosion and Ac	
5.1 Introduction	104
5.2 Objectives and Research Goals	107
5.3 Methods	108
5.3.1 Physical Settings	108
5.3.2 DeepLabV3-Plus	113
5.3.3 Shoreline change calculation	115
5.4 Results	118
5.4.1 Performance of aerial image segmentation	118
5.4.2 Performance of shoreline movement tracking	121
5.4.3 Performance of computation speed	122
5.4.4 Case study: shoreline changes in Michigan City	123
5.5 Discussion	125
5.5.1 Limitation and future improvements	125
5.5.2 Alternative shoreline change classification method using d	istance metrics
	127
5.5.3 General application to other sites	130
5.6 Conclusion	131
Chapter 6: Summary and conclusion	132
Reference	136

List of Figures

Figure 1-1 | Flood-related estimate damages and direct fatalities in the Great Lakes States. (a) shows the total estimated flood-associated damages of each state from 1996 to 2020 (Data Source: Zhi L. et al., United States Flood Database v1.1, https://zenodo.org/records/7545697); (b) presents the total reported direct flood-induced fatalities in each state from 2010 to 2023 (National Weather Service Preliminary US Flood Fatality Statistics, https://www.weather.gov/arx/usflood).

Figure 1-2 | Flood-induced stream habitat quality losses in Black Earth Creek. (a) shows the bank erosion with bare soil after the August-2018 flood event; (b) displays the riparian vegetation recession and exposed stream bank after the same flood event.

Figure 1-3 | Rip current incidents in the Great Lakes recorded in GLCID database (https://www.weather.gov/greatlakes/beachhazards_stats#) between 2002 and 2020 (red indicate incidents with fatalities, and yellow mean successful rescues).

Figure 1-4 | Shoreline and bluff erosion in the Great Lakes. Image sources: https://web.s3.wisc.edu/shorelinephotos/2012 photos/MW-0637.jpg

Figure 2-1 | Study area of Black Earth Creek in Dane County, WI. (a) Black Earth Creek Watershed. G_1 and G_2 are the two USGS stream gauges. (b) The 2010 straightened stream (dashed line) and the 2015 meandered stream (solid line) channel. B_1 and B_2 are the upstream and downstream bridges, respectively. (c) An oblique aerial photo of the study site. The symbol "W" represents the flowing direction of Black Earth creek toward the west. The vegetated riparian area, A_{veg} , is partly blocked by trees and shown as a white solid rectangle.

Figure 2-2 | A flowchart with (i) Toolkit I as flight route design, (ii) Toolkit II as image processing, and (iii) Toolkit III as stream habitat quality assessment.

Figure 2-3 | Illustration for Toolkit I. (a) Marked trees, buildings, the river and flying boundary. (b) Buffer distances for blocked buildings, trees, and surveyed streams. (c) Overlaid sketch of blocked areas, focusing areas, and flight boundaries. (d) An example of a high-elevation flying route in an S-shape pattern. (e) An example of a low-elevation flying route generated using the Modified D-Lite algorithm. (f) Two routes with the straight route blocked by obstacles (solid line) and the detoured route after the MDL algorithm (dashed line from D1' to D1).

Figure 2-4 | Illustration for Toolkit II. (a) Drone images obtained from both high-elevation flying and low-elevation flying routes. (b) Five image processing steps and in-situ ground control points (GCPs) surveyed using a total station. (c) Ortho-images and terrain maps.

Figure 2-5 | Illustration for Toolkit III: stream habitat indices definition. (a) Schematic of a meandered stream with eroded bank E, coarse wood debris CWB, bends Be, and tree T. (b) Definition of eroded bank width E, stream width W, fish cover width F, buffer width B, bank top width BT, and average stream depth D. (c) Definition of pool length. (d) Stream length calculation using the MAT algorithm. (e) Stream width calculation for a median axis point. (f) Bend identification. (g) Pool length calculation.

Figure 2-6 | The sampling methods of on-site validation. (a) Locations of ground control points (GCPs, yellow dots) and the instrument point (IP, blue star); (b) Locations of 14 transects for tape-based measurements; (c) The way to select transects within a stream segment; (d) The way to equally sample within a transect side view.

Figure 2-7 | The low-elevation flight routes. (a) Flight route without obstacle avoidance. (b) Flight route with obstacle avoidance using the Modified D-Lite algorithm. Obstacles are denoted as O₁, O₂, and O₃, while the take-off point is denoted by a purple triangle. The flight boundary is outlined by a thin orange polygon. The S flight route is depicted as a black dashed line with transition routes to the starting point and from the ending point marked as green and purple lines, respectively. The detours from the original route are highlighted by red boxes.

Figure 2-8 | Ortho-Terrain Map Generated from Toolkit II. (a) Reconstructed ortho-terrain map combining high- and low-elevation flight missions, with yellow lines marking ground elevation contours and the pink area indicating overlaid low-elevation results. (b) and (c) compare stream bank delineations for high-elevation results and overlaid results in area A_{veg} . The blue solid line are stream banks detectable from high-elevation results, while the orange solid line indicates stream banks in shaded (SA) or blocked (BA) areas, which are only delineable in the overlaid results.

Figure 2-9 | Parameter values for the stream habitat between Bridge B₁ and B₂. (a)-(c) show stream width, water depth, and bank top width (m), with solid lines as toolkit measurements and blue diamonds as ground-truth data for 14 transects. (d)-(f) present left- and right-bank vegetation buffer width, erosion width, and in-stream cover width (m), with solid and dashed lines for left-

and right-bank toolkit outputs and orange/purple markers for ground-truth results for the left and right banks, respectively.

Figure 2-10 | Detected stream bend and pool positions between Bridge B₁ and B₂. Eight bends (Bend 1 to Bend 8, marked as orange triangle) and six pools (Pool 1 to Pool 6, marked as dark blue line) are identified.

Figure 2-11 | MMI-based stream habitat quality assessment (spatially continuous indices: M₂, M₃, M₄, M₆, and M₈). (a) Visualizes the health condition of M₂. (b) Highlights the health condition of M₃, (c) Displays the distribution of M₄ health conditions. (d) Maps the spatial distribution of M₆. (e) depict the spatial distribution of M₈. The right column includes histograms for each index, showing the percentages of categories: excellent, good, fair, and poor.

Figure 2-12 | Comparative analysis of stream habitat quality assessments using MMIs. (a) presents the MMI scores for 14 transects evaluated using our toolkits, (b) depicts the MMI scores using onsite methods for the same transects, and (c) displays the MMI scores of the entire study site (spatially continuous), obtained using our toolkits.

Figure 2-13 | The decrease of tied points caused by water surface. (a) (c) (e) are images with different water body ratio, (b) (d) (f) show the ranked number of tie points we can extract from each image pair.

Figure 2-14 | Spatial variation of stream habitat quality condition. (a) displays the health condition of each index at each transect, (b) indicates the stream segment's poorest health condition category for each index in the vicinity of each transect.

Figure 3-1 | Study Site of Black Earth Creek. (a) depicts the Black Earth Creek watershed, featuring four USGS gauges (G1, G2, G3, and G4) that record gauge height and discharge data. (b) illustrates our surveying area located between two bridges, B1 and B2. The dashed purple line represents the straight stream in 2010, and it was meandered in 2015 following a habitat restoration program in 2012.

Figure 3-2 | Historical Observations from USGS Gauges Along Black Earth Creek. (a)-(d) correspond to gauge stations G1 (USGS 05406457), G2 (USGS 05406469), G3 (USGS 05406479), and G4 (USGS 05406500) as shown in Figure 3-1. Red lines represent gauge height observations, while black lines indicate discharge values. The maximum discharge was recorded during the flood event on August 20-21, 2018, as marked by the black arrows.

Figure 3-3 | MMI Criteria for Assessing Health Condition. Green indicates excellent condition, light green represents good condition, orange denotes fair condition, and red corresponds to poor condition.

Figure 3-4 | Different Types of Loss-Resilience Curve

Figure 3-5 | Orthophoto of the Study Site. (a), (b), and (c) show results collected on 08/09/2018, 09/29/2018, and 11/01/2022, respectively. In (b), areas A, B, and C highlight visible flood damages, while area D serves as a comparison with minimal flood impacts.

Figure 3-6 | Zoom-in views of the damage and recovery of stream habitat quality. The first row (a, b, and c) presents orthophotos taken on 08/09/2018, before the flood. The second row (d, e, and f) shows orthophotos from 09/29/2018, after the flood. The third row (g, h, and i) displays orthophotos from 11/01/2022, several years later. The loss-resilience patterns are illustrated for: Site A in the first column (a, d, g), Site B in the second column (b, e, h), Site C in the third column (c, f, i).

Figure 3-7 | Pre-flood stream habitat quality conditions. (a-c) Spatially continuous results for left and right riparian vegetation buffers, left and right bank stability, and in-stream cover. (d-h) Percentage distribution of habitat conditions (poor, fair, good, excellent) for left riparian vegetation buffer, right riparian vegetation buffer, left bank stability, right bank stability, and in-stream cover. Figure 3-8 | Post-flood stream habitat quality conditions. (a–c) Spatially continuous results for left and right riparian vegetation buffers, left and right bank stability, and in-stream cover. (d-h) Percentage distribution of habitat conditions (poor, fair, good, excellent) for left riparian vegetation buffer, right riparian vegetation buffer, left bank stability, right bank stability, and in-stream cover. Figure 3-9 | Steady stream habitat quality conditions. (a-c) Spatially continuous results for left and right riparian vegetation buffers, left and right bank stability, and in-stream cover. (d-h) Percentage distribution of habitat conditions (poor, fair, good, excellent) for left riparian vegetation buffer, right riparian vegetation buffer, left bank stability, right bank stability, and in-stream cover. Figure 3-10 | Loss of stream habitat quality. (a–c) Spatially continuous results for the relative loss of left and right riparian vegetation buffers, left and right bank stability, and in-stream cover. (dh) Percentage distribution of the relative loss of stream habitat quality for left riparian vegetation buffer, right riparian vegetation buffer, left bank stability, right bank stability, and in-stream cover. Figure 3-11 | Resilience of stream habitat quality in year one. (a–c) Spatially continuous results for the relative resilience at year one of left and right riparian vegetation buffers, left and right

bank stability, and in-stream cover. (d-h) Percentage distribution for the relative resilience at year one of stream habitat quality for left riparian vegetation buffer, right riparian vegetation buffer, left bank stability, right bank stability, and in-stream cover.

Figure 3-12 | Resilience of stream habitat quality in year three. (a–c) Spatially continuous results for the relative resilience at year three of left and right riparian vegetation buffers, left and right bank stability, and in-stream cover. (d–h) Percentage distribution for the relative resilience at year three of stream habitat quality for left riparian vegetation buffer, right riparian vegetation buffer, left bank stability, right bank stability, and in-stream cover.

Figure 3-13 | Resilience of stream habitat quality in year four. (a–c) Spatially continuous results for the relative resilience at year four of left and right riparian vegetation buffers, left and right bank stability, and in-stream cover. (d–h) Percentage distribution for the relative resilience at year four of stream habitat quality for left riparian vegetation buffer, right riparian vegetation buffer, left bank stability, right bank stability, and in-stream cover.

Figure 3-14 | Loss–resilience types of stream habitat health based on six UAV survey outputs (2018–2022). (a–c) Spatially continuous results of relative resilience at year four for left and right riparian vegetation buffers, left and right bank stability, and in-stream cover. (d–h) Percentage distributions of loss–resilience types for the same metrics. Note: I, II, and III denote the three types of loss–resilience curves; a, b, c, and d represent the original conditions of poor, fair, good, and excellent, respectively.

Figure 3-15 | Loss–resilience curves for MMIs at the whole study site. (a) Left riparian vegetation buffer, (b) right riparian vegetation buffer, (c) left bank stability, (d) right bank stability, and (e) instream cover. Surveying numbers 1–6 correspond to the dates 08/09/2018, 09/29/2018, 06/07/2019, 09/14/2019, 10/18/2021, and 10/31/2022.

Figure 4-1 | Study site and remote camera systems. (a) illustrates the geographical location of Port Washington within Lake Michigan and pinpoints the positions of camera system within Port Washington by the yellow dot, respectively. The camera's fields of view demarcated by dashed triangles, while the bathymetry of our study site is displayed using white contours. (b) provides a real-world image of the on-site camera system. (c) shows the remote-control system used for image recording and processing. (d) – (f) present Examples of flash rips under three driving mechanisms. (d) an event occurred on 2019/08/08 at 13:47 CST caused by water level fluctuations. (e) an event

occurred on 2019/08/26 at 16:49 CST induced by normal wave incidents; (f) an event observed on 2019/09/03 at 12:23 CST triggered by oblique wave incidents.

Figure 4-2 | Workflow for Flash Rip Detection. (a) is the sketch of orthophoto, sediment plumes are marked as orange, and the other parts are marked as blue; (b) demonstrates the division into square orthophotos; (c) shows the flash rip detection applied to each square orthophoto by cascade R-CNN; (d) presents the refinement for deep learning outputs, where purple boxes (A, B, C, D) would be eliminated; and finally, (e) displays the merging step to generate detection results for the whole orthophoto.

Figure 4-3 | Cascade R-CNN with Refinement Steps. (a) Initial detection employs ResNet to identify hotspots of potential objects and uses a Regional Proposal Network (RPN) to approximate the positions of likely flash rips. (b) Cascading adjustments modify these positions and refine the probability estimates for each flash rip using incremental Intersection over Union (IoU) thresholds. (c) Post-detection refinement eliminates detections with low probability values, flat shapes, and boundary issues, while also optimizing overlapping flash rip detections.

Figure 4-4 | Performance of Refined Cascade R-CNN model. (a)-(f) show examples of refined cascade R-CNN detection. The first row (a and b) represents water-level-induced conditions, the second row (c and d) corresponds to normal wave-induced conditions, and the third row (e and f) depicts oblique wave-induced conditions. The first column shows the raw outputs of the Cascade R-CNN, while the second column presents results after applying the refinement process. (g) False positive rate of Cascade R-CNN and Faster R-CNN across the first 25 training epochs.(h) Missing rate trends for the same models over the same training period.(i) Model performance on the testing dataset: comparison between Cascade R-CNN with refinement, without refinement, and Faster R-CNN.

Figure 4-5 | Flash rip occurrences and the associated environmental variables. (a) Daily flash rip counts from 05/16 to 09/14/2019. (b–c) High-pass filtered water level and air pressure. (d–e) Wind velocity and direction. (f–g) Routed significant wave height and direction. Colored lines indicate example cases: blue (08/08, water-level-induced), orange (08/26, normal wave-induced), green (09/03, oblique wave-induced).

Figure 4-6 | Distribution of flash rip offshore distance and alongshore position. (a–c) show offshore distance (OD, red) and peak maximum offshore distance (PMOD, blue) for WLF-, NW-,

and OW-induced flash rip events. (d–f) show alongshore position (AP, red) and alongshore position of peak objects (APP, blue) for the same event types.

Figure 4-7 | Cumulative distribution of flash rip temporal and kinematic features. (a), (b), and (c) represent the cumulative distributions of duration, growing time cost, and front-line growing speed, respectively. Blue, orange, and green correspond to water-level-fluctuation (WLF)-induced, normal wave (NW)-induced, and oblique wave (OW)-induced flash rips.

Figure 4-8 | Sensitivity test of characterization settings. The default settings include a 0.3 m threshold for significant wave height, an incident wave angle range of -30° to 30°, and a wave routing termination depth of 2 m. The first row (a, b, c, d) presents sensitivity results for significant wave height thresholds of 0.25m and 0.3m. The second row (e, f, g, h) shows sensitivity results for incident wave angle criteria of -25° to 25° and -30° to 30°. The third row (i, j, k, l) illustrates sensitivity results for wave routing termination depth of 1.5m and 2.5m. The first column (a, e, i) displays the ratio of water-level-fluctuation (WLF)-induced, normal wave (NW)-induced, and oblique wave (OW)-induced flash rips. The second to fourth columns present the mean values of peak maximum offshore distance (PMOD), alongshore position for peak rips (APP), and duration, respectively.

Figure 4-9 | Probability density map for two characteristics across different flash rip driven factors. The first row (a,b,c) illustrates the relationship between alongshore position for peak rips (APP) and peak maximum offshore distance (PMOD): (a) for water-level-fluctuation-induced (WLF) rips, (b) for normal-wave-induced (NW) rips, and (c) for oblique-wave-induced (OW) rips. The second row (d, e, f) shows the relationship between duration and PMOD: (d) for WLF-induced, (e) for NW-induced, and (f) for OW-induced flash rips.

Figure 5-1 | Study site for SCET toolkit development and case study. (a) The Great Lakes' location and bathymetry, with black dots indicating validation sites. The site outlined in red is used for visualizing validation delineations. (b) The case study site, Michigan City, Indiana, selected for indepth shoreline change analysis using the SCET toolkit. The Michigan City Harbor is highlighted with a yellow dashed rectangle, and coastal defenses A, B, and C are marked within the harbor area.

Figure 5-2 | Labeling examples for special cases. (a, b) structures labeled as land and water, respectively; (c, d) plants and algae labeled as land and water, respectively; (e, f) ships and boats

labeled as land and water, respectively; (g) sandbars labeled as either land or water; (h) an island, always labeled as land.

Figure 5-3 | DeepLabV3-Plus Architecture. The encoder part (a) includes deep convolutional neural network (DCNN) contains two normal ResNet blocks (B_1 and B_2) and one ResNet block (B_3) with Arous rate (r) of 2, and Atrous Spatial Pyramid Pooling (ASPP) with four different convolution and Atrous settings. The encoder part (b) combines the raw data with encoding outputs and upsamples to generate the detection outputs.

Figure 5-4 | Modified DSAS Workflow. (a) Segmented binary image generated by the deep learning model (red: water; white: land). (b) Edge detection to extract the land—water interface; the earthy line marks the shoreline, and the blue line indicates the boundary of the inner water body. (c) Shoreline translation to establish the baseline. (d) Generation of evenly spaced transects. (e) Intersection of transects with the shoreline for precise positioning. (f) Application of regression methods to calculate shoreline change rates.

Figure 5-5 | Training curves of DeepLabV3+ for water (a) and background (b) classes.

Figure 5-6 | Water segmentation examples for DeepLabV3. (a)–(f) show water body segmentation results across various water hues, while (g)–(l) present results from different landscape types. Green pixels indicate true positives, blue pixels indicate false negatives, and yellow pixels indicate false positives.

Figure 5-7 | SCET performance for shoreline positioning. (a) Spatial proximity between SCET-derived shorelines and manual delineations. (b) Error distribution of shoreline positioning for each Great Lake. (c) Error distribution of shoreline positioning for each Great Lakes state.

Figure 5-8 | Shoreline change rates calculated by modified DSAS.

Figure 5-9 | Shoreline change rates calculated by modified DSAS with water level calibration.

Figure 5-10 | Water conditions and landscapes requiring further refinement. (a) Water body with severe eutrophication; (b) highly wavy water body; (c) complex harbor or pier area; (d) wetlands with floating plants and algae. Green pixels indicate true positives, blue pixels indicate false negatives, and yellow pixels indicate false positives.

Figure 5-11 | Distance metrics for shoreline change classification. (a) Shoreline accretion condition; (b) relatively stable shoreline; (c) shoreline erosion condition. Red indicates the shoreline position in 2008, green indicates the shoreline position in 2018, and the blue dashed line

represents the 2018 shoreline aligned to match the start and end points of the 2008 shoreline. Blue arrows indicate land-to-water movement, while orange arrows indicate water-to-land movement.

List of Tables

- Table 2-1 | The Modified D-Lite algorithm
- Table 2-2 | An example of processing quality using computer hardware settings
- Table 2-3 | Estimated memory requirement for point cloud and 3-D texture mesh computation
- Table 2-4 | Multi-metric indices (MMIs) for stream habitat quality assessment
- Table 2-5 | Flight route Performance matrix with different flying

Abstract

Natural hazards are environmental events that pose significant risks to societies and human environments. In the Great Lakes region, natural hazards such as flooding, dangerous currents, and rapid shoreline changes are common concerns. These hazards have led to numerous incidents, resulting in fatalities, socio-economic losses, and ecological damage. Given the severe consequences of natural hazards, the Great Lakes region faces two primary challenges: effectively detecting these hazards with high spatial resolution while minimizing labor and time costs; and comprehensively characterizing their occurrence and features to support informed management and mitigation efforts. I hypothesize that combining remote sensing and deep learning techniques can enhance the detection and characterization of natural hazards in the Great Lakes region. To examine this hypothesis, the overall objective of this study is characterizing natural hazards using remote monitoring and deep learning methods. Specifically, the research investigates flood impacts on stream habitat quality, and flash rip currents and rapid shoreline changes in coastal areas. First, to assess flood impacts on stream habitat quality, a UAV-based toolkit was developed to characterize stream habitat quality conditions using multi-metric indices (MMIs). Applied before and after the August 2018 flood, this approach revealed patterns of loss and resilience in riparian vegetation, bank stability, and in-stream cover. Second, for flash rip currents, webcam imagery was analyzed with a refined Cascade R-CNN model, enabling reliable detection and classification of flash rips into three driving factors: water-level fluctuations, normal waves, and oblique waves. Their spatial, temporal, and kinematic features were then characterized to quantify differences among driving factors. Third, to detect and characterize rapid shoreline changes, a DeepLab-based segmentation framework was applied to aerial images for shoreline extraction and coupled with an improved Digital Shoreline Analysis System to compute change rates, identify

hotspots, and distinguish true morphological change from shoreline retreats driven by water-level fluctuations. Overall, this research contributes to improving detection methodologies and enriching the characterization of natural hazards in the Great Lakes region. The findings aim to reduce hazard-related risks and provide valuable insights into effective management and mitigation efforts.

Chapter 1: Introduction

1.1 Background

1.1.1 Natural hazards in the Great Lakes region

Natural hazards, defined as environmental events that pose risks to societies and ecosystems (UNDRR, 2009), encompass a wide range of threats such as flooding and dangerous currents (Borden and Cutter, 2008). These events typically lead to three types of impacts: human casualties (injuries, illnesses, and deaths), damage to equipment, infrastructure, and property, and disruptions to ecological and environmental systems (Kappes et al., 2008; Marzocchi et al., 2012). In the North American Great Lakes region, natural hazards are a recurring issue (Jones and Corotis, 2012). Among all natural hazards occurring within this region, flooding in river and coastal areas, dangerous currents near lakeshore, and rapid shoreline changes are particularly common. Flooding in the Midwest could be caused by heavy rains, rapid snowmelt, lake water level fluctuation, or

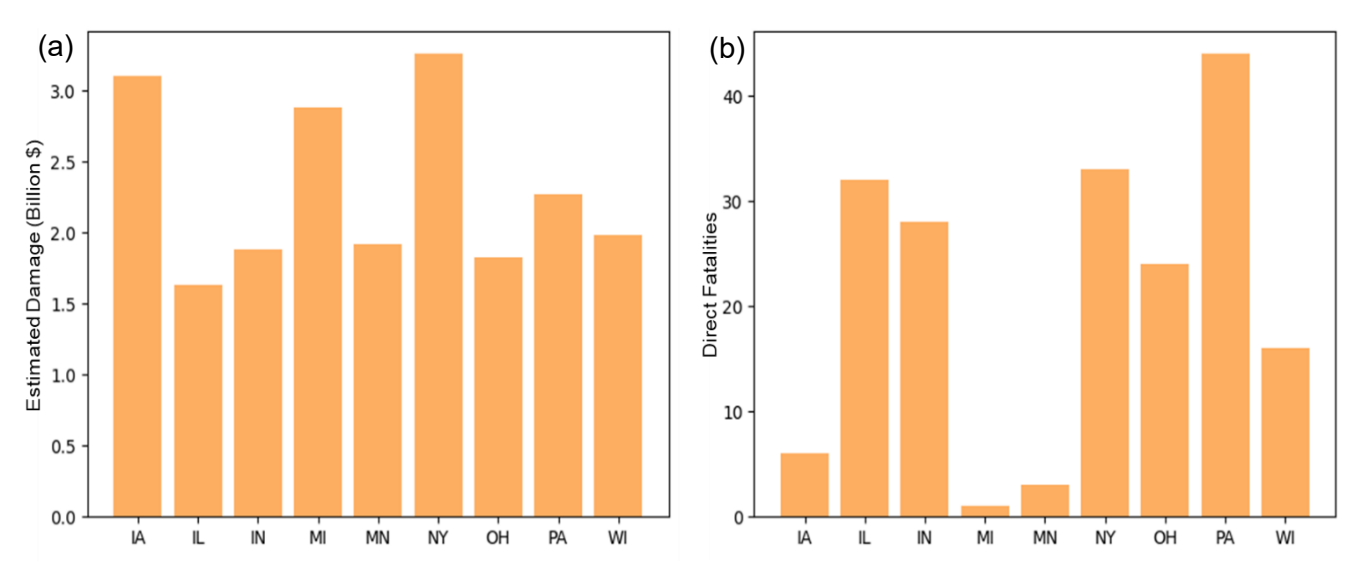


Figure 1-1 | Flood-related estimate damages and direct fatalities in the Great Lakes States. (a) shows the total estimated flood-associated damages of each state from 1996 to 2020 (Data Source: Zhi L. et al., United States Flood Database v1.1, https://zenodo.org/records/7545697); (b) presents the total reported direct flood-induced fatalities in each state from 2010 to 2023 (National Weather Service Preliminary US Flood Fatality Statistics, https://www.weather.gov/arx/usflood).

their compounds (Rasid et al., 1992; Kunkel et al., 1993; Velasquez et al., 2023). As shown in Fig. 1-1, flood events caused approximately 20.76 dollars of billion US estimated economic damage from 1996 to 2020 (Li et al., 2021), and 187 direct fatalities from 2010 to 2023 in the Great Lakes (National Weather states Service, 2024). Within this context, Wisconsin reported \$1.98 billion alone economic damage and 16 fatalities during the same period. Also, riverine floods incur some severe impacts on river and stream habitats, such as stream bank failure (Fig. 1-2a) and recessed





Figure 1-2 | Flood-induced stream habitat health losses in Black Earth Creek. (a) shows the bank erosion with bare soil after the August-2018 flood event; (b) displays the riparian vegetation recession and exposed stream bank after the same flood event.

riparian vegetation cover (Fig. 1-2b), thereby posing considerable challenges for freshwater species communities. According to an investigation in Minnesota, the August 2007 flood reduced invertebrate densities by 75–95% and taxa richness by 30–70% in some southeastern Minnesota streams, and assemblage structure was reduced to poor and very poor levels in first- and second-order streams (Mundahl and Hunt, 2011). Dangerous currents, characterized as rapid seaward water jets, can unexpectedly sweep people in nearshore areas to deeper offshore zones (Garnier et al., 2008; McCarroll et al., 2014) and cause drownings (Castelle et al., 2016). Numerous drowning

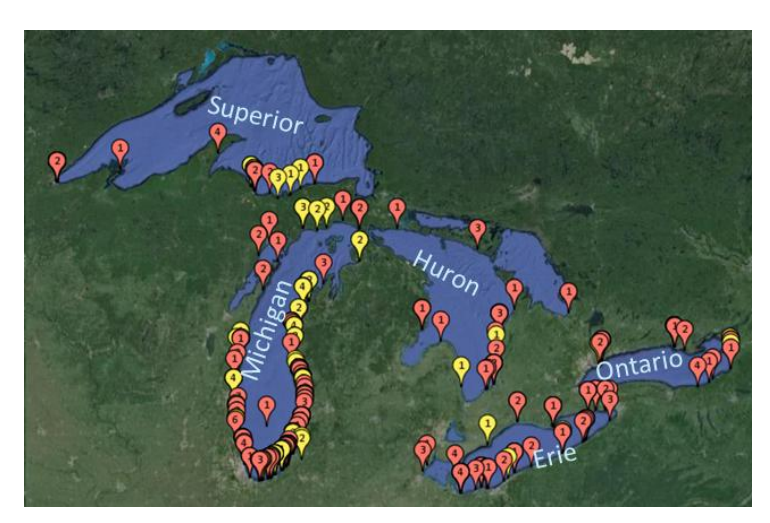


Figure 1-3 | Rip current incidents in the Great Lakes recorded in GLCID database (https://www.weather.gov/greatlakes/beachhazards_stats#) between 2002 and 2020 (red indicate incidents with fatalities, and yellow mean successful rescues).



Figure 1-4 | Shoreline and bluff erosion in the Great Lakes. Image sources: https://web.s3.wisc.edu/shorelinephotos/2012_photos/MW-0637.jpg

incidents have occurred in the five Great Lakes and adjacent freshwater systems, as shown in Fig. 1-3. The Great Lakes Current Incident Database reports an average of 21 rescues and 12 fatalities annually from 2002 to 2020, associated with these currents in the Great Lakes area (NOAA, 2024). Shoreline change refers to the loss or gain of land area, or alterations to the landscape along the water's edge (Camfield and Morang, 1996). It represents a significant environmental threat to beaches, with the potential to degrade natural habitats, damage cultural resources, and endanger facilities, properties, and infrastructure (Jin et al., 2015; Porst et al., 2019). In the Great Lakes region, shoreline change has emerged as an urgent issue,

driven by rapid water-level fluctuations and the widespread expansion of coastal structures (Mattheus et al., 2022). The risks are particularly acute during the fall and winter months, as highlighted by a case study from Muskegon County, Michigan (Acheampong et al., 2025).

Between 2010 and 2020, some sites, such as Jeorse Park Beach, experienced shoreline recession exceeding 20 m (Abdelhady and Troy, 2023). Similar concerns have been reported in Kenosha County (Fig. 1-4), where shoreline retreat and bluff recession pose severe risks to homeowners. In addition to these property-related impacts, certain locations recorded habitat losses of more than 10 m per year between 2010 and 2022 (Theuerkauf and Braun, 2021). Furthermore, the proportion of armored shoreline in Lake Michigan increased sharply from 3.9% in 2014 to 18.7% in 2021, leaving remaining unarmored areas increasingly vulnerable (Theuerkauf et al., 2025). *In view of the consequences of natural hazards in the Great Lake region, effective monitoring and detection to characterize their occurrence and features are imperative*.

1.1.2 Monitoring

Monitoring natural hazards, such as floods, dangerous currents, and rapid shoreline changes is important for acquiring data to characterize their features and impacts. There are three monitoring approaches. First, direct measurements and observation in the field provide foundational data on these hazards. Transects and quadrats are widely used to collect hydraulic, geomorphological, and ecological data in in-situ surveying (Pascoe et al., 1993; Simonson, 1994). This approach is labor-intensive, requiring significant manual effort to gather samples that accurately represent conditions across the entire area of interest. Second, sensors, such as gauges and buoys, are installed at strategic locations, offering continuous, real-time monitoring of environmental parameters such as temperature (Yao et al., 2015), wave patterns (Naffaa, 1995), flow rates (Kawanisi et al., 2012), and current speed (Lane et al., 1999). However, these devices allow for ongoing observation but are often restricted by their high cost and the complexity of their deployment, limiting their application to extensive areas. Given these limitations, achieving long-term, real-time monitoring with high accuracy and broad coverage through in-situ or sensor-based

methods alone is challenging. Remote sensing is a technique used to gather information about objects, areas, or phenomena without making physical contact with them (Elachi and Van Zyl, 2021). This technology, encompassing satellite and aerial imagery, web cameras, and unmanned aerial vehicles (UAVs), is increasingly incorporated into natural hazard monitoring. For instance, satellite data has been widely utilized for flood hazard management (Van Westen, 2000), webcams have been employed to monitor dangerous currents in coastal areas (Holman and Stanley, 2007), aerial images and UAV imagery have been used for observing coastal geomorphological changes (Ford, 2013; Troy et al., 2021). Despite advancements in remote sensing, manual efforts are still required to process the remote sensing data for monitoring natural hazards. *Therefore, monitoring tools that automate remote sensing data processing and enhance the characterization of natural hazard features remain an area needing further exploration and development.*

1.1.3 Detection

The detection of natural hazards through remote sensing data is critical for understanding their occurrence and impacts. Traditional detection techniques often rely on image processing methods such as Fast Fourier Transformation (FFT) and Otsu thresholding. For instance, FFT and other Fourier-based approaches have been employed to detect channel rip currents from velocity images (Trizna, 2017) and video monitoring systems (Stephens et al., 1997). However, these methods encounter limitations in detecting flash rips due to their transient and intermittent nature, as well as their inability to directly capture temporal and spatial rip features. Similarly, Otsu thresholding, Normalized Difference Water Index, Super Water Index, and their derivatives have been applied to detect water boundaries for river channels and coastal regions and further identify geomorphological changes (Otsu, 1975; Gao 1996; Sharma et al., 2015; Zhu et al., 2015). Despite their applications, thresholding techniques struggle to distinguish between sand and water surface

with bubbles, as well as between saturated wet soil and water (Fuse and Ohkura, 2018; Castelle et al, 2021). Furthermore, thresholding methods are susceptible to image noise (Jiao et al., 2006), making it difficult to deliver accurate detection outputs in less-than-ideal environmental conditions. Recent advancements of artificial intelligence (AI) facilitate the detection of natural hazards. There are two branches of AI approaches, traditional machine learning (ML) and deep learning (DL). Traditional ML approaches train models using training dataset, then make decisions based on trained models without being explicitly programmed for each specific task. For example, supported vector machine (SVM) and its variations have been implemented to monitor and map flood inundation from image data (Dandotiya et al., 2014, Chang et al., 2018), principal component analysis (PCA) has been used to detect rip channels from images (Maryan et al., 2019). Although traditional ML approaches have achieved notable successes in detecting natural hazards, their ability to generalize to larger datasets and more complex features presents significant challenges (Lai, 2019; Wang et al., 2021b). DL, with its multi-layered neural networks, offers a robust framework for natural hazard detection in complex datasets. For example, U-Net-based DL models have been crafted for flood extent mapping using remote sensing imagery (Zhao et al., 2022; Li and Demir, 2023), and Region-based Convolutional Neural Networks (R-CNN) have been deployed to detect rip currents from images and videos (de Silva et al., 2021). While these approaches are increasingly being developed and applied worldwide, their deployment for natural hazard detection in the Great Lakes region remains insufficient. Therefore, there is a critical need to advance and tailor deep learning-based detection methods for natural hazards in the Great Lakes, leveraging diverse remote sensing data to overcome the limitations of traditional approaches.

1.1.4 Characterization

The characterization of natural hazards is crucial for understanding their patterns and associated mechanisms, thereby aiding in the management and mitigation of their consequences. Several studies have been conducted to characterize the features of natural hazards, such as temporal and spatial variations in flood magnitude, seasonality, and response time (Saharia et al., 2017), as well as its impacts on erosion and inundation under different watershed settings (Casali and Heinimann, 2019; Rana and Suryanarayana, 2021). However, these studies often rely on gauge data or coarse satellite imagery to identify watershed-level features, overlooking finer spatial variations within the watershed, particularly ecological impacts that exhibit significant variability at micro-scales. In the context of dangerous currents, previous studies have summarized the shape, temporal, and spatial features of rip currents (Castelle et al., 2014; Liu and Wu, 2019; Kim, 2021). However, the characterization of more transient and intermittent rip currents, often referred to as flash rips, remains limited due to detection difficulties. Furthermore, existing studies are largely confined to a small number of cases, lacking the comprehensive information needed to summarize their characteristics with large datasets and integrate associated physical mechanisms. Similarly, studies of characterizing shoreline changes have often relied on manual delineation or thresholding methods, followed by DSAS-based calculations of annual shoreline movement (Peterson and Wu, 2025; Williams et al., 2025). While useful, these approaches require substantial manual effort and are subject to digitizer bias in the case of manual delineation, or reduced accuracy when thresholding is applied. Moreover, they typically do not distinguish true shoreline change (erosion or accretion) from apparent retreat caused by water-level fluctuations. Although characterizing natural hazards is critical, existing methods for high-resolution, long-term, and scalable characterization remain constrained by the labor-intensive nature of fieldwork and the limitations

of traditional image-processing techniques. Therefore, there is a pressing need to leverage highresolution remote sensing data in combination with deep learning approaches to achieve more detailed, scalable, and systematic characterization of natural hazards.

1.2 Research questions and objectives

The background in Sec 1.1 leads to the following research questions:

- 1. Deep Learning and Remote Sensing: How can deep learning and remote sensing be combined to improve natural hazard monitoring in the Great Lakes?
- 2. Detection of Hazards: *How can flood impacts, flash rip currents, and rapid shoreline changes be reliably detected using automated approaches?*
- 3. Characterization of Hazards: *How can these hazards be systematically characterized to capture their driving factors, features, dynamics, and resilience patterns?*

Following the above research questions, the overall objective of this research is to characterize natural hazards in the Great Lakes using remote monitoring and deep learning approaches. The proposed research includes four chapters, each dedicated to addressing the critical yet underserved needs in the monitoring and detection of natural hazards. This study seeks not only to offer more effective monitoring and detection methods, but also to characterize their distinct features in ways that can guide future management. For each chapter, the specific research question, objective, and contribution are summarized in the following table:

1.3 Outline of proposed chapters

	Chapter 2	
Topic	Characterization of stream habitat quality using UAV-based toolkit	
Question	How can we evaluate stream habitat quality conditions using remote sensing	
	methods?	
Objective	To provide quantitative, automatic, and accurate evaluation on stream habitat	
	quality condition.	
Contribution	Develop a UAV-based toolkit for automatically and accurately evaluating	
	stream habitat quality metrics.	
	Chapter 3	
Topic	Loss and resilience of stream habitat due to flooding	
Question	How are different metrics of stream habitat quality affected by flood events?	
Objective	To evaluate flood impacts, including loss and resilience, on stream habitat	
	quality using remote sensing methods.	
Contribution	Employ UAV-based technology to observe changes in stream habitat quality	
	metrics and characterize the loss-resilience responses triggered by flood events.	
Chapter 4		
Topic	Detection and characterization of flash rips in Lake Michigan	
Question	What are the variations in flash rip currents induced by three different driving	
	mechanisms?	

Objective	To identify flash rip mechanisms and compare flash rip features under different	
	mechanisms.	
Contribution	Develop a deep-learning-based tool for flash rip detection and compare the	
	differences in flash rip features driven by waves and water level fluctuations.	
Chapter 5		
Topic	Shoreline Change Estimation Toolkit (SCET): A Deep Learning Framework	
	for Detecting and Characterizing Coastal Erosion and Accretion	
Question	How can rapid shoreline changes be reliably detected and distinguished	
	between true morphological change and apparent retreat driven by water level	
	fluctuations?	
Objective	To automate shoreline extraction, calculate shoreline change rates, and identify	
	hotspots of rapid change while separating erosion/accretion from water-level-	
	driven fluctuations.	
Contribution	Develop a deep-learning-based shoreline segmentation and analysis	
	framework that rapidly detects shoreline change and distinguishes	
	morphological change from water-level-driven shifts.	

Overall, the contribution of this research aims to enhance the monitoring and analysis approaches for natural hazards and provide more comprehensive understanding of natural hazard features in the Great Lakes region.

Chapter 2: Characterization of stream habitat quality using UAV-based toolkit

2.1 Introduction

Stream habitat quality, referred to the condition of places where fish and other aquatic organisms need for concealment, breeding and feeding (Karr, 1999; USEPA, 2022), plays an important role in determining the efficacy of aquatic communities (Maddock, 1999) in several ways. First, stream habitat quality is associated with the species density and community composition of riparian vegetation (Nilsson & Svedmark, 2002; Hough-Snee, et al., 2013), as well as aquatic organisms such as fish and macroinvertebrates (Sonkar et al., 2023; Zheng et al., 2023). Second, stream habitat quality is essential for providing ecosystem services, such as mitigate flood risk (Darby, 1999), soil conservation (Saad et al., 2018), pollutant assimilation (Dosskey et al., 2010), and recreation (Hughes, 2015). Third, stream habitat quality is sensitive to anthropogenic alterations (Allan, 2004; Arthington et al, 2010) such as urbanization, dams, and pollutant discharge (Malmqvist & Rundle, 2002; Roni, et al., 2008) as well as other disturbances like invasive species (Scott & Helfman, 2001) and climate change (Null, et al., 2013). In view of the importance and vulnerabilities, characterization of stream habitat quality to address environmental concern or conservation relies on monitoring and scientific-based evaluation.

The evaluation of stream habitat quality, in practice, relies on multi-metric indices (MMIs), which integrate a variety of attributes from streams and riparian zones to provide a holistic assessment. Early-stage MMIs, such as like an index of biotic integrity (IBI), focus on comparing fish population and species richness influenced by human activities to natural circumstances (Karr, 1981). Revised MMIs incorporate more physical, chemical, and biological attributes for comprehensive assessments of regional stream habitat. Key attributes include physical habitat (Fausch et al., 1984), water quality (Karr, 1986), biological activity (Fore et al., 1996), and

sediment transport (Allan et al., 1997). These MMIs have become a cornerstone for monitoring programs conducted by local and national agencies, as summarized in an EPA report (Barbour et al, 1999). Recent advancements have expanded MMIs to account for human disturbances relative to unimpaired conditions (Oberdorff et al., 2002; Somerville, 2010) and to be applicable across a broader range of stream types (Bolding et al., 2020; Mamun & An, 2020). As MMIs continue to be developed and refined, their effectiveness hinges on the implementation of reliable and systematic monitoring systems.

Conventional stream monitoring measures physical geometry data such as width, depth, and bed slope using a tape measurement (Simonson, 1994), and surveys ecological data like biodiversity of species, vegetation covers, and substrates by transect or quadrat sampling (Wang et al., 1996). However, these approaches have several limitations. First, assessments of some descriptors, such as riffles and pools, are subjective and could be affected by accessor bias (Woodget et al., 2016). Second, some locations are difficult to access due to deep or fast-flowing water (Cavanagh et al., 1997). Third, discrete sampling data with limited transects or quadrats can lead to misinterpret the spatial variation of highly diverse landscapes (Cooper et al., 1997). Finally, data collection is labor-intensive and time-consuming (Simonson et al., 1994), especially for larger streams. While traditional methods provide valuable ground truth data, these challenges underscore the need for alternative monitoring approaches that are reliable, safe, continuous, and efficient.

Remote sensing techniques, such as satellite-based imagery, aerial photogrammetry, and Light Detection and Ranging (LiDAR), are widely applied in stream and river habitat monitoring nowadays (Marcus et al., 2003; Dietrich, 2016; Tompalski et al., 2017). For instance, satellite land cover metrics have been employed in ranking methods to assess stream habitat quality (Snyder et

al., 2005), and a combination of LiDAR and aerial photogrammetry has been developed to accurately delineate riparian terrains and monitor floodplain morphology changes (Lallias-Tacon et al., 2017). Nevertheless, these techniques face notable constraints. Spatial resolutions of remote sensing data, such as 30 m for LandSat 8 and 10 m for Sentinel-2, are challenging to capture fine-scale in-stream and riparian habitat features (Marcus & Fonstad, 2008; Nagendra et al., 2013). Additionally, low revisit frequencies, ranging from weeks or months for satellite imagery to revisiting the same area, make it difficult to collect up-to-date information for rapid habitat changes caused by extreme weather events (Wulder et al., 2015). Furthermore, the high cost of advanced techniques, such as airborne LiDAR, as well as the complications of aligning data from multiple surveying tasks, can limit their practicality for achieving the required data quality (Okyay et al., 2019). To date, developing cost-effective and efficient remote sensing methods for stream habitat monitoring remains an ongoing challenge.

In recent years, drone-based surveying technologies, particularly unmanned aerial vehicles (UAVs), have rapidly advanced and been increasingly applied to monitor stream habitat quality (Flener et al., 2013; Langhammer, 2019). This growth is driven by several factors. Advances in optical sensors, hovering stabilization, and GPS integration now enable UAVs to capture high-quality 4K images or 1080P videos with precise flight paths. Additionally, improvements in drone flight control applications, featuring autopilot capabilities for tasks such as takeoff, route-following, image capture, and landing, allow for fully automated operation via mobile devices (Terry et al., 2021). Moreover, image processing algorithms, such as Structure from Motion (SfM), can reconstruct high-resolution three-dimensional terrains with mean horizontal errors below 0.1 m and vertical errors under 0.3 m (Turner et al., 2013; Elkhrachy, 2021). Despite these technological advancements, the application of UAVs for stream habitat quality evaluation

remains rare. To date, there are no integrated UAV tools for multi-metric stream habitat quality evaluation, as far as the authors are aware.

2.2 Objectives and research goals

The objective of this chapter is to develop a suite of drone-based cost-effective monitoring toolkits that are applied to evaluate stream habitat quality. Currently, there are no comprehensive UAV-based tools available for evaluating stream habitat quality using Multi-metric Indices (MMIs). This study hypothesizes that UAV technology can provide automatic, continuous, and high-accuracy evaluations, yielding MMI results comparable to those obtained through traditional methods for reference transects. To achieve this, three specific research goals are outlined:

- 1. Develop algorithms for automating UAV operations and subsequent image processing tasks for stream habitat surveys.
 - 2. Provide continuous evaluation of stream habitat quality based on MMIs.
- 3. Validate the UAV-derived evaluation outcomes against traditional survey results from reference transects.

2.3 Study site

The study site is the area between bridges B₁ and B₂ at the headwater of Black Earth Creek in the village of Cross Plains, Wisconsin (see Fig. 2-1). Black Earth Creek, a high-quality trout stream, is a 27-mile-long tributary flowing westward to Blue Mounds Creek, Dane County, WI in Fig. 2-1a. The main creek has an average width and water depth of 8.6 meters and 1.4 meters, respectively (Wisconsin DNR, 2019). The base flow is approximately 0.8 m³/s, based upon the two upstream gauges (USGS 05406457 and 05406469), denoted as G₁ and G₂. The stream is

classified as a Class 1 type with sufficient natural reproduction to sustain wild trout populations (Wisconsin DNR, 2017). The original straight channel between B₁ and B₂ (the dashed line in Fig. 2-1b) was restored in 2014. The meandering stream, shown as the solid line in Fig. 2-1b, with riparian grasses and a sequence of riffles and pools in Fig. 2-1c built to enhance fish habitat (Wisconsin DNR, 2019). In the summer of 2018, an extreme rainfall storm event yielded a historically high flow rate of 29.73 m³/s that surpassed the previously recorded water level and

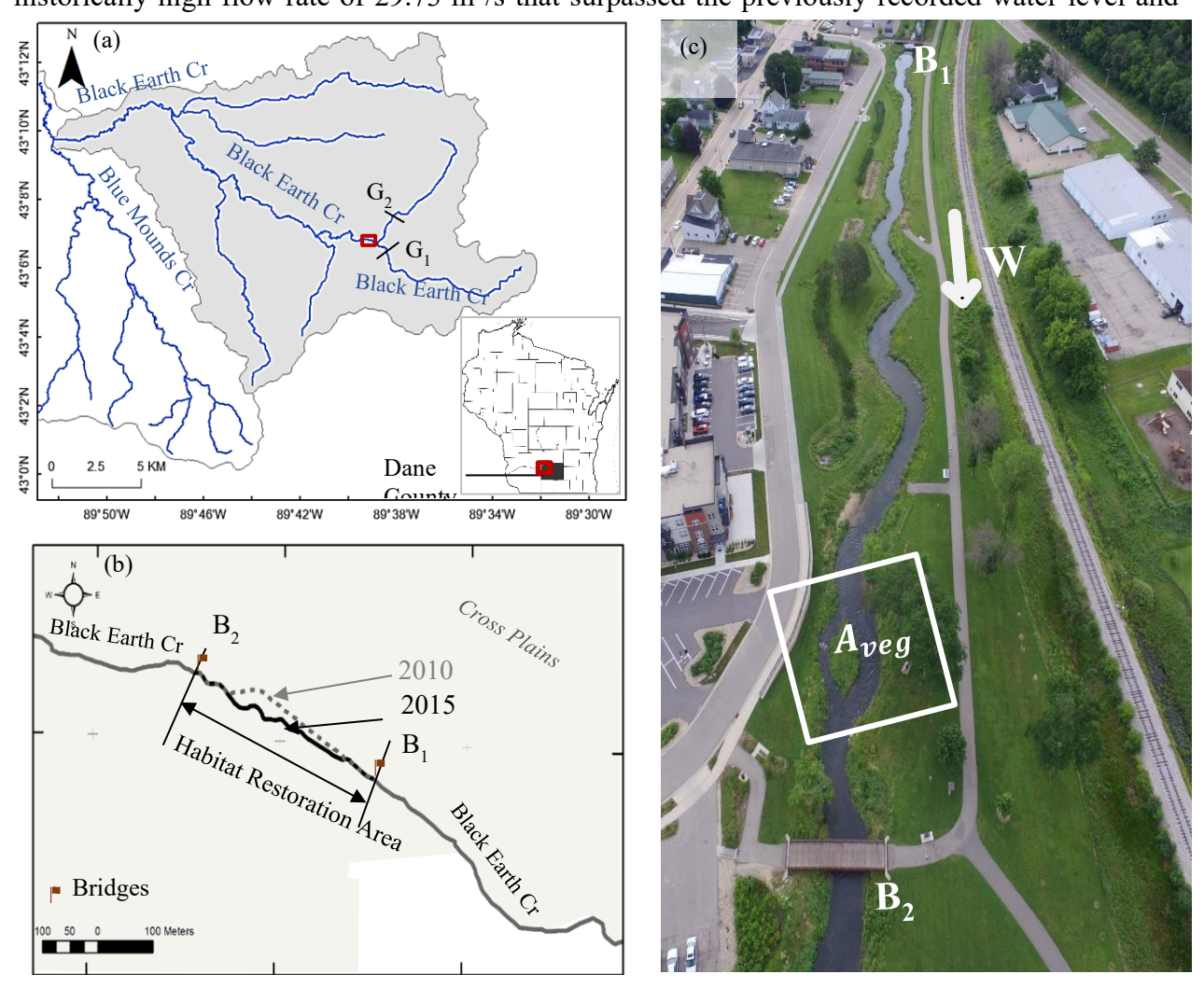


Figure 2-1 | Study area of Black Earth Creek in Dane County, WI. (a) Black Earth Creek Watershed. G_1 and G_2 are the two USGS stream gauges. (b) The 2010 straightened stream (dashed line) and the 2015 meandered stream (solid line) channel. B_1 and B_2 are the upstream and downstream bridges, respectively. (c) An oblique aerial photo of the study site. The symbol "W" represents the flowing direction of Black Earth creek toward the west. The vegetated riparian area, A_{veg} , is partly blocked by trees and shown as a white solid rectangle.

incurred severe floods. One vegetated riparian area, shown as a dashed rectangle A_{veg} in Fig. 2-1c, experienced degradation and severe erosion.

2.4 Methods

The toolkits were developed as a suite of Python scripts designed to streamline three key tasks: flight route planning for stream surveys, image processing for generating terrain maps and digital elevation models (DEMs), and MMI computation for evaluating stream habitat quality, as

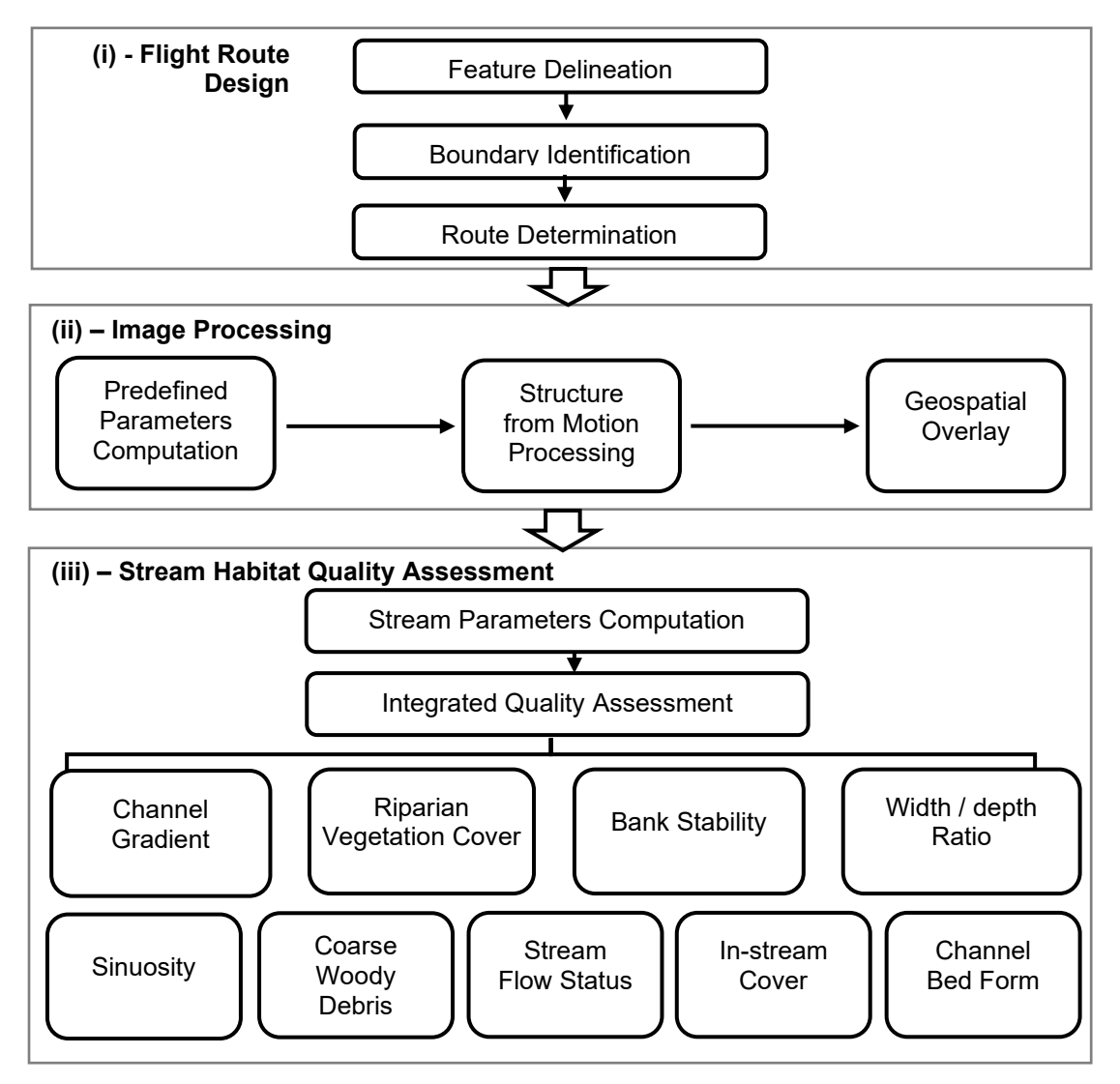


Figure 2-2 | A flowchart with (i) Toolkit I as flight route design, (ii) Toolkit II as image processing, and (iii) Toolkit III as stream habitat quality assessment.

illustrated in Fig. 2-2. Detailed descriptions of each toolkit are provided in the following subsections.

2.4.1 Flight route design

Toolkit I, shown in Fig. 2-2i, optimizes flight routes for stream surveys by minimizing flying time, avoiding obstacles, and achieving desired image resolution in three steps. First, feature delineation involves digitizing georeferenced aerial maps using ArcMap 10.8 to classify features such as trees, buildings, streams, and flight areas. Fig. 2-3a illustrates a sample map, where trees are marked as light green points, buildings as brown polygons, streams as blue polylines, and the

flight area outlined in yellow. Second, boundary identification processes these features to establish buffer zones for obstacle avoidance and focusing areas that require greater attention. Buffer distances are set to 5 m for trees and buildings, while a 10 m from stream channel is set as the

Table 2-1 | The Modified D-Lite algorithm

```
Let N = length(R(S \rightarrow T)), s_{start} = R(1), s_{end} = R(2), res = [] for i in 3 to N if R(i) in the line s_{start} \rightarrow s_{end} then s_{end} = R(i) else s_{start} = R(i), res = res + s_{start}

Let N_1 = length(res), s_{start} = res(1), output = [] for j in 3 to N_1 if line s_{start} \rightarrow res(j) is blocked or j = N_1 then output = output + res(j), s_{start} = res(j)

Return output
```

focusing area. Fig. 2-3b shows these buffer zones and focusing area, and the overlaid sketch for flight boundary is shown in Fig. 2-3c. Third, route determination generates two optimized flight routes for high-elevation (30 m above ground) and low-elevation (5 m above ground) surveys. The high-elevation route covers the overall study site, as illustrated in Fig. 2-3d. The routes are connected in an S-shaped pattern (e.g., $A_1 \rightarrow A_2 \rightarrow A_3 \rightarrow A_4 \rightarrow B_2 \rightarrow B_1 \rightarrow C_1 \rightarrow C_2 \rightarrow D_2 \rightarrow D_1$). The interval between parallel flight boundaries (the two red lines, denoted as F_{max} and F_{min}) is set to Δd to achieve at least a 75% image overlap, with a 90% overlap applied in focused areas. The low-elevation route addresses areas blocked or shaded by canopy in the high-elevation route. The

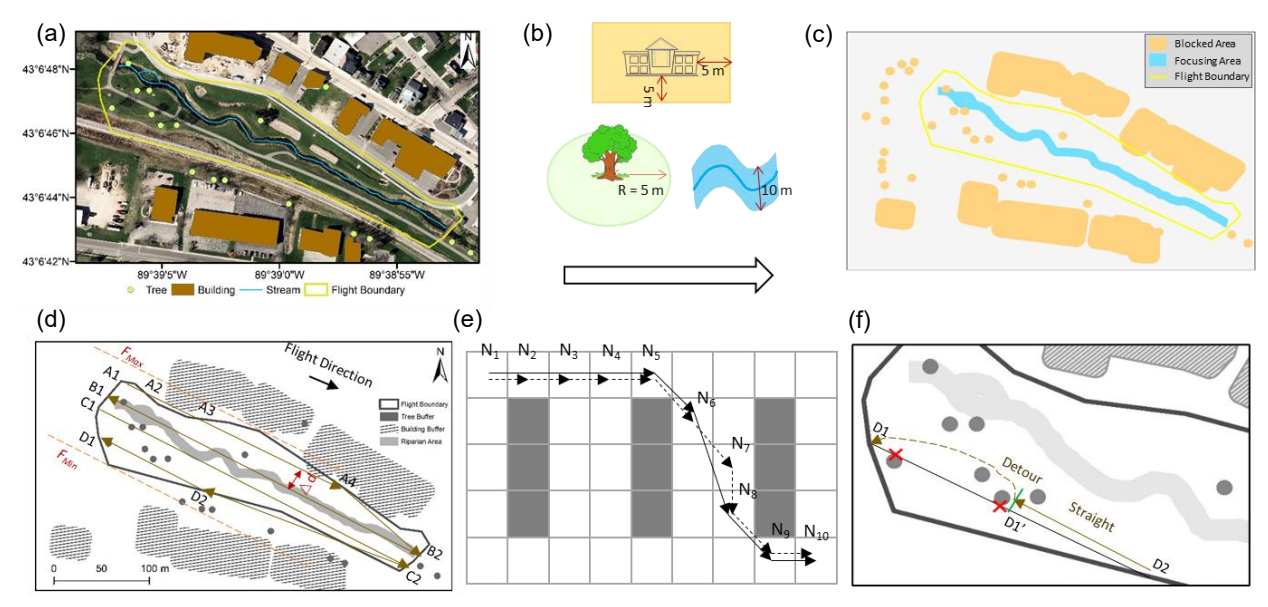


Figure 2-3 | Illustration for Toolkit I. (a) Marked trees, buildings, the river and flying boundary. (b) Buffer distances for blocked buildings, trees, and surveyed streams. (c) Overlaid sketch of blocked areas, focusing areas, and flight boundaries. (d) An example of a high-elevation flying route in an S-shape pattern. (e) An example of a low-elevation flying route generated using the Modified D-Lite algorithm. (f) Two routes with the straight route blocked by obstacles (solid line) and the detoured route after the MDL algorithm (dashed line from D1' to D1).

Modified D-Lite (MDL) algorithm (Ramalingam & Reps, 1996; Koenig & Likhachev, 2002) is employed to generate detoured paths that avoid obstacles. Detailed MDL steps are provided in Table 2-1. Fig. 2-3e demonstrates an example of an original route $(N_1 \rightarrow N_2 \rightarrow N_3 \rightarrow N_4 \rightarrow N_5 \rightarrow N_6 \rightarrow N_7 \rightarrow N_8 \rightarrow N_9 \rightarrow N_{10})$. After applying the MDL algorithm, redundant nodes along the same straight line (e.g., node N_2 , N_3 , and N_4) and unnecessary turning nodes that do not influence obstacle avoidance (such as N_7) are removed, resulting in a smoother detoured route $(N_1 \rightarrow N_5 \rightarrow N_6 \rightarrow N_8 \rightarrow N_9 \rightarrow N_{10})$. Fig. 2-3f compares the two routes: the original straight route blocked by obstacles (solid line) and the detoured route after applying the MDL algorithm (dashed line from D_1 ' to D_1). Finally, the flight route designs are saved as shapefiles for UAV deployment, ensuring efficient and obstacle-free drone operation.

2.4.2 Image processing

Toolkit II, as shown in Fig. 2-2ii, processes UAV imagery to reconstruct three-dimensional georeferenced terrains using Agisoft Metashape, chosen for its compatibility with the Python application programming interface (API). To optimize processing time, the toolkit applies predefined output quality parameters (lowest, low, medium, high, ultra-high) based on two factors: computer hardware settings (e.g., CPU cores, frequency, GPU cores) and memory requirements determined by image number, size, and quality (Table 2-2 and Table 2-3). Fig. 2-4 depicts the workflow for Structure from Motion (SfM) and geospatial overlay, where imagery from high- and low-elevation flights (Fig. 2-4a) is processed in separate pipelines, represented by brown arrows

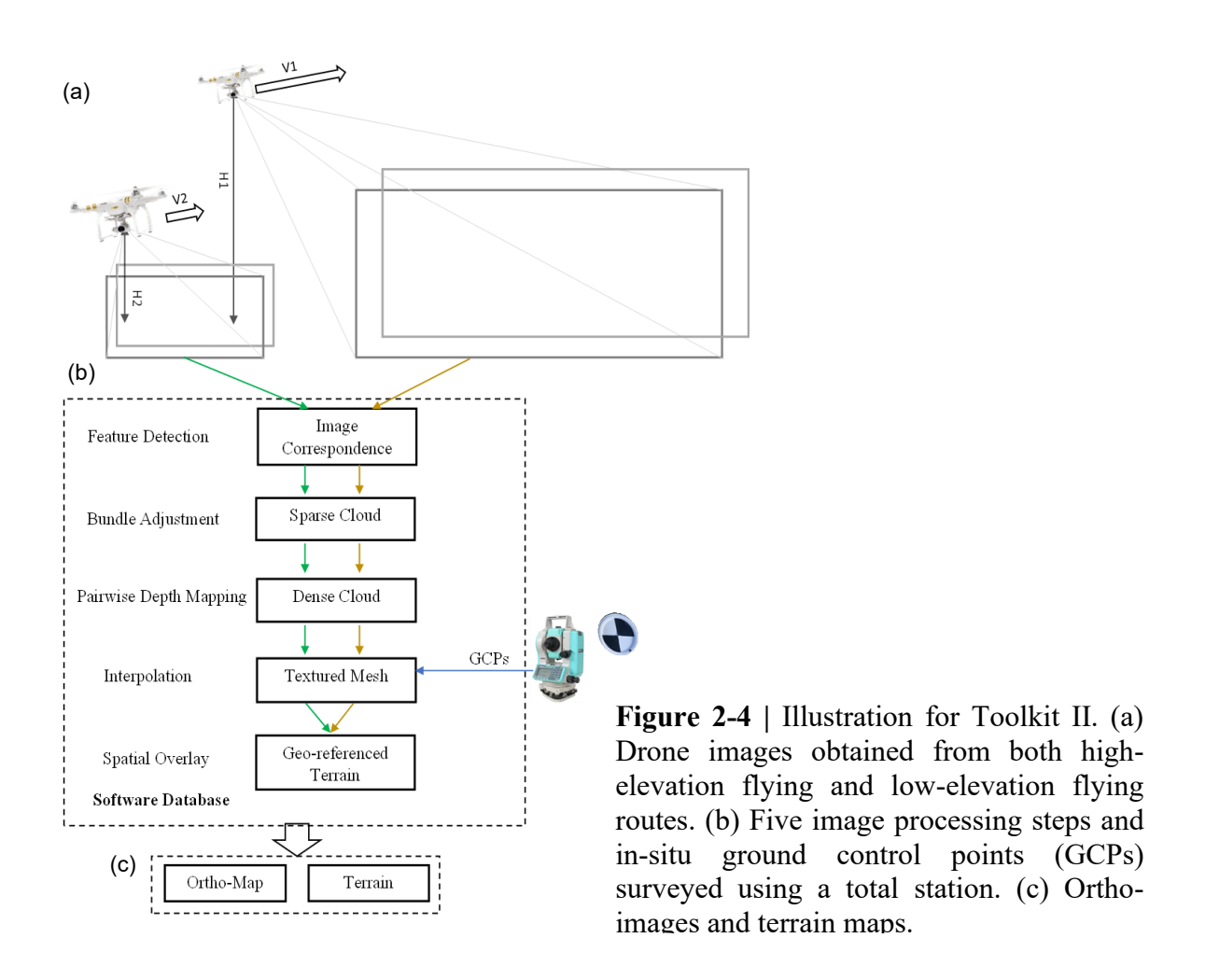
Table 2-2 | An example of processing quality using computer hardware settings

Code	CPU Cores	CPU	GPU	Suggested Processing Quality							
		Frequency (GHZ)	cuda cores	Alignment	Dense Point Cloud	Mesh	Orthomap				
A	4	2+	# GPU	Lowest	Lowest	Lowest	Lowest				
В	6	3+	1000	Low	Low	Low	Low				
C	8	3.5+	2000	Medium	Medium	Medium	Medium				
D	12	4+	3600	High	High	Medium	Medium				
E	16	4+	7200	High	High	High	High				
F	24	4+	9600	Ultra High	Ultra High	High	High				
G	32	4+	10250	Ultra High	Ultra High	Ultra High	Ultra High				

Table 2-3 | Estimated memory requirement for point cloud and 3-D texture mesh computation

	Image N.O.		Estimated Memory Requirement (GB) ¹														
Image Quality		Point Cloud	3-D Textured Mesh (Lowest)		3-D Textured Mesh (Low)		3-D Textured Mesh (Medium)		3-D Textured Mesh (High)			3-D Textured Mesh (Ultra High)					
			Min	Avg	Max	Min	Avg	Max	Min	Avg	Max	Min	Avg	Max	Min	Avg	Max
1080P ²	20	0.02	0.01	0.01	0.02	0.03	0.06	0.08	0.10	0.23	0.33	0.41	0.91	1.33	1.66	3.65	5.31
	50	0.05	0.01	0.03	0.04	0.06	0.14	0.21	0.26	0.57	0.83	1.04	2.28	3.32	4.15	9.12	13.27
	100	0.50	0.03	0.06	0.08	0.13	0.29	0.41	0.52	1.14	1.66	2.07	4.56	6.64	8.29	18.25	26.54
	200	1.00	0.05	0.11	0.17	0.26	0.57	0.83	1.04	2.28	3.32	4.15	9.12	13.27	16.59	36.50	53.08
	500	2.50	0.13	0.29	0.41	0.65	1.43	2.07	2.59	5.70	8.29	10.37	22.81	33.18	41.47	91.24	132.71
	1000	5.00	0.26	0.57	0.83	1.30	2.85	4.15	5.18	11.40	16.59	20.74	45.62	66.36	82.94	182.48	265.42
4K ³	20	0.02	0.02	0.05	0.07	0.11	0.23	0.33	0.44	0.91	1.33	1.77	3.65	5.31	7.08	14.60	21.23
	50	0.05	0.06	0.11	0.17	0.28	0.57	0.83	1.11	2.28	3.32	4.42	9.12	13.27	17.69	36.50	53.08
	100	0.50	0.11	0.23	0.33	0.55	1.14	1.66	2.21	4.56	6.64	8.85	18.25	26.54	35.39	72.99	106.17
	200	1.00	0.22	0.46	0.66	1.11	2.28	3.32	4.42	9.12	13.27	17.69	36.50	53.08	70.78	145.98	212.34
	500	2.50	0.55	1.14	1.66	2.76	5.70	8.29	11.06	22.81	33.18	44.24	91.24	132.71	176.95	364.95	530.84
	1000	5.00	1.11	2.28	3.32	5.53	11.40	16.59	22.12	45.62	66.36	88.47	182.48	265.42	353.89	729.91	1061.68
	20	0.02	0.09	0.18	0.27	0.44	0.91	1.33	1.77	3.65	5.31	7.08	14.60	21.23	28.31	58.39	84.93
	50	0.05	0.22	0.46	0.66	1.11	2.28	3.32	4.42	9.12	13.27	17.69	36.50	53.08	70.78	145.98	212.34
8K ⁴	100	0.50	0.44	0.91	1.33	2.21	4.56	6.64	8.85	18.25	26.54	35.39	72.99	106.17	141.56	291.96	424.67
	200	1.00	0.88	1.82	2.65	4.42	9.12	13.27	17.69	36.50	53.08	70.78	145.98	212.34	283.12	583.93	849.35
	500	2.50	2.21	4.56	6.64	11.06	22.81	33.18	44.24	91.24	132.71	176.95	364.95	530.84	707.79	1459.81	2123.37
	1000	5.00	4.42	9.12	13.27	22.12	45.62	66.36	88.47	182.48	265.42	353.89	729.91	1061.68	1415.58	2919.63	4246.73

for high-elevation and green arrows for low-elevation images (Fig. 2-4b). The five key processing steps include feature detection to align images, bundle adjustment to identify drone camera positions and create sparse point clouds, pairwise depth mapping to generate dense point clouds, geospatial interpolation and color blending to produce textured terrain surfaces, and spatial overlay to merge high- and low-elevation surfaces into georeferenced terrain maps. Predefined parameters are applied at each step to optimize efficiency, and the final outputs are ortho-images and terrain maps (Fig. 2-4c).



2.4.3 Stream habitat quality assessment

Toolkit III, illustrated in Fig. 2-2iii, computes MMIs to perform an integrative stream habitat quality assessment. The first step involves selecting relevant parameters based upon the definitions in the Wisconsin DNR guidelines (Wisconsin DNR, 2018), USDA guidelines (Simonson, 1994) and EPA reports (Somerville, 2010). Fig. 2-5a shows the schematic of a stream with various features such as bends (e.g., Be₁ and Be₂), erosion areas (e.g., E₁ and E₂), trees (T), and coarse woody debris (C). For each transect (Fig. 2-5b), we calculate a set of geometry parameters including stream width (W), eroded bank width (E), vegetation buffer width (B), fish cover width (F), bank top width (BT) between the left and right banks, and stream depth (D). Along the stream (Fig. 2-5c), additional parameters such as the meandered stream length (L_0) and pool lengths (e.g., L_1 and L_2) are measured. These parameters are delineated from orthomaps generated by Toolkit II: stream banks represent the land-water interface, eroded zones are areas of bare soil or recessed vegetation, in-stream cover includes emergent vegetation near the land-water interface, and vegetation buffer zones are undisturbed vegetated areas adjacent to the stream. Once all geometry parameters were delineated, the medial axis transformation (MAT) algorithm (Lee, 1982; McAllister & Snoeyink, 2000) is applied to construct the stream centerline C, as depicted in Fig. 2-5d. The stream width W at a centerline node is determined as the shortest segment length connecting the left (L) and right (R) banks through the node, as shown in Fig. 2-5e. The erosion width E, fish cover width F, and vegetation buffer width B can be obtained following similar ways. The bank top width (BT) is the distance between the left and right bank tops. Average stream depth (D) at each transect is estimated as the difference between the water surface elevation derived from the terrain map and the riverbed elevation obtained through field measurements. Bend locations are identified as points along the centerline (M) where the turning angle (θ) exceeds 30 degrees

(Fig. 2-5f). Pool lengths are computed by intersecting pool area polygons with centerline (M) based on three thresholds: an average stream depth above 70% of transects, an estimated velocity below 70% of transects, and a percentage of white surface water pixels below 10% (Fig. 2-5g).

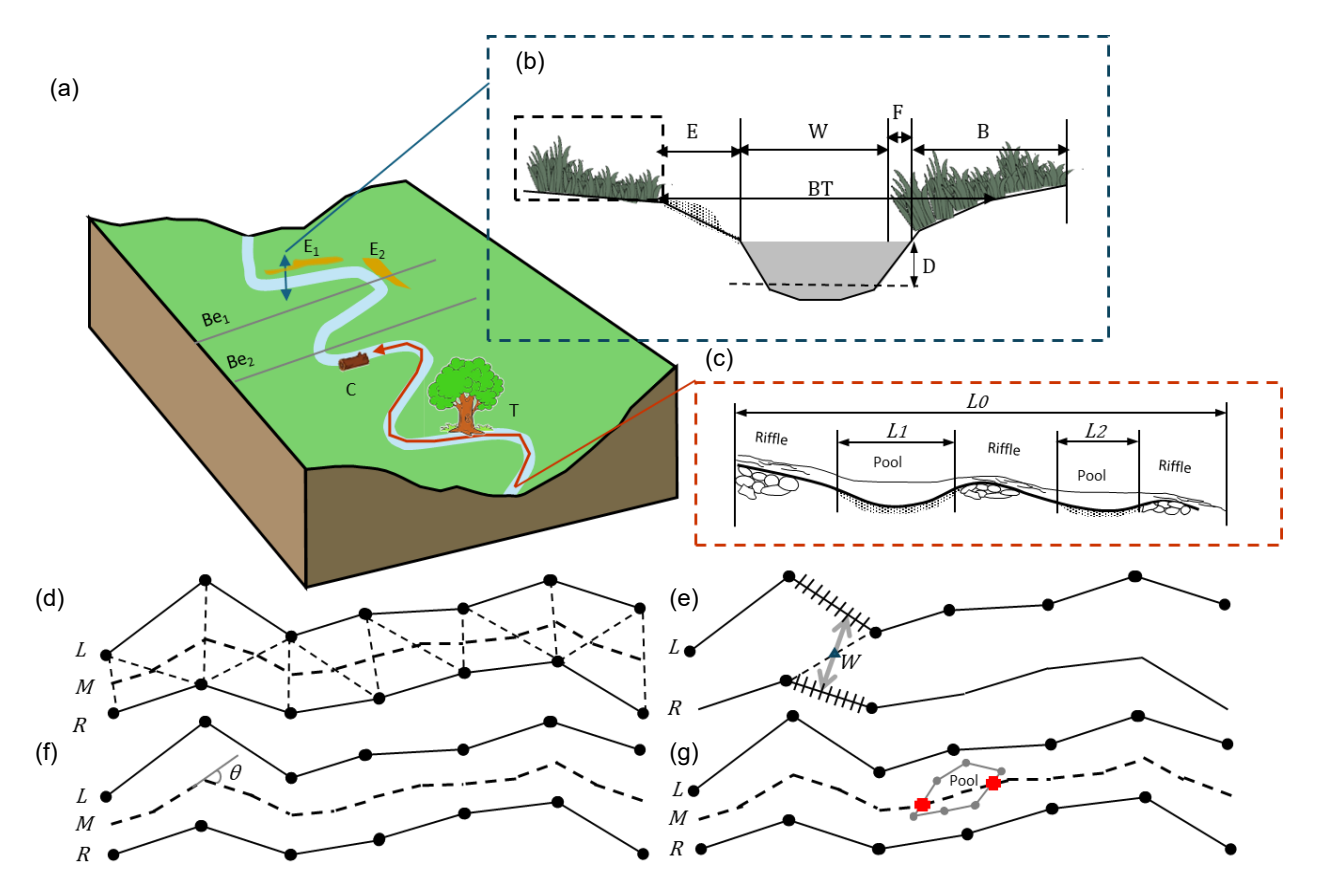


Figure 2-5 | Illustration for Toolkit III: stream habitat indices definition. (a) Schematic of a meandered stream with eroded bank E, coarse wood debris CWB, bends Be, and tree T. (b) Definition of eroded bank width E, stream width W, fish cover width F, buffer width B, bank top width BT, and average stream depth D. (c) Definition of pool length. (d) Stream length calculation using the MAT algorithm. (e) Stream width calculation for a median axis point. (f) Bend identification. (g) Pool length calculation.

The integrated stream habitat quality is then assessed based upon the MMIs with nine parameters out of 67 stream habitat assessment protocols (Somerville, 2010), based on their frequent usage and feasibility of assessment via UAV without additional sensors. Table 2-4 lists the nine MMIs: channel gradient M₁; riparian vegetation buffer M₂; bank stability M₃; width /

depth ratio M₄; sinuosity M₅; stream flow status M₆; coarse woody debris M₇; in-stream cover M₈; and channel bed forms M₉. Detailed definitions and assessment criteria of each metric can refer to Simonson (1994), Somerville (2010), and Wisconsin DNR (2018). Except for the index M₁ that is classified as a high- or mild-gradient stream, the rest of indices (i.e., from M₂ to M₉) are scored as 10, 7.5, 5, and 2.5 for excellent, good, fair, and poor quality, respectively. The integrated assessment is by summing up the scores of scored indices. The overall stream habitat quality status is identified as excellent if the total score is greater than 60, good if greater than 50, fair if greater than 40, and poor if less than 40.

Table 2-4 | Multi-metric indices (MMIs) for stream habitat quality assessment

			Score							
Code	Code Name		Description	Excellent	Good	Fair	Poor			
Coue	Name		Description	10	7.5	5	2.5			
M ₁	Channel Gradient ¹		The change of channel bed elevation per unit length (m / m) ²							
M ₂	Riparian Vegetation Buffer	The w	idth of riparian zone covered by continuous and undisturbed natural lands (m)	> 10	5~10	1~5	< 1			
M ₃	Bank Stability	The a	verage width of stream bank has been eroded or have the erosion potential (m)	< 0.2 m	0.2 m – 0.5 m	0.5 m – 1 m	> 1 m			
M ₄	Width / depth Ratio	The r	atio of average stream width to the average thalweg depth (m / m)	< 7:1	7:1 – 15:1	15:1 – 25:1	> 25:1			
M ₅	Sinuosity	Н	Ratio of the distance between bends or riffles to the stream width $\left(m/m\right)$	7:1	7:1 – 15:1	15:1 – 25:1	> 25:1			
		М	The ratio of meandered channel length to straight line (m / m)	> 3:1	3:1 – 2:1	2:1 – 1:1	1:1			
M ₆	Stream Flow Status		The ratio of stream channel saturated with water (%)	90%-100%	75% - 90%	25% - 75%	0 – 25%			
M ₇	Coarse Woody Debris	Н	The ratio of stream banks covered by trees, logs, and branches (%)	> 70 %	40% - 70%	20% - 40%	< 20%			
IVI ₇	Coarse Woody Debris	M		> 50%	30% - 50%	10% - 30%	< 10%			
M ₈	In-stream Cover	The pe	ercent of stream surface water having overtop vegetated fish shelter $(\%)$	> 12%	7% - 12%	2% - 7%	< 2%			
M ₉	Channel Bed Forms		The percent of stream length with pools (%)	40% - 60%	30% - 40%,	10% - 30%,	< 10%,			
					60% - 70%	70% - 90%	> 90%			
	Total Score			> 60	45 - 60	30 - 45	< 30			
Note: 1. Channel gradient determines the channel category – high gradient channel (H) if M ₁ value > 0.02, mild gradient channel (M) otherwise.										

2.4.4 Field measurements

Drone flight missions and an in-situ field survey were conducted in September 2019. The drone mission consisted of a high-elevation route covering the entire study site and a low-elevation route focused on a severely eroded vegetated riparian area, indicated by the dashed polygon in Fig. 2-6a. The in-situ field survey provided independent elevation measurements and transect-based habitat health assessments to validate results from the toolkits, 46 ground control points (GCPs,

yellow dots in Fig. 2-6a) were measured using a Nikon Nivo total station instrument, which has a stated accuracy of 3 mm \pm 2 ppm. Two types of GCPs were employed: easily identifiable points visible from an aerial view, such as building corners, and points marked with 1-inch plates for those less distinguishable in aerial imagery. For each GCP, the x, y, and z coordinates corresponding to the instrument point (IP) were recorded. The z-coordinate data were transformed into elevation values using the North American Vertical Datum of 1988 (NAVD 88), with reference elevations (B₁ and B₂) derived from a 2017 LiDAR survey by Dane County, Wisconsin. Among the 46 GCPs, 25 were used to calibrate the reconstructed landscape generated by Toolkit

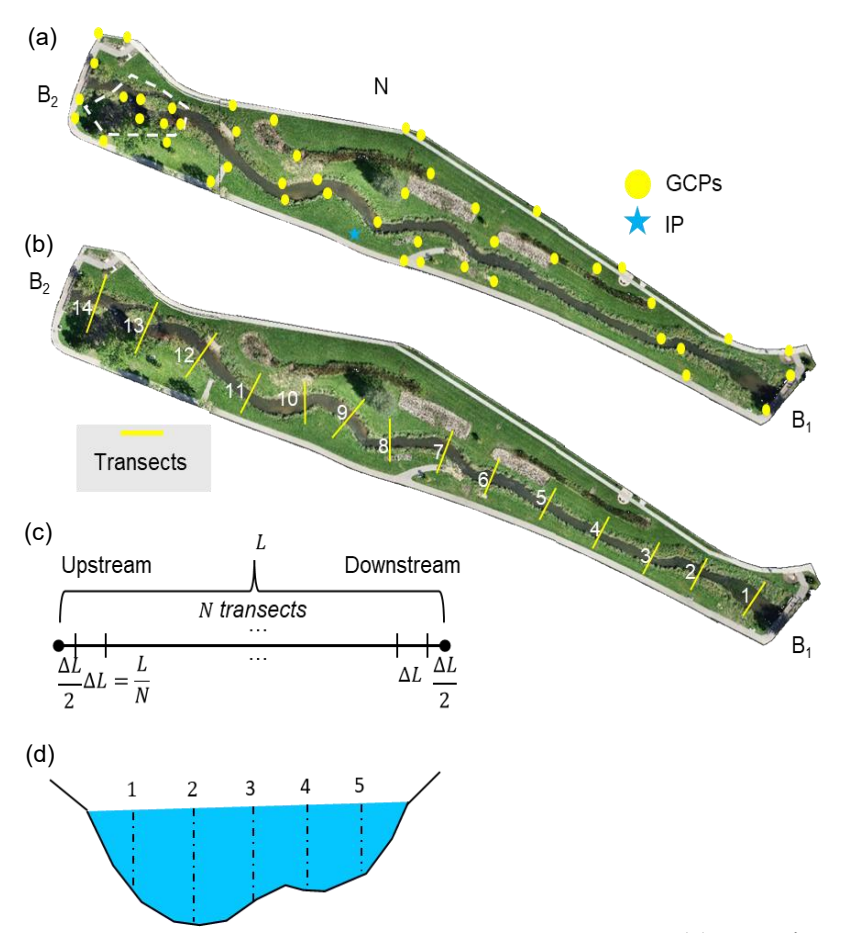


Figure 2-6 | **The sampling methods of on-site validation.** (a) Locations of ground control points (GCPs, yellow dots) and the instrument point (IP, blue star); (b) Locations of 14 transects for tape-based measurements; (c) The way to select transects within a stream segment; (d) The way to equally sample within a transect side view.

II, while the remaining 21 were used to validate the terrain output through root mean square error (RMSE) analysis between the reconstructed and measured elevations. For the transect-based health assessment, Fig. 2-6b shows the 14 surveyed transects across the study site. The first transect was conducted downstream of bridge B_1 , with the subsequent 13 transects spaced equally at intervals of ΔL until reaching bridge B_2 (Fig. 2-6c). At each transect, stream width (W), vegetated buffer width (B), in-stream fish cover (F), bank top width (BT), and erosion width (E) were measured using measuring tapes. Additionally, coarse woody debris (C), riffle-pool sequences, tree shadows (T), and the number of bends (Be) were surveyed and recorded. Stream depth (D) was measured at five equally spaced points within each transect (Fig. 2-6d), and the average of these measurements was taken as the mean stream depth.

2.5 Results

2.5.1 Performance of flight routes

Performance of the designed flight routes is evaluated in terms of obstacle avoidance capability and total flight time. Fig. 2-7 shows the effectiveness of avoiding obstacles for the design of a low-elevation route. The original design of an S-shape flight route with 90% overlapping ratio would hit the three obstacles, O₁, O₂, and O₃, as shown in black solid lines in Fig. 2-7a. The Modified D-Lite (MDL) algorithm developed in the Toolkit I avoids obstacles by applying the strategic detours around O₁, O₂, and O₃, as shown by the red boxes in Fig. 2-7b. Specifically, the MDL algorithm refines the detours near O₂ and O₃, removing 94% of unnecessary nodes (i.e., from 265 to 15) in the original flight route and maintaining a minimum drone-to-tree/building obstacle distance of 5 meters. The flight time for the low-elevation flight route is 800.94 seconds, based upon a 2 m/s flight speed for the transition (i.e., starting and ending) routes and 1 m/s for the S-shape flight route. Adding 30 seconds for liftoff and landing, the total flight

time falls within the allowable range (75%) of the maximum 20-minute (i.e., 1,200 seconds) battery capability. For the high-elevation route, the total flight time is 697.0 seconds, based upon an 8 m/s flight speed for the transition segments and a 4 m/s flight speed for the S-shape flight route. The time is also within the allowable range of batteries. Overall, the good performance on obstacle avoidance and flight time efficiency demonstrates the capability of Toolkit I.

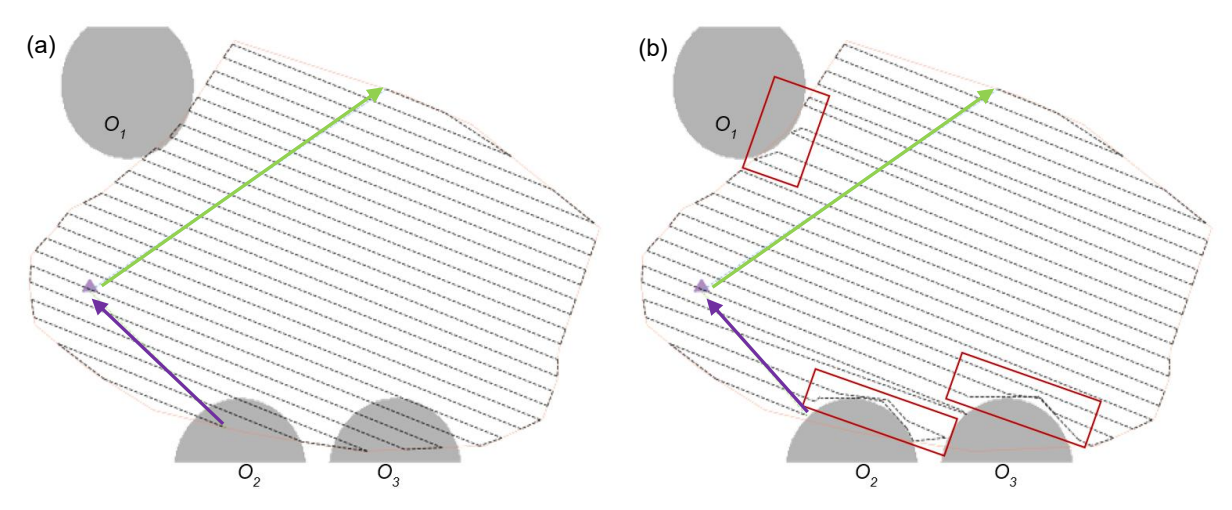


Figure 2-7 | The low-elevation flight routes. (a) Flight route without obstacle avoidance. (b) Flight route with obstacle avoidance using the Modified D-Lite algorithm. Obstacles are denoted as O₁, O₂, and O₃, while the take-off point is denoted by a purple triangle. The flight boundary is outlined by a thin orange polygon. The S flight route is depicted as a black dashed line with transition routes to the starting point and from the ending point marked as green and purple lines, respectively. The detours from the original route are highlighted by red boxes.

2.5.2 Ortho-terrain map

Fig. 2-8a presents the ortho-terrain map generated using 253 high-elevation images for the entire site and 488 low-elevation images specifically for A_{veg} , a canopy-blocked area highlighted in pink squares. Structure-from-Motion (SfM) processing was performed at medium quality, requiring 4.7 hours for high-elevation images and 7.4 hours for low-elevation images, achieving

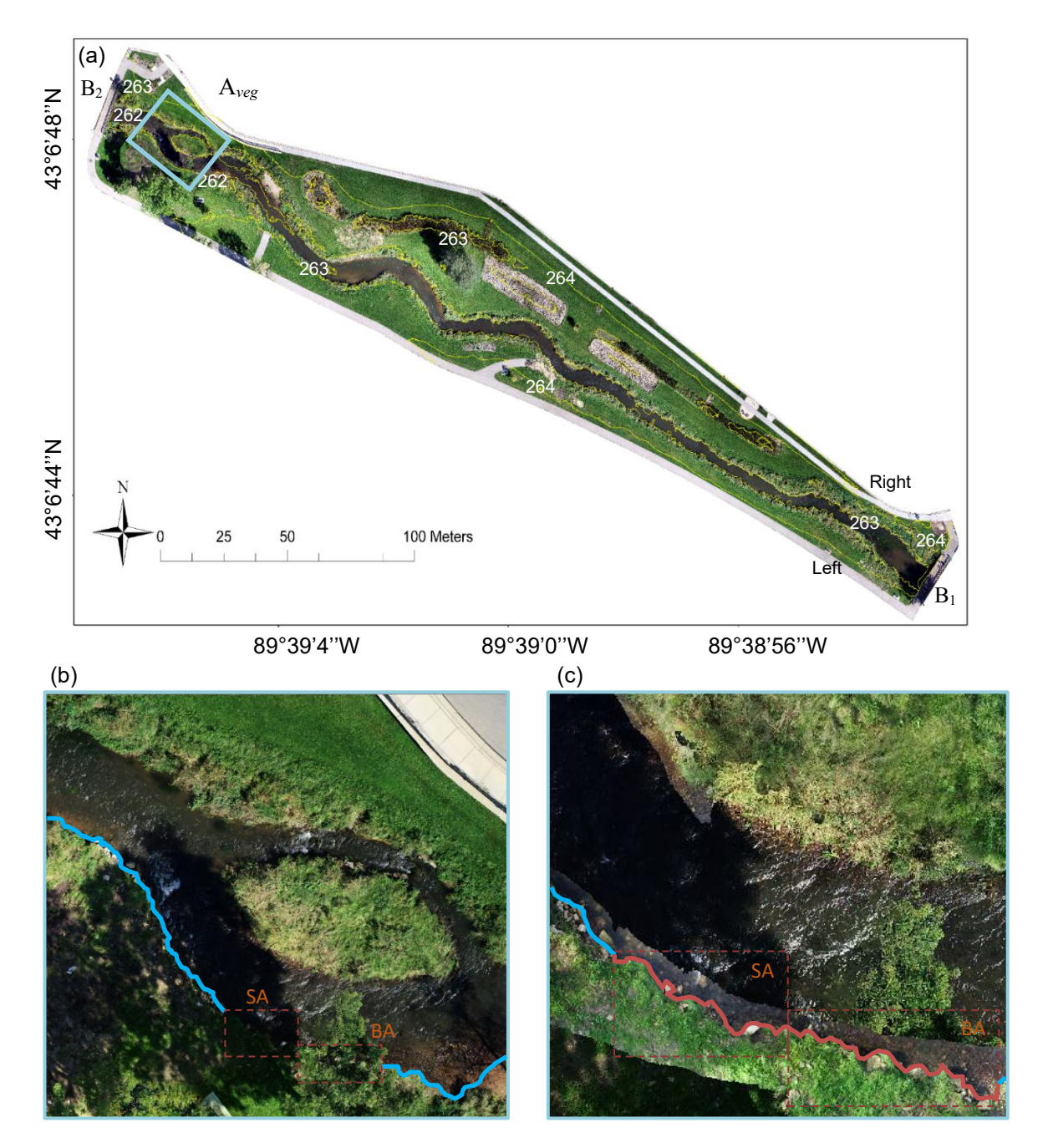


Figure 2-8 | Ortho-Terrain Map Generated from Toolkit II. (a) Reconstructed orthoterrain map combining high- and low-elevation flight missions, with yellow lines marking ground elevation contours and the pink area indicating overlaid low-elevation results. (b) and (c) compare stream bank delineations for high-elevation results and overlaid results in area A_{veg} . The blue solid line are stream banks detectable from high-elevation results, while the orange solid line indicates stream banks in shaded (SA) or blocked (BA) areas, which are only delineable in the overlaid results.

texture resolutions of 0.008 m for the overall site and 0.004 m for A_{veg} . Ground elevation is depicted

with 1-meter interval yellow contour lines. Validation against ground control points (GCPs) shows an RMSE of 0.04 m horizontally and 0.17 m vertically for the entire site (high elevation, excluding A_{veg}). However, for A_{veg} (low elevation), the RMSE increases to 0.09 m horizontally and 0.27 m vertically due to limited image overlaps near obstacles and low texture contrast caused by the reduced field of view (FOV). Fig. 2-8b and 2-8c underscore the critical role of integrating low-elevation imagery to enhance resolution and clarify features in complex areas. As shown in Fig. 6b, the high-elevation-only result struggles to delineate key features such as the water-land interface in shaded areas (SA) and blocked areas (BA) within A_{veg} (marked by dashed-line rectangles), even when magnified. In contrast, after overlaying with low-elevation results, these critical features, including the stream bank, are clearly delineated, as indicated by the red lines in Fig. 2-8c. This integration highlights the significant value of low-elevation imagery in overcoming limitations posed by obstructed views and ensuring accurate terrain mapping in challenging environments.

2.5.3 Stream habitat parameters

Values of stream habitat parameters (concepts illustrated in Fig. 2-5) are shown in Fig. 2-9 and Fig. 2-10. The study examines a 389.59 m stream with an upstream elevation at B₁ (263.36 m) and downstream elevation at B₂ (262.09 m). Fig. 2-9 compares continuous drone-based measurements (lines) from our toolkit with transect-based ground truth measurements (blue, orange, and purple markers). The stream width (W) ranges from 2.68 m to 9.50 m after excluding the island width, with the widest section located 14.74 m downstream of B₁ and the narrowest 64.42 m downstream of B₁ (Fig. 2-9a). Water depth (D) varies between 0.27 m and 1.60 m, with the deepest point 1.23 m downstream of B₁ and the shallowest near the island at 41.38 m upstream

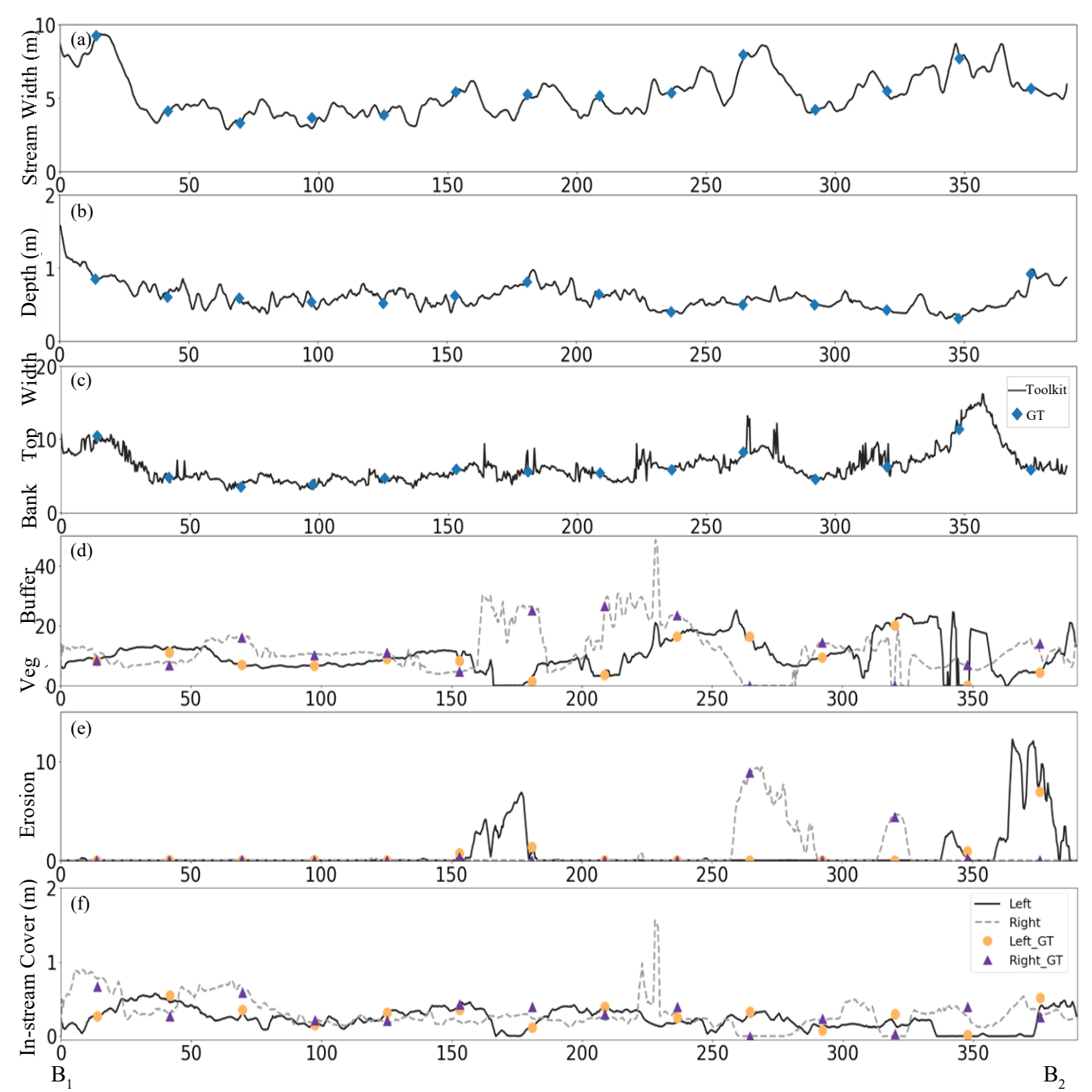


Figure 2-9 | Parameter values for the stream habitat between Bridge B₁ and B₂. (a)-(c) show stream width, water depth, and bank top width (m), with solid lines as toolkit measurements and blue diamonds as ground-truth data for 14 transects. (d)-(f) present left- and right-bank vegetation buffer width, erosion width, and in-stream cover width (m), with solid and dashed lines for left- and right-bank toolkit outputs and orange/purple markers for ground-truth results for the left and right banks, respectively.

of B₂ (Fig. 2-9b). Bank top width (BT) ranges from 3.14 m (64.42 m downstream of B₁) to 15.64 m (32.25 m upstream of B₂) (Fig. 2-9c). Vegetative buffer width (B) generally exceeds 1 m, with

maximums of 25.19 m (left bank) and 48.74 m (right bank). However, five zones along the banks have no buffer: three on the left bank and two on the right bank (Fig. 2-9d). Erosion width (E) peaks at 13.05 m (left bank) and 10.74 m (right bank), with significant erosion observed in five specific zones (Fig. 2-9e). In-stream fish cover width (F) ranges between 0 m and 0.58 m (left bank) and 0 m to 1.57 m (right bank) (Fig. 2-9f). Fig. 2-10 demonstrates the toolkit outputs of pool and bend positions. A total of six pools is characterized, located at 0.11 - 27.51 m, 31.44 - 33.46 m, 47.14 -49.34 m, 187.41 - 192.62 m, 276.19 - 277.31 m, and 284.30 – 285.85 m, respectively. Additionally, eight bends are identified, located at 66.61 m, 168.52 m, 190.54 m, 225.68 m, 251.62 m, 285.06 m, 331.76 m, and 364.14 m, respectively. The UAV-derived parameters were then compared against tape-based field measurements. The mean absolute difference (MAD) was 0.21 m for stream width (W) and 0.29 m for bank top width (BT). For vegetative buffer width (B), MAD values were 0.57 m and 0.59 m for the left and right banks, respectively, corresponding to

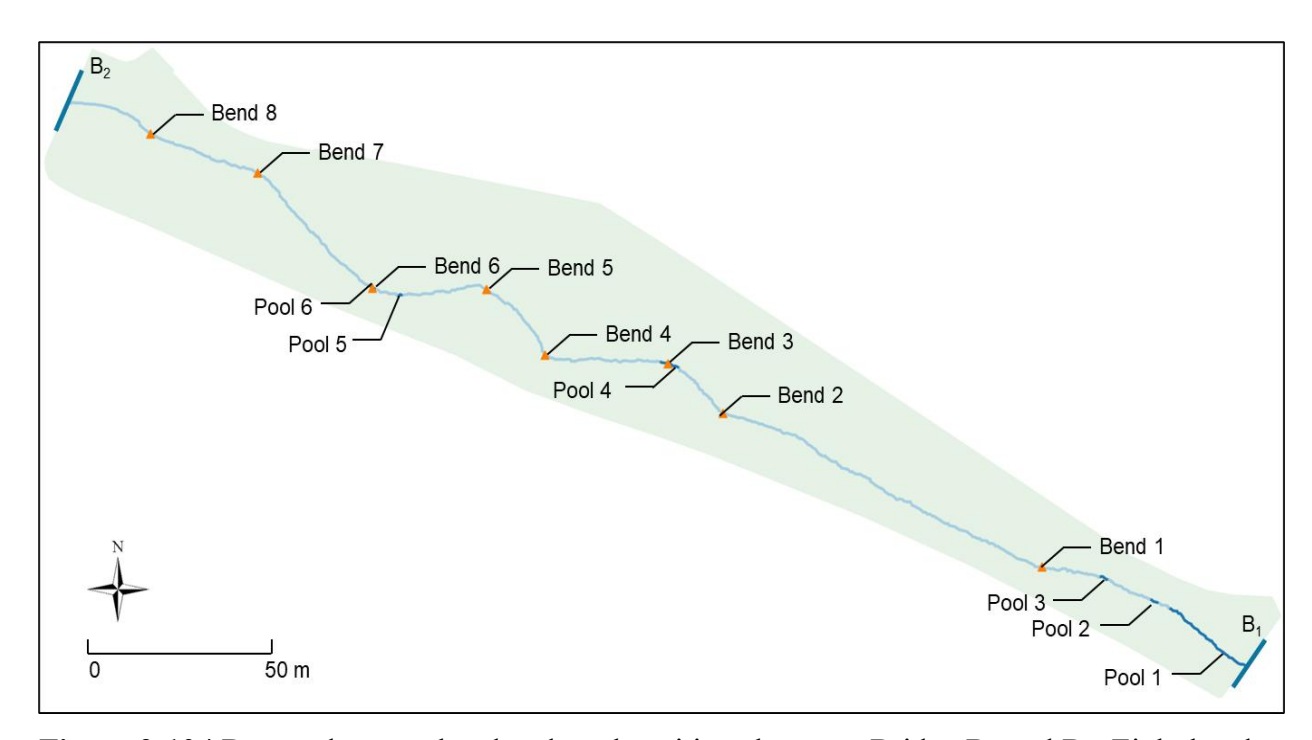


Figure 2-10 | Detected stream bend and pool positions between Bridge B₁ and B₂. Eight bends (Bend 1 to Bend 8, marked as orange triangle) and six pools (Pool 1 to Pool 6, marked as dark blue line) are identified.

relative differences of 6.54% and 4.91%. For erosion width (E), MAD was 0.12 m (left bank) and 0.08 m (right bank), while for in-stream fish cover width (F), MAD was 0.06 m (left bank) and 0.08 m (right bank). Water depth accuracy was assessed using five additional transects located approximately at 50 m, 120 m, 190 m, 260 m, and 330 m along the stream, yielding a mean absolute difference of 0.13 m. Overall, the close agreement between UAV-based and field-based measurements demonstrates the reliability of the proposed toolkits in assessing stream habitat parameters.

2.5.4 Multi-metric indices (MMIs) assessment

MMIs assessment of stream habitat quality for the segment between B₁ and B₂ is shown in Fig. 2-11. This segment is characterized as a mild-gradient stream, with an average channel slope (M₁) of 0.0023 and a maximum slope of 0.0052. Accordingly, the mild-gradient multi-metric system, encompassing M_2 – M_9 indices, is applied. The riparian vegetation cover metric (M_2 , Fig. 2-11a) indicates that most stream banks are in excellent or good condition, with undisturbed vegetation buffers exceeding 10 meters along 43.0% of the left bank and 56.3% of the right bank. Impaired conditions, spanning 5.8% of the left bank and 6.3% of the right bank (Fig. 2-11, M₂-Left and M₂-Right), are primarily caused by vegetation and soil loss during the 2019 summer flood (e.g., L₂ and L₃ on the left bank, and R₁ and R₂ on the right bank) or human structures near the stream (e.g., L₁). The bank stability (Fig. 2-11b, M₃) reveals that 81.7% of the left bank and 87.4% of the right bank are stable (Fig. 2-11, M₃-Left and M₃-Right), while poor conditions are observed in zones with material loss (e.g., L₄ and R₃) or the presence of bare soil and/or exposed gravel (e.g., L₅, L₆, and R₄). The width/depth ratio (Fig. 2-11c, M₄) shows that over 90% of the stream is classified as excellent or good, except for the downstream segment near B₂ (C₁), which features wide and shallow channels. The sinuosity metric (M_5) , with a sinuosity ratio of 1.09:1, is rated fair,

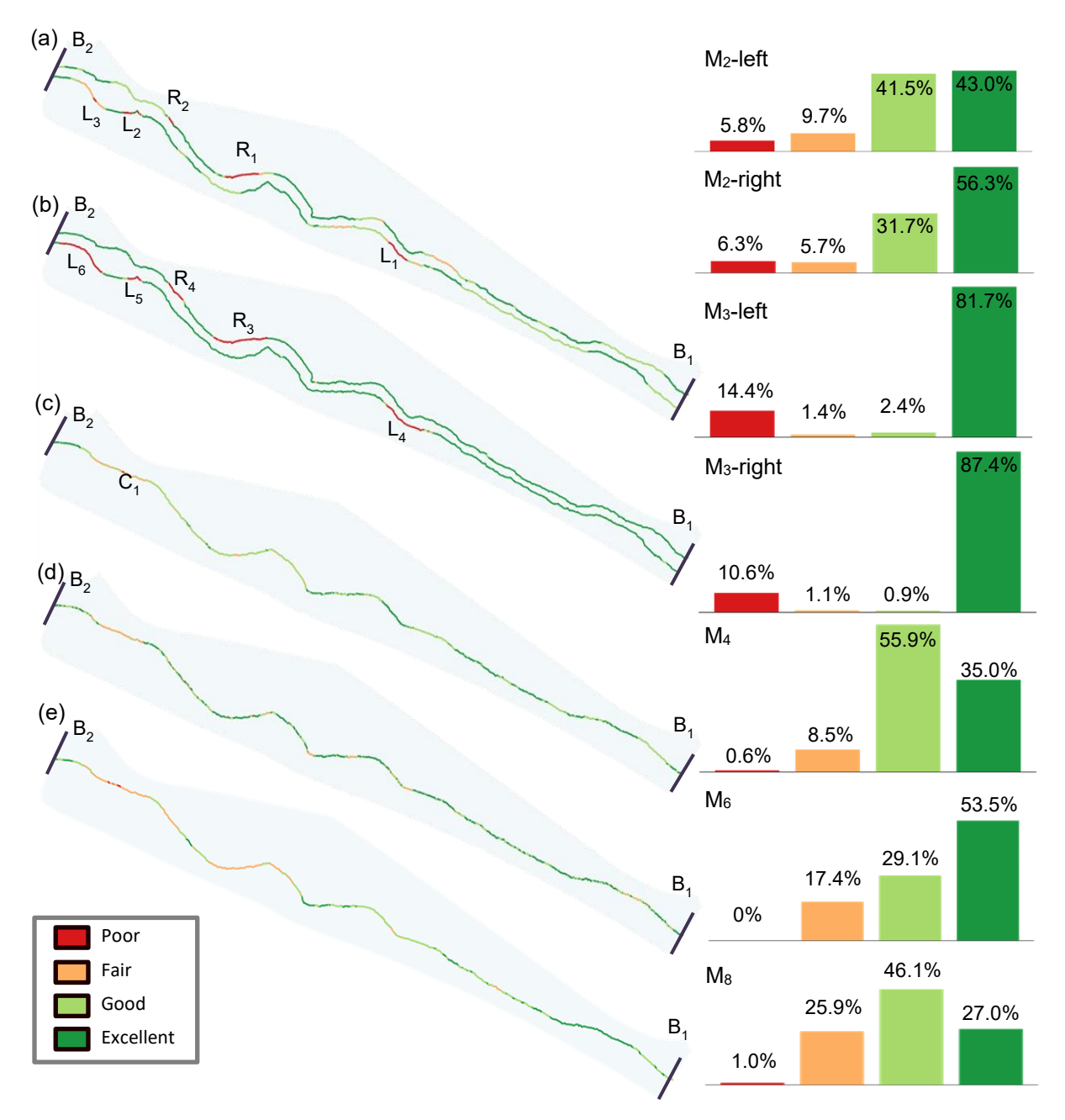


Figure 2-11 | MMI-based stream habitat quality assessment (spatially continuous indices: M_2 , M_3 , M_4 , M_6 , and M_8). (a) Visualizes the quality of M_2 . (b) Highlights the quality of M_3 , (c) Displays the distribution of M_4 conditions. (d) Maps the spatial distribution of M_6 . (e) depict the spatial distribution of M_8 . The right column includes histograms for each index, showing the percentages of categories: excellent, good, fair, and poor.

as the meandering channel length (389.59 m) is slightly longer than the straight distance between B₁ and B₂ (357.98 m). The stream flow status metric (Fig. 2-11d, M₆) indicates that 29.1% and

53.5% of the channel are rated as good and excellent, respectively, while 17.4% is under-saturated (i.e., less than 75% water coverage), primarily near the in-stream island. The coarse woody debris metric (M₇) is poor due to the absence of wood logs. The in-stream cover metric (Fig. 2-11e, M₈) shows good or excellent conditions in 46.1% and 27.0% of the stream, respectively, with poor conditions (1%) concentrated near the in-stream island. Lastly, the channel bed form metric (M₉) is rated as fair, with pools comprising 10.68% of the stream length.

The comparison of habitat health assessment results using our toolkits and in-situ transect measurements is shown on Fig. 2-12. Fig. 2-12a and 2-12b present results from 14 transects, showing consistent health conditions across metrics: excellent for right M₂, good for left M₂, M₄, and M₆, fair for M₃, M₅, and M₈, and poor for M₇ and M₉. The overall MMI score is 43.75, indicating a fair condition consistent between the toolkit and in-situ methods, demonstrating the reliability of drone-based assessments. Fig. 2-12c shows integration of continuous results for the entire site, where conditions are excellent for left and right M₂, good for M₄ and M₆, fair for left

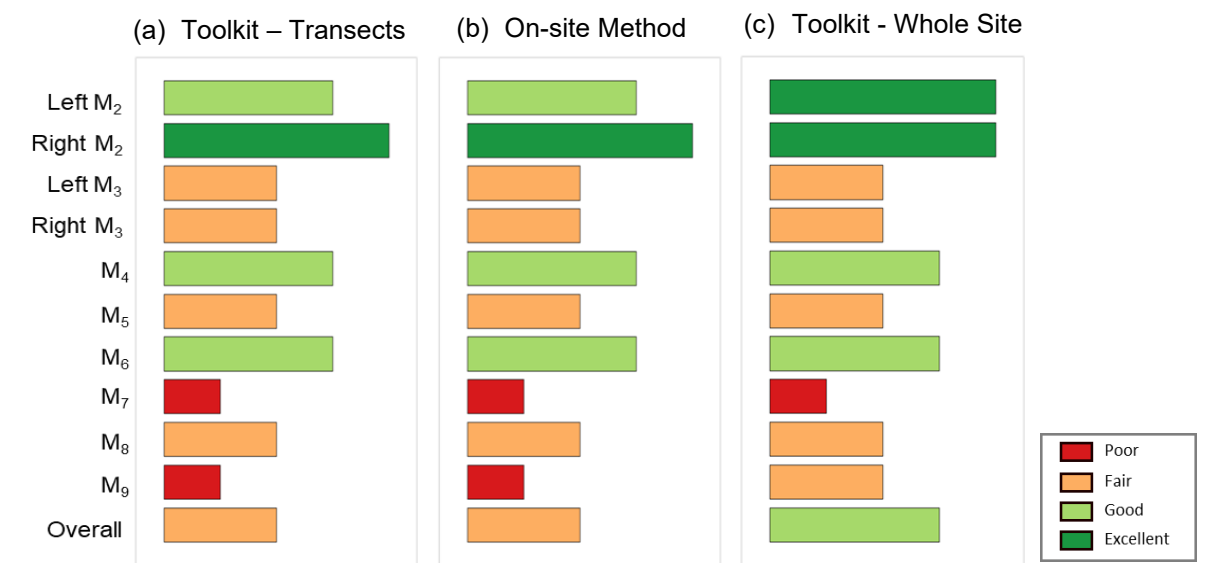


Figure 2-12 | Comparative analysis of stream habitat quality assessments using MMIs. (a) presents the MMI scores for 14 transects evaluated using our toolkits, (b) depicts the MMI scores using on-site methods for the same transects, and (c) displays the MMI scores of the entire study site (spatially continuous), obtained using our toolkits.

and right M₃, M₅, M₈, and M₉, and poor for M₇. The overall score is 47.5, reflecting good habitat quality. While most MMI values match between transects and continuous measurements, transect-based assessments underestimate conditions for left M₂ (excellent to good) and M₉ (fair to poor), probably due to uncaptured spatial variations.

2.6 Discussion

2.6.1 Flying parameters

Flying parameters, such as buffering distance, overlap ratio, and flight height, are associated with toolkit performance factors, including time cost, flight safety, and data quality—characterized by blind area ratio, model accuracy, and image resolution. The relationship between buffering distance (assuming a 90% overlap ratio and 5 m flight height) and time cost is illustrated in the left section of Table 2-5. Increased buffering distance can lead to a slight reduction in flight time due to enlarged blocked positions in area A_{veg} , subsequently reducing the length of parallel routes. However, a larger buffering distance, while promoting flight safety, may contribute to a greater ratio of blind areas unattainable through drone imagery. In our study, blind areas occur when the buffering distance exceeds the flight height, given that the half of angular field of view (AFOV) is 47.5 degrees. The impact of overlap ratio on time cost is presented in the central portion of Table 2-5, assuming a 5 m buffering distance and 5 m flight height. As overlap ratio rises from 75% to 90%, time cost increases from 356.00 to 800.94 seconds, continuing to 1580.33 seconds under a 95% overlap setting, which necessitates battery replacements during the flight mission (denoted in italics). While a higher overlap ratio can enhance structure-from-motion model accuracy, increasing overlap ratio only has small marginal improvements are small at high values, but it will lead to significantly longer flight durations. The effect of flight height on time cost is demonstrated in the right part of Table 2-5. Increasing flight height from 3 m to 7 m reduces the flight duration

from 1319.94 seconds to 590.61 seconds. Nonetheless, the image resolution captured by the drone's camera declines from 0.82 mm/pixel to 1.91 mm/pixel owing to the increased distance between the camera lens and the object. In summary, flying parameters impact toolkit performance factors in various ways; hence, the selection of flight parameters for a specific surveying should be contingent upon the relative significance of time cost, flight safety, and data quality.

Table 2-5 | Flight route Performance matrix with different flying

Buffering Distance (m)	Time Cost (s)	Overlap Ratio (%)	Time Cost (s)	Flight Height (m)	Time Cost (s)
3	821.57	75	356.00	3	1319.94
3.5	807.53	77.5	387.381	3.5	1145.56
4	806.82	80	418.75	4	1011.52
4.5	803.26	82.5	478.772	4.5	906.40
5	800.94	85	559.23	5	800.94
5.5	794.40	87.5	640.82	5.5	732.04
6	790.53	90	800.94	6	690.28
6.5	785.98	92.5	1076.16	6.5	632.71
7	782.52	95	1580.33	7	590.61

2.6.2 Potential errors

Errors are an inherent aspect of surveying. Although UAV-based assessment tools have demonstrated the capacity to provide accurate evaluations of stream habitats, potential errors may arise from the methodologies employed in Toolkit I, II, and III. Toolkit I: Minor errors can result from misalignments in drone positioning caused by strong winds or weak GPS signals (Wang et al., 2019). These inaccuracies are often exacerbated under tree canopies or near buildings, where GPS signals could be obstructed or interfered by multipath effects. While modern drones equipped with RTK or enhanced GPS systems can reduce such errors, some positional drift may still impact image overlap and route precision, especially in complex riparian settings. Toolkit II: The accuracy of 3D reconstruction depends on the number and quality of tie points among images, which are influenced by processing quality settings (e.g., low to ultra-high) and surface texture. High processing settings improve point-of-interest (POI) extraction in software like Agisoft Metashape

but increase computational demand. Homogeneous textures—such as water surfaces, grasslands, tree shadow, and snow—can reduce the number of POIs, limiting effective image matching (Turner et al., 2012; Gebrehiwot & Hashemi-Beni, 2021). These challenges are illustrated in Fig. 2-13, where water surfaces led to sparse tie-point generation and localized errors in alignment. Toolkit III: Errors primarily stem from streambed variation, in-stream vegetation, and running water surface. Streambed profiles with abrupt changes, such as pools, can be challenging. However, in our study site, this issue is minimal, as pools comprise only a small portion of the streambed

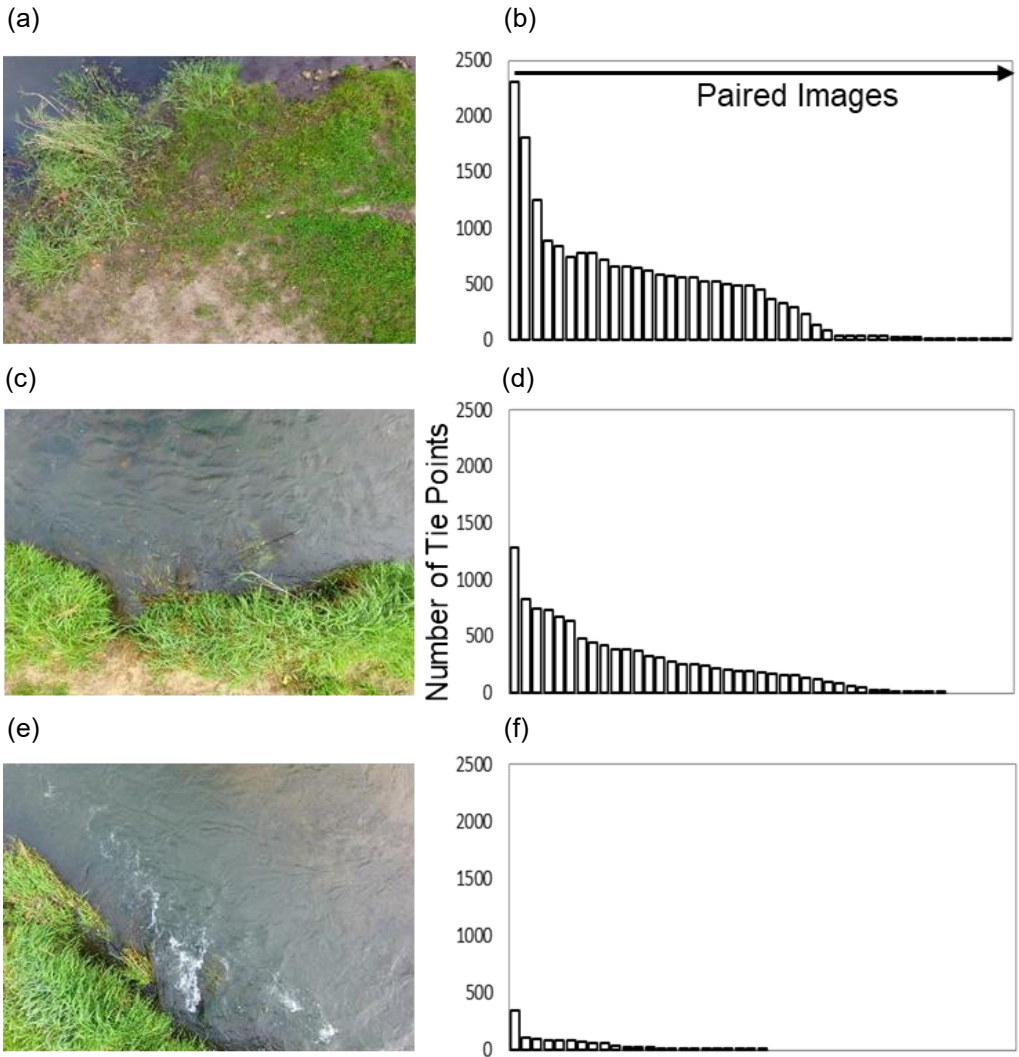


Figure 2-13 | The decrease of tied points caused by water surface. (a) (c) (e) are images with different water body ratio, (b) (d) (f) show the ranked number of tie points we can extract from each image pair.

between B₁ and B₂. Ground truth measurements remain critical for transects with pools, especially in streams with abundant riffle-pool sequences. Additionally, during low-flow periods, tall vegetation may lack sufficient water saturation, requiring supplemental in-situ surveys or airborne humidity sensors for accurate assessment. Another source of error arises from estimating water surface elevation: because running water is rarely perfectly calm, averaging left, right, and mid-channel elevations may not fully capture the true mean water surface level at a transect, and could lead to small variations. In summary, while UAV-based toolkits are efficient and accurate for stream habitat assessment, error mitigation through thoughtful planning, quality control, and selective ground validation is essential to ensure robust results.

2.6.3 Alternative depth measurements

Depth measurements using aerial-based techniques remain challenging due to factors such as stream bottom distortion from reflection (Partama et al., 2018), refraction (Woodget et al., 2019), and water turbidity (Acharya et al., 2021). In this study, water depth is estimated by calculating the difference between the water surface and the interpolated streambed profile, which proves accurate given the site's gradually varied bedforms. Three alternative methods exist for estimating depth with commercial drones. The first method applies to manually dredged channels with regular transect shapes (e.g., trapezoidal or parabolic). By assuming normal flow, Manning's equation can estimate depth based on channel geometry. The second approach uses polarized filters mounted on the camera lens to reduce surface reflection (Dolin & Turlaev, 2020), enabling three-dimensional reconstruction of riverbed textures after eliminating glints (Overstreet & Legleiter, 2017). The third method leverages water surface velocity measurements obtained through particle image velocimetry (PIV) to infer bathymetry, assuming velocity profiles follow either an exponential function (Hauet & Daubagnan, 2018) or an entropy relationship (Moramarco et al.,

2013) with depth. Moreover, for cases requiring higher accuracy and where budget permits, additional airborne sensors mounted on drones can provide improved depth measurements. In specific, two types of recent techniques have been employed for river bathymetry measurements including the use of a topo-bathymetric laser profiler (Mandlburger et al., 2016) for shallow gravel-bed rivers and acoustic sensors (Bandini et al., 2018) for deep and turbid water.

2.6.4 Cost-effectiveness of UAV-based toolkits

The cost-effectiveness of the UAV-based monitoring toolkits becomes increasingly evident when applied to tasks involving broad spatial extents, repeated assessments, or complex terrains, where traditional in-situ methods—while long established and valuable—can be labor-intensive, time-consuming, and spatially limited. In our demonstration, the overall investment remained modest: drones with 30-minute flight durations and 1080P or 4K cameras are now commonly available for under USD 1,000, and commercial photogrammetry software—such as Agisoft Metashape with basic settings—can be obtained for a few hundred dollars, with open-source alternatives like OpenDroneMap also available. Similarly, while ArcMap was used for feature digitization and route planning, free and open-source platforms like QGIS offer comparable functionality and are increasingly adopted in geospatial workflows. Once the initial training is completed, the entire workflow from flight planning to habitat assessment can be conducted by a single person. In terms of time cost, surveying a 500-meter stream segment typically requires 20-30 minutes for an S-shaped flight at high elevation. If certain areas are obstructed (e.g., by canopy cover or tall vegetation), low-elevation supplemental flights may be required to ensure adequate coverage. For example, collecting low-elevation drone images for areas with similar sizes as A_{veg} (approximately 25 m × 25 m) requires at most an extra 20 minutes. Manual delineation of stream features adds one to two hours of indoor efforts, regardless of the number of transects involved.

All remaining tasks, such as flight route generation, image processing, terrain reconstruction, and multi-metric index (MMI) assessment, are automated and can run independently without human supervision. As project workload increases—whether through longer reaches, denser transect coverage, or more frequent monitoring—the UAV-based approach becomes increasingly costeffective while offering high-resolution, spatially continuous outputs. These outputs not only complement but can enhance traditional transect-based methods by revealing habitat degradation patterns or localized impairments that may otherwise go undetected. For water depth estimation, if the streambed profile remains relatively stable over time, depth measurements can be collected once and reused across surveys, further improving efficiency. In cases where bedform changes are expected, alternative depth estimation methods, as discussed in Section 2.6.3, can be employed depending on precision needs and budget. Nevertheless, for short stream segments (e.g., <100 m), one-time assessments, or sites with UAV restrictions, conventional methods may remain more practical. Overall, these UAV-based toolkits are intended not as a replacement, but as a flexible and scalable complement to existing practices—particularly well suited for applications requiring broad spatial coverage, temporal repeatability, and high-resolution data to support informed stream habitat management.

2.6.5 Toolkit limitation and future generalization

The UAV-based toolkits developed in this study provide a comprehensive approach for assessing stream habitat quality, but several limitations must be acknowledged. First, depth measurements rely on the assumption of a gradually varying riverbed. While this does not affect metric scoring, the absolute depth values are subject to greater uncertainty compared to other physical parameters. Second, the MMI framework was designed following Wisconsin and EPA guidelines for trout streams in non-mountain regions; therefore, its applicability to mountain

streams is limited and would require revision. Third, the toolkits focus on physical habitat variables and cannot capture chemical and biological aspects of habitat quality, such as water quality, species richness, or the distribution of fish spawning areas, which are also critical for comprehensive assessments.

To generalize our toolkits for other study sites or stream habitat quality topics, four strategies are proposed. First, the toolkits allow for the exclusion or deemphasis of metrics with significant uncertainty or redundancy, enabling users to prioritize core metrics tailored to specific site conditions. For example, our study site is a restored, meandered channel with sparse vegetation, so metrics such as coarse woody debris are less critical, while vegetation buffer width and instream cover are more significant. Second, stream habitat quality may exhibit high spatial heterogeneity (White & Walsh, 2020), the toolkits can incorporate vicinity-based assessments by modifying the computation of index values to focus on the poorest conditions within localized areas ($\Delta L/2$ of each transect), improving the detection of worst impairments. For instance, at our site, this method identified poor conditions near transects 1, 9, 11, 13, and 14, such as M₂ and M₈, which may have been overlooked by traditional methods (see Fig. 2-14). Third, the toolkits can be expanded to integrate additional indices derived from orthophotos or terrain maps, such as bankfull width and rock and stone embeddedness (Somerville, 2010), using the same processes for parameter computation and quality characterization. Finally, the toolkits can be modified to support indices requiring specialized equipment, such as temperature measured with thermal cameras (Kuhn et al., 2021), and water quality detected via multispectral sensors (Kim et al., 2020).



Figure 2-14 | Spatial variation of stream habitat health condition. (a) displays the health condition of each index at each transect, (b) indicates the stream segment's poorest health condition category for each index in the vicinity of each transect.

By equipping UAVs with portable versions of these instruments, sediment particle size, temperature, and water quality can be processed, assessed, and incorporated into existing MMIs using corresponding function interfaces in our toolkits.

2.7 Conclusions

In this study, a suite of unmanned aerial vehicle (UAV)-based toolkits was developed to evaluate stream habitat quality using multi-metric indices (MMIs). The case study conducted at Black Earth Creek, WI, a region with a well-restored stream habitat impaired by a severe flood event, demonstrated the cost-effectiveness and accuracy of the toolkits in assessing MMIs. The toolkits streamline most processes, thereby significantly reducing labor associated with UAV data collection, processing, and assessment. The toolkits comprise three components. The first designs

flight routes in a zig-zag pattern, optimizing flight duration while considering image quality, overlap ratio, obstacle avoidance, and smooth detouring. The second component processes UAV imagery to obtain topographic data, including orthophotos and terrain maps, with high texture resolution and accuracy by optimally configuring computer hardware settings. The third quantifies stream habitat parameters and evaluates habitat quality using MMIs, yielding results consistent with conventional transect-based ground truth assessments. A key advantage of the toolkits is their ability to provide continuous habitat quality evaluations, offering a comprehensive understanding of spatial heterogeneities in stream habitat quality. This approach addresses the limitations of transect-only methods, which may overlook critical features between adjacent transects. The toolkits also identify critical hotspots for each metric where habitat degradation is severe. Designed for flexibility and compatibility, the toolkits allow users to adjust metric weights, integrate new metrics from regional protocols, exclude redundant metrics, and embed additional geometrical measurements to accommodate diverse landscapes and habitat types. Given the demonstrated performance, future developments could expand the application to a broader range of stream habitats and integrate them with management and decision-making processes to enhance stream habitat restoration.

Chapter 3: Loss and resilience of stream habitat due to flooding

3.1 Introduction

Stream habitat, which provides the living space for in-stream biota, is highly dynamic across both temporal and spatial dimensions, varying in response to the stream's physical condition (Kozarek et al., 2010). Factors such as temperature, flow rate, discharge, and availability of suitable refugia are pivotal in determining stream habitat quality (Hynes, 1970; Aadland, 1993; Freeman et al., 2001) and can be disturbed and altered by climate change, extreme events, and anthropogenic activities (Isaak et al., 2010; Sievert et al., 2016; Liao et al., 2018). Among these disturbances, natural hazards—particularly extreme events like floods—are especially consequential, given their potential to induce abrupt and pronounced changes over short periods (Lake, 2000; Dawson et al., 2002). Floods can significantly reshape streambed morphology, destabilize banks, and degrade riparian zones (Lake et al., 2006), in addition to disrupting established biological communities (Jowett and Richardson, 1989; Pearsons, et al., 1992; Talbot et al., 2018). While previous studies have documented these impacts, they are primarily focused on post-flood assessments, limiting our capacity to observe immediate flood influence and longterm ecological dynamics (Hajdukiewicz et al., 2016). Considering the frequency and severity of flood events, with approximately 6,518 occurrences resulting in annual damages of 3.35 billion USD (Zhou et al., 2019), there is an urgent need for comprehensive studies that assess the full spectrum of flood impacts on stream habitats.

The full spectrum of flood impacts has two fundamental aspects: loss and resilience. Loss refers to the decline of values caused by flooding, which may include damage to physical assets, properties, and infrastructure, typically measured by market and non-market values, as well as degradation of ecological functions and habitat quality (Kliesen, 1994; Modica and Zoboli, 2016).

Resilience is the rate of the stream habitat to recover after a disturbance, reflecting the system's ability to adapt to disruptive events then bounce back to a steady state (Pimm, 1984; Platt et al., 2016; Argyroudis et al., 2020). These concepts of loss and resilience have been widely employed in socio-economic assessments for flood events. For instance, the assessment of flood impacts on residential buildings often focuses on the economic damage and the time required for repairs to components such as roofs, exterior walls, and foundations (Dutta et al., 2003; Baradaranshoraka et al., 2019). Similarly, evaluations of urban infrastructure resilience examine both the loss and the expected time of recovery for critical assets, including bridges, tunnels, and networks for transportation, water, and energy systems (Kellermann et al., 2015; Argyroudis et al., 2020; Martínez-Gomariz et al., 2021). In ecological contexts, responses of stream habitats to flooding are more challenging to measure across space and time comparing to socio-economic perspectives. Although many studies have examined flood-induced habitat loss and subsequent recovery—such as impairments to riparian vegetation (Chia et al., 2020) and alterations in channel morphology (Su and Lu, 2016)—they often lack datasets that capture all three critical stages together: conditions shortly before flooding, conditions shortly after, and long-term trajectories of loss and resilience. Bridging this gap requires integrative, multi-year assessments that encompass both immediate impacts and extended recovery processes to fully characterize flood effects on stream habitat quality.

The assessment of stream habitat quality relies on multi-metric indices (MMIs) that include physical, chemical, and biological indicators (Fausch et al., 1984). Among these, physical habitat variables are the most convenient to survey (Roper et al., 2002). They can be directly measured using basic surveying equipment like a total station or observed through images, without the need for specialized sensors or post-survey laboratory analysis (Walters et al., 2003). Specifically,

physical habitat variables include geomorphological attributes like channel shape, bank structure, and the condition of the riparian zone, as well as hydraulic settings such as depth and flow velocities (Jowett, 1993; Maddock, 1999). Several MMIs based on physical variables have been successfully implemented by government agencies for regular monitoring of stream habitat quality across various transects, including the EPA protocol (Barbour, 1999) and the Wisconsin fish habitat surveying guidelines (Simonson, 1994). Furthermore, the dynamics of physical habitat variables, which capture both their regular fluctuations and the abrupt changes due to disturbances such as inland flooding, are examined by certain transect-based MMI studies (Hajdukiewicz et al., 2016). While transect-based MMI surveying provides a rough estimate of flood-induced losses, it may overlook, underestimate, or exaggerate localized impacts (Del Vecchio et al., 2019), such as bank erosion and riparian zone recession. Additionally, surveying dense transects for long periods to estimate resilience could be labor-intensive. To comprehensively assess flooding impacts against stream habitats, including both losses and resilience, acquiring continuous observation data with high resolution is essential.

Recent advancement in remote sensing techniques, including satellites, aerial photography, and unmanned aerial vehicles (UAVs), enables the acquisition of high-resolution, continuous observation data for stream habitats. Satellite data, such as Landsat and Sentinel, have been widely used to monitor vegetation health conditions in stream habitats using indices such as the Normalized Difference Vegetation Index (NDVI) (Griffith et al., 2002; Pace et al., 2022). However, the resolution of satellite images can be insufficient for monitoring smaller streams, and image quality is sometimes compromised by dense cloud covers and atmospheric pollution. (Dias-Silva et al., 2021). Moreover, aerial imagery from sources like the National Agriculture Imagery Program (NAIP), offering image data with resolutions ranging from 0.6 to 1 meter and updated

approximately every two years, is utilized to measure stream habitat quality variables such as tree canopy and woody riparian vegetation (Dauwalter et al., 2015; Pitt et al., 2017). Nevertheless, the extended time intervals between samplings and complicated setups prevent the timely assessment of rapid habitat quality loss caused by severe flood events. The use of UAVs for assessing stream habitat conditions is on the rise, attributed to their easy deployment, low operational costs, and flexible scheduling (Wang et al., 2025a). In addition, several studies have employed UAV-based methods to determine stream habitat quality and track its dynamics, aiming to evaluate the effectiveness of stream habitat restoration programs (Langhammer, 2019; Roni et al., 2019). Nonetheless, despite recent advancements in UAVs, there are no known studies that have used UAVs to examine the impact of flood events on MMIs of stream habitats, particularly in terms of each index's loss and resilience, as far as the authors are aware.

3.2 Objectives and research goals

The objective of this chapter is to characterize habitat loss and resilience due to inland flooding using a UAV-based approach. I propose that UAVs can provide high-resolution continuous observation data to determine the loss and resilience for MMIs of stream habitat caused by flood events, also, different indices and different initial conditions could be associated with different impacts. Three specific research goals are:

- 1. Track the changes of stream habitat MMIs before and after a severe flood event using UAV-based approach.
- 2. Assess the loss and resilience of stream habitat MMIs associated with a severe flood event.
- 3. Characterize the variation of loss and resilience among stream habitat indices.

3.3 Study Site

In this study, we selected Black Earth Creek near the village of Cross Plains, Wisconsin, as our study site. Black Earth Creek, as shown in Fig. 3-1a, is located in the southern part of

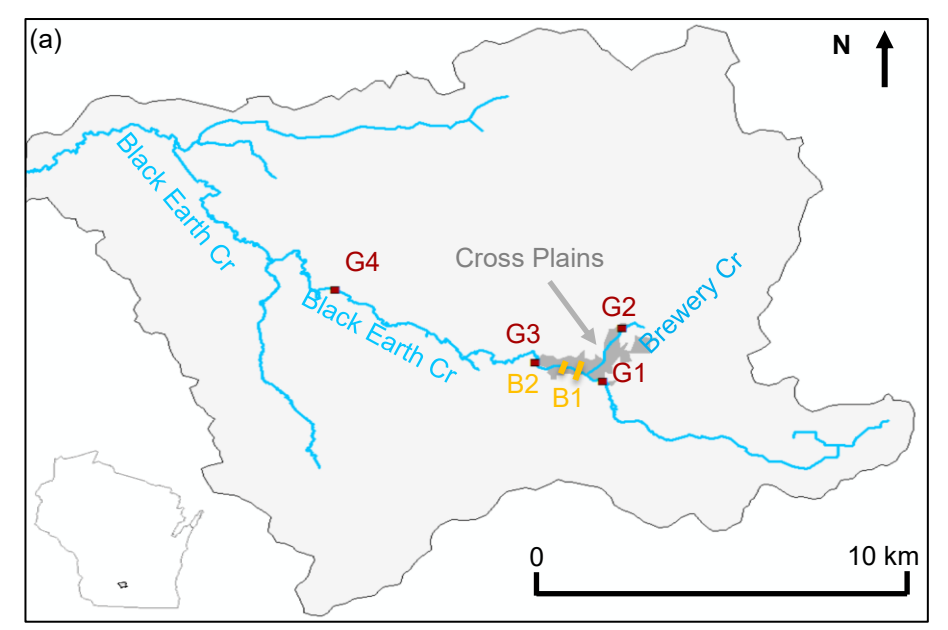




Figure 3-1 | Study Site of Black Earth Creek. (a) depicts the Black Earth Creek watershed, featuring four USGS gauges (G1, G2, G3, and G4) that record gauge height and discharge data. (b) illustrates our surveying area located between two bridges, B1 and B2. The dashed purple line represents the straight stream in 2010, and it was meandered in 2015 following a habitat restoration program in 2012.

Wisconsin and flows northwest for 43.5 kilometers before with the converging Wisconsin River. This creek is recognized as a Class I trout stream, attracting fly-fishers and anglers from across the Midwest due to its high-quality aquatic habitat. The watershed of Black Earth Creek approximately spans 264 square kilometers, with agricultural land being the major land use. Cross Plains is a

village along Black Earth Creek where Brewery Creek joins. Between the two bridges B1 and B2 in Cross Plains, a restoration project was completed in 2014. In this project, the historical straight

stream channel (indicated by the dashed line in Fig. 3-1b) was meandered into an S-shape channel. The adjacent riparian zones were replanted with native flora, such as jewelweed, aster, reed canary grass, and various shrubs, replacing the former lawns to enhance biodiversity and habitat quality condition. There are four USGS gauges (marked as red rectangular dots in Fig. 3-1a), G1 (USGS 05406457), G2 (USGS 05406469), G3 (USGS 05406479), and G4 (USGS 05406500), located at Black Earth Creek and its tributary, Brewery Creek. These gauges record gauge height and

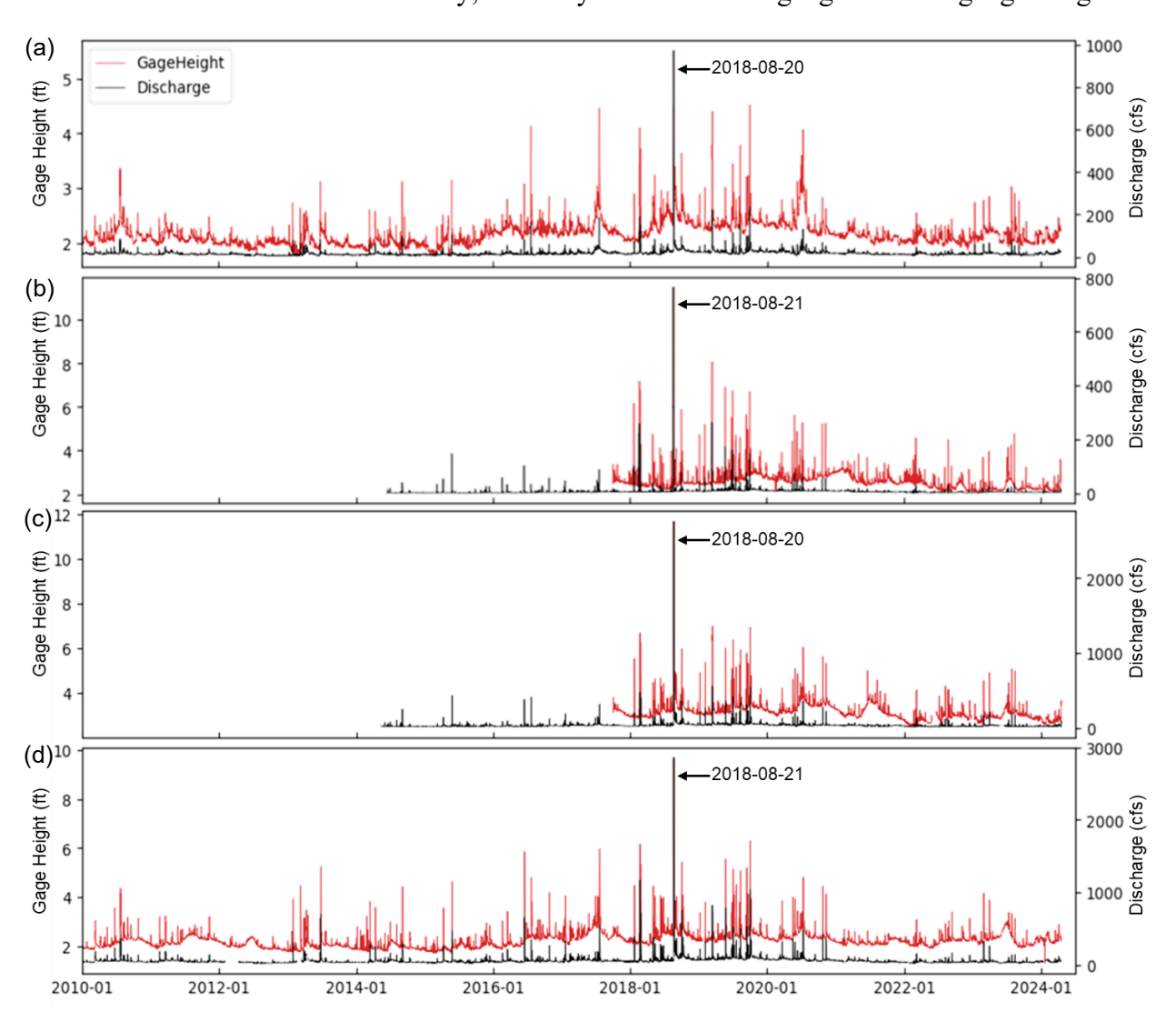


Figure 3-2 | **Historical Observations from USGS Gauges Along Black Earth Creek.** (a)-(d) correspond to gauge stations G1 (USGS 05406457), G2 (USGS 05406469), G3 (USGS 05406479), and G4 (USGS 05406500) as shown in Figure 3-1. Red lines represent gauge height observations, while black lines indicate discharge values. The maximum discharge was recorded during the flood event on August 20-21, 2018, as marked by the black arrows.

discharge data at 15-minute intervals. According to the gauge data, the base flow for Black Earth Creek close to Cross Plains is approximately 0.8 m³/s. A record-breaking rainfall event occurred on August 20-21, 2018, when a low-pressure system delivered 11 to 15 inches of rain over 24 hours (National Weather Service, 2021), leading to unprecedented flash flooding within the Black Earth Creek watershed. As illustrated in Figure 3-2, discharge values reached historical peaks at all four gauges during the event. The highest discharge was recorded at gauge G1, with a peak of 29.73 m³/s at 22:30 on August 20th, and at gauge G3, with a peak of 78.72 m³/s at 23:40 on the same day. Based on the fitted Generalized Extreme Value (GEV) distribution using annual maxima, these peak discharges correspond to return periods of 53 years and 70 years, respectively.

3.4 Methods

3.4.1 UAV observation and MMI assessment

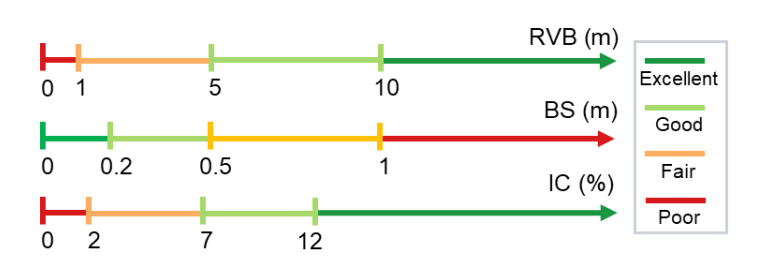


Figure 3-3 | MMI Criteria for Assessing Health Condition. Green indicates excellent condition, light green represents good condition, orange denotes fair condition, and red corresponds to poor condition.

Six UAV flights were conducted to assess stream habitat quality conditions related to the August 2018 flood. The first flight, on August 9, 2018, occurred before the flood, while the second, on September 29,

2018, was conducted after discharge returned to base flow. Additional flights were performed on June 7, 2019, September 14, 2019, October 18, 2021, and October 31, 2022, all using consistent flight settings with a 75% forward and side overlapping ratio. The survey date was selected as a calm day following several consecutive non-rainy days after a rainfall event. This ensured that water surface elevation was close to baseflow rather than flood or drought extremes. Aerial images from each flight were processed into digital elevation models (DEMs) and orthophotos with

centimeter-level resolution. These high-resolution outputs were then used to compute the following MMI values associated with the vegetation disturbance and riverbed scouring: (1) riparian vegetation buffer (RVB) - The width of the riparian zone covered by continuous, undisturbed natural land; (2) bank stability (BS) - The average width of stream banks that have been eroded or are susceptible to erosion; and (3) In-stream cover (IC) - The percentage of the stream surface water with overhanging vegetated fish shelter. Thresholds for scoring stream habitat conditions as excellent, good, fair, or poor were taken from Wisconsin fish habitat survey guideline and listed in Figure 3-3, where green, light green, orange, and red color are associated with ranges of excellent, good, fair, and poor conditions, respectively (Simonson, 1994; Wisconsin DNR, 2018). Other metrics, such as channel gradient, sinuosity, and bed forms, were excluded because they lack spatial variability and represent single values for the entire study site. Stream flow status was omitted due to its high temporal variability, which cannot be reliably captured in single-time surveys. Coarse woody debris was not included because large, saturated logs were absent from the site. Water-depth-dependent metrics such as width/depth ratio were also excluded, as they are highly sensitive to gage height at the time of sampling, especially in this shallow stream, making year-to-year comparisons unreliable. Single MMI values were computed for 1,000 evenly spaced transects (approximately 1-ft intervals) from the upstream bridge (B₁) to the downstream bridge (B₂), with the same set of transects established during the first survey reused for all subsequent surveys to maintain consistency and comparability.

3.4.2 Loss and resilience assessment for MMIs

The impacts of the above-mentioned flood event on each MMI within each transect were assessed from two perspectives, loss and resilience. Loss is defined as the relative change in the multi-metric index (MMI) before and after the flood (Eqn. 3-1):

$$Loss = \frac{Pre\ MMI - Post\ MMI}{Pre\ MMI} \times 100\% \quad Eqn.\ 3-1$$

In this study, the pre-flood MMI was derived from data collected on August 9, 2018, and the post-flood MMI was derived from data collected on September 29, 2018. If the post-flood MMI exceeded the pre-flood value (indicating no degradation or an improvement in habitat quality), or if the pre-flood value was zero, the loss was recorded as NaN to ensure that only negative impacts were captured.

Resilience is defined as the relative recovery rate of MMI values toward pre-flood conditions and was calculated as Eqn. 3-2:

$$Resilience_t = \frac{MMI_t - Post\ MMI}{Pre\ MMI*(t-t_0)} \times 100\%$$
 Eqn. 3-2

The MMI_t indicate the MMI value at the timestamp t, which in our study, 1-yr, 3-yr, and 4-yr were measured, the corresponding field surveying dates are: September 14, 2019, October 18, 2021, and October 31, 2022. If the MMI in the recovery stage was lower than the post-flood MMI, or if the pre-flood MMI was zero, resilience at the associated timestamp was marked as NaN.

The bank stability metric represents the length of stream bank with erosion potential, where smaller values indicate better conditions (zero is ideal). To align its interpretation with other metrics (i.e., higher values = better condition), the calculation was adjusted. Additionally, since a pre-flood value of zero would lead to division by zero, half of the stream width was used as the denominator. This adjustment makes the value dimensionless, consistent with the metric's definition, and expresses changes in bank stability relative to stream width. The formulas are given in Eqn. 3-3 and Eqn. 3-4:

$$Loss_{BS} = \frac{Post \ MMI - Pre \ MMI}{\frac{Pre \ Width}{2}} \times 100\%$$
 Eqn. 3-3

$$Resilience_{BS_t} = \frac{Post \ MMI - Steady \ MMI}{\frac{Pre \ Width}{2}*(t-t_0)} \times 100\%$$
 Eqn. 3-4

As with the general case, if the post-flood value represented the best condition, the metric was marked as NaN.

3.4.3 Loss and resilience characterization for MMIs

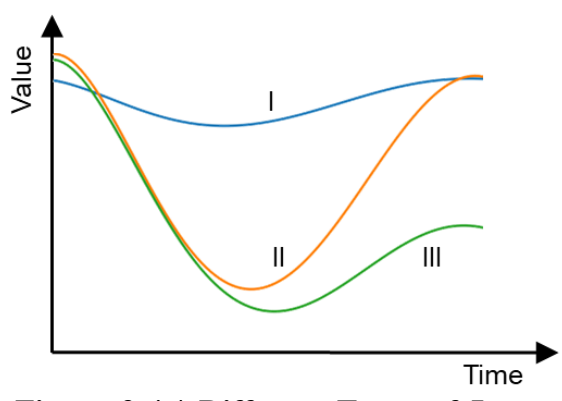


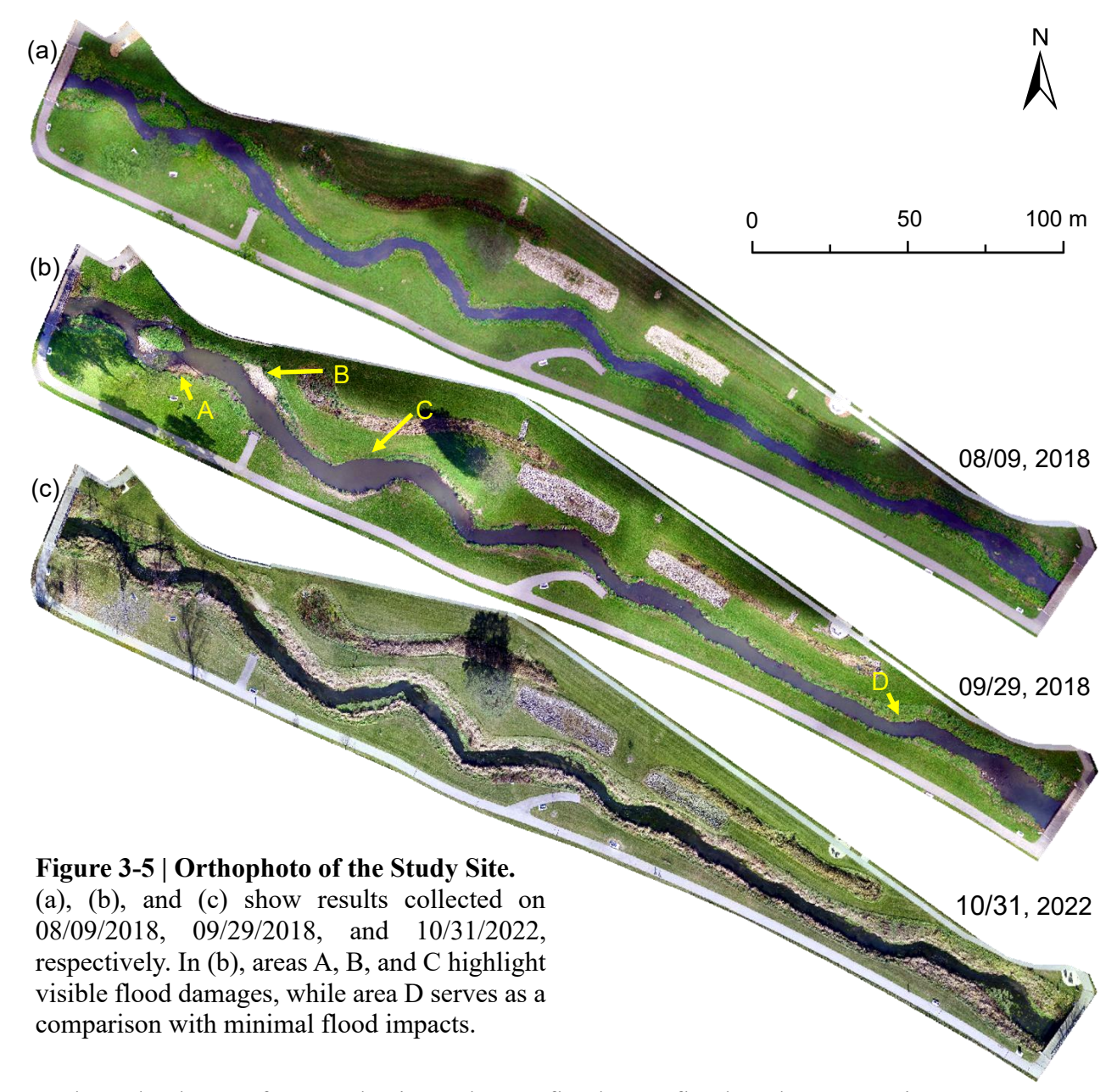
Figure 3-4 | Different Types of Loss-Resilience Curve

Three distinct types of stream habitat quality loss-resilience curves were characterized in this study to describe the response of stream habitat quality conditions to disturbances. Type I (Curve I, Fig. 3-4) represents scenarios where habitat quality remains stable or, in rare cases, improves following the disturbance, consistently maintaining a relatively good state throughout the

observation period, indicating minimal impact from the disturbances. Type II (Curve II, Figure 3-4) reflects situations where habitat quality experiences a significant initial decline, with at least one level falling below its original state (e.g. excellent to good), but recovers fully over time, eventually returning to at least pre-disturbance levels, demonstrating strong recovery capability. Type III (Curve III, Figure 3-4) describes cases where habitat quality initially declines and remains in a degraded state throughout the survey period, with only slight recovery and no return to pre-disturbance conditions, highlighting limited resilience and prolonged impacts. To explore spatial variations in these habitat quality dynamics, this classification was applied to every 1-feet interval transect and compared with the integrated outcome for the entire study site, revealing both localized patterns and broader trends in resilience and recovery.

3.5 Results

3.5.1 Orthophotos of flood damage and recovery



The orthophotos of our study site at the pre-flood, post-flood, and recovery timestamps are shown in Figure 3-5, with data collected on 08/09/2018 in Fig. 3-5a, on 09/29/2018 in Fig. 3-5b, and on 10/31/2022 in Fig. 3-5c. By comparing the pre- and post-flood orthophotos, several signs of habitat quality decline can be observed. For instance, impaired vegetation—particularly the

vegetation near the water surface that provides in-stream cover—is evident in multiple locations. Additionally, increased areas of bare soil, receded vegetation, and exposed gravel indicate elevated bank instability. The impacts of the flood also varied spatially, with some areas experiencing significant habitat deterioration, while others exhibited minimal disturbance. Four spots, labeled A, B, C, and D, were selected to illustrate different patterns of flood impact. In spots A and B, the near-water tall grass was washed away by the flood, exposing the gravel-based surface. At spot C, the original stream banks were severely damaged, resulting in a nearly vertical slope, whereas at spot D, only minor damage, such as bent tall grass, was observed. By 10/31/2022, the majority of the stream habitat in our study site had recovered, demonstrating the overall high resilience of the stream habitat in returning to its original condition.

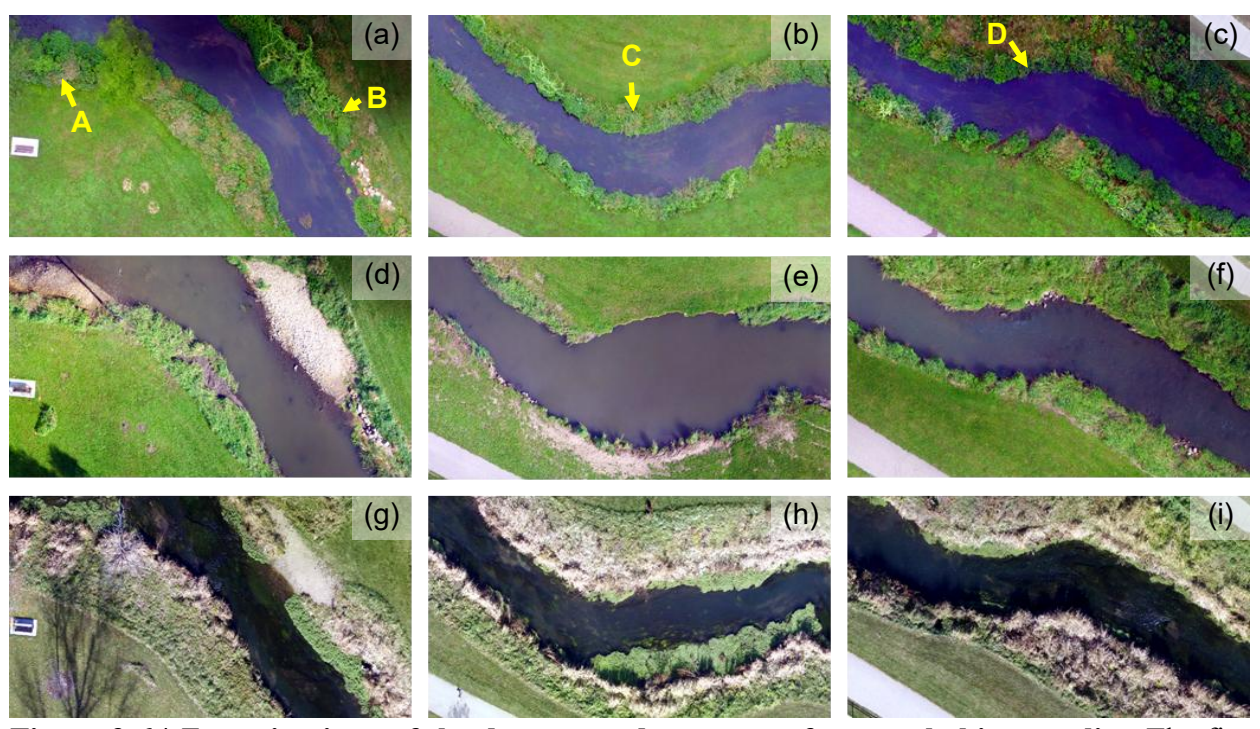


Figure 3-6 | Zoom-in views of the damage and recovery of stream habitat quality. The first row (a, b, and c) presents orthophotos taken on 08/09/2018, before the flood. The second row (d, e, and f) shows orthophotos from 09/29/2018, after the flood. The third row (g, h, and i) displays orthophotos from 10/31/2022, several years later. The loss-resilience patterns are illustrated for: Site A in the first column (a, d, g), Site B in the second column (b, e, h), Site C in the third column (c, f, i).

The detailed loss-resilience patterns for sites A, B, C, and D using orthophotos are illustrated in Figure 3-6. At site A (Fig. 3-6a), the original near-water vegetation was lost, and the ground surface was exposed with gravel deposits accumulating at the bend. By 10/31/2022, the vegetation had fully recovered, and the stream bank was once again covered with healthy vegetation. At site B (Fig. 3-6a), there was initially some minor exposed soil that had not been vegetated. During the flooding event, the site experienced significant damage, with all tall grass being swept away. The bare ground remained impaired through 2022, indicating limited resilience. Site C (Fig. 3-6b) experienced severe flood damage on both sides. The left bank (bottom side) had exposed soil with only sparse vegetation remaining, while the right bank (top side) collapsed entirely, losing all tall vegetation and grasses, resulting in a near-vertical slope. Despite this significant destruction, the site recovered by 2022, with fully functional vegetation restored and the stream bank slightly shifted in position. In contrast, site D (Fig. 3-6c) only experienced minor changes, with some tall vegetation bent and a small area of exposed soil. By 2022, the riparian area at site D had fully recovered. These patterns demonstrate variability in resilience across different sites, highlighting the importance of studying flood impacts on stream habitat at the local scale.

3.5.2 Pre-flood MMIs

The pre-flood MMI conditions at the study site are shown in Figures 3-7. For riparian vegetation buffer (RVB), most sections of both the left and right banks were categorized as good or excellent (Fig. 3-7a and Fig. 3-7d-e), indicating that over 90% of unimpaired sites had a buffer width of at least 5 m. However, 3.2% of the left bank (one site) was in fair condition due to a paved parking lot, and 6.9% of the right bank (two sites) was in fair condition due to rectangular gravel areas adjacent to the stream. For bank stability (BS), the entire left bank was classified as excellent, with no erosion sites or areas with erosion potential (Fig. 3-7b and Fig. 3-7f-g). The right bank

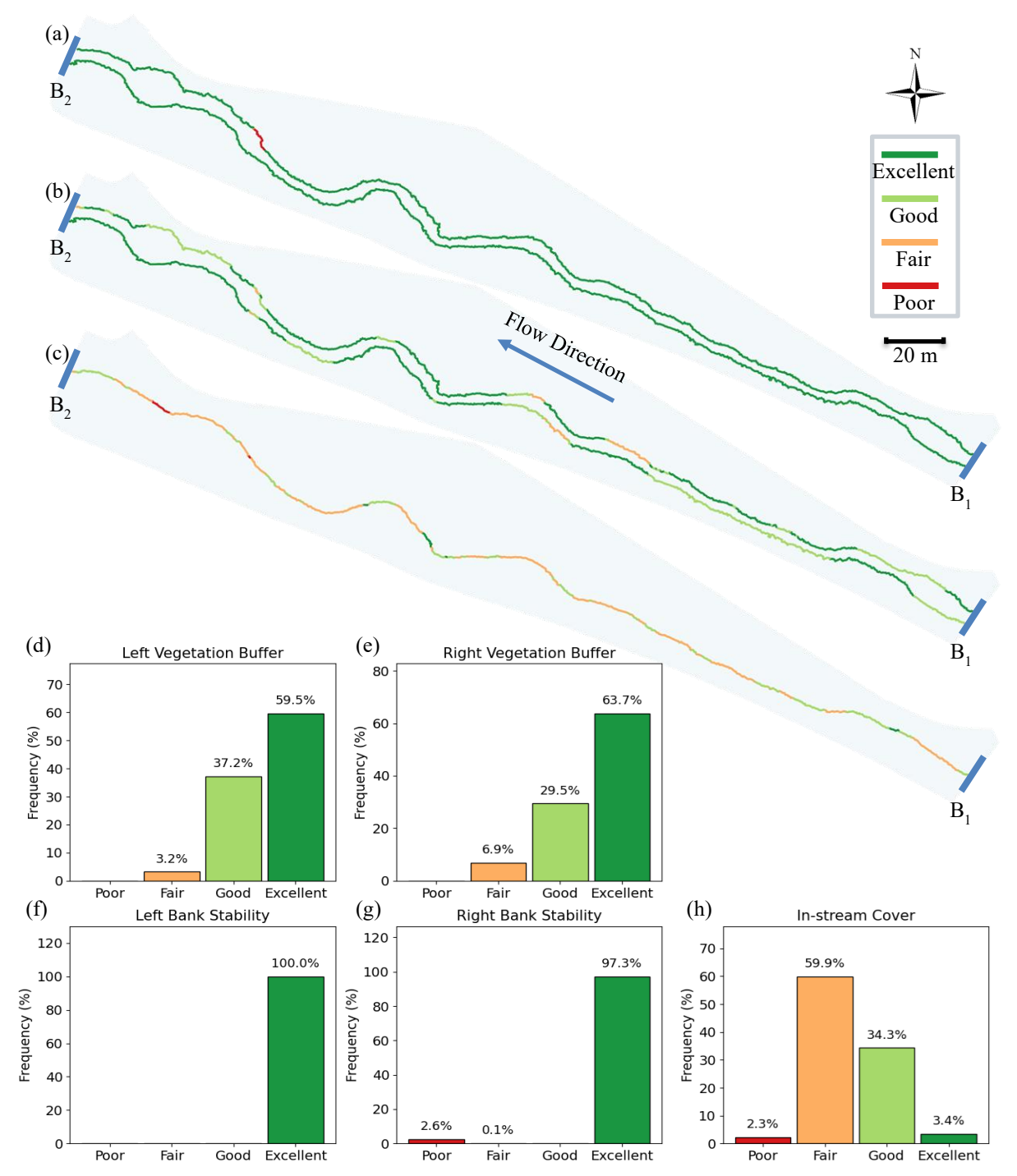


Figure 3-7 | **Pre-flood stream habitat quality conditions.** (a–c) Spatially continuous results for left and right riparian vegetation buffers, left and right bank stability, and in-stream cover. (d–h) Percentage distribution of habitat conditions (poor, fair, good, excellent) for left riparian vegetation buffer, right riparian vegetation buffer, left bank stability, right bank stability, and in-stream cover. was also predominantly excellent, but one site (2.6%) was classified as poor due to an exposed, unarmored surface lacking vegetation cover. For in-stream cover (IC), only 34.3% and 3.4% of

sites were classified as good and excellent, respectively (Fig. 3-7c and Fig. 3-7h). This was primarily because tall grasses were planted along the banks without extending into the water, and both emergent plants and coarse woody debris were largely absent. More than half of the sites (59.9%) were in fair condition, while 2.3% were in poor condition, indicating almost no in-stream cover.

3.5.3 Post-flood MMIs

The post-flood MMI conditions are shown in Figs. 3-8. For riparian vegetation buffer (RVB), both banks showed a marked decline compared to pre-flood conditions (Fig. 3-8a and Fig. 3-8d e). On the left bank, 20.8% of sites were classified as poor, 40.9% as fair, 21.3% as good, and only 17.1% as excellent. On the right bank, 18.3% were poor, 29.4% fair, 30.6% good, and 21.8% excellent. In addition to the severely degraded sites A, B, C, and D described in Section 3.5.1, multiple other sites lost vegetation buffers as the original plants either died or were swept away. For bank stability (BS), extensive erosion was observed (Fig. 3-8b and Fig. 3-8f-g). On the left bank, 48.0% of sites were classified as poor, 9.9% as fair, 7.9% as good, and 34.2% as excellent. On the right bank, 28.5% were poor, 5.5% fair, 9.9% good, and 56.1% excellent. Compared to preflood conditions, where both banks were largely stable, more than half of the left bank and about one-third of the right bank experienced severe instability, primarily due to exposed bare soil. For in-stream cover (IC), conditions also deteriorated substantially (Fig. 3-8c and Fig. 3-8h). After the flood, 21.4% of sites were classified as poor, 68.1% as fair, 9.9% as good, and only 0.6% as excellent. Since in-stream cover was already limited before the flood, this represents further degradation, with nearly 90% of sites falling into poor or fair categories. This decline was mainly due to tall grass being washed away, banks becoming more vertical following scouring, and the absence of vegetation in direct contact with the water.

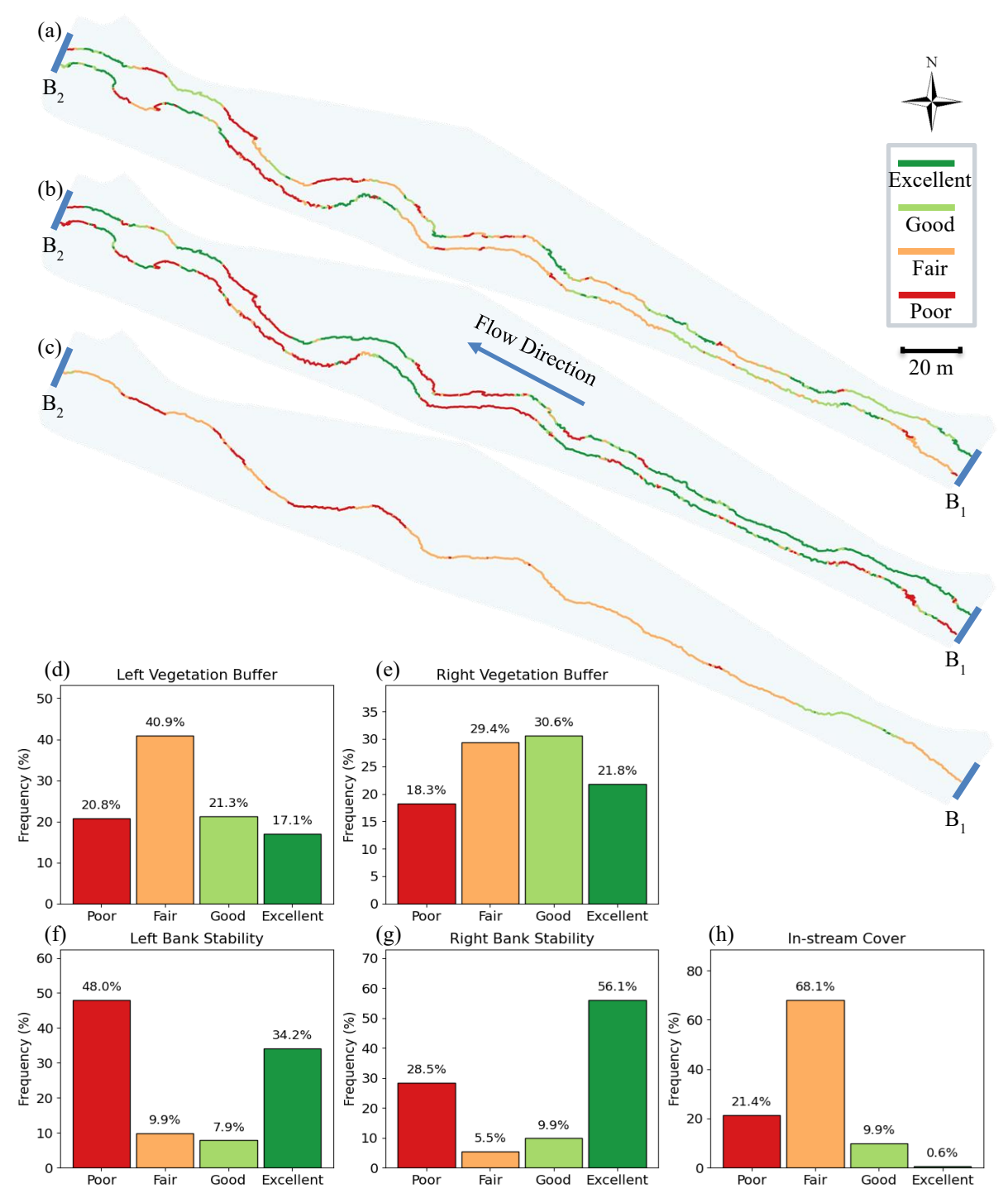


Figure 3-8 | **Post-flood stream habitat quality conditions.** (a–c) Spatially continuous results for left and right riparian vegetation buffers, left and right bank stability, and in-stream cover. (d–h) Percentage distribution of habitat conditions (poor, fair, good, excellent) for left riparian vegetation buffer, right riparian vegetation buffer, left bank stability, right bank stability, and in-stream cover.

3.5.4 Steady MMIs

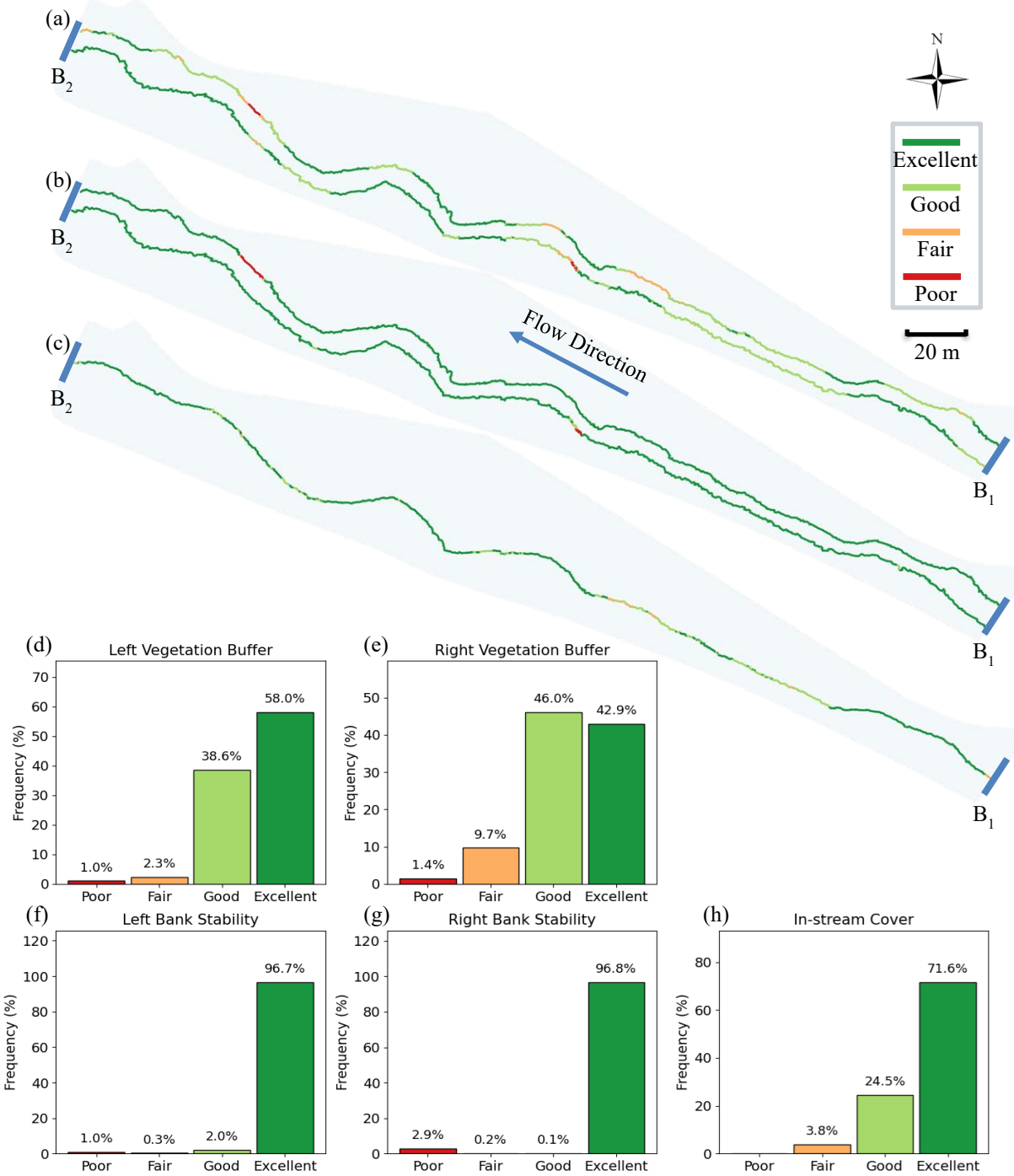


Figure 3-9 | **Steady stream habitat quality conditions.** (a–c) Spatially continuous results for left and right riparian vegetation buffers, left and right bank stability, and in-stream cover. (d–h) Percentage distribution of habitat conditions (poor, fair, good, excellent) for left riparian vegetation buffer, right riparian vegetation buffer, left bank stability, right bank stability, and in-stream cover.

The steady MMI conditions are shown in Figs. 3-9. For riparian vegetation buffer (RVB), most sites showed recovery compared to post-flood conditions, although the distribution was not

as favorable as the original pre-flood state (Fig. 3-9a and Fig. 3-9d-e). On the left bank, 1.1% of sites were classified as poor, 2.3% as fair, 38.6% as good, and 58.0% as excellent. On the right bank, 1.4% were poor, 9.7% fair, 46.0% good, and 42.9% excellent. Overall, the proportions of poor and fair sites were similar to pre-flood conditions, indicating relatively large recovery. For bank stability (BS), conditions values were also much closer to pre-flood conditions than to post-flood conditions (Fig. 3-9b and Fig. 3-9f-g). On the left bank, 1.1% of sites were poor, 0.3% fair, 2.0% good, and 96.7% excellent. On the right bank, 2.9% were poor, 0.2% fair, 0.1% good, and 96.8% excellent. Although not fully restored to pre-flood levels, the majority of transects regained stability, with poor and fair sites occurring at proportions comparable to pre-flood and located at similar sites. For in-stream cover (IC), conditions improved considerably compared to both pre-and post-flood states (Fig. 3-9c and Fig. 3-9h). After recovery, 3.0% of sites were poor, 24.5% fair, and 71.6% good. This improvement was largely due to the establishment of emergent plants, which now cover a substantial portion of the channel and provide increased in-stream habitat.

3.5.5 Loss and resilience of stream habitat quality

The loss of the MMIs is shown in Fig. 3-10. For riparian vegetation buffer (RVB, Fig. 3-10a), 2.62% of left-bank transects and 5.85% of right-bank transects were recorded as NaN, either because the pre-flood buffer width was zero or the post-flood condition was better than the pre-flood condition. Relative losses for both banks ranged from 0% to 100%. On the right bank, more transects exhibited relatively low loss, particularly near the upstream bridge and around the island (both upstream and downstream). On the left bank, relatively low loss occurred in the upstream section but not at transects close to the upstream bridge. Both banks showed high losses in the meandered section and in the vicinity of the island. For bank stability (BS, Fig. 3-10b), no left-bank transects and 4.04% of right-bank transects were recorded as NaN, indicating either pre-flood

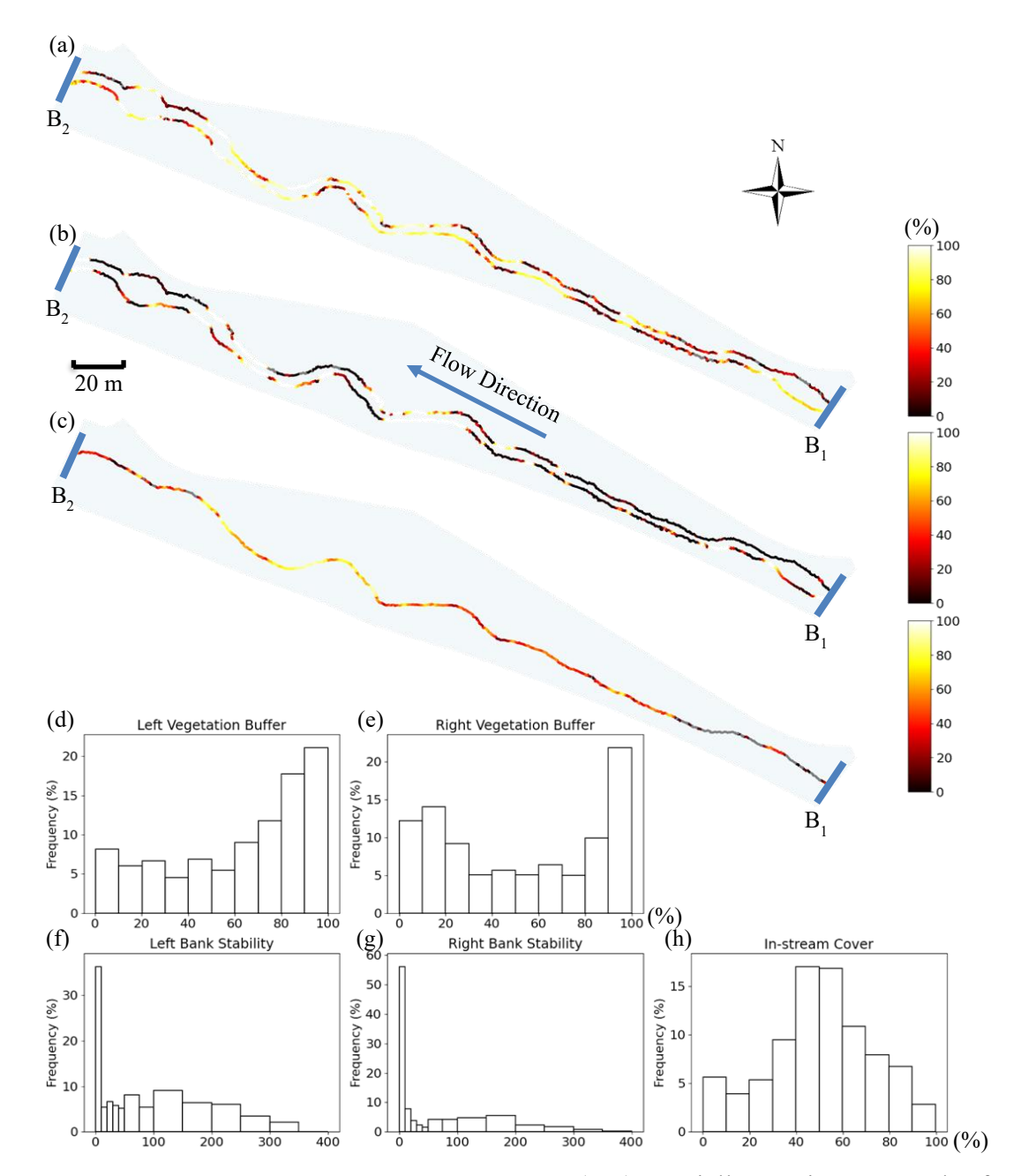


Figure 3-10 | **Loss of stream habitat quality.** (a–c) Spatially continuous results for the relative loss of left and right riparian vegetation buffers, left and right bank stability, and instream cover. (d–h) Percentage distribution of the relative loss of stream habitat quality for left riparian vegetation buffer, right riparian vegetation buffer, left bank stability, right bank stability, and in-stream cover.

high erosion widths or improved conditions after the flood. For most transects on both banks, the eroded width increased for less than 20% of the stream width at the same transect. However, severe losses were observed in the connection area between the first and second bend and from the last

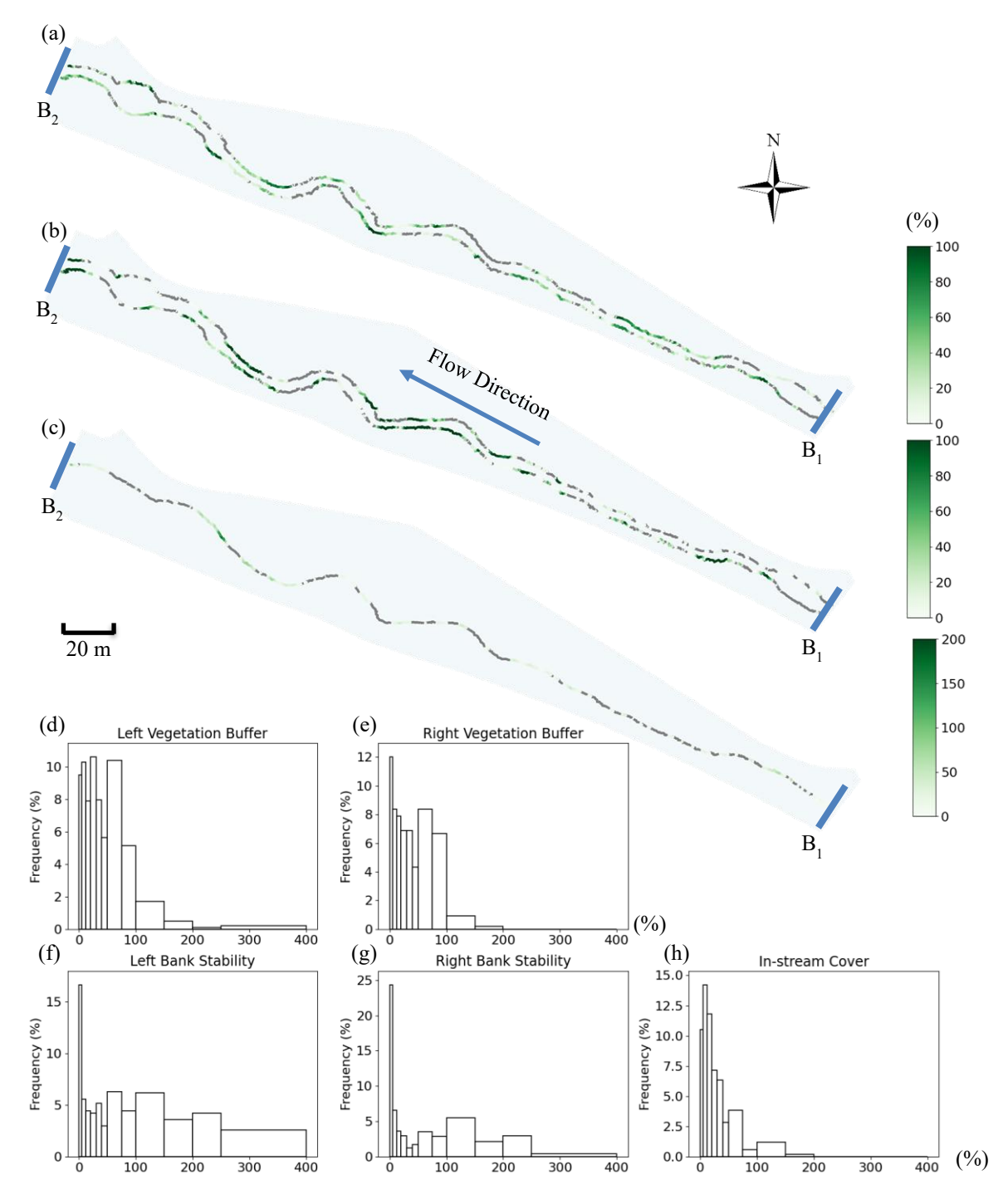


Figure 3-11 | Resilience of stream habitat quality in year one. (a–c) Spatially continuous results for the relative resilience at year one of left and right riparian vegetation buffers, left and right bank stability, and in-stream cover. (d–h) Percentage distribution for the relative resilience at year one of stream habitat quality for left riparian vegetation buffer, right riparian vegetation buffer, left bank stability, right bank stability, and in-stream cover.

bend to the island. The maximum relative loss reached 348.5% on the left bank (transect 739) and

465.1% on the right bank (transect 758). For in-stream cover (IC, Fig. 3-10c), 13.22% of transects

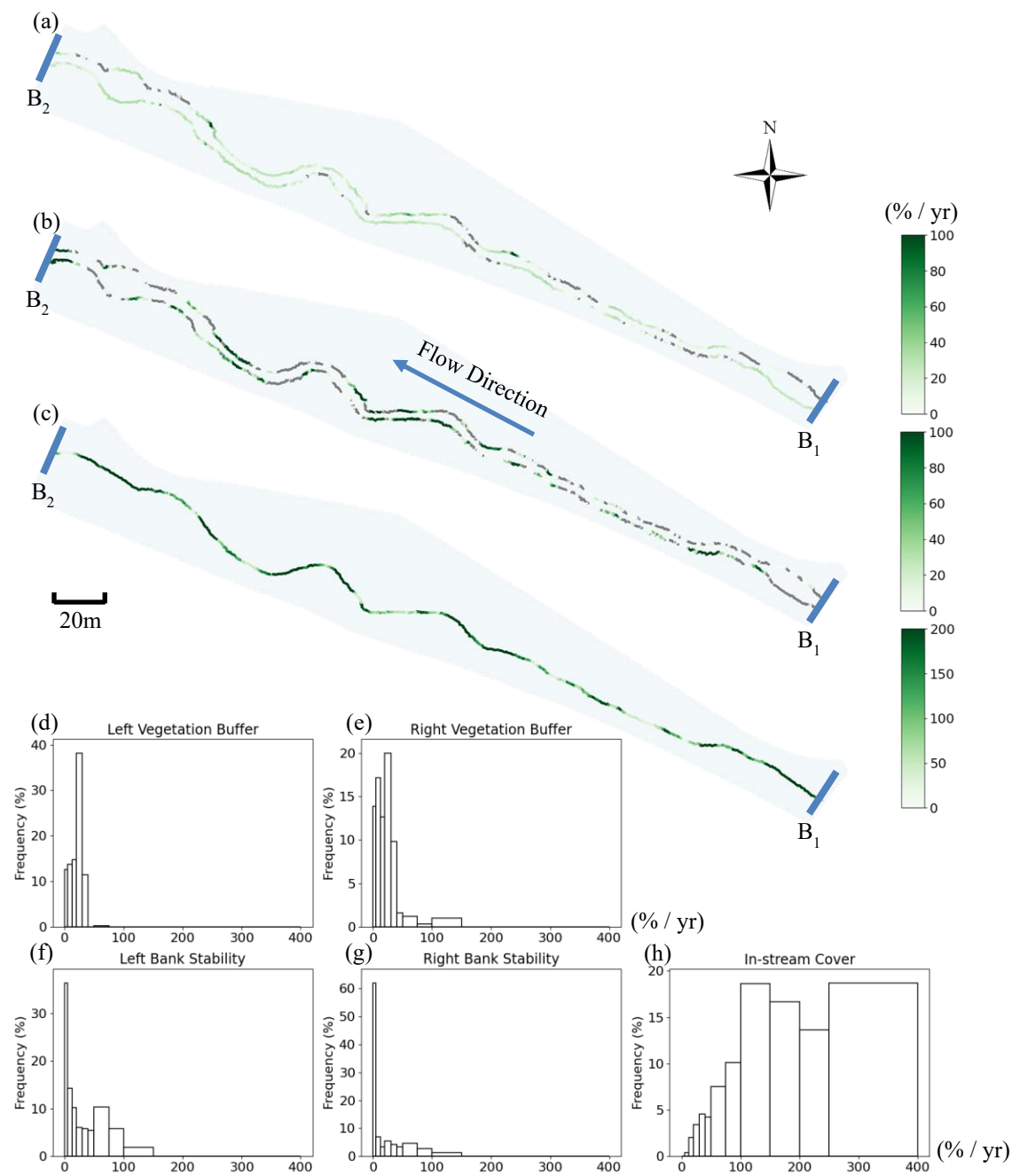


Figure 3-12 | Resilience of stream habitat quality in year three. (a–c) Spatially continuous results for the relative resilience at year three of left and right riparian vegetation buffers, left and right bank stability, and in-stream cover. (d–h) Percentage distribution for the relative resilience at year three of stream habitat quality for left riparian vegetation buffer, right riparian vegetation buffer, left bank stability, right bank stability, and in-stream cover.

were recorded as NaN, either due to pre-flood zero values or improved conditions. Loss values were relatively low in upstream and downstream transects, while the section between the second bend and the island showed consistently high losses (>80%).

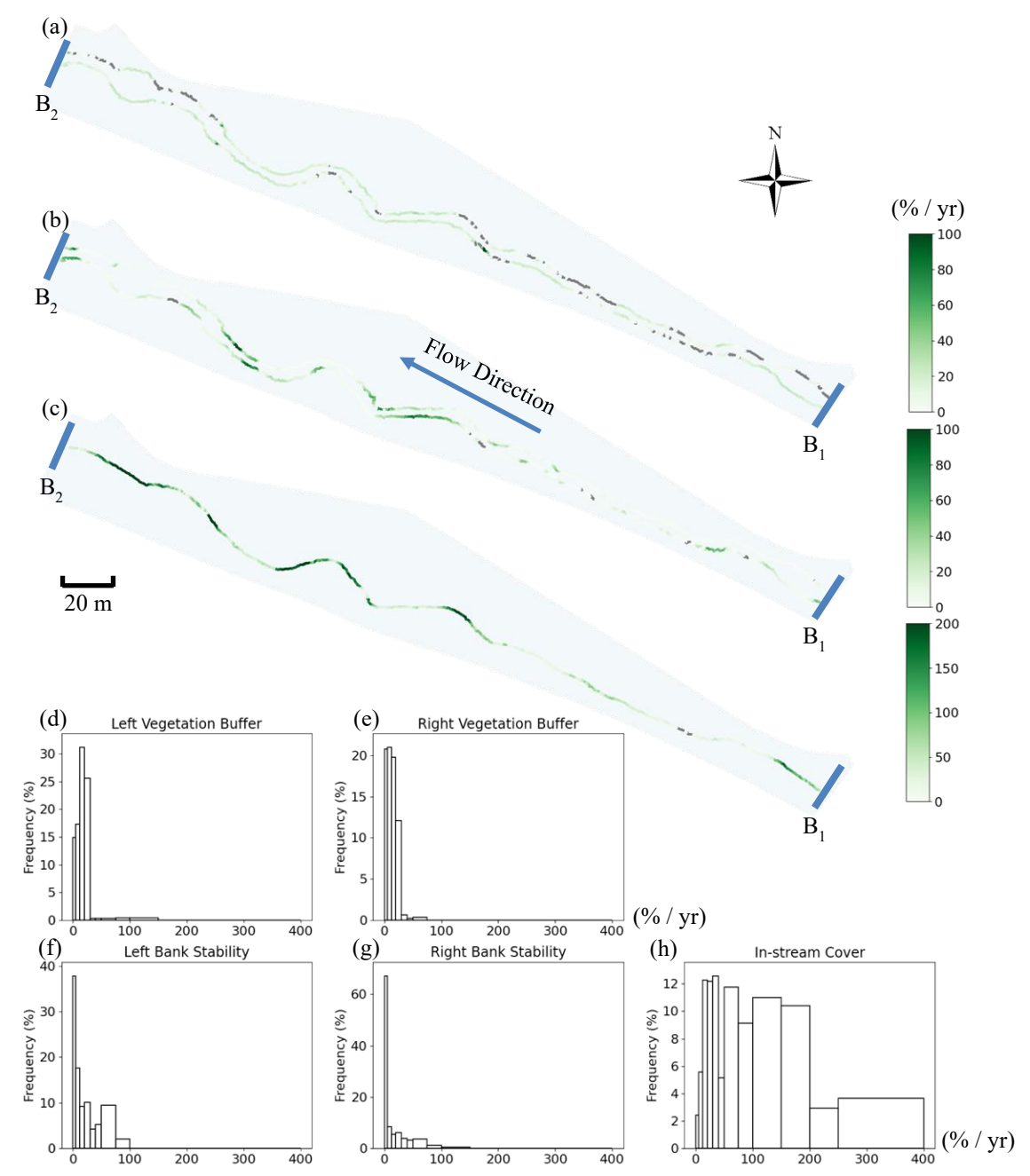


Figure 3-13 | Resilience of stream habitat quality in year four. (a–c) Spatially continuous results for the relative resilience at year four of left and right riparian vegetation buffers, left and right bank stability, and in-stream cover. (d–h) Percentage distribution for the relative resilience at year four of stream habitat quality for left riparian vegetation buffer, right riparian vegetation buffer, left bank stability, right bank stability, and in-stream cover.

The resilience of the MMIs is shown in Fig. 3-11 to Fig. 3-13. In the first year after the 2018 flood, a substantial proportion of riparian vegetation buffer (RVB) transects were recorded as NaN—30.07% on the left bank and 31.54% on the right bank—indicating either zero pre-flood

conditions or stable values lower than post-flood conditions (Fig. 3-11a). In the following years, RVB continued improving, and by year four the NaN ratio had declined to 9.18% on the left bank and 25.23% on the right bank (Fig. 3-12a, Fig. 3-13a). At year one, 17.9% of left-bank transects and 16.0% of right-bank transects showed at least 50% recovery of pre-flood conditions (Fig. 3-11d-e). By year three, 49.3% of left-bank transects and 33.6% of right-bank transects had recovered at least 60% of their initial condition (20% average annual rate), and by year four the proportions were 50.6% and 27.5%, respectively (15% annual rate; Fig. 3-12d-e, Fig. 3-13d-e). The maximum RVB resilience reached 134.0%/yr on the left bank (transect 432) and 71.7%/yr on the right bank (transect 798) in year four, confirming greater resilience on the left bank. For bank stability (BS) (Fig. 3-11b), 32.80% of left-bank transects and 40.57% of right-bank transects were NaN in year one. By year four, these ratios decreased to 4.14% and 0.10%, respectively (Fig. 3-12b, Fig. 3-13b), showing substantial recovery across most sites, with 30-40% of transects recovering between years one and four. At year one, 26.3% of left-bank and 16.6% of right-bank transects had regained at least 50% of half-stream width (Fig. 3-11f-g). By year three, 35.3% of left-bank and 21.4% of right-bank transects reached 60% recovery (Fig. 3-12f-g), with similar levels by year four (35.9% and 22.7%, respectively; Fig. 3-13f-g). High-resilience areas on the left bank included the small upstream curve, the reach between the first and second bends, the section from the last bend to the island, and the downstream reach, while on the right bank they were mainly concentrated near the second bend, from the last bend to the island, and in the downstream area. Maximum BS resilience reached 87.1%/yr at left-bank transect 739 and 116.8%/yr at right-bank transect 759, indicating erosion widths decreased by more than three times half the stream width at these locations. For in-stream cover (IC) (Fig. 3-11c), 41.27% of transects were recorded as NaN in year one, but this proportion dropped sharply to 1.01% by year four,

indicating widespread recovery (Fig. 3-12c, Fig. 3-13c). Only 5.8% of transects achieved at least 50% recovery in year one (Fig. 3-11h), but by year three 96.8% had exceeded 60% recovery (20% annual rate; Fig. 3-12h), and by year four 87.3% still exceeded 60% (15% annual rate; Fig. 3-13h). High resilience in IC was observed in the upstream section near the bridge, the first bend, the segment between the second and last bends, and the island. The maximum resilience in year four reached 283.8%/yr at transect 905, highlighting significant improvement in in-stream cover due to the establishment of emergent vegetation.

3.5.6 Loss-Resilience Types

The loss-resilience types of each transect are shown in Fig. 3-14. For riparian vegetation buffer (RVB, Fig. 3-14a), the left bank was dominated by type II, where conditions first declined after the flood and then recovered to equal or better than pre-flood levels. Other types were mostly concentrated in the upstream area before the first bend. The right bank showed greater diversity, with less than half of the transects classified as type II and considerable proportions of type I (conditions never worse than pre-flood) and type III (conditions worsened and did not recover to pre-flood levels). These type I and type III transects were mainly distributed in the upstream reach before the first bend, around the third bend, from the last bend to the island, and near the downstream bridge. For bank stability (BS, Fig. 3-14b), the left bank was also dominated by type II, followed by type I, which was mainly concentrated in the upstream area before the first bend and between the second and third bends. On the right bank, both type II and type I were prevalent, with type I occurring primarily in the upstream reach, at the second bend, and upstream and downstream of the island. For in-stream cover (IC, Fig. 3-14c), type I and type II were both important. Type I occurred more frequently in the upstream and downstream sections, while type II was more common in the middle portion of the study site.

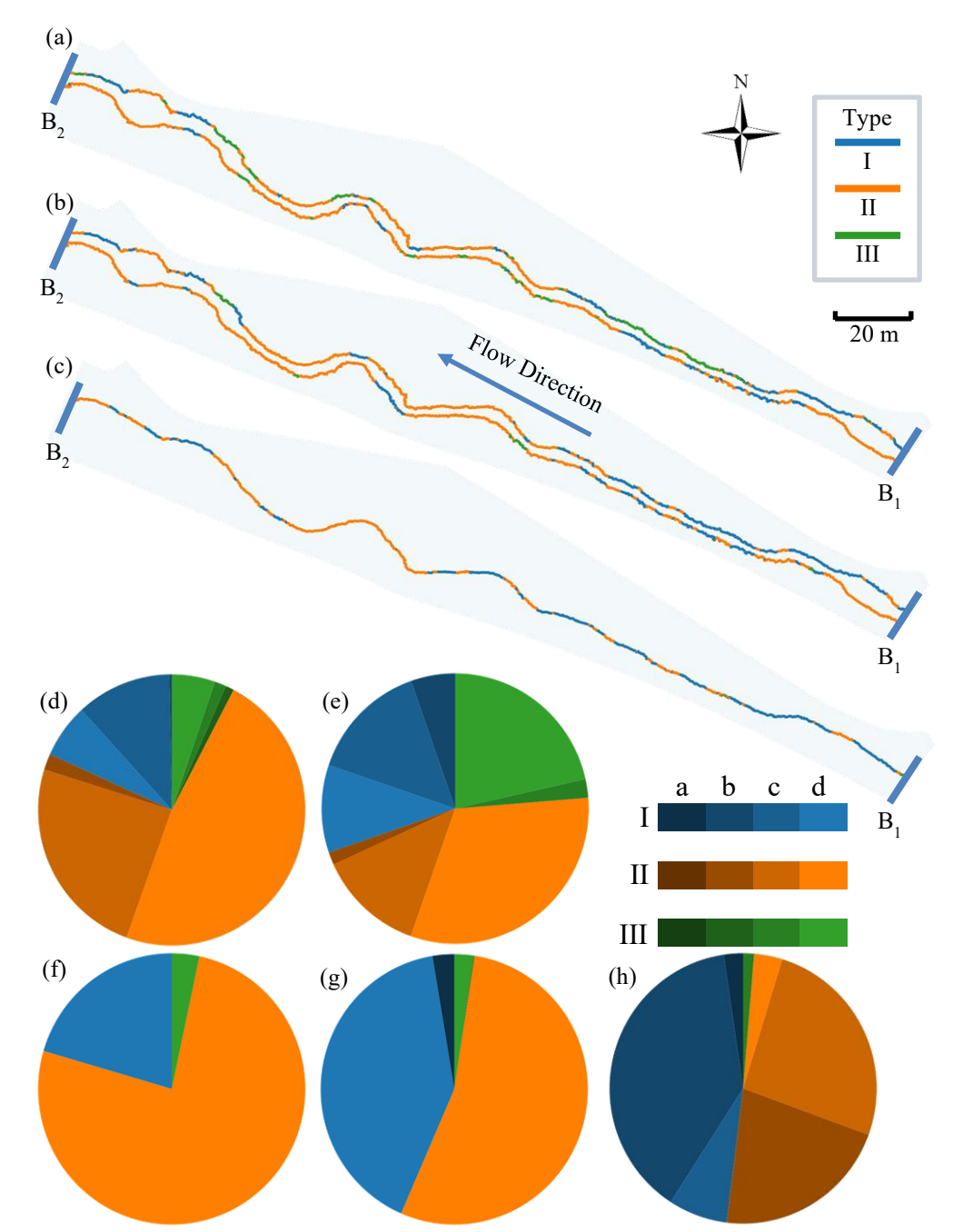


Figure 3-14 | Loss-resilience types of stream habitat health based on six UAV survey outputs (2018–2022). (a–c) Spatially continuous results of relative resilience at year four for left and right riparian vegetation buffers, left and right bank stability, and in-stream cover. (d–h) Percentage distributions of loss-resilience types for the same metrics. Note: I, II, and III denote the three types of loss-resilience curves; a, b, c, and d represent the original conditions of poor, fair, good, and excellent, respectively.

When further subdivided into subtypes (a–d) according to pre-flood condition (poor, fair, good, excellent), distinct patterns were observed (Fig. 3-14d-h). For left riparian vegetation buffer

(RVB) (Fig. 3-14d), the majority of transects were IIc (24.3%) and IId (47.8%), starting from good or excellent condition, declining after the flood, and later recovering to equal or better levels. Smaller shares included Ic (11.5%) and Id (6.5%), which remained good or excellent throughout, and IIb (1.9%). A few transects showed persistent decline, such as IIIb (1.0%), IIIc (1.4%), and IIId (5.2%). For the right RVB (Fig. 3-14e), IId (31.7%) was the largest group, but a substantial portion were IIId (21.5%), where transects started from excellent but did not return to that level. Other notable groups included Ic (14.4%), Id (10.5%), and Ib (5.3%), with smaller shares in other II and III categories. For bank stability (BS), most transects began in excellent condition. On the left bank (Fig. 3-14f), IId (76.2%) and Id (20.5%) dominated, while only IIId (3.3%) represented persistent decline. On the right bank (Fig. 3-14g), the pattern was similar, with IId (54.1%) and Id (40.9%) as the majority, and only minor fractions in Ia (2.6%), IIIb (0.1%), and IIId (2.3%). For in-stream cover (IC) (Fig. 3-14h), most transects started from fair conditions. The largest group was Ib (38.5%), which remained fair or better throughout, followed by IIb (21.4%) and IIc (25.8%), where conditions declined and later returned to fair or good states. Smaller fractions included Ic (7.2%), IId (3.4%), and Ia (2.3%), while only a few (IIIc: 1.3%) represented long-term decline.

3.6 Discussion

3.6.1 Limitation and future improvements

This study provides new insights into flood impacts and recovery of stream habitat quality using UAV-based MMI assessment, but several limitations remain that highlight opportunities for future improvements. First, the temporal sampling interval was limited to six UAV surveys between June 2018 and October 2022. Although these surveys captured pre-flood, post-flood, and steady conditions, habitat changes can exhibit seasonal variation, and more frequent sampling would better resolve such dynamics. In addition, resilience is not only defined by whether a system

eventually returns to its unimpaired state but also by the duration required to do so (Greig et al., 2022; Hua et al., 2025); higher-frequency sampling would therefore allow assessment of both recovery extent and recovery time, although this remains challenging given the low frequency and unpredictability of natural hazards. Complementary to UAV surveys, establishing on-site webcam networks could provide continuous visual records that help bridge temporal gaps, particularly when the image resolution requirement is not high (Sushmitha et al., 2024). Such networks would allow short-term or unexpected disturbances to be captured in real time, offering valuable context for UAV-based observations and supporting assessment of both recovery extent and recovery duration. Second, the current approach does not separate natural recovery from human intervention, (Serra-Llobet et al., 2022). For instance, emergent plants were introduced at the study site as part of restoration, making it difficult to attribute recovery solely to natural processes. Future studies could address this by surveying remote sites with minimal human activity to capture natural recovery, or by establishing controlled experiments that compare restored and unrestored reaches to evaluate the effectiveness of interventions. Third, while the 2018 flood was the most severe event at the study site, subsequent floods were much smaller and thus treated as background disturbances within the long-term recovery process. These baseline flood pulses may provide ecological benefits, such as enhancing biological productivity and transporting nutrients and organisms between river and floodplain (Heiler et al., 1995; Tockner and Ward, 2000; Doyle et al., 2005; Cluer and Thorne, 2013), potentially outweighing negative effects. Long-term monitoring would help calibrate the loss-resilience analysis against such baseline impacts. Fourth, only three key indicators were assessed (riparian vegetation buffer, bank stability, and in-stream cover), while other important metrics such as those related to water depth and water quality were not included. The integration of topo-bathymetric green Lidar and drone-mounted hyperspectral

sensors would enable inclusion of additional metrics, thereby providing a more comprehensive view of habitat quality (Islam et al., 2022; Bai et al., 2024). In addition, the link between physical habitats and fish spawning success remains unknown at the study site. In-situ surveys to build stock—recruitment models could help establish MMI thresholds tied more directly to fish protection (Maunder and Deriso, 2013; Skoglund et al., 2022). Fifth, delineation of habitat features still requires human effort, as current segmentation models struggle to reliably distinguish vegetation types with subtle differences. Advances in visual-language foundation models, such as the Segment Anything Model (SAM), may help automate this step and reduce manual intervention (Kirillov et al., 2023). Finally, the loss-resilience classification (Types I-III) provides a useful overview but does not capture the magnitude of impairment within each type. For example, a site that dropped from excellent (4) to good (3) and later returned to excellent is treated the same as a site that dropped from excellent (4) to poor (1) and then recovered, although the ecological significance differs. Developing refined classifications that incorporate both loss-resilience type and severity would improve interpretation. Addressing these limitations would enhance the reliability, scalability, and applicability of UAV-based stream habitat monitoring, enabling more robust assessments of both natural recovery and restoration performance.

3.6.2 Variations among transects

The analysis revealed substantial variation among transects and across different habitat metrics, emphasizing the importance of spatially explicit assessment. For riparian vegetation buffer and bank stability, most transects followed type II loss—resilience classifications, where conditions declined after the flood and subsequently returned to pre-flood or better levels. However, localized differences were evident, with some transects exhibiting type I (never worse than pre-flood) and others showing type III (persistent impairment), particularly around bends and

areas with exposed soil. In-stream cover displayed a distinct pattern, as many transects began in only fair condition and either remained stable (Ib) or showed modest recovery (IIb, IIc), while very few experienced sustained decline. When transect-level results were aggregated to the whole site (Fig. 3-15), the classifications simplified into type IId for both riparian vegetation buffer and bank stability, and Ib for in-stream cover, all representing eventual recovery to unimpaired levels. The integrated change sequences further illustrate this trend: both left and right riparian vegetation buffers followed excellent \rightarrow good \rightarrow good \rightarrow excellent \rightarrow excellent, ending as type IId; left bank stability showed excellent \rightarrow poor \rightarrow poor \rightarrow excellent \rightarrow excellent, both classified as IId. In contrast, in-stream cover followed fair \rightarrow fair \rightarrow fair \rightarrow excellent \rightarrow excellent, reflecting a type Ib pathway of steady improvement. While this whole-site integration highlights dominant resilience patterns, it also masks the presence of type III classifications observed at individual

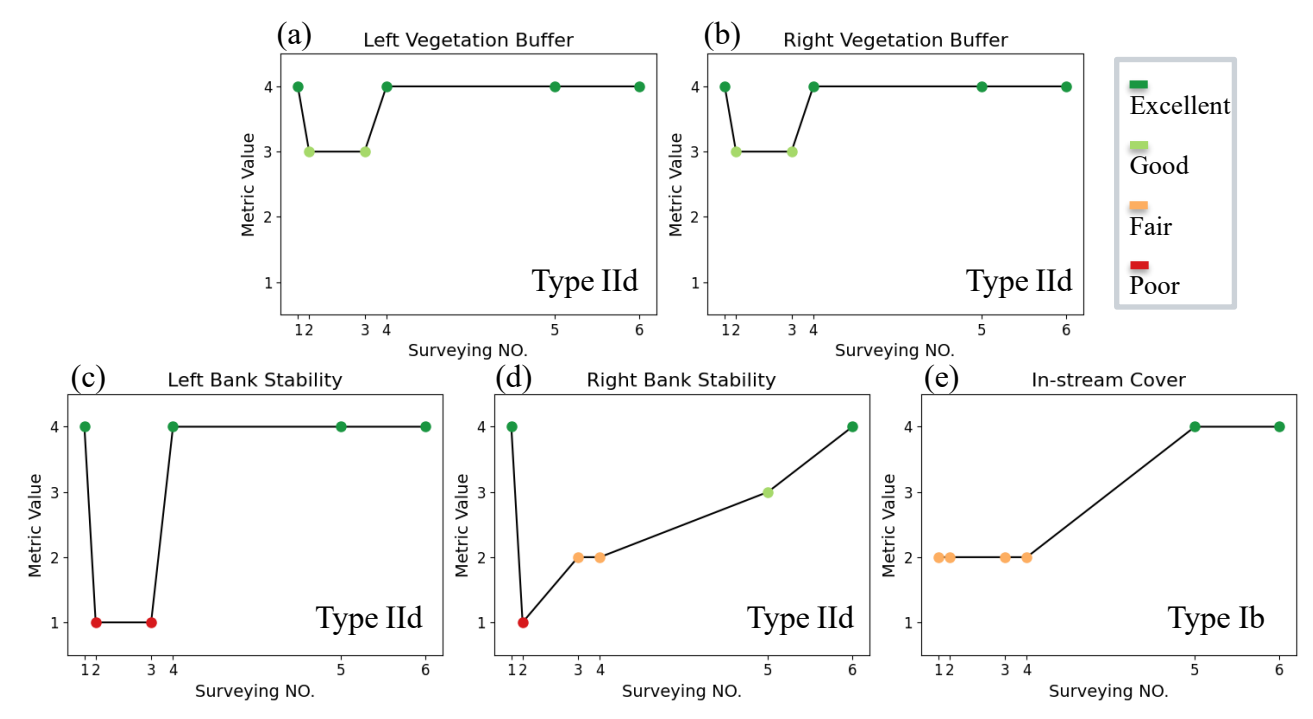


Figure 3-15 | **Loss–resilience curves for MMIs at the whole study site.** (a) Left riparian vegetation buffer, (b) right riparian vegetation buffer, (c) left bank stability, (d) right bank stability, and (e) in-stream cover. Surveying numbers 1–6 correspond to the dates 08/09/2018, 09/29/2018, 06/07/2019, 09/14/2019, 10/18/2021, and 10/31/2022.

transects, where conditions deteriorated and failed to recover. Such persistent declines, though limited in extent, identify the most fragile portions of the stream and are ecologically critical for management. Thus, while site-level integration is useful for summarizing overall system behavior, transect-level variation could provide indispensable insights into localized vulnerabilities that would otherwise be overlooked, underscoring the need for monitoring strategies that capture both overall recovery and persistent local degradation.

3.6.3 Potential generalization

The patterns observed in this study highlight the broader potential of UAV-based MMI assessments for generalizing recovery status across different sites and hazard types. Although this work focused on a single stream impacted by flooding, the loss-resilience classifications and transect-level variation provide a transferable framework that could be applied to other fluvial systems with comparable geomorphic or ecological settings. More importantly, the approach is not restricted to flood disturbances. By tracking how habitat conditions move between impaired and unimpaired states, the same methodology could be extended to other hazard contexts such as nutrient enrichment, sediment loading, or contamination from industrial and agricultural pollution (Hughes et al., 2021; Ogidi and Akpan, 2022 Rios-Touma et al., 2022). In these cases, UAV-based observations of vegetation buffer integrity, bank conditions, or water-surface cover could serve as proxies for ecosystem recovery following stressor reduction or management interventions. The classification of sites into type I, II, or III pathways helps identify which areas are resistant, resilient, or persistently impaired, providing a common language for comparing loss-resilience patterns across disturbance types. Practically, this generalization means that restoration and monitoring strategies informed by UAV-based MMIs can be adapted for diverse hazard settingswhether floods, pollution, or land-use change—supporting decision-makers in prioritizing interventions at both local and regional scales.

3.7 Conclusion

This study demonstrates the utility of UAV-based MMI assessment for quantifying flood impacts and recovery of stream habitat quality. Six UAV flights conducted between August 2018 and October 2022, including one before the August 2018 flood and five after, provided a unique multi-year dataset to track changes in riparian vegetation buffer, bank stability, and in-stream cover. Using the loss-resilience classification (Types I–III with subtypes), we identified how different habitat features responded to disturbance. Most transects showed type II behavior, with declines followed by recovery to pre-flood or better conditions, while some exhibited type I resilience, never falling below initial levels, and others displayed type III, where impairment persisted. The integrated whole-site results simplified to type IId for riparian vegetation and bank stability and Ib for in-stream cover, suggesting overall recovery but masking localized fragilities. This combination of transect-level and site-level perspectives illustrates both the resilience and the heterogeneity of stream habitats under flood stress. UAV-based surveys provided a cost-effective, repeatable, and spatially explicit way to capture these dynamics over multiple years. At the same time, challenges remain, such as limited temporal resolution and the difficulty of distinguishing natural recovery from human interventions, these can be partially addressed through higherfrequency monitoring, complementary tools such as web-cam networks for continuous observation, and the integration of additional habitat indicators. More broadly, the framework developed here can be generalized to other streams and disturbances, including pollution and droughts, offering a practical path forward for resilience-based ecological assessment and restoration planning.

Chapter 4: Detection and characterization of flash rips in Lake Michigan using a deep learning framework

4.1 Introduction

Flash rips, episodic bursts of seaward water flows at featureless beaches (MacMahan et al., 2006; Castelle et al., 2016), can unexpectedly sweep people in nearshore areas to deeper offshore zones (McCarroll et al., 2014). Different from bathymetrically-controlled (Dalrymple et al., 2011) and boundary-controlled rip currents (Castelle and Coco, 2013; Castelle et al., 2016), nonstationary and intermittent flash rips can be caused by mechanisms including shear instability in longshore currents under oblique wave incidence (Özkan-Haller and Kirby, 1999; Feddersen, 2014), or non-uniform wave breaking induced vortices evolving into large-scale surf zone eddies under shore-normal wave incidence (Castelle et al., 2016; Kirby and Derakhti, 2019), or vortices generated by rapid currents due to meteorologically-induced water level oscillations (Linares et al., 2019; Liu and Wu, 2022a). Owing to the transient and intermittent feature, flash rips pose unexpected hazards to beachgoers due to lack of awareness and the difficulty for timely detection (Fallon et al., 2018; Ménard et al., 2018). Flash rip-related drowning incidents have been reported globally, such as China (Zhang et al., 2021), Japan (Ishikawa et al., 2014), Europe (Basterretxea-Iribar et al., 2022), and the U.S. (Slattery et al., 2011). In the Laurentian Great Lakes, flash rips were found to be associated with a series of drowning incidents between 2002 and 2019 (Vlodarchyk et al., 2019; Liu and Wu, 2022a). For instance, on July 13, 2022, four individuals drowned in separate, unexpected rip incidents in South Haven and Ferrysburg, Michigan (Great Lakes Surf Rescue Project, 2024). In view of these consequences, detecting and characterizing dangerous flash rips is an urgent need for coastal communities.

Existing studies have characterized flash rip from several perspectives. Geometrically, flash rips display a "mushroom cloud" head shape with a narrow neck (Dalrymple et al., 2011; Castelle et al., 2016). Flash rips can reach beyond the surf zone, extending several hundred meters seaward (Floc'h et al., 2018; Liu and Wu, 2019). Compared to bathymetry- and boundary-controlled rips, flash rips generally exhibit a smaller offshore scale (Dalrymple et al., 2011). Kinematically, flash rips have smaller offshore flows than rip currents emerging from main rip channels in most cases (Johnson and Pattiaratchi, 2006; Austin et al., 2012). For instance, observations around West Africa showed that approximately 65% of flash rips had a velocity range of 0.2 m/s to 0.6 m/s offshore (Floc'h et al., 2018). Studies in Lake Michigan found maximum velocities of hidden flash rips reaching 0.5 m/s, attributed to either wind waves or water level oscillations (Liu and Wu, 2022a). Temporally, flash rips have varying temporal scales (Schönhofer and Dudkowska, 2021). Durations of flash rips in general are relatively short, extending from a handful of seconds to several minutes (Murray et al., 2003; Liu and Wu, 2019; Kim, 2021). Spatially, occurrences of flash rips are not stationary, unlike fixed hotspots caused by other types of rip currents, such as pocket beaches (Carpi et al., 2021), coastal structures (Liu and Wu, 2022b; Xu et al., 2024), and nearshore bars or terraces (Smit et al., 2012). Flash rips were observed to relocate during the lifespan (Castelle et al., 2014; Liu and Wu, 2019) in morphologically featureless uniform beach areas. Despite the progress in characterizing flash rips in terms of geometric, kinematic, temporal, and spatial features, a comprehensive study of flash rip characteristics affected by different driving factors remains limited, as far as the authors are aware. To address this gap, accurate detection is a critical prerequisite and has become an active area of research in recent years.

Previous methods to detect flash rips can be generally classified into three categories. First, trained lifeguards identify flash rips by utilizing observational information such as colour contrasts

and sediment-laden flows (Brannstrom et al., 2015; Brewster et al., 2019), which have been used to train lifeguards in several projects and agencies, such as United States Lifesaving Association (United States Lifesaving Association, 2024). While effective in reducing drowning incidents (Brander and MacMahan, 2011; Gilchrist and Branche, 2018), the dependency on lifeguard availability and the inability to provide quantitative descriptions have been of concerns (Sotés et al., 2020). Second, drone technology in recent years has been employed to detect rip currents, i.e. regions with seaward flows, through observed videos/images or estimated velocities using traced dye (Leatherman and Leatherman, 2017), debris flows (Fletemeyer, 2014), or mounted velocimeter (Dérian and Almar, 2017). Nevertheless, the limited flight duration of drones and the difficulty in operating drones to acquire data under heavy wind conditions (Gao et al., 2021) are bottlenecks. Third, remote optical cameras are commonly employed to continuously monitor nearshore water surface conditions (Holman and Stanley, 2007; Gallop et al., 2009; Abessolo et al., 2023). In 2019, an innovative cyberinfrastructure, the Lifeguarding Operational Camera Kiosk System (LOCKS), was developed for flash rip detection by applying HSV-based segmentation and an offshore length threshold for rip-induced sediment plumes (Liu and Wu, 2019). However, finetuning thresholds can be tedious and case-dependent, limiting the effectiveness of detecting nonstationary flash rips. The aforementioned concerns and limitations call for the development of quantitative, automated, and robust detection methods for flash rips.

In recent years, deep learning techniques have become popular to detect rip currents. Generally, these techniques can be classified into three types. The basic convolutional neural network (CNN) is straightforward to implement and proficient to detect well-defined rip channels (Maryan et al., 2019). One-step regional CNN methods, such as YOLO (You Only Look Once), can quickly locate rip current objects from images without the need to extract regions of interest

(Zhu et al., 2022; Dumitriu et al., 2023). Two-step regional CNN methods, such as Faster R-CNN, by first identifying and then refining the potential regions of interest, have been validated to achieve higher accuracy than the one-step method (Ren et al., 2017). These methods have been used to detect channel rips from images and videos (de Silva et al., 2021). However, Faster R-CNN relies on a fixed intersection-over-union (IoU) value, often leading to false detection when inferencing testing dataset (Tian et al., 2019), especially for various sizes of rip signage (e.g., bubbles or sediment plumes) or blurred boundaries between rips and the background water body. To resolve the false detection issue, the Cascade R-CNN was developed, introducing a series of gradually increasing IoU thresholds during the refinement stage (Cai and Vasconcelos, 2021; Hoeser et al., 2020). Despite that cascading structure has been shown to improve the inference performance, the Cascade R-CNN has not yet been applied to detect flash rips, to our best knowledge.

4.2 Objectives and Research Goals

The objective of this chapter is to detect and characterize flash rips using a Refined Cascade R-CNN approach. Particularly, flash rips induced by three driving factors, oblique wind waves, normal wind waves, and water level fluctuations, were examined. Features of flash rips due to different driving factors were characterized by several perspectives: spatial (offshore distance and alongshore position), temporal (duration), and kinematic (growing speed). I propose that variations exist among the three mechanisms across all perspectives. In particular, flash rips induced by normal waves are expected to travel farther offshore, while exhibiting shorter durations and faster growing speeds compared to those caused by oblique waves and water level fluctuations. Three specific research goals are:

1. Develop deep-learning-based methods for automating flash rip detection.

- 2. Identify the driving factor associated with each flash rip event.
- 3. Characterize flash rip features across spatial, temporal, and kinematic dimensions, and compare similarities and differences among driving factors.

4.3 Materials and Methods

4.3.1 Study site and data sources

The study site is North Beach in Port Washington, Wisconsin, located on the western shoreline of Lake Michigan (Fig. 4-1a). The beach is aligned northeast, deviating approximately 30° from true north. The bathymetry, shown by the white bottom contours, is characterized by a mild bottom slope of 0.028, with water depth gradually increasing to 12.5 m within 1 km. A 762meter breakwater is situated approximately 375 m south of the beach's starting point. Strong winds are often observed, as the meteorological data from the National Data Buoy Center's PWAW3 station recorded 37, 60, 56, and 63 days with wind gusts exceeding 20 mph in 2019, 2020, 2021, and 2022, respectively. The strong onshore winds can create complex wave conditions, making the site a hotspot for rip currents. Several drowning incidents and rescues have been reported (Great Lakes Surf Rescue Project, 2024), with at least two fatalities between 2016 and 2021. To address water safety concerns, a Real-Time Environmental Observation System (RTEOS) (Liu and Wu, 2019), denoted by the yellow dot in Fig. 4-1a, was installed in 2019 at this site. After the installation, four rescues were reported on 08/18/2021 (Great Lakes Surf Rescue Project, 2024), 06/22/2022 (Ozaukee Press, 2022), 08/30/2022 (Fox6News, 2022a), and 09/08/2022 (Fox6News, 2022b). This sequence of incidents highlights the improved safety measures but also the ongoing challenges posed by flash rip hazards at the site.

To conduct this study, field observations were collected using the RTEOS and additional environmental datasets from 05/16/2019 to 09/14/2019. Water surface images were acquired

through the RTEOS, which consists of a webcam (Cam in Fig. 4-1b) and a remote-controlling system (Fig. 4-1c). The webcam is positioned 30 meters above ground on a pole (yellow dot in Fig. 4-1a) and is equipped with a 7.9 mm focal lens with a 45°×34° field of view (dashed triangle,

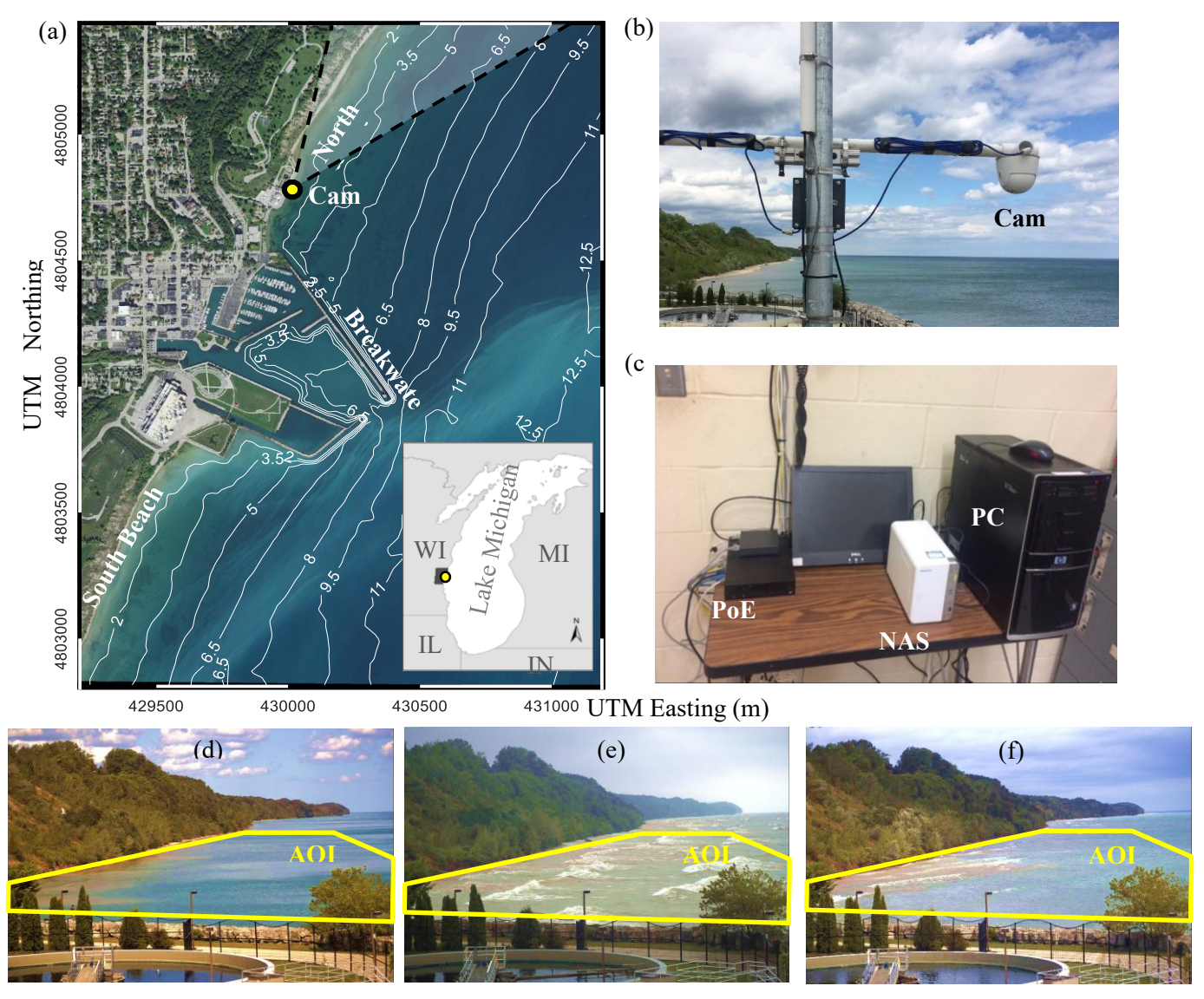


Figure 4-1 | Study site and remote camera systems. (a) illustrates the geographical location of Port Washington within Lake Michigan and pinpoints the positions of camera system within Port Washington by the yellow dot, respectively. The camera's fields of view demarcated by dashed triangles, while the bathymetry of our study site is displayed using white contours. (b) provides a real-world image of the onsite camera system. (c) shows the remote-control system used for image recording and processing. (d) – (f) present Examples of flash rips under three driving mechanisms. (d) an event occurred on 2019/08/08 at 13:47 CST caused by water level fluctuations. (e) an event occurred on 2019/08/26 at 16:49 CST induced by normal wave incidents; (f) an event observed on 2019/09/03 at 12:23 CST triggered by oblique wave incidents.

Fig. 4-1a). The remote system continuously receives image streams via Power over Ethernet (PoE) and archives 1MP resolution images every 10 seconds into network-attached storage (NAS) from 5:00 to 20:00 using a script running on local personal computer (PC). Screenshots from representative timestamps captured by the RTEOS are shown in Fig. 4-1d-f, where flash rip features associated with different driving factors are illustrated: water-level fluctuations (Fig. 4-1d), normal wind waves (Fig. 4-1e), and oblique wind waves (Fig. 4-1f). In addition to RTEOS, the following data was collected from other sources. Nearby wind and sea level pressure data with 1-min intervals were captured from ASOS's MKE station (located at 43.11N, 88.03W). Water level data with 6-min sampling periods was acquired from NOAA National Ocean Service station 9087057, which is located at 43.02N, 87.89W. Additionally, as no wind wave data observation was available during the study period, hourly wave statistics including significant wave height, wave mean direction, and wave period at a nearby Station ST94058 (located at 43.36N, 87.80W) from the hindcast model of U.S. Army Corps of Engineers (USACE) wave information study (WIS) was used. In short, RTEOS observation together with other meteorological and hydrodynamic observation and hindcast data provided the dataset to detect flash rips and characterize their features under different driving factors.

4.3.2 Flash rip detection

The overall workflow for flash rip detection within the area of interest (AOI, yellow boxes in Fig. 4-1d-f), is shown in Fig. 4-2, starting with image ortho-rectification, followed by image division, annotation, Cascade R-CNN training, and final detection with best-performed trained model and post-detection refinement.

4.3.2.1 Image preprocessing and preparation

Image preprocessing involved three steps. First, we ortho-rectified the AOI in each input oblique image into an orthophoto in a geo-referenced coordinate (Fig. 4-2a). This was achieved by computing 3D real-world coordinates (X, Y, Z) from 2D image coordinates (x, y) via the Direct Linear Transform (DLT) equations (Holland et al., 1997) to output an orthophoto of 5001×551 pixel dimension at a 0.1 m/pixel resolution. Second, we enhanced the orthophoto's colour contrast by 25% to improve sediment plume labelling. Third, we divided the orthophoto into square images (551×551 pixels, Fig. 4-2b) following the recommended 1:1 aspect ratio for CNN-based object detection.

To prepare the dataset for deep learning, 6,231 square images containing flash rip signatures were randomly selected from imagery captured between May 15 and September 13, 2019. This period ensured ice-free water surface conditions in Port Washington. Flash rips within each square image were identified using visual clues such as sediment plumes, which appears as narrow, seaward-flowing regions with a red or brown hue in contrast to the surrounding water (Floc'h et al., 2018). To ensure consistency, a feature was labelled as a flash rip object in this study if the following two criteria are satisfied: (1) it extends more than 10 meters from the shoreline, corresponding to a water depth of 0.28 meters based on the nearshore slope of 0.028 during summer 2019; (2) the offshore-to-alongshore length ratio is at least 1:10, ensuring that the detected feature is not a purely muddy water. The boundary of each identified flash rip was annotated using the smallest bounding rectangular box that extends from the base (where the red or brown hue starts to move into surrounding water) to the front of the sediment plumes. Among the 6,231

annotated images, 60% were used for training (model fitting), 20% for validation (performance assessment and hyperparameter tuning), and 20% for testing (final model evaluation).

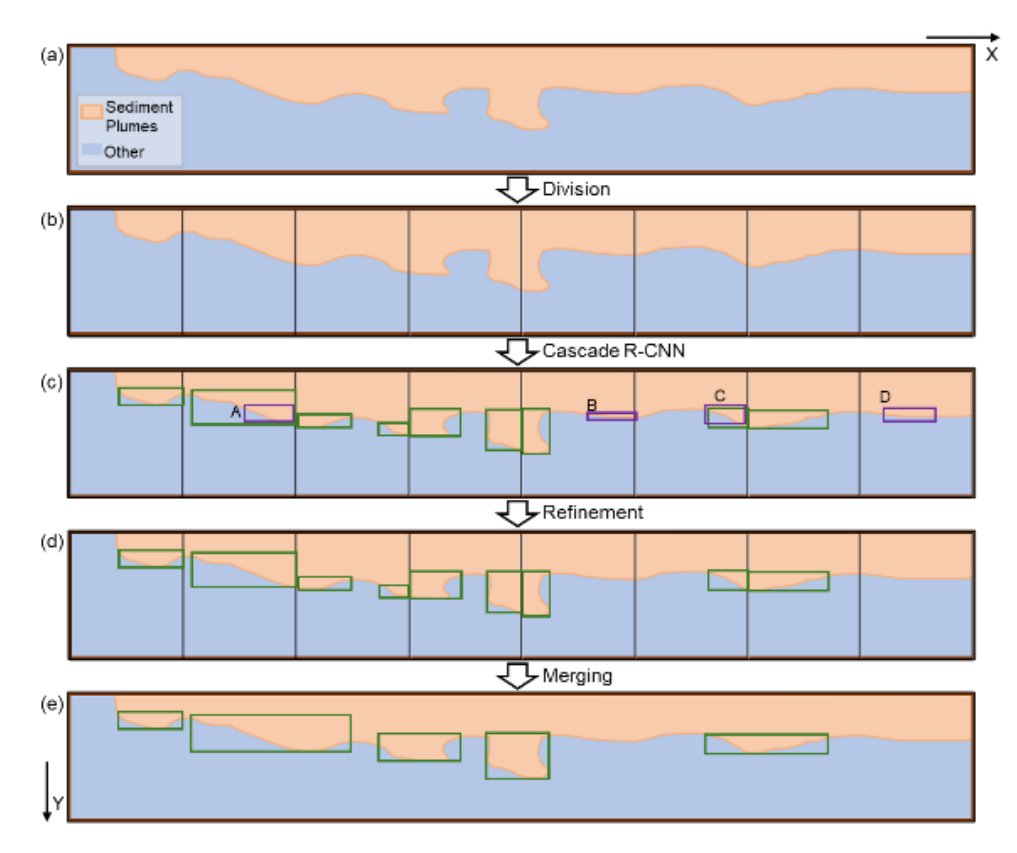


Figure 4-2 | Workflow for Flash Rip Detection. (a) is the sketch of orthophoto, sediment plumes are marked as orange, and the other parts are marked as blue; (b) demonstrates the division into square orthophotos; (c) shows the flash rip detection applied to each square orthophoto by cascade R-CNN; (d) presents the refinement for deep learning outputs, where purple boxes (A, B, C, D) would be eliminated; and finally, (e) displays the merging step to generate detection results for the whole orthophoto.

4.3.2.2 Refined Cascade R-CNN

A Refined Cascade R-CNN model comprised of a Cascade R-CNN module for processing input square images to detect flash rip objects through a two-stage architecture (Fig. 4-3a-b) and a post-detection refinement module (Fig. 4-3c). In the first stage of the Cascade R-CNN module (Fig. 4-3a), we employed ResNet50 as the pre-trained backbone model to extract feature maps from the input image. These feature maps captured essential visual elements such as edges,

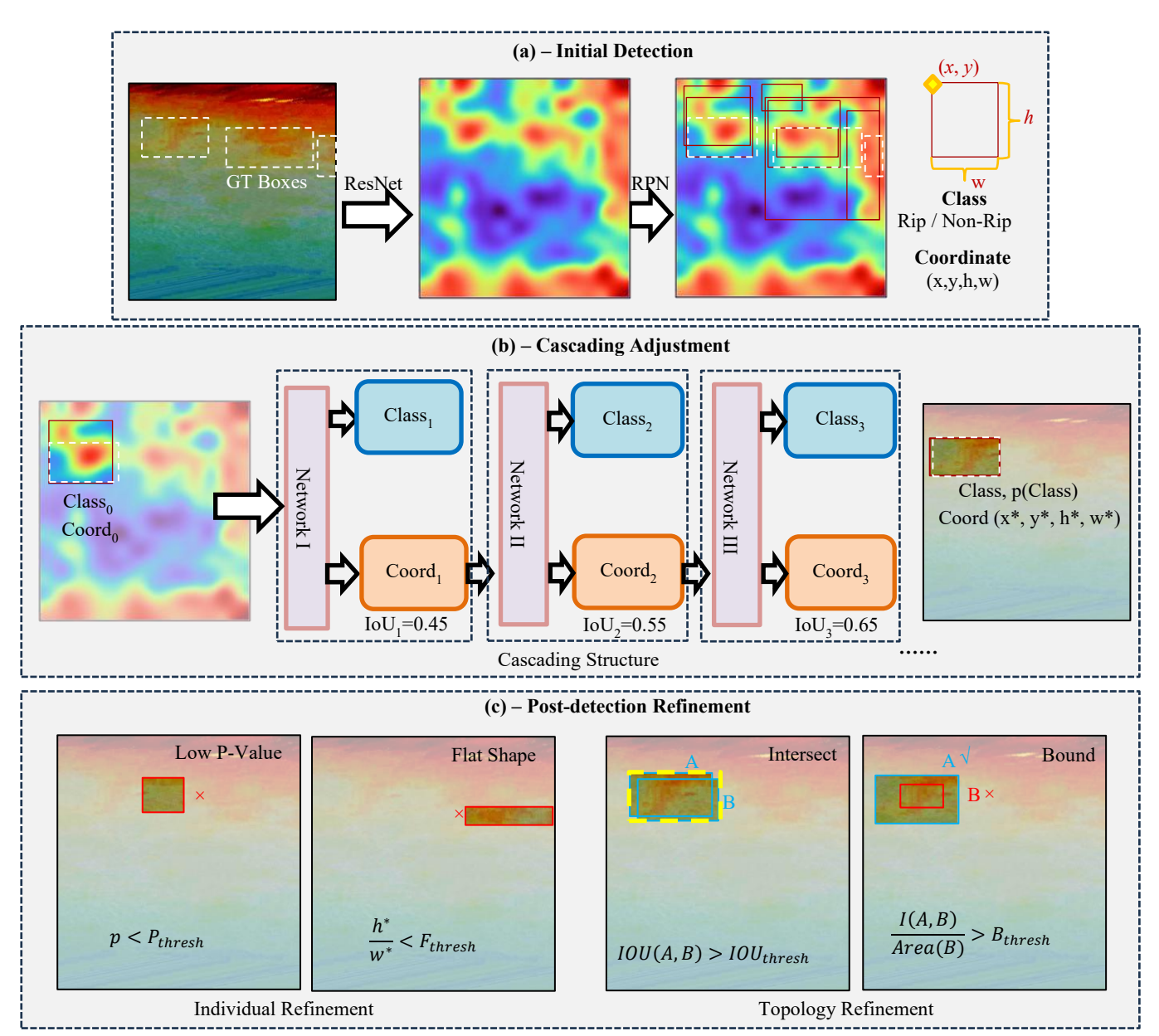


Figure 4-3 | Cascade R-CNN with Refinement Steps. (a) Initial detection employs ResNet to identify hotspots of potential objects and uses a Regional Proposal Network (RPN) to approximate the positions of likely flash rips. (b) Cascading adjustments modify these positions and refine the probability estimates for each flash rip using incremental Intersection over Union (IoU) thresholds. (c) Post-detection refinement eliminates detections with low probability values, flat shapes, and boundary issues, while also optimizing overlapping flash rip detections.

textures, and geometric patterns that are useful for distinguishing flash rips from the background.

The extracted features were then passed to a Region Proposal Network (RPN), which generated candidate Regions of Interest (ROIs, red boxes in Fig. 4-3a) at three scales (128×128, 256×256, 512×512) and aspect ratios (1:1, 1:2, 2:1) to cover different object sizes and shapes. Each ROI was

associated with a preliminary classification (flash rip or background) and bounding box information: x (top-left x-coordinate), y (top-left y-coordinate), h (height), and w (width). In the second stage (Fig. 4-3b), we refined the ROIs using a cascade structure to improve both classification and localization of flash rips. This structure utilized a series of detection units trained with increasing IoU thresholds (0.45, 0.55, 0.65) to enhance bounding box accuracy. Within each detection unit, ROIs underwent ROI pooling, which normalized them to a uniform size. The pooling output was then imported into two modules: a classification module (C) that discriminated whether a specified ROI is a flash rip (object) or not (background), and a boundary regression module (B) focused on refining the bounding box coordinates. Each ROI processed by the cascading architecture produced six output variables: Class (flash rip or background), p(Class) (probability of being a flash rip), and refined bounding box coordinates (x*, y*, h*, w*). In this study, the Refined Cascade R-CNN model was trained for 25 epochs (learning rate: 0.0002) using training and validation datasets. During training, we monitored model performance, checked convergence, and saved the checkpoint that achieved the best validation accuracy. This optimal model was later applied to the entire image dataset to detect flash rips with the defined bounding boxes (x^*, y^*, h^*, w^*) .

The post-detection refinement process was applied after obtaining the initial detection results from the best-performing Cascade R-CNN model. This refinement step aimed to reduce false positives by filtering out unconfident and redundant detections and merging overlapping or adjacent boxes when appropriate (Fig. 4-2c-e, Fig. 4-3c). Specifically, flash rip bounding boxes with a classification probability p(Class)<0.6 were considered insufficiently confident to be distinguished from the background and were therefore discarded. Boxes with an extremely flat shape, defined by an aspect ratio h*/w* < 1:10, were also removed to avoid misidentification of

sediment plumes, consistent with our labeling criteria. Bounded boxes—where a flash rip box was entirely contained within another, or more than 90% of its area overlapped with another box—were removed to eliminate duplicates. Intersected boxes with an Intersection-over-Union (IoU) greater than 70% were merged into a single detection. The new bounding box was adjusted to the minimum bounding rectangle (MBR) that enclosed both original boxes, and its classification probability, p(Class), was set to the mean value of the two. Lastly, adjacent boxes, defined as two flash rip boxes from neighboring square images that shared a common edge, were combined into one. The resulting bounding box was again expanded to the MBR of both, and the final p(Class) was assigned as the average of the two values.

4.3.3 Identification and classification of flash rip events

Using the Refined Cascade R-CNN, we applied the best-performed model to all orthophotos to detect flash rip objects. Detected flash rip objects were tracked over time based on their maximum offshore distance (MOD) within each orthophoto. To ensure consistency with the visual marking criteria, timestamps were excluded from analysis if no flash rip was detected or if the MOD was less than 10 meters offshore. A new flash rip event was considered to initiate when the MOD exceeded 10 meters for the first time following the termination of any previous event. From that point, the MOD was continuously monitored and updated as long as the flash rip remained active. The event was considered to terminate under either of the following two conditions: (1) the MOD decreased to less than half of the peak MOD observed during the event, or (2) the MOD consistently declined for five minutes without rebounding. If the MOD increased within five minutes, the flash rip event was treated as ongoing and therefore not separated into two events. Upon termination, an flash rip event was labeled as valid only if it met two criteria: (1) the duration from start to end was at least 45 seconds—corresponding to at least three timestamps based on the

10- to 15-second sampling interval—and (2) the starting timestamp was not the same as the timestamp with the peak MOD, to avoid including events that immediately decayed. This sequence of MOD growth, peak, and termination defined the life cycle of a single flash rip event.

Flash rip events were classified into three types based on the driving factors: (I) highfrequency water level fluctuations, such as meteotsunamis (2-minute to 2-hour periods) and seiches (lasting over 2 hours), where the water surface remains relatively calm with minimal wind wave activity, such as the example shown in Fig. 4-1d; (II) normal wind waves, characterized by waves breaking within the surf zone and moving perpendicular or nearly perpendicular to the shoreline, such as the example shown in Fig. 4-1e; (III) oblique wind waves, which also break within the surf zone but approach at an oblique angle to the shoreline, such as the example shown in Fig. 4-1f. To classify the identified rip currents into these three types, the water level data at the nearby NOAA station (9087057) and wave data from the nearby WIS station (ST94058) were preprocessed. High-frequency water level fluctuations (ΔWL) were extracted using a high-pass digital filter with a 6-hour cutoff frequency (Bechle and Wu, 2015) to isolate oscillations within the meteotsunami wave frequency band. Wave data corresponding to each event's starting timestamp were processed using a wave routing method to track wave movement from the WIS station located approximately 6 km southeast of the study site—to the outer edge of the surf zone (defined here as a water depth of 2 m, or approximately 70 m offshore based on the local bottom slope of 0.028). This method accounts for lake bathymetry and wave angle variations using Snell's Law (Eqn. 4-1) and the Conservation of Wave Power (C.W.P., Eqn. 4-2) expressed as,

$$\frac{\sin \alpha_1}{\sin \alpha_2} = \frac{L_1}{L_2}$$
 Eqn. 4-1

$$\frac{H_2}{H_1} = \left(\frac{\cos \alpha_1}{\cos \alpha_2}\right)^{\frac{1}{2}} \left(\frac{n_1 L_1}{n_2 L_2}\right)^{\frac{1}{2}}$$
 Eqn. 4-2

where L represents wavelength, α is the wave incident angle, H is wave height, and n is wave number. The subscripts 1 and 2 represent the two locations of routing. By using these equations iteratively, the wave height and angle at the next location (\mathbf{H}_2 , $\mathbf{\alpha}_2$) were estimated by the wave height and angle at current location (\mathbf{H}_1 , $\mathbf{\alpha}_1$). If waves were predicted to break—defined as the wave height, exceeding 0.78 times the local water depth (Dean, 1969)—before reaching the 2 m contour, the wave height was replaced with the calculated breaking wave height \mathbf{H}_b using Goda's formula (Eqn. 4-3; Goda, 1970; Rattanapitikon and Shibayama, 2000).

$$\frac{H_b}{L_0} = \frac{1}{7} \left\{ 1 - \exp\left(\frac{\pi d_b}{L_0} (16.21 \text{m}^2 - 7.07 \text{m} - 1.55)\right) \right\}$$
 Eqn. 4-3

where $\mathbf{L_0}$ is offshore wavelengths, $\mathbf{d_b}$ is water depth at breaking position, and m is the mean bottom slope.

Following the above preprocessing procedures, flash rip events were classified based on their associated water level and wave conditions. Water-level-induced flash rips were identified when the fluctuating water level change (Δ WL) prior to a flash rip event fell within the modest (0.1 m < Δ WL < 0.3 m) or high (Δ WL \geq 0.3 m) range (Liu and Wu, 2022), and when the nearshore wave height (Hs) was smaller than both Δ WL and 0.3 m. Conversely, wave-induced flash rips were identified when Hs was greater than 0.3 m, or when it ranged between 0.1m and 0.3m but exceeded Δ WL. Additionally, normal waves were defined as those with a nearshore incident wave angle (θ) between -30° and 30° while oblique waves were those with θ below -30° or above 30°. Additionally, a high-pass filter with a 2-hour cutoff frequency was applied to examine correlations between storm-related high-frequency atmospheric pressure fluctuations and water-level-induced flash rips.

4.3.4 Flash rip characterization

To comprehensively characterize flash rip events, we analysed their spatial, temporal, and kinematic features across the three types associated with different main factors. Spatially, we recorded the peak maximum offshore distance (PMOD), which is the farthest offshore extent among all detected flash rip objects within an event, and identified the peak timestamp as the moment when the PMOD occurred. At this timestamp, we also documented the offshore distance (OD) of each individual flash rip object. Additionally, we assessed the alongshore position (AP) of each flash rip object at the peak timestamp, as well as the alongshore position of peak rips (APP), defined as the AP of flash rip objects with the greatest offshore distance. Temporally, we measured each event's duration from initiation to termination, along with the growing time cost (GTC), defined as the time interval between the start of the event and the timestamp at which the PMOD was first reached. Kinematically, the growing speed of the front line (GSF) was calculated by dividing PMOD by GTC, representing the rate at which sediment plumes move offshore. To minimize the influence of low light conditions, tree shadows, structural rips, and other environmental disturbances, the characterization analysis was conducted to events that occurred between 8:00 a.m. and 6:00 p.m., travelled more than 10 meters offshore, and were located at least 20 meters away from the alongshore starting boundary of the area of interest (AOI).

4.4 Results

4.4.1 Detection performance

The refined Cascade R-CNN model's performance was demonstrated for the three types of flash rips (Fig. 4-4). On 08/08/2019, at 13:47 Central Standard Time (CST), under calm water conditions (Fig. 4-4a-b), the model initially detected 11 seaward sediment plumes. Refinement eliminated two bounding boxes (purple dashed), yielding a MOD of 20.8 m between 124.8 m and

148.4 m alongshore. On 08/26/2019, at 16:49 CST, during normal wave conditions (Fig. 4-4c-d), nine flash rip objects were detected. Refinement removed two overlapping boxes (purple dashed) while merging two high-IOU boxes (white dashed) and two adjacent boxes (white solid). The refined detection showed a MOD of 41.3 m between 61.9 m and 125.7 m alongshore. On 09/03/2019, under oblique waves (Fig. 4-4e-f), nine objects were detected. Refinement removed one low-p-value box (yellow dashed), one bounding box (purple dashed), and one flat box (red dashed), merging three others (white solid and dashed lines). The final detection reached a MOD of 30.1 m offshore, spanning 57.5 m to 142.4 m alongshore. These cases illustrate that the refined Cascade R-CNN was able to detect flash rips generated under the three diverse water level and wave conditions.

Quantitative analysis (Fig. 4-4g-i) further demonstrated the effectiveness of the refined Cascade R-CNN model. Two evaluation metrics were used: the false positive rate (defined as 100% – precision), which quantifies the incorrectly identified flash rips out of the total detected flash rips (Fig. 4-4g), and the missing detection rate (defined as 100% – recall), which quantifies the missed detection out of all ground true flash rips (Fig. 4-4h). The Cascade R-CNN (blue dashed line) converged after 25 epochs, with its optimal performance achieved at the 19th epoch, yielding a false positive rate of 11.3% and a missing detection rate of 5.9% on the validation dataset. In comparison, the Faster R-CNN (red solid line) achieved its best performance at the 20th epoch, with a higher false positive rate of 13.4% and a missing detection rate of 8.1%, confirming that the Cascade R-CNN structure outperformed Faster R-CNN in both metrics. Additional improvements

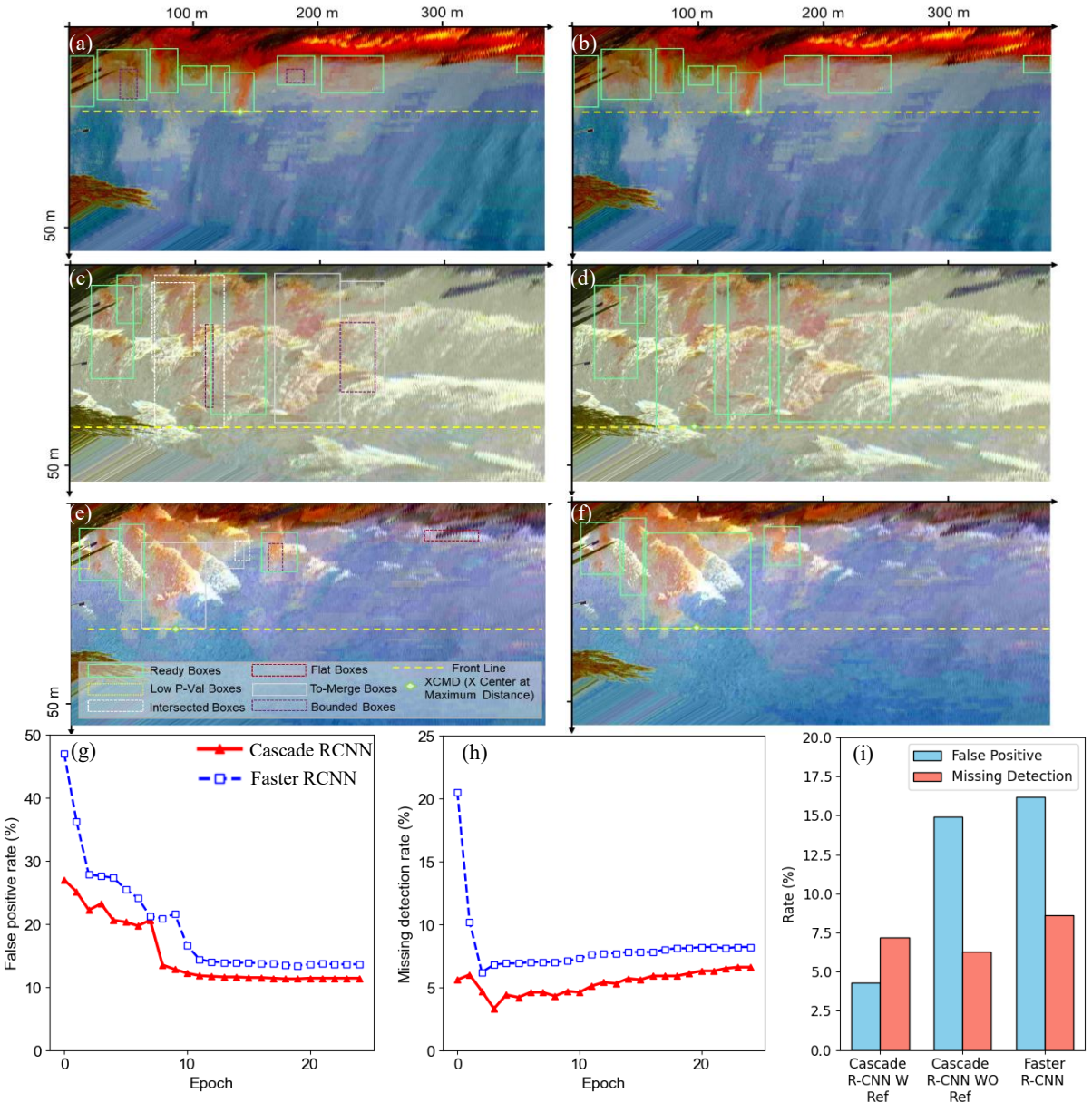


Figure 4-4 | Performance of Refined Cascade R-CNN model. (a)-(f) show examples of refined cascade R-CNN detection. The first row (a and b) represents water-level-induced conditions, the second row (c and d) corresponds to normal wave-induced conditions, and the third row (e and f) depicts oblique wave-induced conditions. The first column shows the raw outputs of the Cascade R-CNN, while the second column presents results after applying the refinement process. (g) False positive rate of Cascade R-CNN and Faster R-CNN across the first 25 training epochs.(h) Missing rate trends for the same models over the same training period.(i) Model performance on the testing dataset: comparison between Cascade R-CNN with refinement, without refinement, and Faster R-CNN.

from the post- detection refinement are demonstrated in Fig. 4-4i which shows the two metrics evaluated using the testing dataset. Without refinement, the Cascade R-CNN yielded a false

positive rate of 14.9% and a missing detection rate of 6.3%, with standard deviations of 0.5% and 0.2%, respectively, under ten-fold testing. After refinement, the false positive rate dropped markedly to 4.3% ($\pm 0.3\%$), a reduction of over 10 percentage points, while the missing detection rate rose slightly to 7.2% ($\pm 0.2\%$), which remained lower than that of Faster R-CNN (8.6%). These results indicate that the refined Cascade R-CNN achieved a superior balance between false positives and missed detections, making it a more reliable and effective method for flash rip detection.

4.4.2 Flash rip occurrence and associated environmental conditions

Flash rip occurrences, along with associated environmental variables (water level changes, pressure variations, wind speed/direction, significant wave height, and wave direction), were summarized in Fig. 4-5. Between 05/16/2019 and 09/14/2019, a total of 1,897 flash rip events were detected (Fig. 4-5a): 607 (32.00%, blue) water level fluctuations (WLF)-induced, 578 (30.47%, orange) normal wave (NW)-induced, 598 (31.52%, green) oblique wave (OW)-induced, and 114 (6.01%) could not be classified due to insufficient or missing environmental data. Flash rips were detected at least once each day when RTEOS operated, except during maintenance (gaps in Fig. 4-5a), with a maximum daily occurrence of 58 events on 05/21. The filtered water level fluctuations (\triangle WL. Fig. 4-5b) showed notable fluctuations multiple times, especially in the range of late May to early June (05/18 to 06/01), late June (06/21 to 07/20), middle July (07/18 to 07/22), middle August (08/18 to 08/21), and September (09/04 to 09/14). These high changes closely aligned with sea surface pressure variations (ΔP; Fig. 4-5c), indicating a connection between atmospheric pressure and water level fluctuations at the study site. The wind speed (v_{wind} , Fig. 4-5d) varied significantly throughout the monitoring period, with peaks exceeding 20 m/s. The wind direction (θ_{wind} , Fig. 4-5e) was widespread across all directions, with gradual transitions among all quadrants. The significant wave height ($\mathbf{H_s}$), as shown in Fig. 4-5f, showed varied values, from relatively low to approximately 2m, some notable peaks occurred at 05/19, 05/21 to 05/23, 06/23 to 06/24, 08/26 to 08/28, and 09/12 to 09/13, matched with the dates that wave-induced flash rip events dominate (the gray line in Fig. 4-5f). The wave direction ($\mathbf{\theta_{wave}}$, Fig. 4-5g), showed random

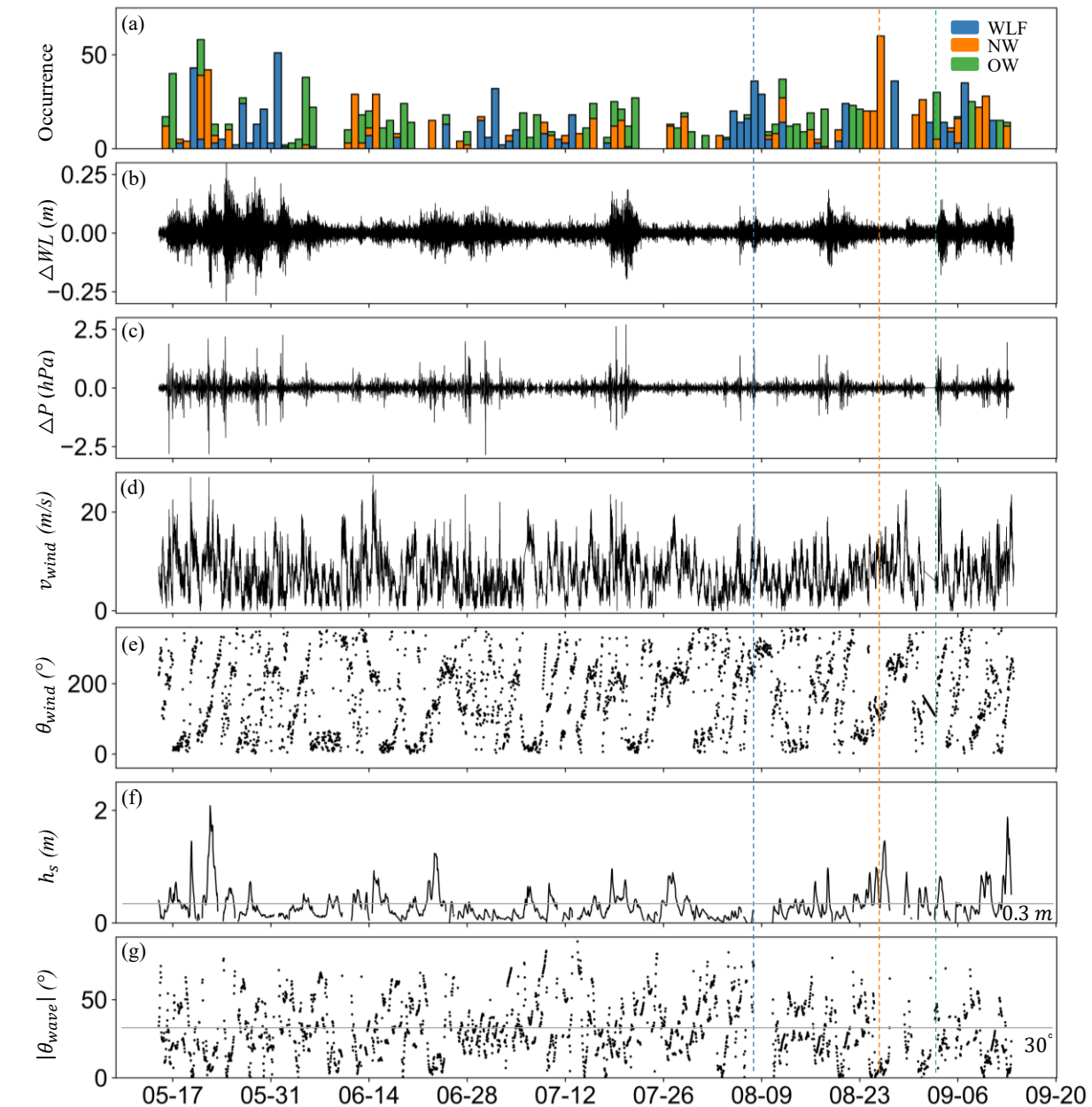


Figure 4-5 | Flash rip occurrences and the associated environmental variables. (a) Daily flash rip counts from 05/16 to 09/14/2019. (b–c) High-pass filtered water level and air pressure. (d–e) Wind velocity and direction. (f–g) Routed significant wave height and direction. Colored lines indicate example cases: blue (08/08, water-level-induced), orange (08/26, normal wave-induced), green (09/03, oblique wave-induced).

patterns and unaligned with wind direction, partially because nearshore waves are comprised of both local wind waves and swells. Moreover, normal wave directions (i.e., $-30^{\circ} \le \theta_{wave} \le 30^{\circ}$, gray lines in Fig. 4-5g) did not exhibit apparent disproportion against oblique waves. Overall, WLF-induced rips dominated in 37 days, NW-induced rips dominated in 29 days, and OW-induced rips dominated in 33 days. Notably, the environmental conditions associated with three specific dates—August 8 (WLF), August 26 (NW), and September 3 (OW)—matched the representative cases shown in Fig. 4-4 (blue, orange, and green dashed lines in Fig. 4-5, respectively), further validating the classification of flash rip mechanisms into WLF-, NW-, and OW-induced types.

4.4.3 Flash rip characteristics

4.4.3.1 Offshore distance

The distribution of offshore distances traveled by flash rip objects is illustrated in Fig. 4-6a-c. Two aspects were analyzed: (1) the offshore distance (OD) of each individual flash rip object at the peak timestamp of a flash rip event (red lines), and (2) the peak maximum offshore distance (PMOD) of each event (blue lines), defined as the greatest OD among all detected flash rip objects at that timestamp. A common feature across all three flash rip types was the long-tailed distribution of OD, with the majority of rips traveling less than 20 meters offshore. In contrast, PMOD distributions showed broader variability, with more than half of the events exceeding the 20-meter mark. Among the three mechanisms, WLF-induced flash rips (Fig. 4-6a) exhibited a single-peaked OD distribution with an average OD of 13.4 m. The corresponding PMOD distribution was also long-tailed, with two moderate peaks around 12 m and 19 m, followed by a gradually declining trend with some fluctuations, and extended to the AOI offshore boundary (55.1 m), where a lower peak was observed. The average PMOD was 25.7 m, and the median was 22.7 m. NW-induced flash rips (Fig. 4-6b) showed a flatter, long-tailed OD distribution with the highest average OD of

13.6 m. Their PMOD distribution was more heavily skewed toward distances exceeding 20 m compared to the other two driving factors, with an average PMOD of 31.1 m, also the highest among the three. Notably, over 7% of NW-induced events reached the AOI boundary, indicating the greatest proportion of far-reaching flash rips. OW-induced flash rips (Fig. 4-6c) displayed a single-peaked but steeply tailed OD distribution, with the highest proportion of small rips (near 10 m) and the lowest average OD of 11.7 m. The PMOD distribution for OW-induced rips was also single-peak long-tailed and had the lowest average PMOD of 22.6 m, with only fewer than 1% of events reaching the AOI boundary. In short, NW-induced flash rips tended to travel the furthest offshore, and OW-induced rips moved generally the shortest and were most constrained near the starting edge of the AOI offshore extent.

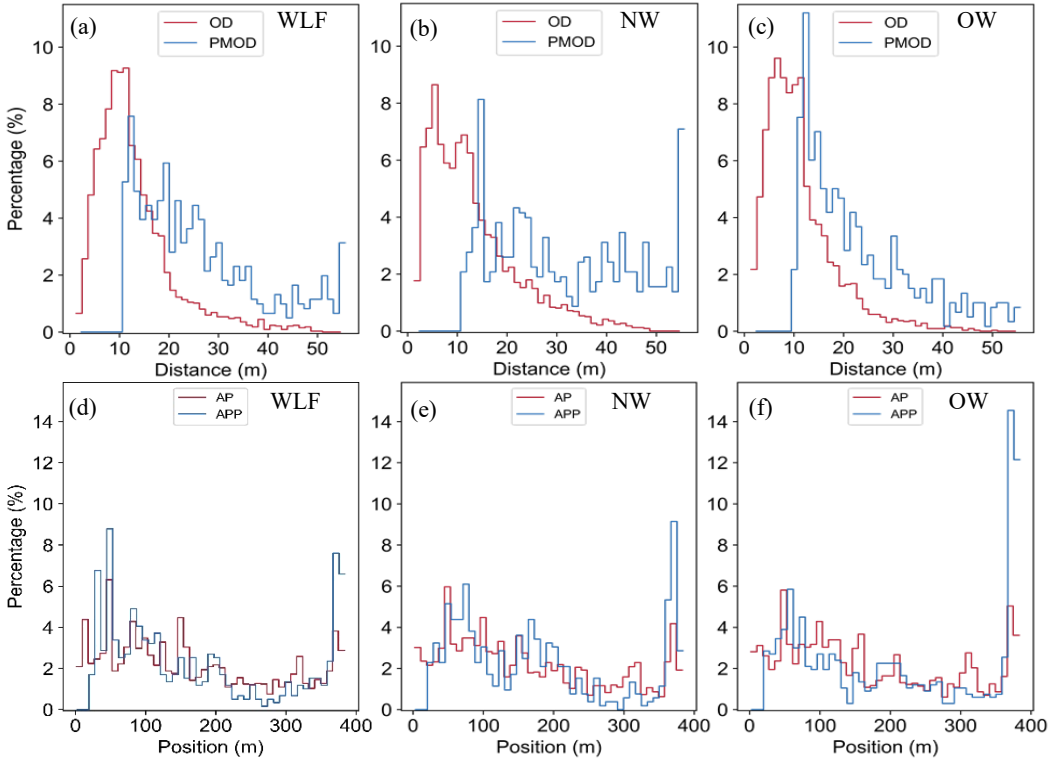


Figure 4-6 | Distribution of flash rip offshore distance and alongshore position. (a–c) show offshore distance (OD, red) and peak maximum offshore distance (PMOD, blue) for WLF-, NW-, and OW-induced flash rip events. (d–f) show alongshore position (AP, red) and alongshore position of peak objects (APP, blue) for the same event types.

4.4.3.2 Alongshore position

The distribution of alongshore distance was assessed from two perspectives (Fig. 4-6d–f): (1) the alongshore position (AP) of each individual flash rip object at the peak timestamp of a flash rip event (red lines), and (2) the alongshore position of peak rips (APP)—the location of the flash rip object with the maximum offshore distance during each event (blue lines). Overall, the AP distribution was less varied across the AOI compared to the APP distribution, which showed distinct clustering at three key zones: near the beginning, middle, and end of the AOI. This suggests that while flash rip occurrences alongshore were relatively widespread, those reaching the furthest offshore distances tended to occur at specific alongshore positions. The AP distribution was similar across three driving factors, with only minor differences: the mean AP values were 166.8 m for WLF-induced, 162.7 m for NW-induced, and 167.9 m for OW-induced rips—reflecting a relative difference of just 3.2%. In contrast, the APP distributions showed clearer variation among driving factors. WLF-induced rips (Fig. 4-6d) exhibited a saddle-shaped APP distribution, with two prominent peaks at both ends of the AOI and a smaller secondary peak between 80 and 100 m, resulting in the lowest average APP of 175.8 m. NW-induced rips (Fig. 4-6e) displayed three clear peaks: between 50 and 90 m, between 150 and 180 m, and near the AOI's alongshore boundary, which yields an average APP of 180.0 m. OW-induced rips (Fig. 4-6f) showed two peaks, with a modest one near 50 m and a dominant concentration at the AOI alongshore boundary, where more than 14% of events occurred, resulting in the highest average APP of 205.5 m. In short, while flash rips occurred across the entire alongshore extent, OW-induced rips were more likely to reach peak offshore distances near the alongshore boundary, whereas WLF- and NW-induced rips exhibited multiple peak positions with similar weights.

4.4.3.3 Duration and growing speed

The temporal and kinematic characteristics of flash rip events were analyzed using three metrics—event duration, growing time cost (GTC), and growing speed of the sediment plume frontline (GSF)—as shown in Fig. 4-7. To enhance interpretability given the wide range of values and high concentration on the small values, the x-axis was log-scaled and the y-axis represented the cumulative distribution function (CDF). For event duration (Fig. 4-7a), most flash rip events reached their peak maximum offshore distance (PMOD) within 10 minutes and terminated within 20 minutes, indicating a generally short lifespan. These durations were longer than those reported

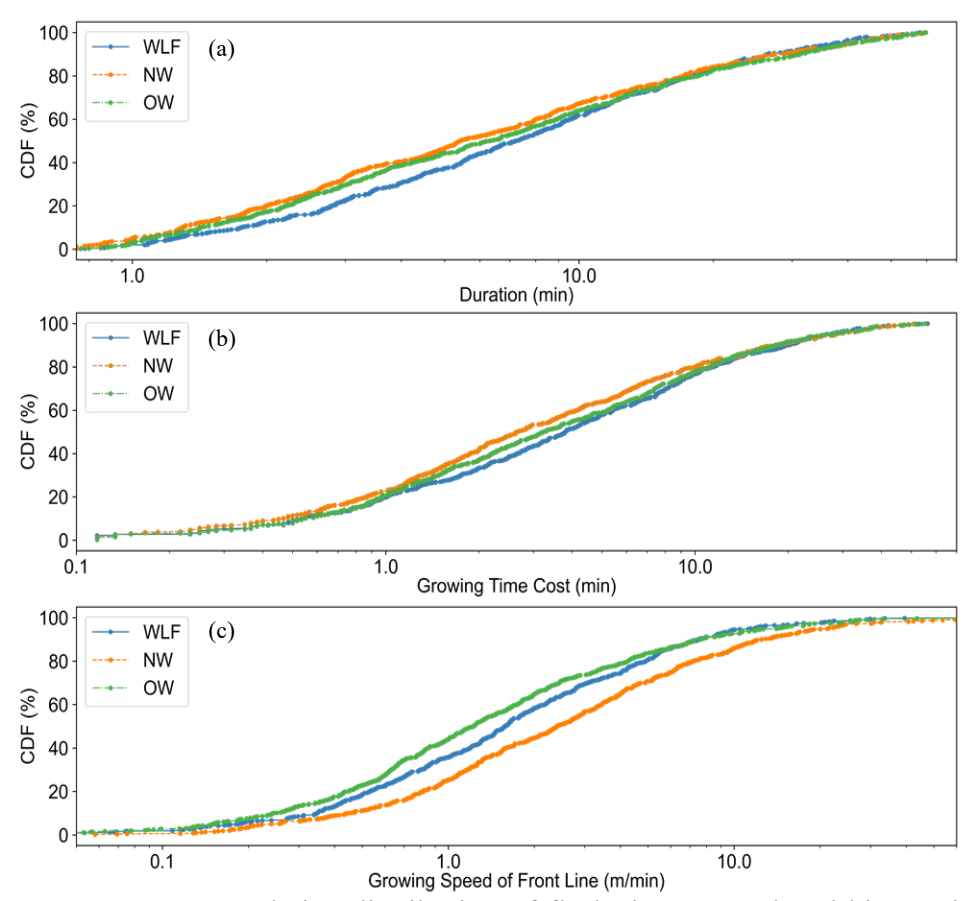


Figure 4-7 | Cumulative distribution of flash rip temporal and kinematic features. (a), (b), and (c) represent the cumulative distributions of duration, growing time cost, and front-line growing speed, respectively. Blue, orange, and green correspond to water-level-fluctuation (WLF)-induced, normal wave (NW)-induced, and oblique wave (OW)-induced flash rips.

by Liu (2019), primarily due to our merging criteria that treated temporally proximate detections as a single event unless they exhibited a sustained decline in MOD for five minutes or a drop below half of PMOD. WLF-induced rips had the lowest proportion of short-lived events (under 3 minutes), with a 25th percentile of 3.3 minutes and a mean duration of 11.3 minutes. NW-induced rips exhibited the shortest durations, with a 25th percentile of 2.4 minutes and a mean of 10.6 minutes. OW-induced rips had a similar 25th percentile (2.6 minutes) with NW-induced ones but matched WLF-induced events in mean duration (11.4 minutes), due to a greater proportion of events exceeding 20 minutes. The GTC distributions (Fig. 4-7b) had similar patterns across three driving factors, particularly within the 0–20% and 80–100% CDF ranges, though WLF-induced rips showed a longer median GTC (3.8 minutes) compared to NW-induced rips (2.7 minutes). Greater variation was observed in growing speed (GS; Fig. 4-7c): most values were below 10 m/min, but NW-induced rips advanced the fastest, followed by WLF- and OW-induced rips. At the 25th, 50th, and 75th percentiles, GSF for NW-induced rips was 1.0, 2.4, and 6.1 m/min; for WLF-induced rips, 0.7, 1.6, and 4.0 m/min; and for OW-induced rips, 0.6, 1.2, and 3.3 m/min, respectively. These results suggest NW-induced flash rips develop most rapidly but are short-lived, WLF-induced rips grow more gradually with longer durations, and OW-induced rips are the slowest to grow.

4.5 Discussion

4.5.1 Sensitivity Analysis

Flash rip classification in this study was based on predefined parameter settings informed by field observations and prior studies, including a significant wave height threshold of 0.3 m to distinguish wave-dominated events, an incident wave angle range of –30° to 30° to define normal waves, and wave routing terminating at 2 m water depth. To evaluate the sensitivity of these

parameters, we tested alternative thresholds—one lower and one higher—for each setting (Fig. 4-8). For significant wave height, thresholds of 0.25 m and 0.35 m were assessed. The proportion of WLF-induced rips (blue) shifted slightly from the default value of 34.16% to 30.41% (0.25 m) and 32.47% (0.35 m), while corresponding changes in PMOD, APP, and event duration across all rip

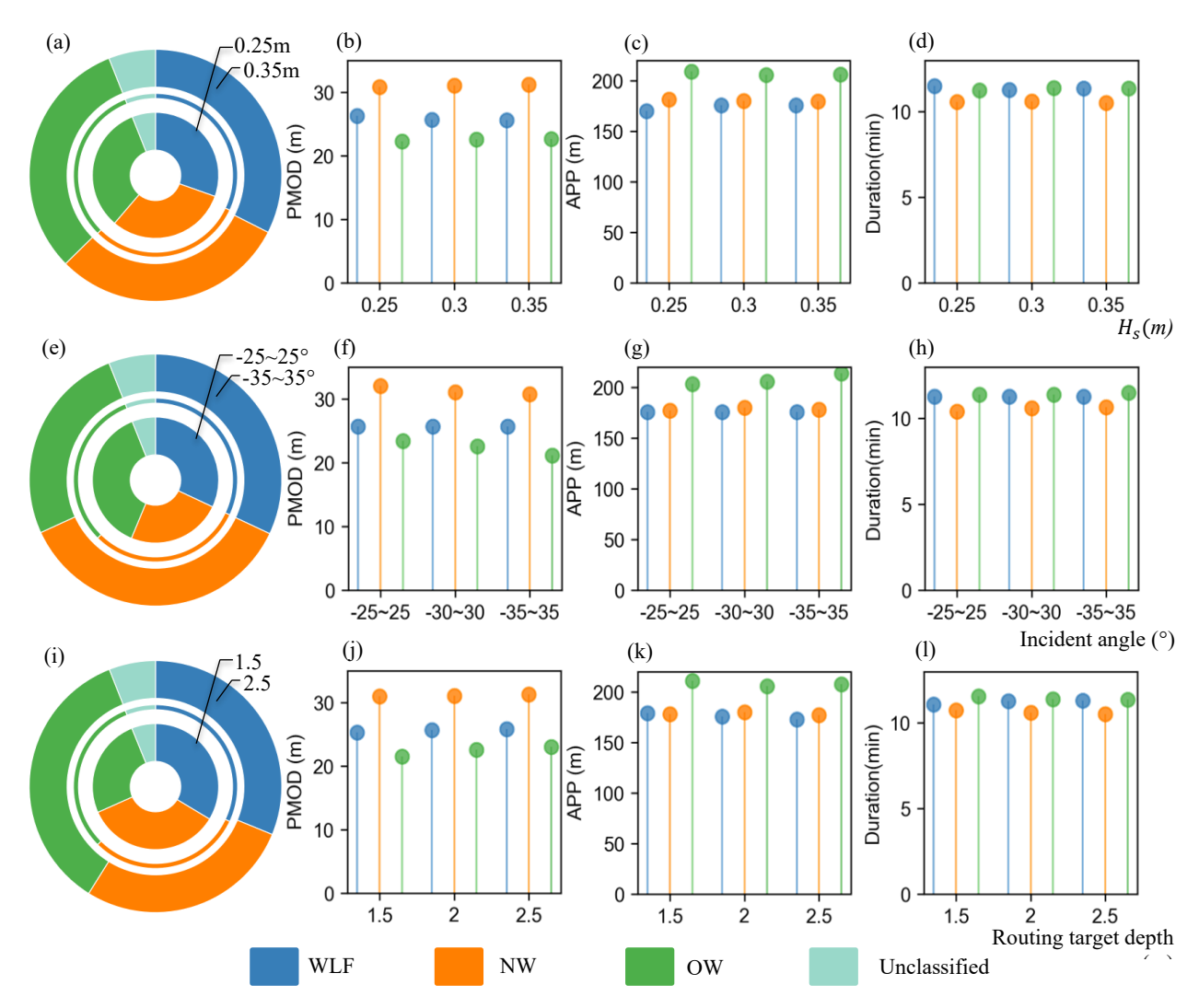


Figure 4-8 | Sensitivity test of characterization settings. The default settings include a 0.3 m threshold for significant wave height, an incident wave angle range of -30° to 30°, and a wave routing termination depth of 2 m. The first row (a, b, c, d) presents sensitivity results for significant wave height thresholds of 0.25m and 0.3m. The second row (e, f, g, h) shows sensitivity results for incident wave angle criteria of -25° to 25° and -35° to 35°. The third row (i, j, k, l) illustrates sensitivity results for wave routing termination depth of 1.5m and 2.5m. The first column (a, e, i) displays the ratio of water-level-fluctuation (WLF)-induced, normal wave (NW)-induced, and oblique wave (OW)-induced flash rips. The second to fourth columns present the mean values of peak maximum offshore distance (PMOD), alongshore position for peak rips (APP), and duration, respectively.

types were minimal (Fig. 4-8a-d), suggesting the classification was relatively insensitive to modest variations in wave height threshold. For incident wave angle, narrowing the range to -25° to 25° increased the proportion of OW-induced rips (green) from 31.52% to 37.74% and decreased NWinduced rips (orange) from 30.47% to 24.25% (Fig. 4-8e). The mean PMOD increased from 31.1 m to 32.0 m for NW-induced rips and from 22.6 m to 23.4 m for OW-induced rips, indicating that near-threshold NW cases tended to move shorter than other NW events but further than OW events. APP and duration showed negligible changes (Fig. 4-8f-h). Conversely, widening the angle range to -35° to 35° reduced the proportion of OW-induced rips to 25.83% and increased NW-induced rips to 36.16%, with corresponding decreases in mean PMOD for both NW-induced (from 31.1 m to 30.8 m) and OW-induced rips (from 22.6 m to 21.1 m). OW-induced rips also showed an increase in mean APP from 205.5 m to 213.7 m, while duration remained stable. For wave routing termination depth, reducing the depth to 1.5 m increased the proportion of WLF-induced rips from 32.00% to 33.63% and NW-induced rips from 30.47% to 34.69%, while OW-induced rips decreased to 25.56% (Fig. 4-8i). The mean PMOD for OW-induced rips dropped to 21.5 m, with minimal changes in APP and duration. Increasing the routing depth to 2.5 m decreased the proportion of WLF-induced and NW-induced rips to 31.20% and 27.68%, respectively, while OWinduced rips increased to 35.16%, again with only mild changes in PMOD, APP, and duration (Fig. 4-8j-1). Overall, while classification proportions and event metrics varied under different thresholds, the relative ranking of driving factors (e.g., NW-induced rips generally exhibiting the greatest PMOD) remained unchanged, indicating that the default parameter settings are appropriate for flash rip characterization. Among the three driving factors, OW-induced rips exhibited the highest sensitivity, particularly to variations in incident wave angle, whereas among

event features, APP and duration remained relatively stable, with PMOD showing the greatest variability.

4.5.2 Co-occurrence patterns of flash rip features

While differences in the distributions of offshore distance, alongshore positions, durations, and growing speeds highlight unique characteristics among the three driving factors, their co-occurrence patterns are also important, as these features are not independent but exhibit covariance in a two-dimensional space. To examine these relationships, we analyzed the two-variable co-

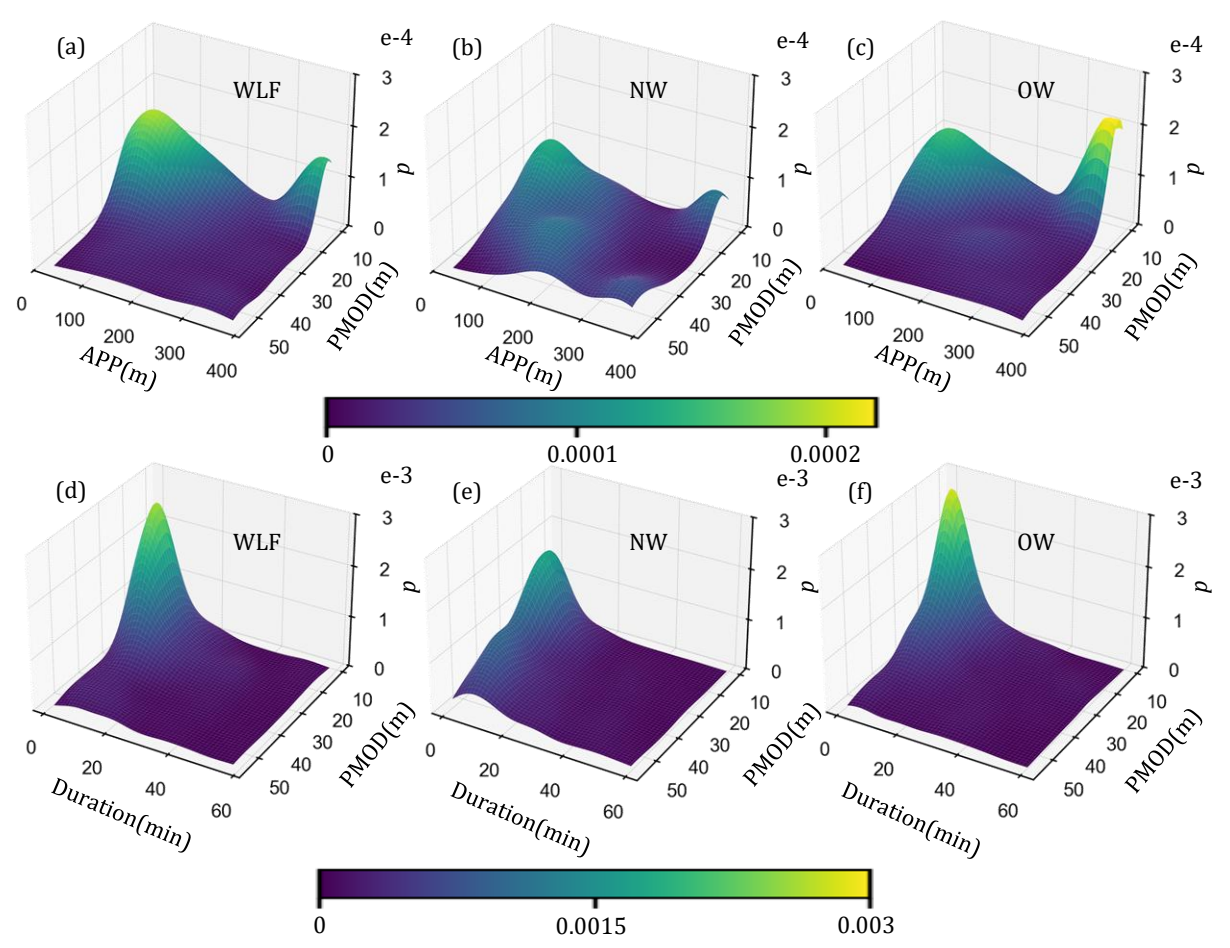


Figure 4-9 | Probability density map for two characteristics across different flash rip driven factors. The first row (a,b,c) illustrates the relationship between alongshore position for peak rips (APP) and peak maximum offshore distance (PMOD): (a) for water-level-fluctuation-induced (WLF) rips, (b) for normal-wave-induced (NW) rips, and (c) for oblique-wave-induced (OW) rips. The second row (d, e, f) shows the relationship between duration and PMOD: (d) for WLF-induced, (e) for NW-induced, and (f) for OW-induced flash rips.

distributions for each type (Fig. 4-9). For the relationship between alongshore APP and PMOD, both WLF-induced (Fig. 4-9a) and OW-induced (Fig. 4-9c) flash rips exhibit a saddle-shaped distribution at the low-PMOD end, with peaks at both low-APP and high-APP, while the mid-APP range is relatively low. However, a key difference between the two is that for WLF-induced rips, the highest peak occurs in the low-APP, low-PMOD region, followed by a second peak in the high-APP, low-PMOD region, whereas OW-induced rips, the highest peak appears in the high-APP, low-PMOD region, with the second highest in the low-APP, low-PMOD region. In contrast, NW-induced (Fig. 4-9b) flash rips follow a different pattern, characterized by a diagonal ridge extending from low-APP, low-PMOD to high-APP, high-PMOD, along with an additional peak in the high-APP, low-PMOD region. Notably, peak probability values for OW-induced rips are much smaller than those for WLF- and NW-induced rips, suggesting a more even distribution for OWinduced rips over the space of APP and PMOD. For the relationship between duration and PMOD, all three mechanisms exhibit a single peak in the short-duration, low-PMOD region. However, OW-induced (Fig. 4-9f) rips show the highest peak, followed by WLF-induced (Fig. 4-9d) rips with a slightly milder peak, while NW-induced (Fig. 4-9e) rips exhibit the mildest peak. This suggests that although short-duration, small-PMOD events dominate regardless of driving factors, NW-induced rips have a wider spread across both dimensions, indicating greater variability in their temporal and spatial characteristics.

4.5.3 Suggestions for future improvements

In this study, a deep learning framework was built to detect flash rips with high accuracy and improve the understanding of flash rip characteristics under three driving factors. To broaden the framework's applicability to hazard management, the following areas are recommended for future improvement: First, adverse weather conditions such as haze, fog, and rain reduce image clarity

and affect detection. Haze and fog scatter light, lowering contrast and making wave patterns and rip currents harder to distinguish (Cai et al., 2016). Rain causes distortions due to raindrops on the lens and surface water disturbances, obscuring rip features. These conditions were not uncommon in our study, with seven rainy days, two days of heavy fog, and several other foggy days recorded. Future studies could apply image enhancement techniques, such as dehazing for haze-affected images (Cai et al., 2016; Ullah et al., 2021) and deraining for rainy conditions (Fu et al., 2017), to improve visibility. Second, nighttime detection remains a challenge due to low luminance. This limitation could be addressed by integrating infrared or thermal cameras, enabling detection in low-light environments. Third, this study does not address bathymetrically-controlled and boundary-controlled rip currents, which may exhibit similar sediment plumes or bubbleless areas as noted in previous studies (De Silva et al., 2021; Liu and Wu, 2022a). However, by applying the same image processing steps, orthorectifying images, and manually annotating data for training, validation, and testing, the current architecture could be adapted to detect these rip types as well. Fourth, the current system operates offline, analyzing a four-month dataset without real-time updates. Integrating this approach with real-time current monitoring platforms like LOCKS (Liu and Wu, 2019) could enable real-time warnings of flash rip locations while continuously tracking and updating long-term statistics to improve feature characterization.

4.6 Conclusions

This study developed a deep learning-based framework to detect and characterize flash rip events at a featureless beach in Lake Michigan using a Refined Cascade R-CNN. By leveraging a four-month dataset from North Beach, Port Washington, Wisconsin, we identified and classified 1,897 flash rip events into three types based on their main driving factors: water-level fluctuations, normal wind waves, and oblique wind waves. The refined model significantly reduced false

positive rates from 14.9% to 4.3% while maintaining a low missing detection rate of 7.2%, outperforming both non-refined Cascade R-CNN and Faster R-CNN baselines. The characterization further offers new insights into flash rip characteristics, including their spatial, temporal, and kinematic differences across different driving factors. Flash rip events with different driving factors have similar occurrence percentages in our study site, with 32.00% of WLFinduced, 30.47% of NW-induced, and 31.52% of OW-induced. Among the three driving factors, NW-induced flash rips exhibited the longest offshore distances, with an average peak maximum offshore distance of 31.1m. They also showed the shortest duration and fastest growing speed. In addition, differences between alongshore position (AP) and alongshore position of peak rips (APP) revealed that extreme values exhibited distinct spatial clustering patterns, whereas general flash rip occurrences were more evenly spread. Building upon the success of this framework, future work to address the remaining challenges in limited performance under haze, fog, and rain and nighttime monitoring conditions are suggested, including enhancing images and integrating infrared or thermal cameras for 24-hour detection. Incorporating real-time processing with platforms like LOCKS could further improve hazard mitigation and beach safety. Overall, this study advances automated flash rip detection, providing a foundation for future improvements in real-time monitoring and risk management strategies.

Chapter 5: Shoreline Change Estimation Toolkit (SCET): A Deep Learning Framework for Detecting and Characterizing Coastal Erosion and Accretion

5.1 Introduction

The shoreline, referring to the area where land meets water, is one of the world's most populous and developed zones, with approximately 2.4 billion people living within 100 kilometers of these areas (Small and Nicholls, 2003; Rahman et al., 2022). Shoreline changes, including erosion and accretion, are driven by both natural forces such as waves, currents, tides, and meteotsunamis (Zacharioudaki and Reeve, 2011; Linares et al., 2018) and human activities like coastal infrastructure development (Ranasinghe and Turner, 2006). Over half of the world's coastal zones are now affected by measurable shoreline changes (Bird, 1985; Luijendijk et al., 2018), leading to substantial impacts on property values, land use, access to recreation, flood risk in estuaries, and the integrity of coastal ecosystems (Paterson et al., 2010; Pollard et al., 2019). In the United States, shoreline changes are widespread along both the East and West coasts, with rates of about -0.5 m/yr in New England and the Mid-Atlantic, up to -2.1 m/yr and -7.1 m/yr in the Gulf of Mexico states like Mississippi and Louisiana (Morton, 2008), and -0.9 meters annually in the Pacific Northwest (Ruggiero et al., 2013). The Great Lakes also see notable shoreline changes due to water level variations, wave actions, storms, and human interventions (Meadows et al., 1997; Theuerkauf et al., 2019; Lu et al., 2025). Recent years have witnessed an exacerbation in shoreline changes for the Great Lakes region, driven by augmented anthropogenic pressures (Anthony et al., 2015; Foti et al., 2023), large inter-annual variation of surface water level (Troy et al., 2021), and global climate changes (Leatherman et al., 2000; Le Cozannet et al., 2014). Given the widespread and persistent consequences of shoreline changes, there is an urgent need for long-term, accurate,

and high-resolution shoreline monitoring systems that can efficiently track changes and inform natural hazard management strategies.

Traditional methods for detecting shoreline changes, based on field surveys with images, videos, and tape measures, were time-consuming, labor-intensive, and limited in temporal and spatial coverage (El-Ashry and Wanless, 1968; Thieler and Young, 1991). These constraints hinder the applications to monitor coastal zones for decades with data of high spatial resolution (Nuyts et al., 2023). In contrast, the advent of remote sensing technologies has revolutionized the monitoring of shoreline changes. Technologies such as satellite imagery (Almeida et al., 2019; Vos et al., 2019; Pardo-Pascual et al., 2024), high-resolution aerial photography (Boak and Turner, 2005; Ford, 2013), and web-cams (Turner and Anderson, 2007; Nuyts et al., 2023), have greatly increased data coverage and availability. For instance, the availability of satellite images from platforms like Landsat and Sentinel-2, offering resolutions between 10-30 meters, aerial photographs from the National Agriculture Imagery Program (NAIP) with a higher resolution of 0.6-1 meters, alongside open-source web-cam platform such as USGS Earth Explorer, provides extensive and regularly updated datasets. These resources have dramatically decreased the challenges associated with data collection, making it possible to conduct comprehensive studies for shoreline changes over large geographic areas and extended periods. Despite these advancements, the quantitative analysis of shoreline changes with high efficiency and accuracy remains a complex task.

Rapid advancements in the field of automatically outlining shorelines positions to quantify shoreline changes have been made in recent years. Image processing approaches involve edge detection algorithms, such as Canny edge detector and Snake algorithm, which extract coastal features via the distinct color gradient between land and water bodies (Niedermeier et al., 2000; Wu and Lee, 2007; Zhang et al., 2013), and the Hough transformation enhanced by a Gaussian

kernel to delineate coastlines with regular geometries (Jianhong and Arshad, 2013; Yousef et al., 2014). Nevertheless, the accuracy of these techniques is compromised by the complexity of jagged shorelines and the presence of image noise (Nascimento et al., 2013; Ribas et al., 2020). Machine learning (ML) approaches, such as decision trees, neural networks, and support vector machines (SVM), have been explored for their potential to discern water pixels in RGB or multi-spectral imagery (Ghorai and Mahapatra, 2020; Minghelli et al., 2020; McAllister et al., 2022). However, ML approaches still face difficulties in differentiating white sands from bubbles, and wet sands within the saturated intertidal domain (Fuse and Ohkura, 2018; Castelle et al., 2021), thereby resulting in inaccuracies or overlooked detections in coastal areas with sandy beaches. The aforementioned concerns and limitations highlight the imperative for the development and implementation of quantitative, automated, accurate, and robust detection methods, such as deep learning, to monitor and track changes along shorelines with high accuracy.

Deep learning (DL) techniques, characterized by their use of multi-layered structures to process input data (LeCun et al., 2015), are recently introduced to the automated segmentation of bodies from images, subsequently facilitating the delineation of shoreline positions. Among these DL techniques, U-Net and its derivatives are adopted as the core framework in most studies. Notably, U-Net has been utilized to develop a global water edge dataset from Sentinel-2 imagery (Seale et al., 2022), while its advanced version, U-Net3+, has been adapted to extract shorelines from Google Earth Engine satellite images in Vietnam (Dang et al., 2022). Furthermore, WaterNet, inspired by U-Net's architecture, was specifically designed for segmenting water bodies across different beaches using Landsat 8 OLI data (Erdem et al., 2021). Another variant, WENet, was applied for mapping tidal flats with complex shapes in the South Yellow Sea using Sentinel-1 SAR imagery (Zhang et al., 2022). Despite the success of these U-Net-based models in satellite image-

based shoreline detection, they encounter challenges such as limited capacity for capturing global contextual information, identifying remote dependencies, and handling large and varied datasets (Beeche et al, 2022; Su et al., 2022). These drawbacks may impede their application in comprehensively analyzing shoreline changes across extensive geospatial areas using highresolution data, like aerial imagery, which could lead to an inaccurate estimation of local shoreline changes. DeepLab-based DL methods, utilized a modified convolution method, named atrous Convolution, to capture multi-scale context more effectively in the encoding phase (Chen et al., 2017), can improve the segmentation performance of complex shapes in high-resolution imagery with similar time cost (Ahmed et al., 2020; Wang et al., 2021a). Additionally, to the best of the authors' knowledge, current DL-based toolkits are not yet integrated with the automatic tracking of shoreline changes, manual efforts are still required for selecting and drawing baselines and transferring data to third-party software, such as the Digital Shoreline Analysis System (DSAS), to obtain shoreline change rates (Dang et al., 2022; Fogarin et al., 2023). Therefore, developing a DL tool using DeepLab as the base model, and integrating it with the automatic shoreline change computation, is crucial for better understanding and management of shoreline changes, in both local scale and large geospatial coverage.

5.2 Objectives and Research Goals

The objective of this chapter is to develop a streamlined and automated toolkit for shoreline detection, change quantification, and hotspot identification in the Great Lakes. In particular, the chapter focuses on distinguishing shoreline changes driven by two mechanisms: true morphodynamical change (erosion or accretion) and apparent change caused by water-level fluctuations. I propose that combining deep learning—based segmentation with high-resolution remote sensing imagery enables more accurate shoreline extraction and mechanism-aware

interpretation of shoreline dynamics. I also hypothesize that shoreline response varies with setting: armored sections are primarily influenced by water-level fluctuations, whereas adjacent unarmored beaches remain sensitive to both erosion/accretion processes and water-level shifts. To address these hypothesis, three specific research goals are defined:

- 1. Develop deep-learning-based methods for automating shoreline detection from high-resolution remote sensing imagery.
- 2. Establish an automatic transect-based framework to calculate shoreline change rates across time and space.
- 3. Differentiate and characterize quick shoreline changes caused by distinct mechanisms (water-level fluctuations vs. erosion/accretion) and identify shoreline hotspots with high vulnerability.

5.3 Methods

5.3.1 Physical Settings

5.3.1.1 Study Site

Our research focuses on the Great Lakes region, a populous and ecologically diverse area characterized by its five interconnected freshwater lakes (Fig. 5-1a). This system includes Lake Superior, Michigan, Huron, Erie, and Ontario, forming the largest group of freshwater lakes on Earth by total surface area and serving as a critical resource for water, wildlife, commerce, and recreation. The combined watershed of the entire Great Lakes basin covers a drainage area of about 513,394 km² (Robertson and Saad, 2011), extending across both Canadian and American territories.

The cumulative shoreline of these lakes measures around 17,017 km, with Lake Superior contributing 4,385 km, Lake Michigan 2,633 km, Lake Huron 6,157 km, Lake Erie 1,402 km, and Lake Ontario 1,146 km (USEPA, 2023). The mean water surface elevation sequentially decreases from Lake Superior at 183 m, to Lake Michigan and Huron at 176 m, Lake Erie at 173 m, and

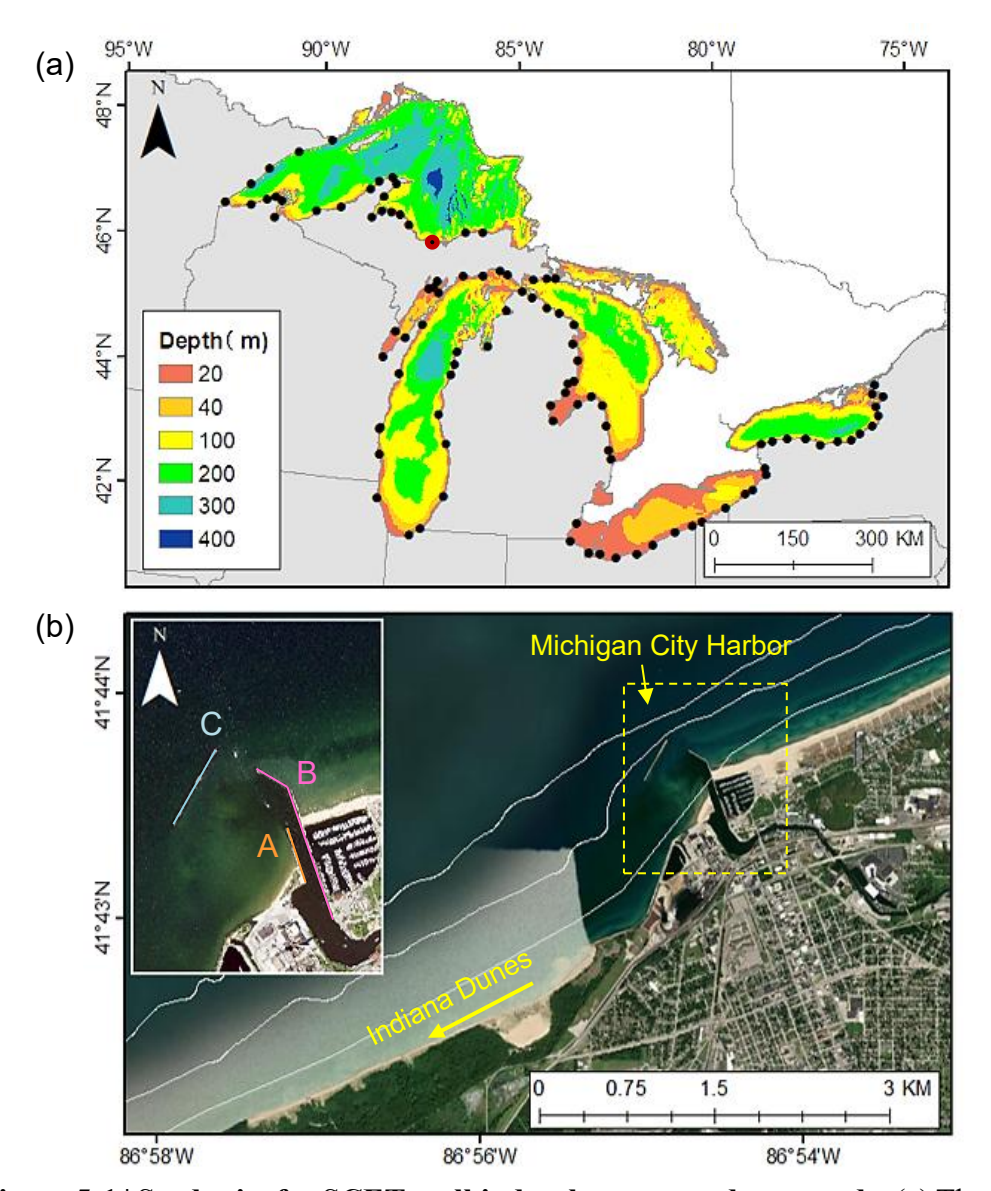


Figure 5-1 | **Study site for SCET toolkit development and case study.** (a) The Great Lakes' location and bathymetry, with black dots indicating validation sites. The site outlined in red is used for visualizing validation delineations. (b) The case study site, Michigan City, Indiana, selected for in-depth shoreline change analysis using the SCET toolkit. The Michigan City Harbor is highlighted with a yellow dashed rectangle, and coastal defenses A, B, and C are marked within the harbor area.

Lake Ontario at 74 m above sea level (NOAA, 2023). The average shoreline change rate was estimated to be between -0.4 m/yr and -1.3 m/yr in each lake according to a field survey conducted in 1983 (May et al., 1983).

In addition to the overall study site of the Great Lakes, we selected Michigan City as the case study location to present our results on a local scale (Fig. 5-1b, 41°44′04″N, 86°52′23″W). Michigan City is located in northern Indiana on the southern shore of Lake Michigan. The area's shoreline includes Washington Park, a major recreational zone situated on the eastern side of the city, encompassing 140 acres and featuring two miles of sandy beach. To the west, the city borders Indiana Dunes National Park, which covers 15,349 acres and is notable for its varied ecological and geological characteristics (National Parks Zone, 2021). Central to Michigan City's shoreline is the harbor at the outlet of Trail Creek. To safeguard the harbor and adjacent shoreline, three major coastal defense structures have been constructed (Fig. 5-1b), including the west breakwater (A, 258 m), the east breakwater (B, 682 m), and the offshore breakwater (C, 390 m). These coastal structures play a critical role in shaping the local shoreline and are important for ongoing shoreline management and erosion mitigation. Overall, the combination of natural features and engineered coastal defenses in Michigan City provides an ideal setting for evaluating shoreline segmentation and shoreline change detection methods.

5.3.1.2 Data source and dataset preparation

The primary data source for shoreline change identification is the National Agriculture Imagery Program (NAIP) dataset, which provides high-resolution, georeferenced aerial imagery of the continental U.S. during the agricultural growing season. For the Great Lakes region, NAIP imagery is available from 2005–2023, with a resolution of 1 m/pixel before 2011 and 0.6 m/pixel in recent years. Using NAIP, we created the Coastal Aerial Imagery Dataset (CAID) for shoreline

segmentation (Wang et al., 2025b). NAIP images were retrieved from 850 unique site IDs along the Great Lakes shoreline, with one image per site to avoid duplicates. Each NAIP image was divided into 500×500 pixel squares, retaining only those with center points within 500 meters of the shoreline, resulting in 20,689 images focused on coastal zones.

Water body delineation followed these criteria: (1) Coastal structures were addressed based on their interaction with water. Fixed structures made of stone or concrete, such as groins, breakwaters, and harbors, were labeled as land (Fig. 5-2a), while floating docks or small piers built on pillars that allow water to flow underneath were classified as water (Fig. 5-2b). (2) For plants and algae, emergent plants, such as cattails and reeds, were labeled as land if they grow above water and are dense enough to obscure the water surface (Fig. 5-2c). In contrast, floating plants, such as Lemna minor (duckweed), and algae, were labeled as water since they remain on the water surface (Fig. 5-2d). (3) Boats and ships were marked based on their sizes and usages. Large transport ships, barges, and sand carriers were labeled as land to avoid confusion with land areas (e.g., construction areas) of similar texture (Fig. 5-2e), small recreational boats, such as kayaks, canoes, and family-sized motorboats, were labeled as water (Fig. 5-2f). (4) Sandbars were marked according to their submersion state. Submerged sandbars were labeled as water, while exposed ones were marked as land (Fig. 5-2g). (5) Islands, regardless of their size, were always marked as land (Fig. 5-2h). Once all the data are marked, 70% was used as the training dataset, 15% as the validation dataset, and the remaining 15% as the testing dataset.

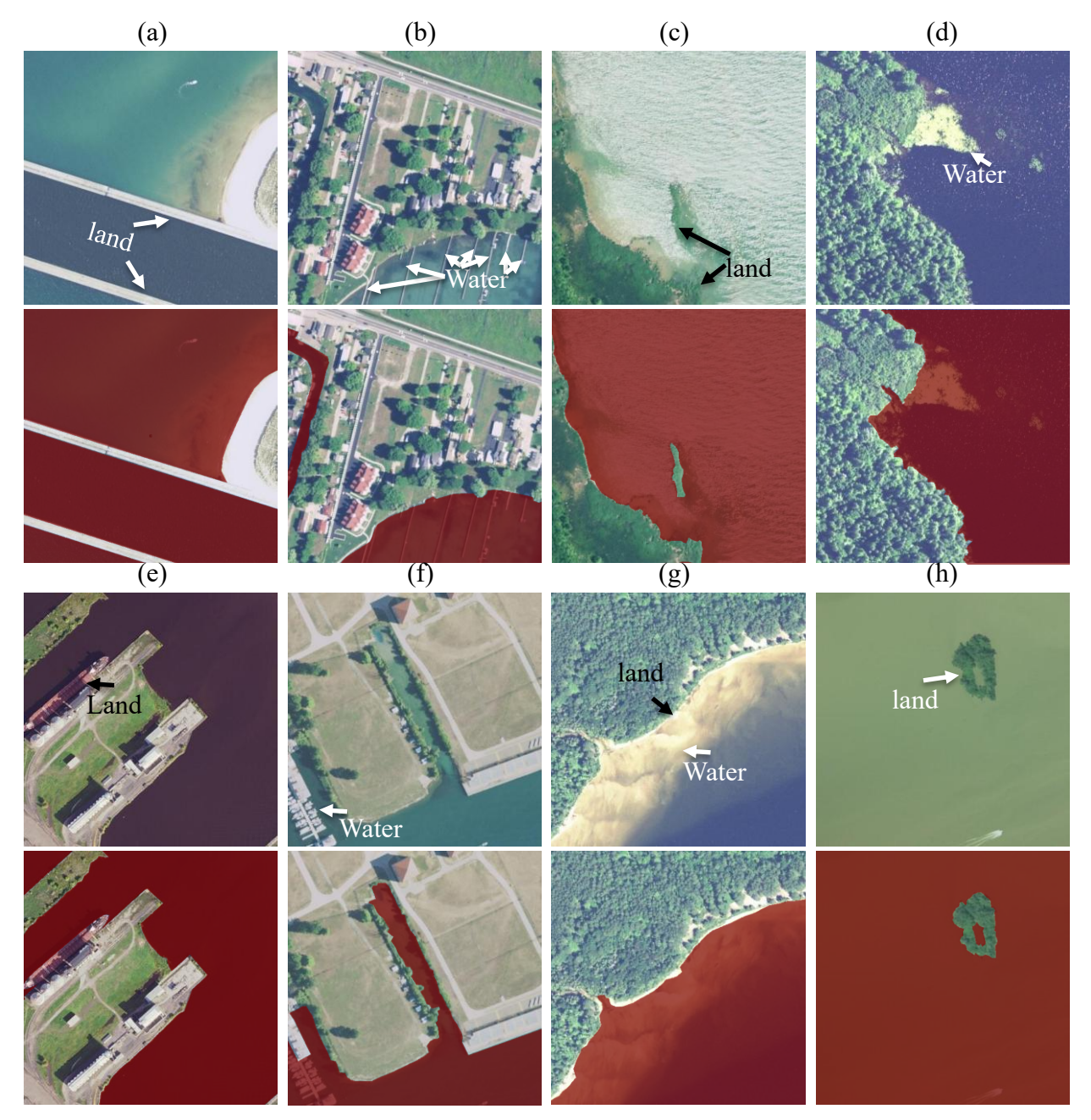


Figure 5-2 | Labeling examples for special cases. (a, b) structures labeled as land and water, respectively; (c, d) plants and algae labeled as land and water, respectively; (e, f) ships and boats labeled as land and water, respectively; (g) sandbars labeled as either land or water; (h) an island, always labeled as land.

Additionally, 6-minute water level data were obtained from NOAA's National Ocean Service, and 1-meter resolution nearshore bathymetry data were acquired from the Coastal Topobathy Lidar

Program, which is jointly collected by USACE, NOAA, and USGS. For this study, Great Lakes bathymetry data collected in 2020 were used.

5.3.2 DeepLabV3-Plus

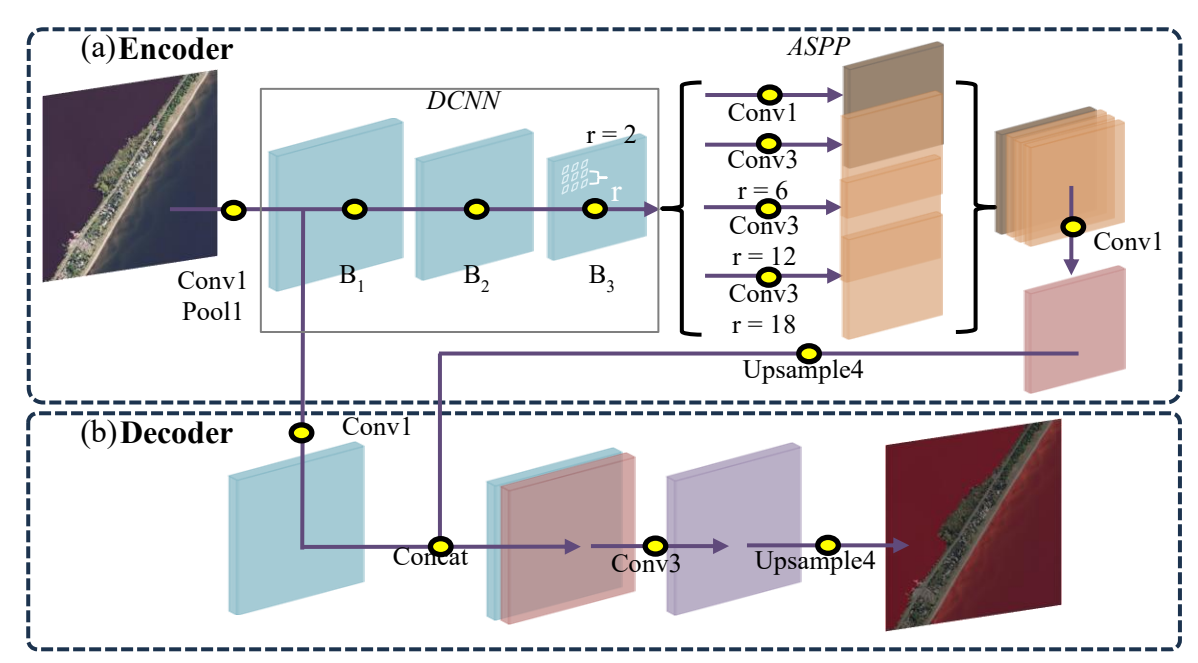


Figure 5-3 | **DeepLabV3-Plus Architecture.** The encoder part (a) includes deep convolutional neural network (DCNN) contains two normal ResNet blocks (B_1 and B_2) and one ResNet block (B_3) with Arous rate (r) of 2, and Atrous Spatial Pyramid Pooling (ASPP) with four different convolution and Atrous settings. The encoder part (b) combines the raw data with encoding outputs and upsamples to generate the detection outputs.

The deep learning approach used in this study is DeepLabV3-Plus, a deep-learning network designed for image semantic segmentation. The architecture of DeepLabV3-Plus is shown in Figure 5-3. This network first uses DeepLabV3 as the encoder part for processing the input images to extract high-level semantic information. Then, these high-level features are combined with low-level features from earlier layers of the network to decode and generate water body detection results. In specific, the encoding process (See Fig. 5-3a) imports NAIP image into a 1×1 convolution followed by a 1×1 pooling layer. The output is fed into a deep convolutional neural network (DCNN), where the backbone model (B) is configured using ResNet50. In our study, the first two backbone models (B₁ and B₂) in DCNN utilize the standard ResNet50 architecture, while

the third one (B₃) is modified with Atrous convolution. Atrous convolution, also known as dilated convolution, is a technique used in DeepLab-based architectures. Instead of performing convolution using adjacent pixels, it introduces a parameter called the rate (r) to insert intervals (dilations) between the kernel elements. This allows the model to capture broader contextual information without increasing computational complexity. The output from the DCNN is then passed into a structure called Atrous Spatial Pyramid Pooling (ASPP). ASPP consists of multiple convolution layers with different kernel sizes and Atrous rates. The top layer in ASPP is a 1×1 convolution, the second layer is a 3×3 convolution with r set to 6, the third layer is a 3×3 convolution with r set to 12, and the bottom layer is a 3×3 convolution with r set to 18. The outputs of these four ASPP layers are stacked using a 1×1 convolution to merge features and reduce the number of channels back to one. Finally, the processed output is upsampled by four times and passed into the decoding section to generate water body segmentation results. Regarding the decoding part, DeepLabv3-Plus (See Fig. 5-3b) employs a series of upsampling and refinement operations to generate high-resolution water body segmentation results. Initially, the low-level features from earlier layers (before entering the DCNN) of the encoder are processed by a 1×1 convolution layer. These are then concatenated with the upsampled high-level features from the ASPP module in order to provide detailed spatial and contextual information. The concatenated layers are subsequently passed through a 3×3 convolution, followed by an upsampling layer to progressively resize the layers to match the input dimensions. The decoding output is a mask image, where the water body is marked as 1 (red color in Fig. 5-3b), and the background is labeled as 0.

The model was trained for 100 epochs, with each epoch consisting of 20,000 iterations and a learning rate of 0.0001. Every 2,000 iterations, the validation set was used to assess model

convergence. After convergence, the best-performing model was selected to segment water bodies on the test set and was subsequently used for shoreline calculation.

5.3.3 Shoreline change calculation

The Digital Shoreline Analysis System (DSAS) is a widely used GIS tool for quantifying shoreline change by analyzing historical shoreline positions and calculating erosion or accretion rates (Moussaid et al., 2015; Himmelstoss et al., 2018). However, the current version of DSAS requires users to manually define the shoreline baseline, which can be highly time-consuming, especially for large-scale analyses. To address this limitation and reduce manual effort, we developed a modified DSAS workflow that automatically generates shoreline delineations from model-inferenced results, establishes the baseline, and computes shoreline change rates. The workflow begins by merging model-inferenced segmentation results from all square image tiles for each NAIP siteID, ensuring continuous shoreline representation across the study area. Shorelines are then extracted using an edge detection algorithm (specifically, the Canny descriptor) to identify the boundaries of segmented water bodies (red areas in Fig. 5-4a). Shorelines are defined as the interface between open water and land (Fig. 5-4b). To ensure accurate detection, boundaries classified as shorelines must (1) not coincide with the image boundary (to avoid edge effects) and (2) touch at least one side of the image edge, which helps distinguish the shoreline (marked as a brown line) from inland water boundaries (blue line). To further refine shoreline delineation, if two vertices are spatially close (closer than 50 m) but separated by a long detour (detour length more than five times the direct distance), this pattern typically indicates the presence of a coastal structure (when the detour is seaward) or a river estuary (when the detour is landward). In such cases, the workflow connects these vertices directly and eliminates the unnecessary detour, resulting in a more accurate and continuous shoreline. The detected shoreline for 2020 is then

smoothed and uniformly shifted inland by $\Delta d = 500m$ using a homothetic transformation to generate the baseline (Fig. 5-4c). Along this baseline, transects are automatically created at 10-meter intervals, oriented perpendicular to the baseline (Fig. 5-4d). For each year, intersection points between the detected shoreline and each transect are recorded (Fig. 5-4e). Outlier shoreline positions—those exceeding three standard errors from the multi-year mean—are excluded. The distance from these intersection points to the baseline is then regressed against time to estimate

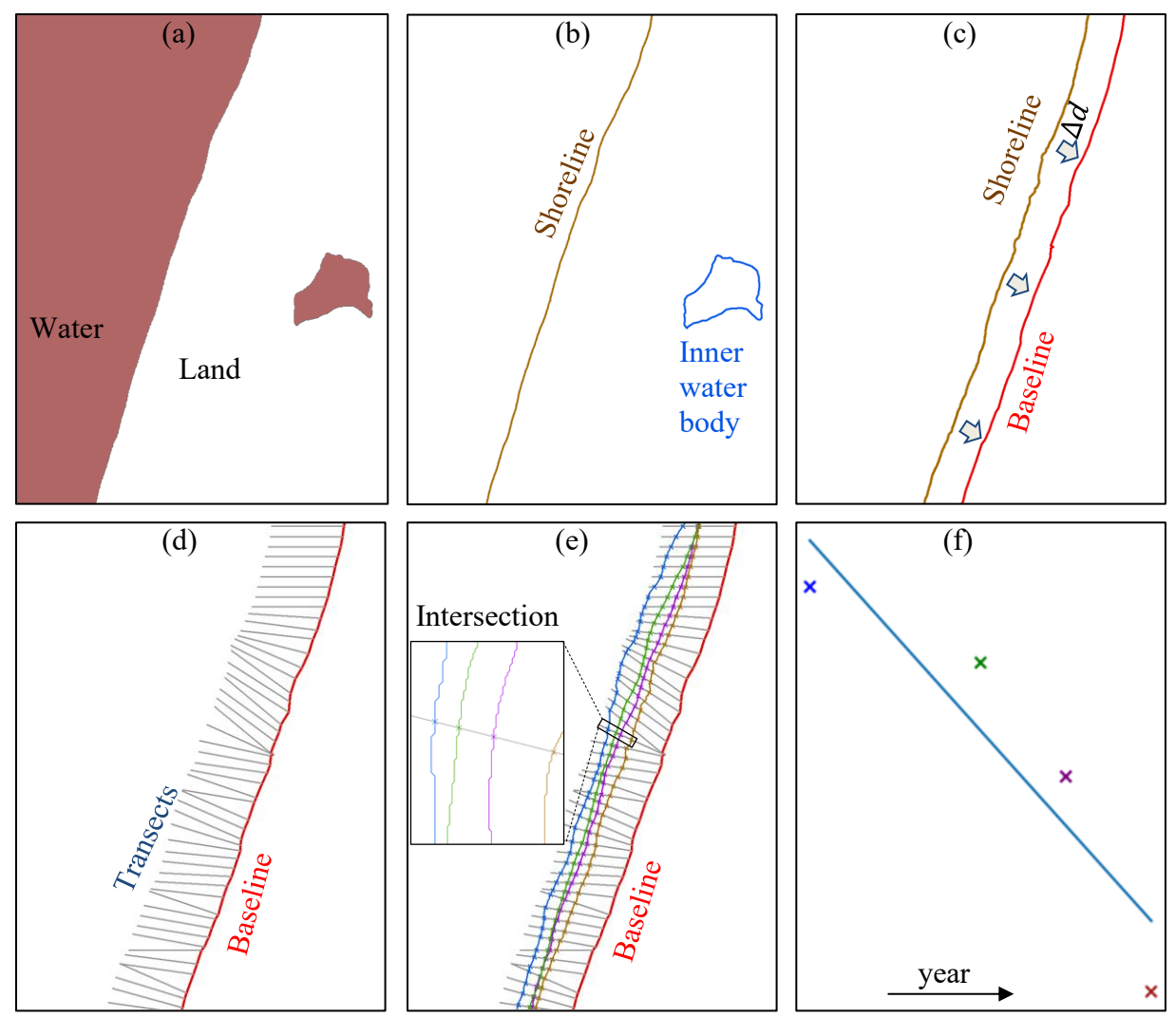


Figure 5-4 | **Modified DSAS Workflow.** (a) Segmented binary image generated by the deep learning model (red: water; white: land). (b) Edge detection to extract the land—water interface; the earthy line marks the shoreline, and the blue line indicates the boundary of the inner water body. (c) Shoreline translation to establish the baseline. (d) Generation of evenly spaced transects. (e) Intersection of transects with the shoreline for precise positioning. (f) Application of regression methods to calculate shoreline change rates.

the average shoreline movement rate, where a positive trend indicates accretion and a negative trend indicates erosion.

To validate the accuracy of shoreline movement calculations, our automated results were compared with those obtained from DSAS. Several validation sites, indicated by black dots in Fig. 5-1a, were selected across the Great Lakes. Specifically, we chose 25 sites each for Lake Superior and Lake Michigan, 21 for Lake Huron, 16 for Lake Erie, and 14 for Lake Ontario. These validation sites were randomly distributed to represent diverse coastal landscapes. At each site, 10 consecutive transects were used for analysis. For each validation site, shorelines were manually delineated for the start and end years, covering the same time span as the automatic calculations. We then calculated the average distance between the manually delineated shoreline and the SCET output at each transect intersection point. Finally, we computed the shoreline change rate for each site by averaging the results of the ten transects and compared these rates between the traditional and modified DSAS methods.

The calculated shoreline change rates were further calibrated using water level data. For each NAIP aerial image, we determined the corresponding water level by averaging measurements from the three nearest stations at the time of image acquisition. Bathymetric data were used to extract the local bottom profile and estimate the theoretical shoreline position (DW_i) for each year, assuming no shoreline erosion or accretion. Assuming a linear relationship between observed shoreline position, theoretical (water-level-adjusted) shoreline position, and year, we used the following equations (5-1 to 5-3), where D_i is the observed distance from the shoreline to the baseline in year y_i , and DW_i is the theoretical shoreline position based solely on water level and bottom profile:

$$D_i = k_0 y_i + b_0$$
 Eqn. 5-1

$$DW_i = k_1 y_i + b_1$$
 Eqn. 5-2

$$D_i - DW_i = k'y_i + b'$$
 Eqn. 5-3

Here, DW_i is independent of shoreline erosion or accretion processes and represents the shoreline position expected purely from water level variation. The calibrated shoreline change rate, k', is thus obtained by subtracting the water level-related rate (k_1) from the observed rate (k_0) , effectively isolating the impact of actual shoreline movement from interannual water level fluctuations. Once this k' is calculated, the shoreline is classified as accreting or eroding based on the NAIP image resolution. If k' exceeds 1 m per two years for pre-2011 imagery or 0.6 m per two years for post-2011 imagery, the shoreline is considered accreted if it moves lakeward and eroded if it moves landward.

5.4 Results

5.4.1 Performance of aerial image segmentation

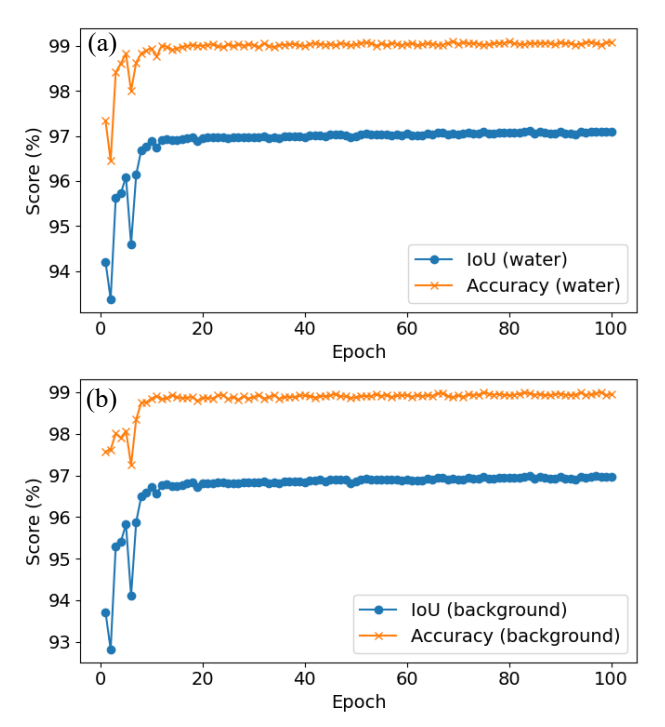


Figure 5-5 | Training curves of DeepLabV3+ for water (a) and background (b) classes.

The performance of the DeepLabV3+ model for water body segmentation is presented in Figure 5-5. The model's accuracy converged within 15 epochs, as determined by validation set results after each epoch. Pixel-level mean accuracy, shown as orange lines in Figure 5-5a and 5-5b, measures the proportion of correctly identified pixels. The highest pixel accuracy achieved was 99.1% for water bodies at epoch 69 and 99.0% for the background at epoch 75. Mean Intersection over Union (mIoU),

illustrated by the blue lines, assesses the overlap between predicted segmentation and the manually annotated ground truth. The optimal mIoU reached 97.1% for water and 97.0% for background, both at epoch 84. The rapid convergence, along with high pixel accuracy and mIoU values,

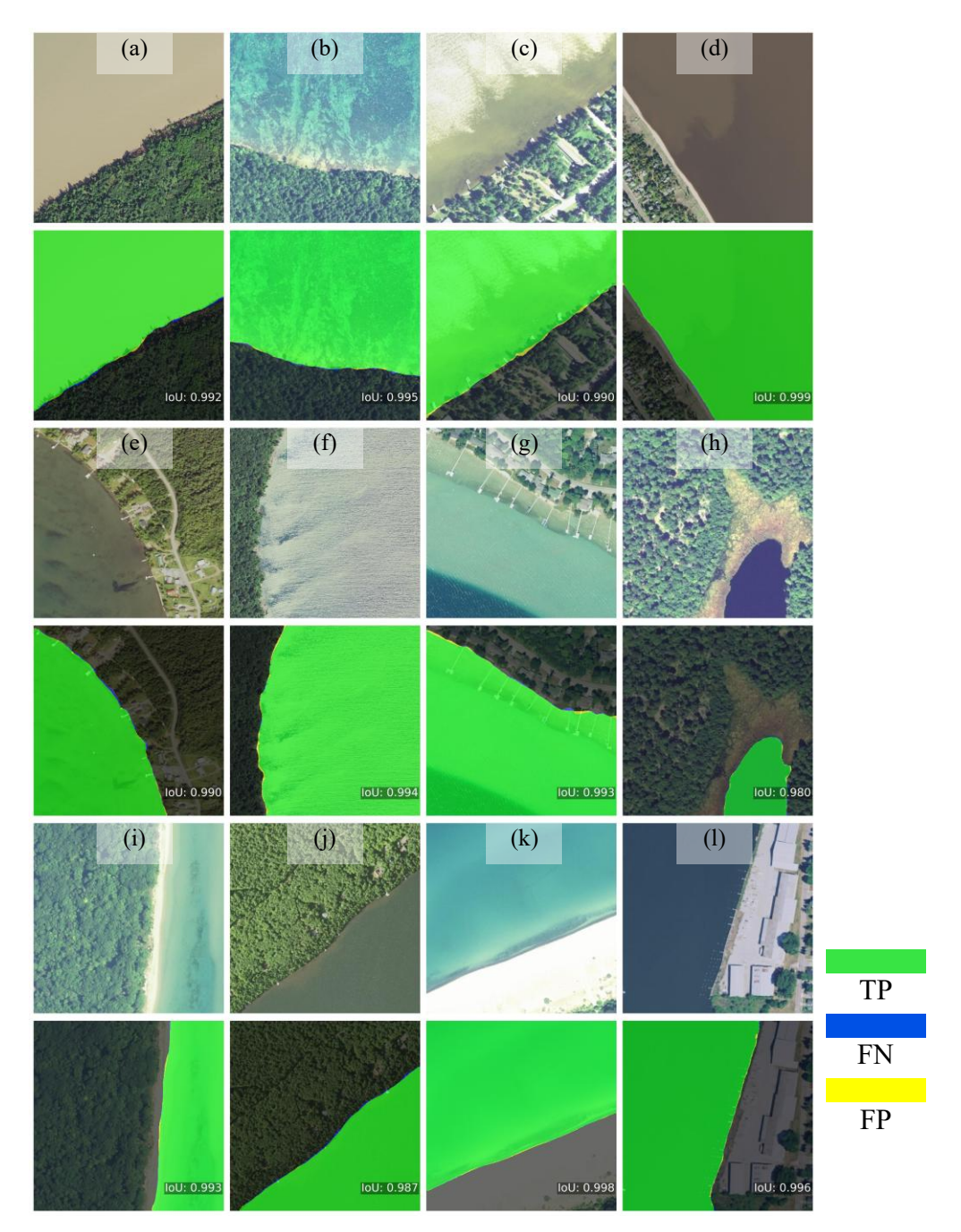


Figure 5-6 | Water segmentation examples for DeepLabV3. (a)–(f) show water body segmentation results across various water hues, while (g)–(l) present results from different landscape types. Green pixels indicate true positives, blue pixels indicate false negatives, and yellow pixels indicate false positives.

demonstrates that DeepLabV3+ performs robustly during training. Based on both mIoU and pixel accuracy, the model from epoch 84 was selected for final evaluation using the held-out test dataset. On the test set, DeepLabV3+ achieved a water body mIoU of 91.5% and a pixel accuracy of 99.0%. The close agreement in pixel accuracy between the training and test sets indicates strong generalization. However, the slight decrease in mIoU on the test set suggests that some non-water pixels were misclassified as water, especially in challenging or ambiguous areas, as further discussed in the Discussion section. This finding underscores the importance of refining segmentation outputs, particularly through post-processing steps to remove non-shoreline water boundaries in the modified DSAS workflow. Model performance is further illustrated in Figure 5-6, which presents segmentation results under a variety of water surface and landscape conditions. In these examples, green regions indicate correct agreement between model inference and manual annotation, blue pixels represent ground truth water missed by the model, and yellow pixels indicate false positives where non-water pixels were misclassified as water. For six representative water surface types (Fig. 5-6a-f: muddy, clear-deep, light green, brown, clear-shallow, wavy), DeepLabV3+ achieved high IoU values ranging from 0.990 to 0.999. The water boundaries closely aligned with the true shoreline, and both false positives and false negatives were minimal. For six different landscape types (Fig. 5-6g-1: rural area, wetland, narrow beach, vegetated shoreline, wide beach, and armored urban shoreline), IoU values ranged from 98.0% to 99.8%, demonstrating consistently strong performance across diverse settings. The model performed especially well in areas with regular shoreline shapes, such as beaches and armored urban shorelines. Overall, these results confirm that DeepLabV3+ delivers robust segmentation performance across a wide range of water and landscape conditions, supporting its use for further shoreline movement analysis.

5.4.2 Performance of shoreline movement tracking

The performance of shoreline tracking using SCET is illustrated in Figure 5-7. At the local validation site (siteID: 4608633, 46°28'35"N, 86°56'54"W; Fig. 5-7a), the SCET output (blue line) closely matched the manual delineation (green line) for both 2010 and 2020, demonstrating strong spatial agreement. Across all validation sites, the mean shoreline positioning error for all transects was 0.92 m, with a median error of 0.57 m. We further summarized the results by lake and by state. For each lake (Fig. 5-7b), the mean errors were: Lake Superior, 1.06 m; Lake Michigan, 0.88 m; Lake Huron, 1.03 m; Lake Erie, 0.78 m; and Lake Ontario, 0.83 m. The corresponding median

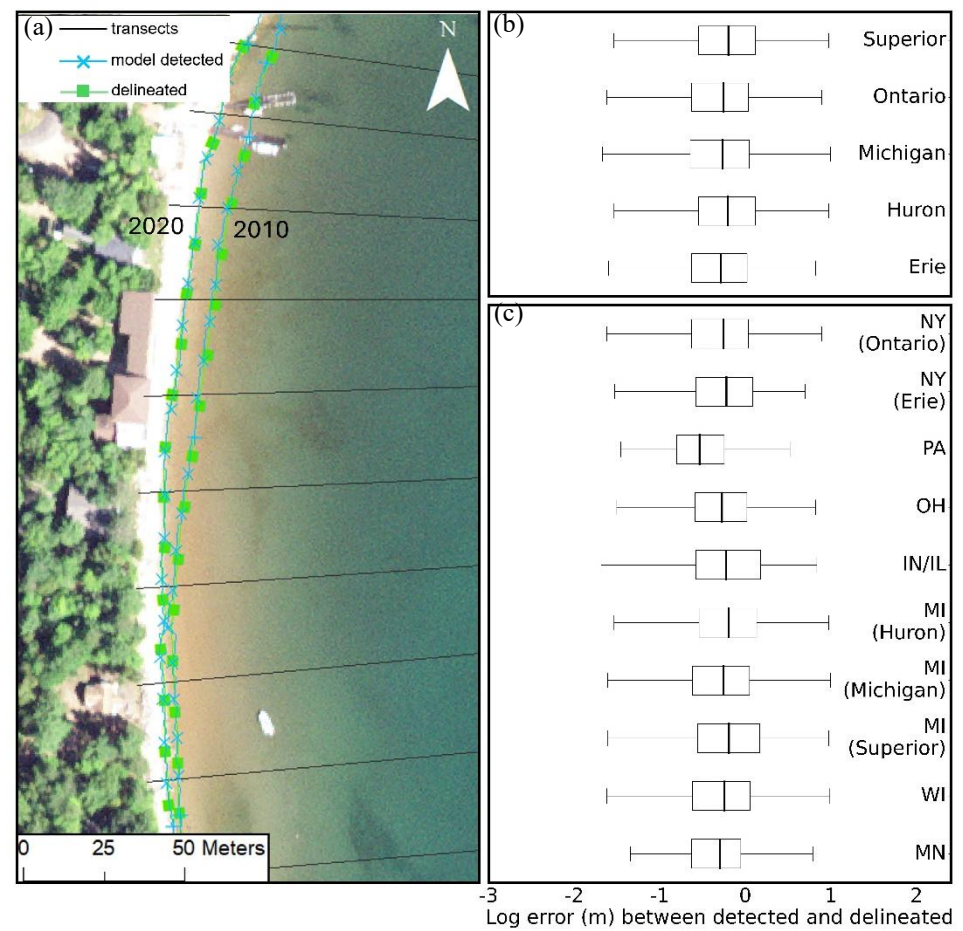


Figure 5-7 | **SCET performance for shoreline positioning.** (a) Spatial proximity between SCET-derived shorelines and manual delineations. (b) Error distribution of shoreline positioning for each Great Lake. (c) Error distribution of shoreline positioning for each Great Lakes state.

errors were: Lake Superior, 0.64 m; Lake Michigan, 0.54 m; Lake Huron, 0.63 m; Lake Erie, 0.52 m; and Lake Ontario, 0.55 m. Given the NAIP image resolution (1 m before 2011 and 0.6 m after), the mean error was less than two pixels, and the median error corresponds to, at most, a one-pixel mismatch. By state (Fig. 5-7c), Minnesota shorelines showed a mean error of 0.84 m and a median of 0.50 m; Wisconsin, 0.97 m mean and 0.57 m median; Illinois/Indiana, 0.98 m mean and 0.60 m median. Michigan shorelines showed mean errors of 1.09 m (Lake Superior), 0.99 m (Lake Michigan), and 1.03 m (Lake Huron), with median errors of 0.65 m, 0.55 m, and 0.64 m, respectively. For Pennsylvania, the mean and median errors were 0.47 m and 0.29 m; for New York, 0.86 m (Lake Erie) and 0.83 m (Lake Ontario) mean, with median errors of 0.69 m and 0.55 m, respectively. In summary, the SCET toolkit consistently delivered sub-meter accuracy in shoreline positioning across different lakes and states. The mean error was typically less than two image pixels, and the median error was generally within a single pixel of the ground truth delineations. This high level of accuracy makes SCET a valuable tool for monitoring shoreline dynamics throughout the Great Lakes region.

5.4.3 Performance of computation speed

The overall computation speed of SCET was evaluated on a system equipped with a 12-core CPU and an RTX 3090 GPU. For each site ID, which typically includes aerial images sized $4 \times 9,000 \times 12,000$ pixels (post-2011, 0.6 m/pixel) or $4 \times 5,000 \times 7,000$ pixels (pre-2011, 1 m/pixel) per sampling, it took approximately 2.5 minutes (pre-2011) and 6.5 minutes (post-2011) to unzip the images and divide them into 500×500 pixel tiles while preserving geoinformation. Image inference for segmentation required an additional 12 minutes (post-2011) or 5 minutes (pre-2011) per site, followed by 5 minutes (post-2011) or 2 minutes (pre-2011) for shoreline extraction, cleaning, and merging the results based on the geoinformation. This process was repeated roughly

eight times to cover the two-year sampling interval over a span of about 15 years. After all shorelines were extracted, the baseline translation, transect intersection, and shoreline change rate calculation using the modified DSAS workflow took approximately 1 minute per site ID (typically covering about 20 km of shoreline). Excluding the substantial time savings from automating manual delineation, the modified DSAS workflow implemented in SCET reduced processing time by more than 80% compared to the traditional DSAS tool in ArcMap.

5.4.4 Case study: shoreline changes in Michigan City

The shoreline change rates for Michigan City are presented in Figures 5-8 and 5-9. The original shoreline change rates generated by the modified DSAS indicate widespread recession across most transects in Michigan City and the nearby Indiana Dunes National Park. The majority of sites displayed annual shoreline change rates ranging from -7.65 m/yr to 2.50 m/yr (Fig. 5-8).

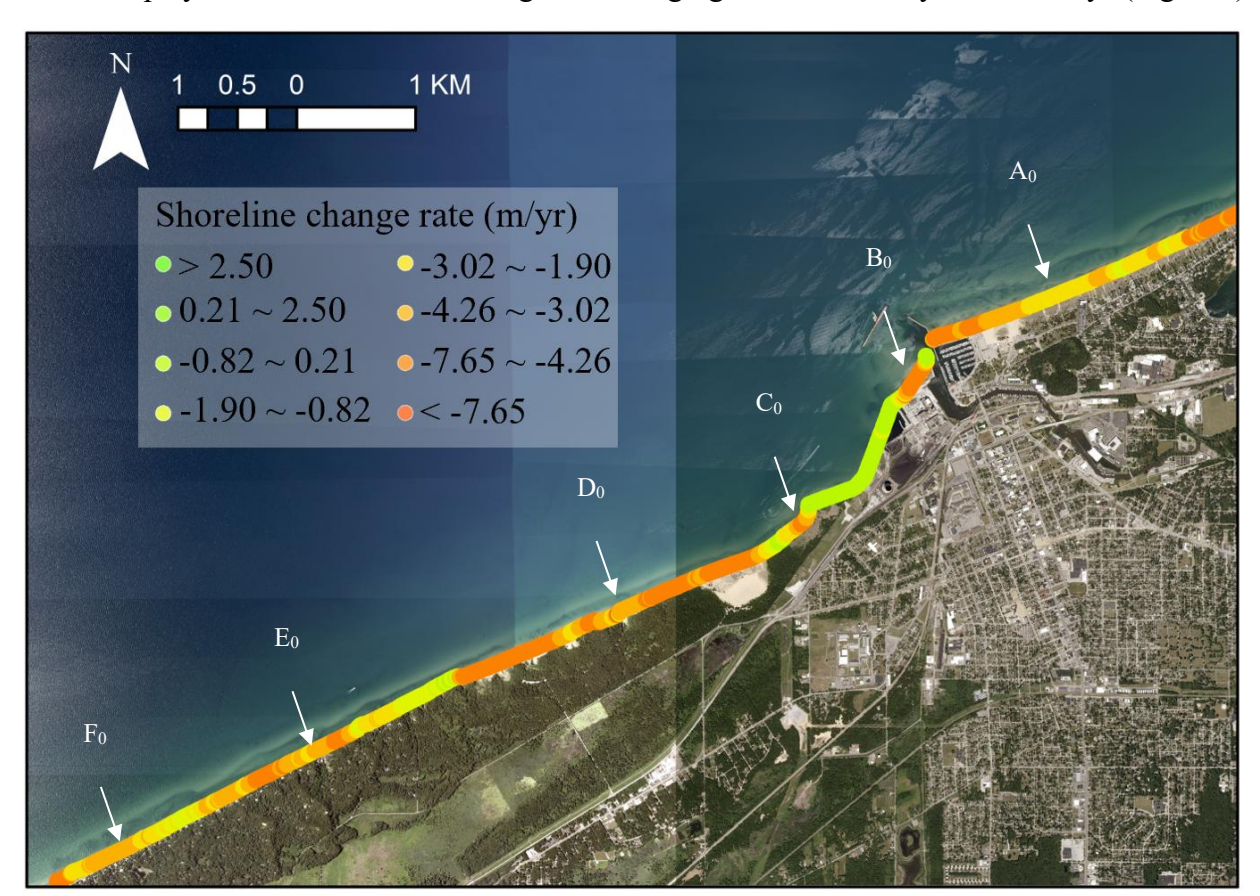


Figure 5-8 | Shoreline change rates calculated by modified DSAS.

In Michigan City, particularly at Washington Park to the right of the river outlet (site A₀), the shoreline exhibited significant recession, with rates between –7.65 m/yr and –3.02 m/yr. The most severe erosion was concentrated near coastal defenses and at the far eastern end. On the left side of Michigan City, the shoreline remained relatively stable or exhibited slight changes close to coastal defenses and at the revetment, while recession was observed between these structures (sites B₀ and C₀). The Indiana Dunes area also showed overall recession, with rates ranging from –7.65 m/yr to a relatively stable 0.21 m/yr. Notably, sites D₀, E₀, and F₀ along Indiana Dunes experienced severe recession. After calibrating for water level fluctuations, the shoreline change rates became more diverse, as illustrated in Figure 5-9. The calibrated rates better distinguished between erosion, accretion, and stability. For example, Washington Park (right of the outlet, site A in Fig. 5-9)

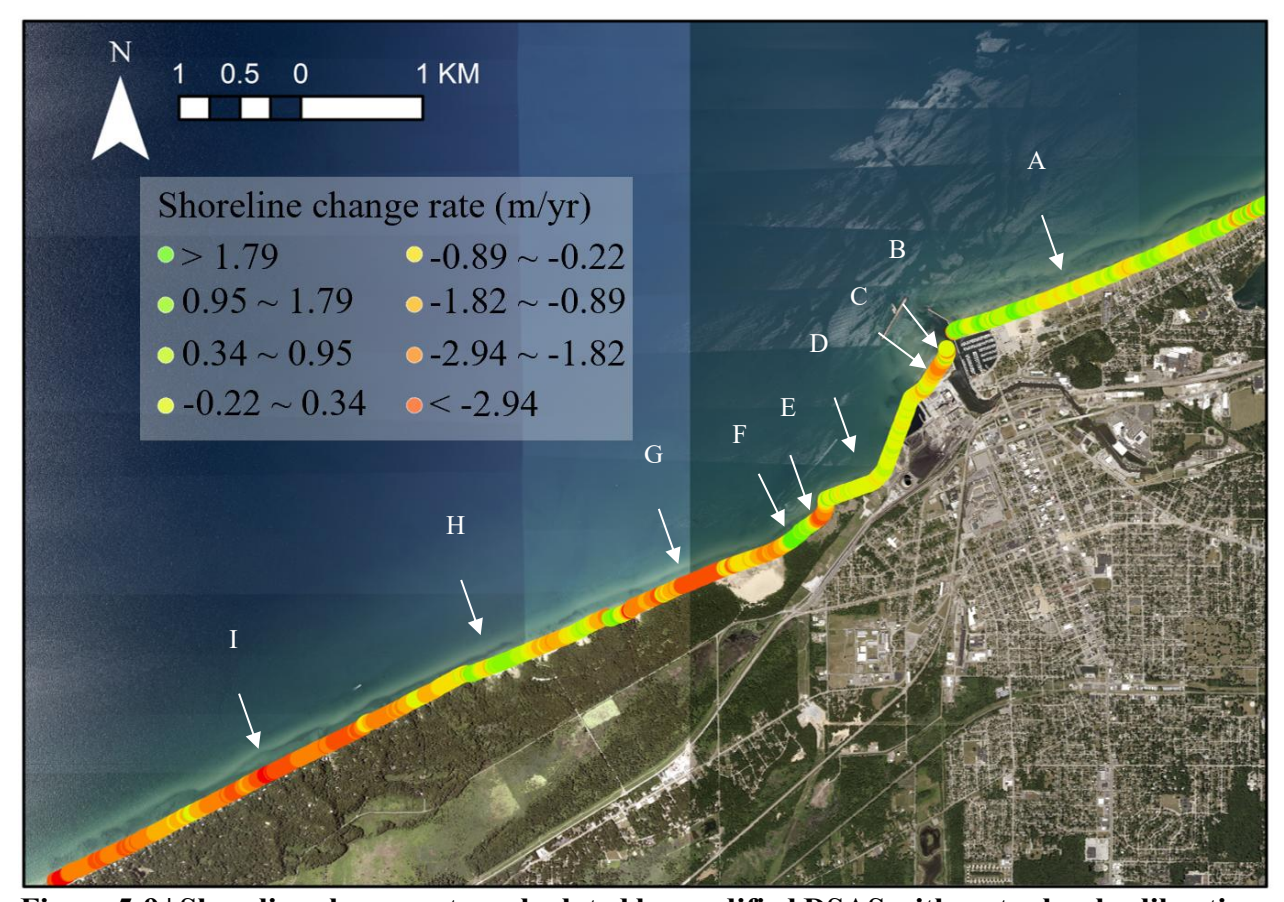


Figure 5-9 | Shoreline change rates calculated by modified DSAS with water level calibration.

shifted to a stable or accreting condition, indicating that previous recession in this area was largely driven by water level changes. This stable shoreline was also observed at sites B and D, which are armored sections to the right of the river outlet, consistent with their structural protection. In contrast, sites C and E exhibited severe erosion (less than –2.94 m/yr); these beaches are adjacent to armored shoreline, suggesting a flanking effect where alongshore protection leads to increased erosion next to structures. Sites F and H were identified as accretion areas with rates exceeding 1.79 m/yr. However, the majority of Indiana Dunes continued to experience severe erosion, especially at site G and the extended area at site I to the west, both with rates below –2.94 m/yr. The persistence of severe retreat at G and I aligns with previous UAV LiDAR survey findings conducted at Indiana Dunes, further validating the observed patterns (Troy et al., 2021). Overall, these findings highlight the spatial variability in shoreline change dynamics and underscore the importance of both structural interventions and hydrological calibration for accurate shoreline management in the region.

5.5 Discussion

5.5.1 Limitation and future improvements

Although our toolkit provides accurate water body segmentation and yields results comparable to traditional manual delineation and DSAS-based calculations, all while significantly reducing processing time, several limitations remain that point to areas for future improvement. First, the current evaluation metrics used for model training and validation are Intersection over Union (IoU) and pixel accuracy. They primarily reflect the accuracy over the entire water body, rather than the shoreline itself, which comprises only a small fraction of the total area. Consequently, these overall metrics can overestimate true accuracy at the land-water interface, as illustrated in Figure 5-10, where high IoU values are observed despite notable shoreline pixel

mismatches. In the present toolkit, since our main focus is on tracking shoreline movement over time rather than absolute shoreline positioning, these errors are treated as systematic. However, in applications where precise shoreline positioning is critical, metrics specifically targeting the shoreline—such as the shoreline coverage ratio (i.e., the proportion of ground truth shoreline pixels correctly predicted)—should be incorporated into both model training and evaluation. This would prevent shoreline accuracy from being overshadowed by the much larger water area. Second, the current version of SCET simplifies analysis by only tracking a single intersection point between each transect and each year's shoreline. This approach is not suitable for areas with islands, where multiple intersection points may occur. In such cases, island shapefiles must be provided separately for the modified DSAS computation to ensure accurate shoreline tracking. Third, while the submeter (0.6 m) resolution of NAIP aerial imagery is suitable for monitoring broad-scale shoreline changes, it may not be sufficient for detecting localized failures of engineered shoreline structures, such as revetments or seawalls. These failures can occur at scales of just a few meters. Detecting them would require higher-resolution imagery from commercial aerial sources or drones, along

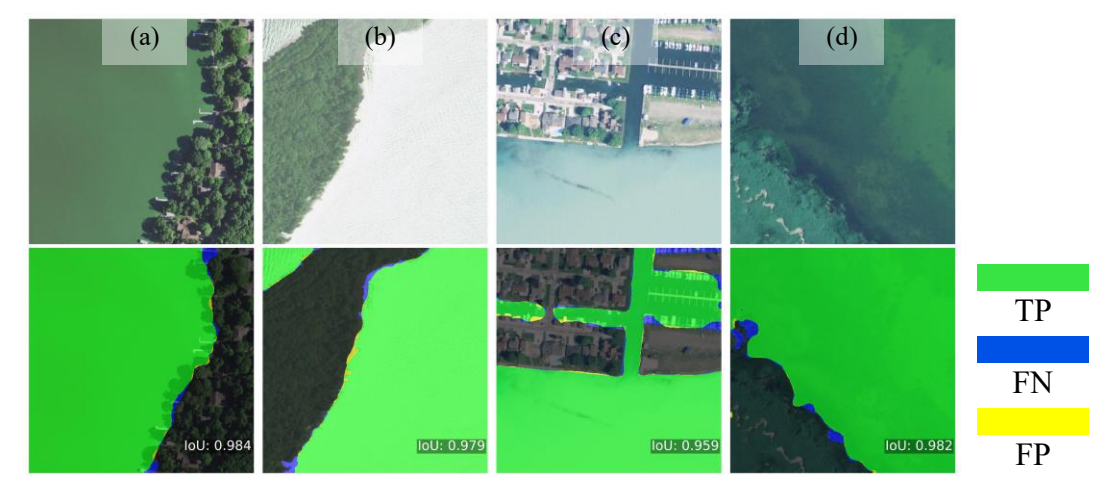


Figure 5-10 | Water conditions and landscapes requiring further refinement. (a) Water body with severe eutrophication; (b) highly wavy water body; (c) complex harbor or pier area; (d) wetlands with floating plants and algae. Green pixels indicate true positives, blue pixels indicate false negatives, and yellow pixels indicate false positives.

with retraining the model to maintain segmentation accuracy. Fourth, NAIP's biennial (approximately two-year) sampling interval works well for tracking long-term shoreline trends, but is not frequent enough to monitor short-term changes caused by events like coastal flooding or storm surges. To observe such events, more frequent imagery from commercial satellites or open-access sources like Sentinel-2 could be used, though the model would also need retraining for these data types.

5.5.2 Alternative shoreline change classification method using distance metrics

In SCET, shoreline movement is calculated based on georeferenced shoreline positions by setting a series of transects and applying a regression method to estimate shoreline change rates. To improve accuracy, water level calibration is incorporated, adjusting shoreline positions according to concurrent water level data. While this approach is effective, it is subject to several constraints: first, bathymetry data are not always available for all locations; second, existing bathymetric datasets often have low spatial and temporal resolution, making it difficult to ensure that the bathymetry remains unchanged over time. Additionally, running sediment transport models to account for bathymetric changes can be computationally expensive (Papanicolaou et al., 2008). As an alternative, the Fréchet distance offers a rigorous mathematical approach for quantifying the similarity between two curves, particularly useful for analyzing the evolution of shoreline positions over time (Eiter and Mannila, 1994; Mascret et al., 2006). Let P = (p_1, p_2, \dots, p_n) and $Q = (q_1, q_2, \dots, q_m)$ denote the polylines representing the shoreline delineations for two different years, with each point corresponding to a spatial location along the shoreline. After aligning such that the start and end points of P with Q by linear transformation, the Fréchet distance $d_F(P, Q)$ is formally defined as:

$$d_F(P,Q) = \inf_{\alpha,\beta} \max_{t \in [0,1]} ||P(\alpha(t)) - Q(\beta(t))|| \quad \text{Eqn. 5-4}$$

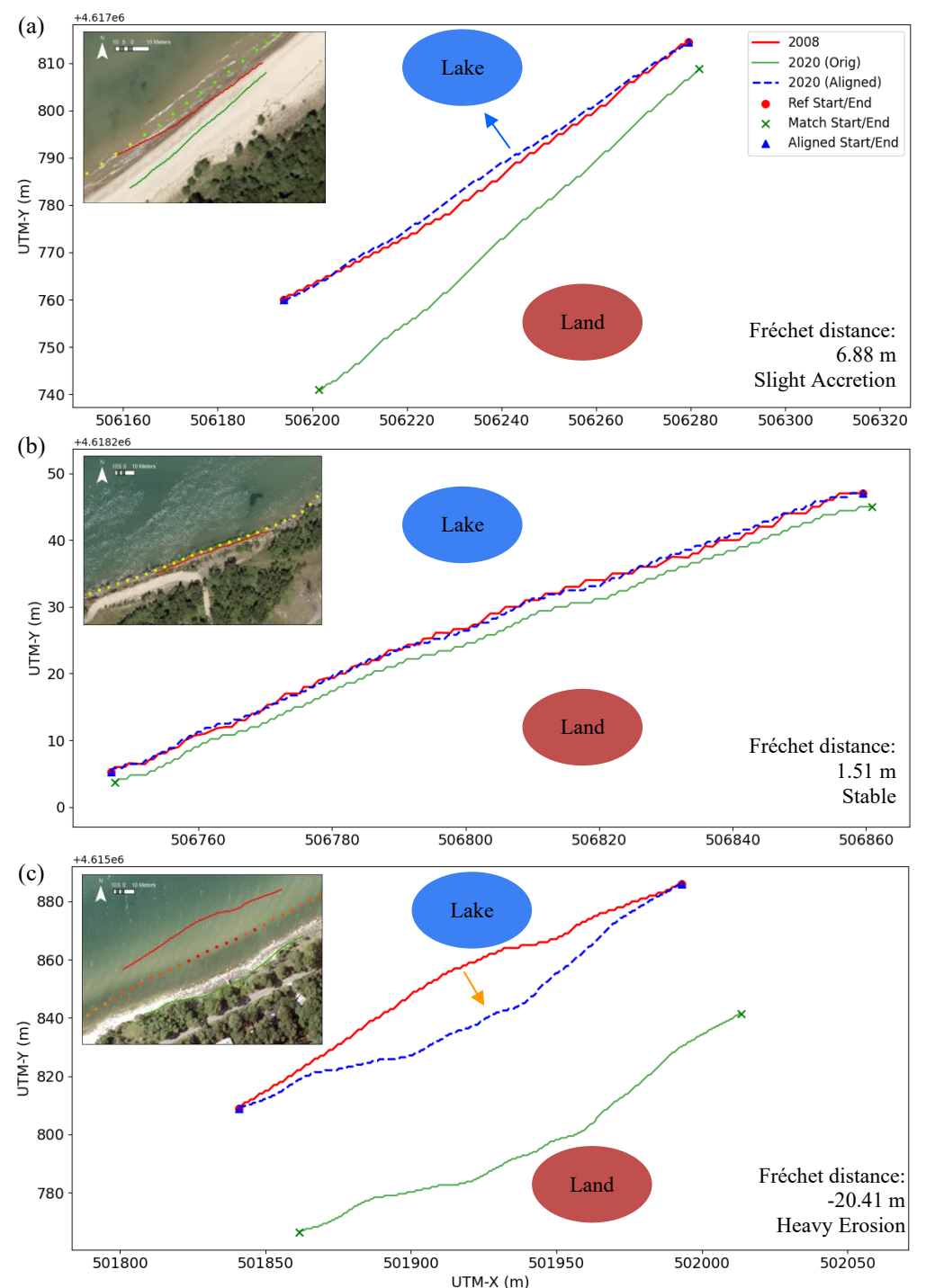


Figure 5-11 | Distance metrics for shoreline change classification. (a) Shoreline accretion condition; (b) relatively stable shoreline; (c) shoreline erosion condition. Red indicates the shoreline position in 2008, green indicates the shoreline position in 2018, and the blue dashed line represents the 2018 shoreline aligned to match the start and end points of the 2008 shoreline. Blue arrows indicate land-to-water movement, while orange arrows indicate water-to-land movement.

where α and β are continuous non-decreasing reparameterizations of the interval [0,1] over

the two curves, and ||·|| denotes the Euclidean distance. This distance metric captures the greatest spatial deviation between shoreline positions from two different years after alignment, and thus can be used as an alternative method for classifying shoreline movement as accretion, stable, or erosion. While the Fréchet distance does not represent the exact magnitude of shoreline movement at every point, a higher Fréchet distance indicates more significant change—lakeward movement corresponds to greater accretion, while landward movement indicates greater erosion. This approach was applied at the Michigan City site and compared with the water level-calibrated regression method (Fig. 5-11). For the accretion site (Fig. 5-11a), the Fréchet distance between the 2008 and aligned 2018 shorelines is 6.88 m in the lakeward direction, exceeding the NAIP pixel resolution and confirming detectable accretion. At the armored, stable site (Fig. 5-11b), the Fréchet distance is 1.51 m, within the pixel resolution and consistent with a stable shoreline. For the erosion site (Fig. 5-11c), the Fréchet distance is -20.41 m (negative, indicating landward movement), far exceeding the image resolution and indicating significant erosion, which is in agreement with the results obtained using the previous method. In summary, while the SCET approach with water level calibration provides detailed, quantitative estimates of shoreline movement, the Fréchet distance offers a practical and efficient alternative for shoreline change classification—particularly in the context of coastal management. For many management applications, it is often sufficient to identify areas experiencing severe erosion or accretion, rather than obtaining exact values of shoreline displacement. The Fréchet distance is especially valuable for rapid assessment and prioritization, as it enables the detection of significant shoreline changes even in locations with limited data availability. This allows coastal managers to quickly pinpoint and respond to highrisk areas, supporting targeted interventions and resource allocation for shoreline protection and restoration.

5.5.3 General application to other sites

While SCET was primarily developed for the Great Lakes region, its framework is adaptable to other regions with appropriate considerations. For sites with similar shoreline landscapes as those included in our dataset—such as beach, urban, rural, and vegetated shorelines—and where NAIP data or orthorectified aerial imagery of comparable resolution are available, SCET can be directly applied for shoreline dynamics analysis. However, the current dataset contains limited examples of rocky and wetland shorelines, which are not dominant in the Great Lakes. Additionally, other shoreline types, such as reef, mangrove, and polar environments (Elliff and Silva, 2017; Kaiser et al., 2021; Thakur et al., 2021), are found globally but are absent from our training data. For users interested in applying SCET to such regions, it is recommended to augment the training dataset with representative examples from these specific shoreline types. When adding new data, key considerations include: (1) Shoreline length ratio: The ratio of shoreline length to the average of image height and width should span the range from 0 to 6. (2) Water body area: The proportion of water pixels to total image pixels should be as evenly distributed as possible, covering the full range from 0% to 100%. After expanding the dataset and fine-tuning the model, performance benchmarks should be maintained—mean pixel accuracy above 98% and mean IoU above 90%—to ensure consistency with current results. Once these criteria are met, the full SCET workflow, from inference to the modified DSAS analysis, can be directly applied. It is also important to note that water level calibration in SCET was designed to account for the primary environmental variability in the Great Lakes: water level fluctuations. In other coastal regions, such as the U.S. East and West Coasts and the Gulf of Mexico, tidal and wave influences can be substantial, with tidal and wind wave reaching several meters (Larson and Kraus, 1994; Allan and Komar, 2000; Atkinson et al., 2013). For these settings, calibration must incorporate more comprehensive water level and wave spectrum data to accurately capture shoreline dynamics.

5.6 Conclusion

This study introduces the Shoreline Change Estimation Toolkit (SCET), a deep learningbased solution for efficient, high-resolution shoreline change analysis. By integrating DeepLabV3+ segmentation with a modified DSAS workflow, SCET achieves sub-meter shoreline positioning accuracy, with a mean error of 0.92 m and a median error of 0.57 m across validation sites. The model's water segmentation performance exceeds 99.0% pixel accuracy and achieves a 91.5% mean IoU, enabling robust shoreline delineation across diverse landscapes. Compared to traditional DSAS implementations, SCET accelerates shoreline change rate calculations by more than 80%, supporting practical, large-scale monitoring efforts. The toolkit's ability to rapidly detect and quantify spatial patterns of shoreline erosion and accretion offers significant benefits for natural hazard monitoring and coastal risk management. SCET enables early identification of dynamic erosion hotspots, facilitating timely risk assessments and guiding mitigation strategies for at-risk communities and infrastructure. By distinguishing true shoreline erosion and accretion from water-level-driven fluctuations—as demonstrated in Michigan City case studies—SCET provides critical insights to support infrastructure vulnerability assessments, resilience planning, and adaptation initiatives. While this toolkit was developed and validated for the Great Lakes region, its workflow is highly adaptable to other coastal environments through the incorporation of expanded training datasets and site-specific environmental calibration. As climate change continues to intensify coastal hazards worldwide, SCET offers an accurate and efficient approach for shoreline monitoring and management, providing essential data for decision-makers tasked with reducing risk and enhancing coastal resilience.

Chapter 6: Summary and conclusion

Natural hazards in the Great Lakes are common and have caused hundreds of fatalities, as well as serious socio-economic and ecological consequences. Currently, our understanding of the characterization of natural hazards and the effectiveness of detection in the Great Lakes region remains underexplored, partially due to the difficulty of data acquisition, the complexity of natural hazard patterns, and the limitations in the accuracy of automatic methods. To address this challenge, my hypothesis is that combining remote sensing and deep learning techniques with an understanding of physical processes can enhance the detection and characterization of natural hazards in the Great Lakes region. Based on this hypothesis, the study focuses on flooding, flash rip currents, and rapid shoreline changes, utilizing remote sensing and deep learning techniques for detection and characterization.

Chapter 2 developed an integrated UAV-based toolkit to characterize stream habitat quality, addressing key limitations of conventional monitoring such as subjectivity, sparse transects, and labor-intensive fieldwork. The toolkit was organized into a three-part pipeline: Toolkit I for optimized flight route design (with obstacle avoidance and overlap controls), Toolkit II for automated photogrammetric processing (generating ortho- and terrain products via structure-frommotion), and Toolkit III for multi-metric index (MMI) computation. The outputs were validated against field measurements, demonstrating continuous, high-resolution assessments of critical habitat attributes and MMI scores consistent with traditional transect surveys. Assessments of route efficiency, mapping accuracy, and agreement with ground truth confirmed the toolkit as a cost-effective, scalable, and repeatable approach for stream habitat quality monitoring.

Chapter 3 then applied this UAV-based toolkit for a severe inland flood case in Black Earth Creek, and introduced a loss and resilience analysis to quantify both immediate impairment and

subsequent recovery of stream habitat. Using six flights spanning pre-flood and post-flood till the steady periods, the study computed transect-level MMI values (riparian vegetation buffer, bank stability, and in-stream cover) and quantified loss (pre-to-post relative decline) and resilience (relative recovery rate at subsequent years), with careful treatment of edge cases to ensure interpretable metrics. This approach revealed spatially heterogeneous responses: many transects declined and later returned to pre-flood or better conditions, while a subset showed persistent impairment, highlighting localized fragility that site-level aggregation can mask.

Chapter 4 developed a deep learning framework to detect and characterize flash rip currents at a featureless beach in Lake Michigan. Using a refined Cascade R-CNN architecture, combined with post-processing steps to reduce false positives, the framework achieved high detection accuracy and outperformed baseline deep learning models. Applied to a four-month webcam dataset, the approach identified and classified nearly two thousand flash rip events into three driving factors: water-level fluctuations, normal waves, and oblique waves. Characterization showed that these factors generated distinct spatial, temporal, and kinematic patterns. For instance, normal-wave-driven rips tended to extend further offshore but lasted for shorter durations with faster growth speeds, while water-level- and oblique-wave-driven rips exhibited more moderate behaviors. Overall, the study demonstrated the potential of automated detection and characterization to advance both scientific understanding and practical beach safety monitoring.

Chapter 5 introduced the Shoreline Change Estimation Toolkit (SCET), a deep learning—based framework for automated shoreline detection and change analysis. Built on DeepLabV3+ segmentation and a modified DSAS workflow, SCET integrates shoreline extraction, transect-based change computations, and water-level calibration into an end-to-end pipeline. This design enables rapid detection of shoreline positions, efficient calculation of change rates, and early

identification of erosion and accretion hotspots. A key contribution of SCET is its ability to separate true morphological change from shoreline shifts driven by lake-level fluctuations, improving interpretability and reducing false alarms. Case studies in Michigan City and Indiana Dunes National Park demonstrated how water-level calibration clarified site-specific dynamics: in some armored sections, apparent recession was reclassified as stability or accretion, while adjacent unarmored stretches showed severe erosion consistent with flanking effects. Together, these results show that integrating deep learning with water-level calibration improves the efficacy of shoreline change assessments, enabling more reliable and timely identification of at-risk shorelines.

Overall, this dissertation validates the central hypothesis that remote sensing combined with deep learning can substantially improve the detection and characterization of natural hazards in the Great Lakes. Chapter 2 developed and validated a UAV-based toolkit for continuous, MMI-based assessment of stream habitat quality. Chapter 3 extended this framework to quantify flood-induced loss and resilience, revealing both overall recovery and localized transect-level vulnerabilities critical for restoration planning. Chapter 4 advanced operational beach-hazard monitoring by detecting flash rip currents, classifying them by driving factors, and characterizing their spatial, temporal, and kinematic differences. Chapter 5 introduced the Shoreline Change Estimation Toolkit (SCET), which integrates segmentation, transect analysis, and water-level calibration to distinguish true morphological change from water-level-driven variability and to rapidly flag erosion hotspots. Together, these contributions establish a cost-effective and scalable foundation for hazard monitoring across rivers, nearshore zones, and shorelines, providing new insights into the dynamics of natural hazards in the Great Lakes region.

In addition, several avenues for future work could extend the impact and practical deployment of this research. (1) **Flood impacts on stream habitats:** Temporal continuity is essential for

capturing both the extent and timing of recovery. Coupling periodic UAV surveys with continuous camera networks would help bridge temporal gaps, capture short-lived disturbances, and provide context for UAV-based observations, particularly where high spatial resolution is not required. Expanding the range of indicators to include bathymetry (via UAV bathy-LiDAR), water quality (via hyperspectral sensors), and substrate metrics would also enrich ecological inference beyond the three indices used here, enabling a more comprehensive evaluation of flood-related loss and resilience in freshwater habitat. (2) Flash rip currents: Future work should focus on increasing the robustness and generality of the detection framework. This includes improving performance under adverse weather and low-light conditions, extending applicability to a wider range of rip types, and moving from offline analysis toward integration with real-time monitoring platforms. (3) Rapid shoreline change: Future work should focus on improving shoreline-specific accuracy metrics, extending applicability to complex settings such as islands, and adapting the toolkit to higher-resolution and higher-frequency imagery. These steps would increase the robustness of shoreline detection and broaden its utility for both long-term trend analysis and short-term event monitoring.

Finally, beyond these three natural hazard examples, the frameworks developed in this study are broadly adaptable. The combination of high-resolution sensing and deep learning can also be applied to other freshwater hazards, including pollution events, algal blooms, drought-induced low water, ice-related impacts, and compound disturbances. Extending the approach in this way would support more comprehensive hazard mitigation and adaptation strategies across the changing Great Lakes region.

Reference

- 1. Aadland, L. P. (1993). Stream habitat types: their fish assemblages and relationship to flow. *North American Journal of Fisheries Management*, *13*(4), 790-806. https://doi.org/10.1577/1548-8675(1993)013<0790:SHTTFA>2.3.CO;2
- 2. Abdelhady, H. U., & Troy, C. D. (2023). A reduced-complexity shoreline model for coastal areas with large water level fluctuations. *Coastal Engineering*, *179*, 104249. https://doi.org/10.1016/j.coastaleng.2022.104249
- 3. Abessolo, G. O., Almar, R., Angnuureng, D. B., Bonou, F., Sohou, Z., Camara, I., ... & Dada, O. A. (2023). African coastal camera network efforts at monitoring ocean, climate, and human impacts. *Scientific Reports*, *13*(1), 1514. https://doi.org/10.1038/s41598-023-28815-6
- 4. Acharya, B.S., Bhandari, M., Bandini, F., Pizarro, A., Perks, M., Joshi, D.R., Wang, S., Dogwiler, T., Ray, R.L., Kharel, G., & Sharma, S. (2021). Unmanned Aerial Vehicles in Hydrology and Water Management: Applications, Challenges, and Perspectives. *Water Resources Research* 57, e2021WR029925. https://doi.org/10.1029/2021WR029925
- 5. Acheampong, E., Lafreniere, D., Williams, R., & Meadows, G. (2025). Improving geospatial coastal vulnerability indices for the Great Lakes. *Journal of Great Lakes Research*, 102544. https://doi.org/10.1016/j.jglr.2025.102544
- 6. Ahmed, I., Ahmad, M., Khan, F. A., & Asif, M. (2020). Comparison of deep-learning-based segmentation models: Using top view person images. *IEEE Access*, 8, 136361-136373. https://doi.org/10.1109/ACCESS.2020.3011406
- 7. Allan, D., Erickson, D., & Fay, J. (1997). The influence of catchment land use on stream integrity across multiple spatial scales. *Freshwater Biology* 37, 149–161. https://doi.org/10.1046/j.1365-2427.1997.d01-546.x

8. Allan, J.D. (2004). Landscapes and Riverscapes: The Influence of Land Use on Stream Ecosystems. *Annu. Rev. Ecol. Evol. Syst.* 35, 257–284.

https://doi.org/10.1146/annurev.ecolsys.35.120202.110122

9. Allan, J., & Komar, P. (2000). Are ocean wave heights increasing in the eastern North Pacific?. *Eos, Transactions American Geophysical Union*, 81(47), 561-567. https://doi.org/10.1029/EO081i047p00561-01

10. Almeida, L. P., de Oliveira, I. E., Lyra, R., Dazzi, R. L. S., Martins, V. G., & da Fontoura Klein, A. H. (2021). Coastal analyst system from space imagery engine (CASSIE): shoreline management module. *Environmental Modelling & Software*, *140*, 105033. https://doi.org/10.1016/j.envsoft.2021.105033

- 11. Anthony, E. J., Brunier, G., Besset, M., Goichot, M., Dussouillez, P., & Nguyen, V. L. (2015). Linking rapid erosion of the Mekong River delta to human activities. *Scientific reports*, 5(1), 14745. https://doi.org/10.1038/srep14745
- 12. Argyroudis, S. A., Mitoulis, S. A., Hofer, L., Zanini, M. A., Tubaldi, E., & Frangopol, D. M. (2020). Resilience assessment framework for critical infrastructure in a multi-hazard environment: Case study on transport assets. *Science of the Total Environment*, 714, 136854. https://doi.org/10.1016/j.scitotenv.2020.136854
- 13. Arthington, A.H., Naiman, R.J., McCLAIN, M.E., & Nilsson, C. (2010). Preserving the biodiversity and ecological services of rivers: new challenges and research opportunities. Freshwater Biology 55, 1–16. https://doi.org/10.1111/j.1365-2427.2009.02340.x
- 14. Atkinson, J., McKee Smith, J., & Bender, C. (2013). Sea-level rise effects on storm surge and nearshore waves on the Texas coast: Influence of landscape and storm

- characteristics. *Journal of Waterway, Port, Coastal, and Ocean Engineering*, 139(2), 98-117. https://doi.org/10.1061/(ASCE)WW.1943-5460.0000187
- 15. Austin, M. J., Scott, T. M., Russell, P. E., & Masselink, G. (2013). Rip current prediction: development, validation, and evaluation of an operational tool. *Journal of coastal research*, *29*(2), 283-300. https://doi.org/10.2112/JCOASTRES-D-12-00093.1
- 16. Bai, X., Wang, J., Chen, R., Kang, Y., Ding, Y., Lv, Z., ... & Feng, H. (2024). Research progress of inland river water quality monitoring technology based on unmanned aerial vehicle hyperspectral imaging technology. *Environmental Research*, 257, 119254. https://doi.org/10.1016/j.envres.2024.119254
- 17. Bandini, F., Olesen, D., Jakobsen, J., Kittel, C.M.M., Wang, S., Garcia, M., & Bauer-Gottwein, P. (2018). Technical note: Bathymetry observations of inland water bodies using a tethered single-beam sonar controlled by an unmanned aerial vehicle. *Hydrol. Earth Syst. Sci.* 22, 4165–4181. https://doi.org/10.5194/hess-22-4165-2018
- 18. Baradaranshoraka, M., Pinelli, J. P., Gurley, K., Zhao, M., Peng, X., & Paleo-Torres, A. (2019). Characterization of coastal flood damage states for residential buildings. *ASCE-ASME Journal of Risk and Uncertainty in Engineering Systems, Part A: Civil Engineering*, *5*(1), 04019001. https://doi.org/10.1061/AJRUA6.0001006
- 19. Barbour, M. T. (1999). Rapid bioassessment protocols for use in wadeable streams and rivers: periphyton, benthic macroinvertebrates and fish. US Environmental Protection Agency, Office of Water.
- Basterretxea-Iribar, I., Sotés, I., Sanchez-Beaskoetxea, J., & de las Mercedes Maruri, M.
 Beach management policy analysis concerning safety flag systems in Northern
 Marine Policy, 144, 105226. https://doi.org/10.1016/j.marpol.2022.105226

- 21. Bechle, A. J., Kristovich, D. A., & Wu, C. H. (2015). Meteotsunami occurrences and causes in L ake M ichigan. *Journal of Geophysical Research: Oceans*, *120*(12), 8422-8438. https://doi.org/10.1002/2015JC011317
- 22. Beeche, C., Singh, J. P., Leader, J. K., Gezer, N. S., Oruwari, A. P., Dansingani, K. K., ... & Pu, J. (2022). Super U-Net: A modularized generalizable architecture. *Pattern recognition*, 128, 108669. https://doi.org/10.1016/j.patcog.2022.108669
- 23. Bird, E. C. (1985). Coastline changes. A global review.
- 24. Boak, E. H., & Turner, I. L. (2005). Shoreline definition and detection: a review. *Journal of coastal research*, 21(4), 688-703. https://doi.org/10.2112/03-0071.1
- 25. Bolding, M.T., Kraft, A.J., Robinson, D.T., & Rooney, R.C. (2020). Improvements in multi-metric index development using a whole-index approach. *Ecological Indicators* 113, 106191. https://doi.org/10.1016/j.ecolind.2020.106191
- 26. Borden, K. A., & Cutter, S. L. (2008). Spatial patterns of natural hazards mortality in the United States. *International journal of health geographics*, 7(1), 64. https://doi.org/10.1186/1476-072X-7-64
- 27. Brander, R. W., & MacMahan, J. H. (2011). 1 Future Challenges for Rip Current. *Rip Currents: Beach Safety, Physical Oceanography, and Wave Modeling*, 1.
- 28. Brannstrom, C., Brown, H. L., Houser, C., Trimble, S., & Santos, A. (2015). "You can't see them from sitting here": Evaluating beach user understanding of a rip current warning sign. *Applied Geography*, *56*, 61-70. https://doi.org/10.1016/j.apgeog.2014.10.011
- 29. Brewster, B. C., Gould, R. E., & Brander, R. W. (2019). Estimations of rip current rescues and drowning in the United States. *Natural Hazards and Earth System Sciences*, *19*(2), 389-397. https://doi.org/10.5194/nhess-19-389-2019

- 30. Cai, B., Xu, X., Jia, K., Qing, C., & Tao, D. (2016). Dehazenet: An end-to-end system for single image haze removal. *IEEE transactions on image processing*, 25(11), 5187-5198. https://doi.org/10.1109/TIP.2016.2598681
- 31. Cai, Z., & Vasconcelos, N. (2019). Cascade R-CNN: High quality object detection and instance segmentation. *IEEE transactions on pattern analysis and machine intelligence*, 43(5), 1483-1498. https://doi.org/10.1109/TPAMI.2019.2956516
- 32. Camfield, F. E., & Morang, A. (1996). Defining and interpreting shoreline change. *Ocean & Coastal Management*, 32(3), 129-151. https://doi.org/10.1016/S0964-5691(96)00059-2
- 33. Carpi, L., Mucerino, L., Bonello, G., Besio, G., & Ferrari, M. (2021). Rip currents investigation on a Ligurian pocket beach, NW Mediterranean. *Estuarine, Coastal and Shelf Science*, 262, 107579. https://doi.org/10.1016/J.ECSS.2021.107579
- 34. Casali, Y., & Heinimann, H. R. (2019). A topological characterization of flooding impacts on the Zurich road network. *PLoS one*, *14*(7), e0220338. https://doi.org/10.1371/journal.pone.0220338
- 35. Castelle, B., & Coco, G. (2013). Surf zone flushing on embayed beaches. *Geophysical Research Letters*, 40(10), 2206-2210. https://doi.org/10.1002/grl.50485
- 36. Castelle, B., Almar, R., Dorel, M., Lefebvre, J. P., Senechal, N., Anthony, E. J., ... & Penhoat, Y. D. (2014). Rip currents and circulation on a high-energy low-tide-terraced beach (Grand Popo, Benin, West Africa). *Journal of Coastal Research*, (70), 633-638. https://doi.org/10.2112/SI70-107.1
- 37. Castelle, B., Scott, T., Brander, R. W., & McCarroll, R. J. (2016). Rip current types, circulation and hazard. *Earth-Science Reviews*, *163*, 1-21.

https://doi.org/10.1016/j.earscirev.2016.09.008

- 38. Castelle, B., Masselink, G., Scott, T., Stokes, C., Konstantinou, A., Marieu, V., & Bujan, S. (2021). Satellite-derived shoreline detection at a high-energy meso-macrotidal beach.

 Geomorphology, 383, 107707. https://doi.org/10.1016/j.geomorph.2021.107707
- 39. Cavanagh, N., Nordin, R. N., & Warrington, P. D. (1997). *Freshwater biological sampling manual*. Resources Inventory Committee.
- 40. Chang, M. J., Chang, H. K., Chen, Y. C., Lin, G. F., Chen, P. A., Lai, J. S., & Tan, Y. C. (2018). A support vector machine forecasting model for typhoon flood inundation mapping and early flood warning systems. *Water*, *10*(12), 1734. https://doi.org/10.3390/w10121734
- 41. Chen, L. C., Papandreou, G., Schroff, F., & Adam, H. (2017). Rethinking atrous convolution for semantic image segmentation. *arXiv preprint arXiv:1706.05587*. https://arxiv.org/abs/1706.05587
- 42. Chia, B., Wang, Y., & Chen, Y. (2020). Flood resilience of urban river restoration projects: Case studies in Hong Kong. *Journal of Management in Engineering*, *36*(5), 05020009. https://doi.org/10.1061/(ASCE)ME.1943-5479.0000809
- 43. Cluer, B., & Thorne, C. (2014). A stream evolution model integrating habitat and ecosystem benefits. *River Research and Applications*, *30*(2), 135-154. https://doi.org/10.1002/rra.2631
- 44. Cooper, S.D., Barmuta, L., Sarnelle, O., Kratz, K., & Diehl, S. (1997). Quantifying Spatial Heterogeneity in Streams. *Journal of the North American Benthological Society* 16, 174–188. https://doi.org/10.2307/1468250
- 45. Dalrymple, R. A., MacMahan, J. H., Reniers, A. J., & Nelko, V. (2011). Rip currents. *Annual Review of Fluid Mechanics*, 43(1), 551-581. https://doi.org/10.1146/annurev-fluid-122109-160733

- 46. Dandotiya, R., Singh, S., & Jalori, S. (2014, December). A survey of image classification techniques for flood monitoring system. In *Proceedings of the International Conference on Emerging Trends in Computer and Image Processing (ICETCIP'2014), Pattaya, Thailand* (pp. 12-16).
- 47. Dang, K. B., Vu, K. C., Nguyen, H., Nguyen, D. A., Nguyen, T. D. L., Pham, T. P. N., ... & Do, T. H. (2022). Application of deep learning models to detect coastlines and shorelines.

 Journal of Environmental Management, 320, 115732.

 https://doi.org/10.1016/j.jenvman.2022.115732
- 48. Darby, S.E. (1999). Effect of riparian vegetation on flow resistance and flood potential. Journal of hydraulic engineering 125, 443–454. https://doi.org/10.1061/(ASCE)0733-9429(1999)125:5(443)
- 49. Dauwalter, D. C., Fesenmyer, K. A., & Bjork, R. (2015). Using aerial imagery to characterize redband trout habitat in a remote desert landscape. *Transactions of the American Fisheries Society*, *144*(6), 1322-1339.

https://doi.org/10.1080/00028487.2015.1088471

50. Dawson, K. (2002). Fish kill events and habitat losses of the Richmond River, NSW Australia: an overview. *Journal of Coastal Research*, (36), 216-221.

https://doi.org/10.2112/1551-5036-36.sp1.216

- 51. Dean, R. G. (1969). Breaking wave criteria; a study employing a numerical wave theory. In *Coastal Engineering 1968* (pp. 108-123).
- 52. Del Vecchio, S., Fantinato, E., Silan, G., & Buffa, G. (2019). Trade-offs between sampling effort and data quality in habitat monitoring. *Biodiversity and Conservation*, 28(1), 55-73. https://doi.org/10.1007/s10531-018-1636-5

- 53. de Silva, A., Mori, I., Dusek, G., Davis, J., & Pang, A. (2021). Automated rip current detection with region based convolutional neural networks. *Coastal Engineering*, *166*, 103859. https://doi.org/10.1016/j.coastaleng.2021.103859
- 54. Dias-Silva, K., Vieira, T. B., de Matos, T. P., Juen, L., Simiao-Ferreira, J., Hughes, R. M., & Júnior, P. D. M. (2021). Measuring stream habitat conditions: Can remote sensing substitute for field data?. *Science of the Total Environment*, 788, 147617. https://doi.org/10.1016/j.scitotenv.2021.147617
- 55. Dietrich, J.T. (2016). Riverscape mapping with helicopter-based Structure-from-Motion photogrammetry. *Geomorphology* 252, 144–157. https://doi.org/10.1016/j.geomorph.2015.05.008
- 56. Dolin, L.S., & Turlaev, D.G. (2020). Polarization method for imaging through the water surface. *Appl. Opt.* 59, 5772. https://doi.org/10.1364/AO.394082
- 57. Dosskey, M.G., Vidon, P., Gurwick, N.P., Allan, C.J., Duval, T.P., & Lowrance, R. (2010). The Role of Riparian Vegetation in Protecting and Improving Chemical Water Quality in Streams¹. *J American Water Resour Assoc* 46, 261–277. https://doi.org/10.1111/j.1752-1688.2010.00419.x
- Doyle, M. W., Stanley, E. H., Orr, C. H., Selle, A. R., Sethi, S. A., & Harbor, J. M. (2005). Stream ecosystem response to small dam removal: Lessons from the Heartland. *Geomorphology*, 71(1-2), 227-244. https://doi.org/10.1016/j.geomorph.2004.04.011 Dumitriu, A., Tatui, F., Miron, F., Ionescu, R. T., & Timofte, R. (2023). Rip current segmentation: A novel benchmark and yolov8 baseline results. In *Proceedings of the IEEE/CVF conference on computer vision and pattern recognition* (pp. 1261-1271).

https://doi.org/10.1109/CVPRW59228.2023.00133

60. Dutta, D., Herath, S., & Musiake, K. (2003). A mathematical model for flood loss estimation. *Journal of hydrology*, 277(1-2), 24-49. https://doi.org/10.1016/S0022-1694(03)00084-2

- 61. Eiter, T., & Mannila, H. (1994). Computing discrete Fréchet distance.
- 62. Elachi, C., & Van Zyl, J. J. (2021). *Introduction to the physics and techniques of remote sensing*. John Wiley & Sons.
- 63. El-Ashry, M. T., & Wanless, H. R. (1968). Photo interpretation of shoreline changes between Capes Hatteras and Fear (North Carolina). *Marine Geology*, *6*(5), 347-379. https://doi.org/10.1016/0025-3227(68)90001-7
- 64. Elkhrachy, I. (2021). Accuracy Assessment of Low-Cost Unmanned Aerial Vehicle (UAV) Photogrammetry. *Alexandria Engineering Journal* 60, 5579–5590. https://doi.org/10.1016/j.aej.2021.04.011
- 65. Elliff, C. I., & Silva, I. R. (2017). Coral reefs as the first line of defense: Shoreline protection in face of climate change. *Marine environmental research*, *127*, 148-154. https://doi.org/10.1016/j.marenvres.2017.03.007
- 66. Erdem, F., Bayram, B., Bakirman, T., Bayrak, O. C., & Akpinar, B. (2021). An ensemble deep learning based shoreline segmentation approach (WaterNet) from Landsat 8 OLI images.

 *Advances in Space Research, 67(3), 964-974.

https://doi.org/10.1016/j.asr.2020.10.043

67. Fallon, K. M., Lai, Q., & Leatherman, S. P. (2018). Rip current literacy of beachgoers at Miami Beach, Florida. *Natural hazards*, 90(2), 601-621. https://doi.org/10.1007/s11069-017-3060-7

- 68. Fausch, K.D., Karr, J.R., & Yant, P.R. (1984). Regional application of an index of biotic integrity based on stream fish communities. *Transactions of the American Fisheries Society* 113, 39–55. https://doi.org/10.1577/1548-8659(1984)113%3C39:RAOAIO%3E2.0.CO;2
- 69. Feddersen, F. (2014). The generation of surfzone eddies in a strong alongshore current. *Journal of Physical Oceanography*, 44(2), 600-617. https://doi.org/10.1175/JPO-D-13-051.1
- 70. Flener, C., Vaaja, M., Jaakkola, A., Krooks, A., Kaartinen, H., Kukko, A., Kasvi, E., Hyyppä, H., Hyyppä, J., & Alho, P. (2013). Seamless Mapping of River Channels at High Resolution Using Mobile LiDAR and UAV-Photography. *Remote Sensing* 5, 6382–6407. https://doi.org/10.3390/rs5126382
- 71. Fletemeyer, J. (2014). The reliability of turbidity and debris moving seaward to spot rip currents on Florida beaches and the need for better warning and education programs. *Journal of Coastal Research*, (72), 39-43. https://doi.org/10.2112/SI72-008.1
- 72. Floc'h, F., Mabiala, G. R., Almar, R., Castelle, B., Hall, N., Du Penhoat, Y., ... & Delacourt, C. (2018). Flash rip statistics from video images. *Journal of Coastal Research*, (81), 100-106. https://doi.org/10.2112/SI81-013.1
- 73. Fogarin, S., Zanetti, M., Dal Barco, M. K., Zennaro, F., Furlan, E., Torresan, S., ... & Critto, A. (2023). Combining remote sensing analysis with machine learning to evaluate short-term coastal evolution trend in the shoreline of Venice. *Science of The Total Environment*, 859, 160293. https://doi.org/10.1016/j.scitotenv.2022.160293
- 74. Ford, M. (2013). Shoreline changes interpreted from multi-temporal aerial photographs and high resolution satellite images: Wotje Atoll, Marshall Islands. *Remote Sensing of Environment*, 135, 130-140. https://doi.org/10.1016/j.rse.2013.03.027

- 75. Fore, L.S., Karr, J.R., & Wisseman, R.W. (1996). Assessing Invertebrate Responses to Human Activities: Evaluating Alternative Approaches. *Journal of the North American Benthological Society* 15, 212–231. https://doi.org/10.2307/1467949
- 76. Foti, G., Barbaro, G., Barillà, G. C., Mancuso, P., & Puntorieri, P. (2023). Shoreline erosion due to anthropogenic pressure in Calabria (Italy). *European Journal of Remote Sensing*, 56(1), 2140076. https://doi.org/10.1080/22797254.2022.2140076
- 77. Fox6News, 2022a. Port Washington Lake Michigan search, report of "child on log" [WWW Document]. URL https://www.fox6now.com/news/port-washington-lake-michigan-search-report-of-child-on-log (accessed 12.5.24).
- 78. Fox6News, 2022b. Friends rescued Port Washington swimmer from Lake Michigan [WWW Document]. URL https://www.fox6now.com/video/1115754 (accessed 12.5.24).
- 79. Freeman, M. C., Bowen, Z. H., Bovee, K. D., & Irwin, E. R. (2001). Flow and habitat effects on juvenile fish abundance in natural and altered flow regimes. *Ecological applications*, *11*(1), 179-190. https://doi.org/10.1890/1051-0761(2001)011[0179:FAHEOJ]2.0.CO;2
- 80. Fu, X., Huang, J., Ding, X., Liao, Y., & Paisley, J. (2017). Clearing the skies: A deep network architecture for single-image rain removal. *IEEE Transactions on Image Processing*, 26(6), 2944-2956. https://doi.org/10.1109/TIP.2017.2691802
- 81. Fuse, T., & Ohkura, T. (2018). Development of shoreline extraction method based on spatial pattern analysis of satellite SAR images. *Remote Sensing*, *10*(9), 1361. https://doi.org/10.3390/rs10091361
- 82. Gallop, S. L., Bryan, K. R., & Coco, G. (2009). Video observations of rip currents on an embayed beach. *Journal of coastal research*, 49-53. https://www.jstor.org/stable/25737535

- 83. Gao, B. C. (1996). NDWI—A normalized difference water index for remote sensing of vegetation liquid water from space. *Remote sensing of environment*, *58*(3), 257-266. https://doi.org/10.1016/S0034-4257(96)00067-3
- 84. Gao, M., Hugenholtz, C. H., Fox, T. A., Kucharczyk, M., Barchyn, T. E., & Nesbit, P. R. (2021). Weather constraints on global drone flyability. *Scientific reports*, *11*(1), 12092. https://doi.org/10.1038/S41598-021-91325-W
- 85. Garnier, R., Calvete, D., Falqués, A., & Dodd, N. (2008). Modelling the formation and the long-term behavior of rip channel systems from the deformation of a longshore bar. *Journal of Geophysical Research: Oceans*, 113(C7). https://doi.org/10.1029/2007JC004632
- 86. Gebrehiwot, A.A., & Hashemi-Beni, L. (2021). Three-Dimensional Inundation Mapping Using UAV Image Segmentation and Digital Surface Model. *IJGI* 10, 144. https://doi.org/10.3390/ijgi10030144
- 87. Gilchrist, J., & Branche, C. (2018). Lifeguard effectiveness. In *The science of beach lifeguarding* (pp. 29-35). CRC Press. Goda, Y. (1970, August). A synthesis of breaker indices. In *Proceedings of the Japan society of civil engineers* (Vol. 1970, No. 180, pp. 39-49). Japan Society of Civil Engineers. https://doi.org/10.2208/jscej1969.1970.180 39
- 88. Ghorai, D., & Mahapatra, M. (2020). Extracting shoreline from satellite imagery for GIS analysis. *Remote Sensing in Earth Systems Sciences*, *3*(1-2), 13-22. https://doi.org/10.1007/s41976-019-00030-w
- 89. Great Lakes Surf Rescue Project, 2024. Statistics [WWW Document]. URL http://www.glsrp.org/statistics/ (accessed 12.5.24).

90. Greig, H. S., McHugh, P. A., Thompson, R. M., Warburton, H. J., & McIntosh, A. R. (2022). Habitat size influences community stability. *Ecology*, *103*(1), e03545. https://doi.org/10.1002/ecy.3545

91. Griffith, J. A., Martinko, E. A., Whistler, J. L., & Price, K. P. (2002). Interrelationships among landscapes, NDVI, and stream water quality in the US Central Plains. *Ecological Applications*, *12*(6), 1702-1718.

https://doi.org/10.1890/1051-0761(2002)012[1702:IALNAS]2.0.CO;2

92. Hajdukiewicz, H., Wyżga, B., Mikuś, P., Zawiejska, J., & Radecki-Pawlik, A. (2016). Impact of a large flood on mountain river habitats, channel morphology, and valley infrastructure. *Geomorphology*, 272, 55-67.

https://doi.org/10.1016/j.geomorph.2015.09.003

- 93. Hapke, C. J., Himmelstoss, E. A., Kratzmann, M. G., List, J. H., & Thieler, E. R. (2010). *National assessment of shoreline change: Historical shoreline change along the New England and Mid-Atlantic coasts*. US Geological Survey.
- 94. Hauet, A., Morlot, T., & Daubagnan, L. (2018). Velocity profile and depth-averaged to surface velocity in natural streams: A review over alarge sample of rivers. In *E3s web of conferences* (Vol. 40, p. 06015). EDP Sciences.
- 95. Heiler, G., Hein, T., Schiemer, F., & Bornette, G. (1995). Hydrological connectivity and flood pulses as the central aspects for the integrity of a river-floodplain system. *Regulated Rivers: Research & Management*, 11(3-4), 351-361. https://doi.org/10.1002/rrr.3450110309

 96. Himmelstoss, E. A., Henderson, R. E., Kratzmann, M. G., & Farris, A. S. (2021). *Digital shoreline analysis system (DSAS) version 5.1 user guide* (No. 2021-1091). US Geological Survey.

- 97. Hoeser, T., Bachofer, F., & Kuenzer, C. (2020). Object detection and image segmentation with deep learning on Earth observation data: A review—Part II: Applications. *Remote*Sensing, 12(18), 3053. https://doi.org/10.3390/rs12183053
- 98. Holland, K. T., Holman, R. A., Lippmann, T. C., Stanley, J., & Plant, N. (1997). Practical use of video imagery in nearshore oceanographic field studies. *IEEE Journal of oceanic engineering*, 22(1), 81-92. https://doi.org/10.1109/48.557542
- 99. Holman, R. A., & Stanley, J. (2007). The history and technical capabilities of Argus. *Coastal engineering*, *54*(6-7), 477-491. https://doi.org/10.1016/j.coastaleng.2007.01.003 100. Hough-Snee, N., Roper, B.B., Wheaton, J.M., Budy, P., & Lokteff, R.L. (2013). Riparian vegetation communities change rapidly following passive restoration at a northern Utah stream. *Ecological Engineering* 58, 371–377. https://doi.org/10.1016/j.ecoleng.2013.07.042 101. Hua, J., Wang, W., Huo, J., Wu, L., Huang, L., & Zhong, H. (2025). Effects of Ecosystem Recovery Types on Soil Phosphorus Bioavailability, Roles of Plant and Microbial

https://doi.org/10.1002/ece3.71172

102. Hughes, R.M. (2015). Recreational fisheries in the USA: economics, management strategies, and ecological threats. *Fish Sci* 81, 1–9. https://doi.org/10.1007/s12562-014-0815-x

Diversity: A Meta-Analysis. *Ecology and Evolution*, 15(4), e71172.

- 103. Hughes, R. M., & Vadas Jr, R. L. (2021). Agricultural effects on streams and rivers: A western USA focus. *Water*, *13*(14), 1901. https://doi.org/10.3390/w13141901
- 104. Hynes, H.B.N., 1970. The ecology of running waters. Liverpool university press Liverpool.
- 105. Isaak, D. J., Luce, C. H., Rieman, B. E., Nagel, D. E., Peterson, E. E., Horan, D. L., ... & Chandler, G. L. (2010). Effects of climate change and wildfire on stream temperatures and

salmonid thermal habitat in a mountain river network. *Ecological Applications*, 20(5), 1350-1371. https://doi.org/10.1890/09-0822.1

106. Ishikawa, T., Komine, T., Aoki, S. I., & Okabe, T. (2014). Characteristics of rip current drowning on the shores of Japan. *Journal of Coastal Research*, (72), 44-49.

107. Islam, M. T., Yoshida, K., Nishiyama, S., Sakai, K., & Tsuda, T. (2022). Characterizing vegetated rivers using novel unmanned aerial vehicle-borne topo-bathymetric green lidar: Seasonal applications and challenges. *River Research and Applications*, 38(1), 44-58.

https://doi.org/10.1002/rra.3875

https://doi.org/10.2112/SI72-009.1

108. Jianhong, M., & Arshad, M. R. (2013, November). Adaptive shorelines detection for autonomous surface vessel navigation. In *2013 IEEE International Conference on Control System, Computing and Engineering* (pp. 221-225). IEEE.

https://doi.org/10.1109/ICCSCE.2013.6719962

109. Jiao, S., Li, X., & Lu, X. (2006, November). An improved Ostu method for image segmentation. In 2006 8th international Conference on Signal Processing (Vol. 2). IEEE. https://doi.org/10.1109/ICOSP.2006.345705

110. Jin, D., Hoagland, P., Au, D. K., & Qiu, J. (2015). Shoreline change, seawalls, and coastal property values. *Ocean & Coastal Management*, *114*, 185-193.

https://doi.org/10.1016/j.ocecoaman.2015.06.025

111. Johnson, D., & Pattiaratchi, C. (2006). Boussinesq modelling of transient rip currents. *Coastal Engineering*, *53*(5-6), 419-439.

https://doi.org/10.1016/j.coastaleng.2005.11.005

- 112. Jones, J. M., & Corotis, R. B. (2012). The regional consequences of individual natural hazard events. *International Journal of Risk Assessment and Management*, *16*(1-3), 78-111. https://doi.org/10.1504/IJRAM.2012.047557
- 113. Jowett, I. G., & Richardson, J. (1989). Effects of a severe flood on instream habitat and trout populations in seven New Zealand rivers. *New Zealand journal of marine and freshwater research*, 23(1), 11-17. https://doi.org/10.1080/00288330.1989.9516335
- 114. Jowett, I. G. (1993). A method for objectively identifying pool, run, and riffle habitats from physical measurements. *New Zealand journal of marine and freshwater research*, 27(2), 241-248. https://doi.org/10.1080/00288330.1993.9516563
- 115. Kaiser, S., Grosse, G., Boike, J., & Langer, M. (2021). Monitoring the transformation of arctic landscapes: Automated shoreline change detection of lakes using very high resolution imagery. *Remote Sensing*, *13*(14), 2802. https://doi.org/10.3390/rs13142802
- 116. Kappes, M. S., Keiler, M., von Elverfeldt, K., & Glade, T. (2012). Challenges of analyzing multi-hazard risk: a review. *Natural hazards*, *64*(2), 1925-1958. https://doi.org/10.1007/s11069-012-0294-2
- 117. Karr, J. R. (1981). Assessment of biotic integrity using fish communities. Fisheries, 6(6), 21-27.
- 118. Karr, J. R. (1986). Assessing biological integrity in running waters: a method and its rationale. *Illinois Natural History Survey Special Publication no.* 05.
- 119. Karr, J. R. (1999). Defining and measuring river health. *Freshwater biology*, *41*(2), 221-234. https://doi.org/10.1046/j.1365-2427.1999.00427.x

- 120. Kawanisi, K., Razaz, M., Ishikawa, K., Yano, J., & Soltaniasl, M. (2012). Continuous measurements of flow rate in a shallow gravel-bed river by a new acoustic system. *Water Resources Research*, 48(5). https://doi.org/10.1029/2012WR012064
- 121. Kellermann, P., Schöbel, A., Kundela, G., & Thieken, A. H. (2015). Estimating flood damage to railway infrastructure—the case study of the March River flood in 2006 at the Austrian Northern Railway. *Natural Hazards and Earth System Sciences*, *15*(11), 2485-2496. https://doi.org/10.5194/nhess-15-2485-2015
- 122. Kim, W., Jung, S., Moon, Y., & Mangum, S. C. (2020). Morphological band registration of multispectral cameras for water quality analysis with unmanned aerial vehicle. *Remote Sensing*, *12*(12), 2024. https://doi.org/10.3390/rs12122024
- 123. Kim, D. H. (2021). Flash rip current driven suspended sediment flushing amplification in depth-integrated modeling framework. *Advances in Water Resources*, *155*, 103997. https://doi.org/10.1016/j.advwatres.2021.103997
- 124. Kirby, J. T., & Derakhti, M. (2019). Short-crested wave breaking. *European Journal of Mechanics-B/Fluids*, 73, 100-111. https://doi.org/10.1016/j.euromechflu.2017.11.001
- 125. Kirillov, A., Mintun, E., Ravi, N., Mao, H., Rolland, C., Gustafson, L., ... & Girshick, R. (2023). Segment anything. In *Proceedings of the IEEE/CVF international conference on computer vision* (pp. 4015-4026). https://arxiv.org/abs/2304.02643
- 126. Kliesen, K.L., 1994. The Economics of Natural Disasters. The regional economist 332.
- 127. Koenig, S., & Likhachev, M. (2002, July). D* lite. In *Eighteenth national conference on Artificial intelligence* (pp. 476-483).
- 128. Kozarek, J. L., Hession, W. C., Dolloff, C. A., & Diplas, P. (2010). Hydraulic complexity metrics for evaluating in-stream brook trout habitat. *Journal of Hydraulic Engineering*, *136*(12),

- 1067-1076. https://doi.org/10.1061/(ASCE)HY.1943-7900.0000197
- 129. Kuhn, J., Casas-Mulet, R., Pander, J., & Geist, J. (2021). Assessing stream thermal heterogeneity and cold-water patches from UAV-based imagery: A matter of classification methods and metrics. *Remote Sensing*, *13*(7), 1379. https://doi.org/10.3390/rs13071379
- 130. Kunkel, K. E., Changnon, S. A., & Shealy, R. T. (1993). Temporal and spatial characteristics of heavy-precipitation events in the Midwest. *Monthly Weather Review*, *121*(3), 858-866. https://doi.org/10.1175/1520-0493(1993)121%3C0858:TASCOH%3E2.0.CO;2
- 131. Lai, Y. (2019, October). A comparison of traditional machine learning and deep learning in image recognition. In *Journal of Physics: Conference Series* (Vol. 1314, No. 1, p. 012148). IOP Publishing. https://doi.org/10.1088/1742-6596/1314/1/012148
- 132. Lake, P. S. (2000). Disturbance, patchiness, and diversity in streams. *Journal of the north american Benthological society*, *19*(4), 573-592. https://doi.org/10.2307/1468118
- 133. Lake, S., Bond, N., & Reich, P. (2006). Floods down rivers: from damaging to replenishing forces. *Advances in Ecological Research*, 39, 41-62. https://doi.org/10.1016/S0065-2504(06)39003-4
- 134. Lallias-Tacon, S., Liébault, F., & Piégay, H. (2017). Use of airborne LiDAR and historical aerial photos for characterising the history of braided river floodplain morphology and vegetation responses. *Catena*, *149*, 742-759. https://doi.org/10.1016/j.catena.2016.07.038
- 135. Lane, A., Knight, P. J., & Player, R. J. (1999). Current measurement technology for near-shore waters. *Coastal Engineering*, *37*(3-4), 343-368. https://doi.org/10.1016/S0378-3839(99)00033-2
- 136. Langhammer, J. (2019). UAV monitoring of stream restorations. *Hydrology*, *6*(2), 29. https://doi.org/10.3390/hydrology6020029

- 137. Larson, M., & Kraus, N. C. (1994). Temporal and spatial scales of beach profile change, Duck, North Carolina. *Marine Geology*, 117(1-4), 75-94. https://doi.org/10.1016/0025-3227(94)90007-8
- 138. Leatherman, S. P., Zhang, K., & Douglas, B. C. (2000). Sea level rise shown to drive coastal erosion. *Eos, Transactions American Geophysical Union*, 81(6), 55-57. https://doi.org/10.1029/00EO00034
- 139. Leatherman, S. B., & Leatherman, S. P. (2017). Techniques for detecting and measuring rip currents. *Int J Earth Sci Geophys*, *3*(014), 1-2. https://doi.org/10.35840/2631-5033/1814
- 140. Le Cozannet, G., Garcin, M., Yates, M., Idier, D., & Meyssignac, B. (2014). Approaches to evaluate the recent impacts of sea-level rise on shoreline changes. *Earth-science reviews*, *138*, 47-60. https://doi.org/10.1016/j.earscirev.2014.08.005
- 141. LeCun, Y., Bengio, Y., & Hinton, G. (2015). Deep learning. *nature*, *521*(7553), 436-444. https://doi.org/10.1038/nature14539
- 142. Lee, D. T. (1982). Medial axis transformation of a planar shape. *IEEE Transactions on pattern analysis and machine intelligence*, (4), 363-369.

https://doi.org/10.1109/TPAMI.1982.4767267

- 143. Li, Z., Chen, M., Gao, S., Gourley, J. J., Yang, T., Shen, X., ... & Hong, Y. (2021). A multi-source 120-year US flood database with a unified common format and public access. *Earth System Science Data Discussions*, 2021, 1-25. https://doi.org/10.5194/essd-13-3755-2021
- 144. Li, Z., & Demir, I. (2023). U-net-based semantic classification for flood extent extraction using SAR imagery and GEE platform: A case study for 2019 central US flooding. *Science of The Total Environment*, 869, 161757. https://doi.org/10.1016/j.scitotenv.2023.161757
- 145. Liao, H., Sarver, E., & Krometis, L. A. H. (2018). Interactive effects of water quality,

physical habitat, and watershed anthropogenic activities on stream ecosystem health. *Water research*, *130*, 69-78. https://doi.org/10.1016/j.watres.2017.11.065

146. Linares, Á., Wu, C. H., Anderson, E. J., & Chu, P. Y. (2018). Role of meteorologically induced water level oscillations on bottom shear stress in freshwater estuaries in the Great Lakes. *Journal of Geophysical Research: Oceans*, 123(7), 4970-4987.

https://doi.org/10.1029/2017JC013741

147. Linares, Á., Wu, C. H., Bechle, A. J., Anderson, E. J., & Kristovich, D. A. (2019). Unexpected rip currents induced by a meteotsunami. *Scientific Reports*, *9*(1), 2105. https://doi.org/10.1038/s41598-019-38716-2

148. Liu, Y., & Wu, C. H. (2019). Lifeguarding Operational Camera Kiosk System (LOCKS) for flash rip warning: Development and application. *Coastal engineering*, *152*, 103537. https://doi.org/10.1016/j.coastaleng.2019.103537

149. Liu, Y., & Wu, C. H. (2022). Rip currents near coastal structures in Lake Michigan: characterization and assessment for warnings. *Journal of Great Lakes research*, 48(3), 645-658. https://doi.org/10.1016/j.jglr.2022.03.001

150. Liu, Y., & Wu, C. H. (2022). Drowning incidents and conditions due to hidden flash rips in Lake Michigan. *Science of the total environment*, 827, 154314.

https://doi.org/10.1016/j.scitotenv.2022.154314

151. Lu, B., Wang, W., Jordan, N., Bechle, A., Wu, C. H., Wright, D. B., & Zoet, L. K. A (2025). Multi-scale assessment for managing coastal geomorphic changes in southwestern Lake Michigan, Great Lakes. *SSRN preprint*. https://dx.doi.org/10.2139/ssrn.5442370

- 152. Luijendijk, A., Hagenaars, G., Ranasinghe, R., Baart, F., Donchyts, G., & Aarninkhof, S. (2018). The state of the world's beaches. *Scientific reports*, 8(1), 6641. https://doi.org/10.1038/s41598-018-24630-6
- 153. MacMahan, J. H., Thornton, E. B., & Reniers, A. J. (2006). Rip current review. *Coastal engineering*, *53*(2-3), 191-208. https://doi.org/10.1016/j.coastaleng.2005.10.009
- 154. Maddock, I. (1999). The importance of physical habitat assessment for evaluating river health. *Freshwater biology*, 41(2), 373-391. https://doi.org/10.1046/j.1365-2427.1999.00437.x
- 155. Malmqvist, B., & Rundle, S. (2002). Threats to the running water ecosystems of the world. *Environmental conservation*, 29(2), 134-153.

https://doi.org/10.1017/S0376892902000097

- 156. Mamun, M., & An, K. G. (2020). Stream health assessment using chemical and biological multi-metric models and their relationships with fish trophic and tolerance indicators. *Ecological Indicators*, 111, 106055. https://doi.org/10.1016/j.ecolind.2019.106055 157. Mandlburger, G., Pfennigbauer, M., Wieser, M., Riegl, U., & Pfeifer, N. (2016). Evaluation of a novel UAV-borne topo-bathymetric laser profiler. *The International Archives of the Photogrammetry, Remote Sensing and Spatial Information Sciences*, 41, 933-939. https://doi.org/10.5194/isprs-archives-XLI-B1-933-2016
- 158. Marcus, W. A., Legleiter, C. J., Aspinall, R. J., Boardman, J. W., & Crabtree, R. L. (2003). High spatial resolution hyperspectral mapping of in-stream habitats, depths, and woody debris in mountain streams. *Geomorphology*, *55*(1-4), 363-380. https://doi.org/10.1016/S0169-555X(03)00150-8

- 159. Marcus, W. A., & Fonstad, M. A. (2008). Optical remote mapping of rivers at sub-meter resolutions and watershed extents. *Earth Surface Processes and Landforms: The Journal of the British Geomorphological Research Group*, 33(1), 4-24. https://doi.org/10.1002/esp.1637
 160. Martínez-Gomariz, E., Forero-Ortiz, E., Russo, B., Locatelli, L., Guerrero-Hidalga, M., Yubero, D., & Castan, S. (2021). A novel expert opinion-based approach to compute estimations of flood damage to property in dense urban environments. Barcelona case study. *Journal of Hydrology*, 598, 126244. https://doi.org/10.1016/j.jhydrol.2021.126244
- 161. Maryan, C., Hoque, M. T., Michael, C., Ioup, E., & Abdelguerfi, M. (2019). Machine learning applications in detecting rip channels from images. *Applied Soft Computing*, 78, 84-93. https://doi.org/10.1016/j.asoc.2019.02.017
- 162. Marzocchi, W., Garcia-Aristizabal, A., Gasparini, P., Mastellone, M. L., & Di Ruocco, A. (2012). Basic principles of multi-risk assessment: a case study in Italy. *Natural hazards*, 62(2), 551-573. https://doi.org/10.1007/s11069-012-0092-x
- 163. Mascret, A., Devogele, T., Le Berre, I., & Hénaff, A. (2006). Coastline matching process based on the discrete Fréchet distance. In *Progress in Spatial Data Handling: 12th International Symposium on Spatial Data Handling* (pp. 383-400). Berlin, Heidelberg: Springer Berlin Heidelberg. https://doi.org/10.1007/3-540-35589-8 25
- 164. Mattheus, C. R., Braun, K. N., Theuerkauf, E. J., & Santoro, J. A. (2022). Urban pocket-beach morphodynamics along the wave-dominated southwest coast of Lake Michigan: An analysis of shoreline and sand volumetric changes. *Journal of Great Lakes Research*, 48(1), 52-67. https://doi.org/10.1016/j.jglr.2021.10.009

- 165. Maunder, M. N., & Deriso, R. B. (2013). A stock–recruitment model for highly fecund species based on temporal and spatial extent of spawning. *Fisheries Research*, *146*, 96-101. https://doi.org/10.1016/j.fishres.2013.03.021
- 166. May, S. K., Dolan, R., & Hayden, B. P. (1983). Erosion of US shorelines. *Eos, Transactions American Geophysical Union*, 64(35), 521-523.

https://doi.org/10.1029/EO064i035p00521

167. McAllister, M., & Snoeyink, J. (2000). Medial axis generalization of river networks. *Cartography and Geographic Information Science*, *27*(2), 129-138.

https://doi.org/10.1559/152304000783547966

168. McAllister, E., Payo, A., Novellino, A., Dolphin, T., & Medina-Lopez, E. (2022). Multispectral satellite imagery and machine learning for the extraction of shoreline indicators. *Coastal Engineering*, *174*, 104102.

https://doi.org/10.1016/j.coastaleng.2022.104102

0477(1997)078%3C0675:TRBGLW%3E2.0.CO;2

- 169. McCarroll, R. J., Brander, R. W., MacMahan, J. H., Turner, I. L., Reniers, A. J., Brown, J. A., ... & Sherker, S. (2014). Evaluation of swimmer-based rip current escape
 strategies. *Natural Hazards*, 71(3), 1821-1846. https://doi.org/10.1007/s11069-013-0979-1
 170. Meadows, G. A., Meadows, L. A., Wood, W. L., Hubertz, J. M., & Perlin, M. (1997).
 The relationship between Great Lakes water levels, wave energies, and shoreline damage.
 Bulletin of the American Meteorological Society, 78(4), 675-684. https://doi.org/10.1175/1520-
- 171. Ménard, A. D., Houser, C., Brander, R. W., Trimble, S., & Scaman, A. (2018). The psychology of beach users: importance of confirmation bias, action, and intention to improving rip current safety. *Natural hazards*, *94*(2), 953-973. https://doi.org/10.1007/s11069-018-3424-7

- 172. Minghelli, A., Spagnoli, J., Lei, M., Chami, M., & Charmasson, S. (2020). Shoreline extraction from WorldView2 satellite data in the presence of foam pixels using multispectral classification method. *Remote Sensing*, *12*(16), 2664. https://doi.org/10.3390/rs12162664
- 173. Modica, M., & Zoboli, R. (2016). Vulnerability, resilience, hazard, risk, damage, and loss: a socio-ecological framework for natural disaster analysis. *Web Ecology*, *16*(1), 59-62. https://doi.org/10.5194/we-16-59-2016
- 174. Moramarco, T., Corato, G., Melone, F., & Singh, V. P. (2013). An entropy-based method for determining the flow depth distribution in natural channels. *Journal of hydrology*, 497, 176-188. https://doi.org/10.1016/j.jhydrol.2013.06.002
- 175. Morton, R. A. (2008). *National assessment of shoreline change: Part 1: Historical shoreline changes and associated coastal land loss along the US Gulf of Mexico*. Diane Publishing.
- 176. Moussaid, J., Fora, A. A., Zourarah, B., Maanan, M., & Maanan, M. (2015). Using automatic computation to analyze the rate of shoreline change on the Kenitra coast, Morocco. *Ocean Engineering*, 102, 71-77.

https://doi.org/10.1016/j.oceaneng.2015.04.044

- 177. Mundahl, N. D., & Hunt, A. M. (2011). Recovery of stream invertebrates after catastrophic flooding in southeastern Minnesota, USA. *Journal of Freshwater Ecology*, 26(4), 445-457. https://doi.org/10.1080/02705060.2011.596657
- 178. Murray, A. B., LeBars, M., & Guillon, C. (2003). Tests of a new hypothesis for non-bathymetrically driven rip currents. *Journal of Coastal Research*, 269-277.

https://www.jstor.org/stable/4299168

- 179. Naffaa, M. G. (1995). Wave climate along the Nile Delta coast. *Journal of Coastal Research*, 219-229. https://www.jstor.org/stable/4298323
- 180. Nagendra, H., Lucas, R., Honrado, J. P., Jongman, R. H., Tarantino, C., Adamo, M., & Mairota, P. (2013). Remote sensing for conservation monitoring: Assessing protected areas, habitat extent, habitat condition, species diversity, and threats. *Ecological Indicators*, *33*, 45-59. https://doi.org/10.1016/j.ecolind.2012.09.014
- 181. Nascimento Jr, W. R., Souza-Filho, P. W. M., Proisy, C., Lucas, R. M., & Rosenqvist, A. (2013). Mapping changes in the largest continuous Amazonian mangrove belt using object-based classification of multisensor satellite imagery. *Estuarine, Coastal and Shelf Science*, *117*, 83-93. https://doi.org/10.1016/j.ecss.2012.10.005
- 182. National Oceanic and Atmospheric Administration (2023, June 8). LAKE LEVEL VIEWER United States Great Lakes. https://coast.noaa.gov/llv/
- 183. National Oceanic and Atmospheric Administration (2024). *Beach Hazards Incident Statistics Great Lakes current incidents and statistics*.

https://www.weather.gov/greatlakes/beachhazards_stats (Last Accessed: December 05, 2024).

- 184. National Parks Zone (2021). Indiana Dunes National Park. https://www.nationalparkszone.com/indianadunes.html
- 185. National Weather Service, 2021. Last Week's Flooding and Severe Weather (Aug 17-27) [WWW Document]. URL https://www.weather.gov/mkx/August2018SevereandFlood (accessed 2.2.25).

- 187. Niedermeier, A., Romaneessen, E., & Lehner, S. (2000). Detection of coastlines in SAR images using wavelet methods. *IEEE Transactions on Geoscience and Remote Sensing*, *38*(5), 2270-2281. https://doi.org/10.1109/36.868884
- 188. Nilsson, C., & Svedmark, M. (2002). Basic principles and ecological consequences of changing water regimes: riparian plant communities. *Environmental management*, *30*, 468-480. https://doi.org/10.1007/s00267-002-2735-2
- 189. Null, S. E., Viers, J. H., Deas, M. L., Tanaka, S. K., & Mount, J. F. (2013). Stream temperature sensitivity to climate warming in California's Sierra Nevada: impacts to coldwater habitat. *Climatic Change*, *116*, 149-170. https://doi.org/10.1007/s10584-012-0459-8
- 190. Nuyts, S., Almar, R., Morichon, D., Dealbera, S., Abalia, A., Muñoz, J. M., ... & Regard, V. (2023). CoastCams: A MATLAB toolbox making accessible estimations of nearshore processes, mean water levels, and morphology from timestack images. *Environmental Modelling & Software*, 168, 105800. https://doi.org/10.1016/j.envsoft.2023.105800
- 191. Oberdorff, T., Pont, D., Hugueny, B., & Porcher, J. P. (2002). Development and validation of a fish-based index for the assessment of 'river health'in France. *Freshwater Biology*, 47(9), 1720-1734. https://doi.org/10.1046/j.1365-2427.2002.00884.x
- 192. Ogidi, O. I., & Akpan, U. M. (2022). Aquatic biodiversity loss: impacts of pollution and anthropogenic activities and strategies for conservation. In *Biodiversity in Africa: potentials, threats and conservation* (pp. 421-448). Singapore: Springer Nature Singapore. https://doi.org/10.1007/978-981-19-3326-4_16
- 193. Okyay, U., Telling, J., Glennie, C. L., & Dietrich, W. E. (2019). Airborne lidar change detection: An overview of Earth sciences applications. *Earth-Science Reviews*, *198*, 102929. https://doi.org/10.1016/j.earscirev.2019.102929

- 194. Otsu, N. (1975). A threshold selection method from gray-level histograms. *Automatica*, *11*(285-296), 23-27.
- 195. Overstreet, B. T., & Legleiter, C. J. (2017). Removing sun glint from optical remote sensing images of shallow rivers. *Earth Surface Processes and Landforms*, 42(2), 318-333. https://doi.org/10.1002/esp.4063
- 196. Ozaukee Press, 2022. Men in small boat rescue kayaker from rough lake [WWW Document]. URL https://ozaukeepress.com/content/men-small-boat-rescue-kayaker-rough-lake (accessed 12.5.24).
- 197. Özkan-Haller, H. T., & Kirby, J. T. (1999). Nonlinear evolution of shear instabilities of the longshore current: A comparison of observations and computations. *Journal of Geophysical Research: Oceans*, *104*(C11), 25953-25984. https://doi.org/10.1029/1999JC900104
- 198. Pace, G., Gutiérrez-Cánovas, C., Henriques, R., Carvalho-Santos, C., Cássio, F., & Pascoal, C. (2022). Remote sensing indicators to assess riparian vegetation and river ecosystem health. *Ecological Indicators*, *144*, 109519. https://doi.org/10.1016/j.ecolind.2022.109519
- 199. Papanicolaou, A. T. N., Elhakeem, M., Krallis, G., Prakash, S., & Edinger, J. (2008). Sediment transport modeling review—current and future developments. *Journal of hydraulic engineering*, *134*(1), 1-14. https://doi.org/10.1061/(ASCE)0733-9429(2008)134:1(1)
- 200. Pardo-Pascual, J. E., Almonacid-Caballer, J., Cabezas-Rabadán, C., Fernández-Sarría, A., Armaroli, C., Ciavola, P., ... & Palomar-Vázquez, J. (2024). Assessment of satellite-derived shorelines automatically extracted from Sentinel-2 imagery using SAET. *Coastal Engineering*, 188, 104426. https://doi.org/10.1016/j.coastaleng.2023.104426
- 201. Partama, I. G. Y., Kanno, A., Ueda, M., Akamatsu, Y., Inui, R., Sekine, M., ... & Higuchi, T. (2018). Removal of water-surface reflection effects with a temporal minimum filter

- for UAV-based shallow-water photogrammetry. *Earth Surface Processes and Landforms*, 43(12), 2673-2682. https://doi.org/10.1002/esp.4399
- 202. Pascoe, G. A., Blanchet, R. J., & Linder, G. (1993). Ecological risk assessment of a metals-contaminated wetland: reducing uncertainty. *Science of the total environment*, *134*, 1715-1728. https://doi.org/10.1016/S0048-9697(05)80172-X
- 203. Paterson, S. K., O'Donnell, A., Loomis, D. K., & Hom, P. (2010). The social and economic effects of shoreline change: North Atlantic, South Atlantic, Gulf of Mexico, and Great Lakes regional overview. *MA: Eastern Research Group Inc, Lexington*.
- 204. Pearsons, T. N., Li, H. W., & Lamberti, G. A. (1992). Influence of habitat complexity on resistance to flooding and resilience of stream fish assemblages. *Transactions of the American Fisheries society*, 121(4), 427-436. https://doi.org/10.1577/1548-

8659(1992)121<0427:IOHCOR>2.3.CO;2

- 205. Peterson, S. M., & Wu, C. H. (2025). Coastal geomorphic changes near groin structures under fluctuating water levels in Lake Michigan. *Journal of Great Lakes Research*, 102622. https://doi.org/10.1016/j.jglr.2025.102622
- 206. Pimm, S.L., 1984. The Complexity and Stability of Ecosystems. Nature 307, 321–326. https://doi.org/10.1038/307321a0
- 207. Pitt, A. L., Shinskie, J. L., Tavano, J. J., Hartzell, S. M., Delahunty, T., & Spear, S. F. (2017). Decline of a giant salamander assessed with historical records, environmental DNA and multi-scale habitat data. *Freshwater Biology*, 62(6), 967-976. https://doi.org/10.1111/fwb.12917
 208. Pollard, J. A., Spencer, T., & Brooks, S. M. (2019). The interactive relationship between coastal erosion and flood risk. *Progress in Physical Geography: Earth and Environment*, 43(4), 574-585. https://doi.org/10.1177/0309133318794498

- 209. Porst, G., Brauns, M., Irvine, K., Solimini, A., Sandin, L., Pusch, M., & Miler, O. (2019). Effects of shoreline alteration and habitat heterogeneity on macroinvertebrate community composition across European lakes. *Ecological Indicators*, *98*, 285-296. https://doi.org/10.1016/j.ecolind.2018.10.062
- 210. Rahman, M. K., Crawford, T. W., & Islam, M. S. (2022). Shoreline change analysis along rivers and deltas: A systematic review and bibliometric analysis of the shoreline study literature from 2000 to 2021. *Geosciences*, *12*(11), 410.

https://doi.org/10.3390/geosciences12110410

211. Ramalingam, G., & Reps, T. (1996). An incremental algorithm for a generalization of the shortest-path problem. *Journal of Algorithms*, *21*(2), 267-305.

https://doi.org/10.1006/jagm.1996.0046

- 212. Rana, V. K., & Suryanarayana, T. M. V. (2021). Estimation of flood influencing characteristics of watershed and their impact on flooding in data-scarce region. *Annals of GIS*, 27(4), 397-418. https://doi.org/10.1080/19475683.2021.1960603
- 213. Ranasinghe, R., & Turner, I. L. (2006). Shoreline response to submerged structures: A review. *Coastal Engineering*, *53*(1), 65-79. https://doi.org/10.1016/j.coastaleng.2005.08.003
- 214. Rasid, H., Baker, D., & Kreutzwiser, R. (1992). Coping with Great Lakes flood and erosion hazards: Long Point, Lake Erie, vs. Minnesota Point, Lake Superior. *Journal of Great Lakes Research*, *18*(1), 29-42. https://doi.org/10.1016/S0380-1330(92)71272-6
- 215. Rattanapitikon, W., & Shibayama, T. (2000). Verification and modification of breaker height formulas. *Coastal engineering journal*, 42(04), 389-406.

https://doi.org/10.1142/S0578563400000195

- 216. Ren, S., He, K., Girshick, R., & Sun, J. (2016). Faster R-CNN: Towards real-time object detection with region proposal networks. *IEEE transactions on pattern analysis and machine intelligence*, 39(6), 1137-1149. https://doi.org/10.1109/TPAMI.2016.2577031
- 217. Ribas, F., Simarro, G., Arriaga, J., & Luque, P. (2020). Automatic shoreline detection from video images by combining information from different methods. *Remote Sensing*, *12*(22), 3717. https://doi.org/10.3390/rs12223717
- 218. Rios-Touma, B., Villamarín, C., Jijón, G., Checa, J., Granda-Albuja, G., Bonifaz, E., & Guerrero-Latorre, L. (2022). Aquatic biodiversity loss in Andean urban streams. *Urban Ecosystems*, 25(6), 1619-1629. https://doi.org/10.1007/s11252-022-01248-1
- 219. Robertson, D. M., & Saad, D. A. (2011). Nutrient inputs to the Laurentian Great Lakes by source and watershed estimated using SPARROW watershed models 1. *JAWRA Journal of the American Water Resources Association*, 47(5), 1011-1033. https://doi.org/10.1111/j.1752-1688.2011.00574.x
- 220. Roni, P., Hanson, K., & Beechie, T. (2008). Global review of the physical and biological effectiveness of stream habitat rehabilitation techniques. *North American Journal of Fisheries Management*, 28(3), 856-890. https://doi.org/10.1577/M06-169.1
- 221. Roni, P., Hall, J. E., Drenner, S. M., & Arterburn, D. (2019). Monitoring the effectiveness of floodplain habitat restoration: A review of methods and recommendations for future monitoring. *Wiley Interdisciplinary Reviews: Water*, *6*(4), e1355. https://doi.org/10.1002/wat2.1355
- 222. Roper, B. B., Kershner, J. L., Archer, E., Henderson, R., & Bouwes, N. (2002). An evaluation of physical stream habitat attributes used to monitor streams 1. *JAWRA Journal of the American Water Resources Association*, 38(6), 1637-1646. https://doi.org/10.1111/j.1752-

1688.2002.tb04370.x

- 223. Ruggiero, P., Kratzmann, M. G., Himmelstoss, E. A., Reid, D., Allan, J., & Kaminsky, G. (2013). *National assessment of shoreline change: historical shoreline change along the Pacific Northwest coast*. US Geological Survey.
- 224. Saad, S. I., Mota da Silva, J., Silva, M. L. N., Guimarães, J. L. B., Sousa Junior, W. C., Figueiredo, R. D. O., & Rocha, H. R. D. (2018). Analyzing ecological restoration strategies for water and soil conservation. *Plos one*, *13*(2), e0192325.

https://doi.org/10.1371/journal.pone.0192325

- 225. Saharia, M., Kirstetter, P. E., Vergara, H., Gourley, J. J., & Hong, Y. (2017). Characterization of floods in the United States. *Journal of Hydrology*, *548*, 524-535. https://doi.org/10.1016/j.jhydrol.2017.03.010
- 226. Schönhofer, J., & Dudkowska, A. (2021). Rip currents in the southern Baltic Sea multi-bar nearshore zone. *Continental Shelf Research*, *212*, 104324.

https://doi.org/10.1016/j.csr.2020.104324

227. Scott, M. C., & Helfman, G. S. (2001). Native invasions, homogenization, and the mismeasure of integrity of fish assemblages. *Fisheries*, *26*(11), 6-15.

https://doi.org/10.1577/1548-8446(2001)026<0006:NIHATM>2.0.CO;2

- 228. Seale, C., Redfern, T., Chatfield, P., Luo, C., & Dempsey, K. (2022). Coastline detection in satellite imagery: A deep learning approach on new benchmark data. *Remote Sensing of Environment*, 278, 113044. https://doi.org/10.1016/j.rse.2022.113044
- 229. Serra-Llobet, A., Jähnig, S. C., Geist, J., Kondolf, G. M., Damm, C., Scholz, M., ... & Schmitt, R. (2022). Restoring rivers and floodplains for habitat and flood risk reduction:

- experiences in multi-benefit floodplain management from California and Germany. *Frontiers in Environmental Science*, *9*, 778568. https://doi.org/10.3389/fenvs.2021.778568
- 230. Sharma, R. C., Tateishi, R., Hara, K., & Nguyen, L. V. (2015). Developing superfine water index (SWI) for global water cover mapping using MODIS data. *Remote Sensing*, 7(10), 13807-13841. https://doi.org/10.3390/rs71013807
- 231. Sievert, N. A., Paukert, C. P., Tsang, Y. P., & Infante, D. (2016). Development and assessment of indices to determine stream fish vulnerability to climate change and habitat alteration. *Ecological Indicators*, *67*, 403-416. https://doi.org/10.1016/j.ecolind.2016.03.013
- 232. Simonson, T. D. (1994). *Guidelines for evaluating fish habitat in Wisconsin streams* (Vol. 164). US Department of Agriculture, Forest Service, North Central Forest Experiment Station.
- 233. Simonson, T. D., Lyons, J., & Kanehl, P. D. (1994). Quantifying fish habitat in streams: transect spacing, sample size, and a proposed framework. *North American Journal of Fisheries Management*, *14*(3), 607-615. https://doi.org/10.1577/1548-
- 8675(1994)014<0607:QFHIST>2.3.CO;2
- 234. Skoglund, S., Whitlock, R., Petersson, E., Palm, S., & Leonardsson, K. (2022). From spawner habitat selection to stock-recruitment: Implications for assessment. *Ecology and Evolution*, *12*(12), e9679. https://doi.org/10.1002/ece3.9679
- 235. Slattery, M. P., Bokuniewicz, H., & Gayes, P. (2011). Flash rip currents on ocean shoreline of Long Island, New York. *Rip Currents: Beach Safety, Physical Oceanography, and Wave Modeling. Boca Raton, Florida: CRC*, 31-44.
- 236. Small, C., & Nicholls, R. J. (2003). A global analysis of human settlement in coastal zones. *Journal of coastal research*, 584-599. https://www.jstor.org/stable/4299200

- 237. Smit, M. W. J., Reniers, A. J. H. M., & Stive, M. J. F. (2012). Role of morphological variability in the evolution of nearshore sandbars. *Coastal Engineering*, *69*, 19-28. https://doi.org/10.1016/j.coastaleng.2012.05.005
- 238. Snyder, M. N., Goetz, S. J., & Wright, R. K. (2005). Stream health rankings predicted by satellite derived land cover metrics 1. *JAWRA Journal of the American Water Resources*Association, 41(3), 659-677. https://doi.org/10.1111/j.1752-1688.2005.tb03762.x
- 239. Somerville, D. E. (2010). Stream assessment and mitigation protocols: a review of commonalities and differences. *Contract No. GS-00F-0032M, US Environmental Protection Agency, Washington, DC*.
- 240. Sonkar, G. K., Gaurav, K., Rai, A. K., Taigor, S., & Beg, Z. (2023). Integrating satellite altimeter data and geomorphic in-stream flow tool to assess reach average hydraulic habitat of the Ganga River dolphin. *Ecohydrology*, *16*(2), e2497. https://doi.org/10.1002/eco.2497
- 241. Sotés, I., Basterretxea-Iribar, I., Sanchez-Beaskoetxea, J., & Maruri, M. D. L. M. (2020). Environment understanding, signage perception and safety education in Biscay beachgoers under the view of lifeguards. *Ocean & Coastal Management*, 189, 105149.

https://doi.org/10.1016/j.ocecoaman.2020.105149

242. Stephens, S. A., Healy, T. R., Black, K. P., & de Lange, W. P. (1997, January). Arcuate duneline embayments, infragravity signals and rip currents at Waihi beach, New Zealand.
In Pacific Coasts and Ports' 97: Proceedings of the 13th Australasian Coastal and Ocean Engineering Conference and the 6th Australasian Port and Harbour Conference; Volume 1 (pp. 396-401). Christchurch, NZ: Centre for Advanced Engineering, University of Canterbury.
243. Su, C. C., & Lu, J. Y. (2016). Comparison of sediment load and riverbed scour during

floods for gravel-bed and sand-bed reaches of intermittent rivers: Case study. Journal of

Hydraulic Engineering, 142(5), 05016001. https://doi.org/10.1061/(ASCE)HY.1943-7900.0001119

- 244. Su, Z., Li, W., Ma, Z., & Gao, R. (2022). An improved U-Net method for the semantic segmentation of remote sensing images. *Applied Intelligence*, *52*(3), 3276-3288. https://doi.org/10.1007/s10489-021-02542-9
- 245. Sushmitha, S., Jebaraj, B. S., Vivekrabinson, K., Azarudeen, K., Priyadharshini, S., & Gnanasekaran, T. (2024, July). Internet of Things (IoT) based watercraft for environmental surveillance and maintenance. In 2024 5th International Conference on Image Processing and Capsule Networks (ICIPCN) (pp. 720-724). IEEE.

https://doi.org/10.1109/ICIPCN63822.2024.00125

- Talbot, C. J., Bennett, E. M., Cassell, K., Hanes, D. M., Minor, E. C., Paerl, H., ... & Xenopoulos, M. A. (2018). The impact of flooding on aquatic ecosystem services.
 Biogeochemistry, 141(3), 439-461. https://doi.org/10.1007/s10533-018-0449-7
 Terry, B. B., Baptist, J. R., Rattz, J., Wagner, O., Yetkin, O., & Gowda, S. (2021, July).
 An End-to-End Pipeline for Acquiring, Processing, and Importing UAS Data for Use in the Open Data Cube (ODC). In 2021 IEEE International Geoscience and Remote Sensing Symposium
 IGARSS (pp. 8197-8200). IEEE. https://doi.org/10.1109/IGARSS47720.2021.9553149
- 248. Thakur, S., Mondal, I., Bar, S., Nandi, S., Ghosh, P. B., Das, P., & De, T. K. (2021). Shoreline changes and its impact on the mangrove ecosystems of some islands of Indian Sundarbans, North-East coast of India. *Journal of Cleaner Production*, *284*, 124764. https://doi.org/10.1016/j.jclepro.2020.124764
- 249. Theuerkauf, E. J., Braun, K. N., Nelson, D. M., Kaplan, M., Vivirito, S., & Williams, J. D. (2019). Coastal geomorphic response to seasonal water-level rise in the Laurentian Great

- Lakes: An example from Illinois Beach State Park, USA. *Journal of Great Lakes Research*, 45(6), 1055-1068. https://doi.org/10.1016/j.jglr.2019.09.012
- 250. Theuerkauf, E. J., & Braun, K. N. (2021). Rapid water level rise drives unprecedented coastal habitat loss along the Great Lakes of North America. *Journal of Great Lakes*Research, 47(4), 945-954. https://doi.org/10.1016/j.jglr.2021.05.004
- 251. Theuerkauf, E. J., Burchi, B. M., & Wyns, L. (2025). Quantifying the increase in shoreline armoring along Michigan's Lake Michigan coast associated with rising lake level (2014–2020). *Journal of Great Lakes Research*, 102571.

https://doi.org/10.1016/j.jglr.2025.102571

- 252. Thieler, E. R., & Young, R. S. (1991). Quantitative evaluation of coastal geomorphological changes in South Carolina after Hurricane Hugo. *Journal of Coastal Research*, 187-200. https://www.jstor.org/stable/25735415
- 253. Tian, Z., Wang, W., Zhan, R., He, Z., Zhang, J., & Zhuang, Z. (2019). Cascaded detection framework based on a novel backbone network and feature fusion. *IEEE Journal of Selected Topics in Applied Earth Observations and Remote Sensing*, 12(9), 3480-3491. https://doi.org/10.1109/JSTARS.2019.2924086
- 254. Tockner, K., Malard, F., & Ward, J. V. (2000). An extension of the flood pulse concept. *Hydrological processes*, *14*(16-17), 2861-2883. https://doi.org/10.1002/1099-1085(200011/12)14:16/17%3C2861::AID-HYP124%3E3.0.CO;2-F
- 255. Tompalski, P., Coops, N. C., White, J. C., Wulder, M. A., & Yuill, A. (2017). Characterizing streams and riparian areas with airborne laser scanning data. *Remote sensing of environment*, 192, 73-86. https://doi.org/10.1016/j.rse.2017.01.038

- 256. Trizna, D. B. (2017, September). Coherent marine radar measurements of ocean waves, near surface mean currents and rip current features. In *OCEANS 2017-Anchorage* (pp. 1-9). IEEE.
- 257. Turner, I. L., & Anderson, D. J. (2007). Web-based and 'real-time'beach management system. *Coastal Engineering*, *54*(6-7), 555-565. https://doi.org/10.1016/j.coastaleng.2007.01.002
- 258. Turner, D., Lucieer, A., & Watson, C. (2012). An automated technique for generating georectified mosaics from ultra-high resolution unmanned aerial vehicle (UAV) imagery, based on structure from motion (SfM) point clouds. *Remote sensing*, 4(5), 1392-1410.

https://doi.org/10.3390/rs4051392

- 259. Turner, D., Lucieer, A., & Wallace, L. (2013). Direct georeferencing of ultrahigh-resolution UAV imagery. *IEEE Transactions on Geoscience and Remote Sensing*, 52(5), 2738-2745. https://doi.org/10.1109/TGRS.2013.2265295
- 260. Troy, C. D., Cheng, Y. T., Lin, Y. C., & Habib, A. (2021). Rapid lake Michigan shoreline changes revealed by UAV LiDAR surveys. *Coastal Engineering*, *170*, 104008. https://doi.org/10.1016/j.coastaleng.2021.104008
- 261. Ullah, H., Muhammad, K., Irfan, M., Anwar, S., Sajjad, M., Imran, A. S., & De Albuquerque, V. H. C. (2021). Light-DehazeNet: a novel lightweight CNN architecture for single image dehazing. *IEEE transactions on image processing*, 30, 8968-8982.

https://doi.org/10.1109/TIP.2021.3116790

- 262. United Nations Office for Disaster Risk Reduction (2009). Terminology on disaster risk reduction. *Geneva, Switzerland*.
- 263. United States Environmental Protection Agency, (2022). *Indicators: Shallow Water Habitat/In-stream Fish Habitat*.

- https://www.epa.gov/national-aquatic-resource-surveys/indicators-shallow-water-habitatin-stream-fish-habitat
- 264. United States Environmental Protection Agency (2023, December 13). Physical Features of the Great Lakes. https://www.epa.gov/greatlakes/physical-features-great-lakes
- 265. United States Lifesaving Association, 2024. Rip Currents [WWW Document]. URL https://www.usla.org/page/ripcurrents (accessed 12.8.24).
- 266. Van Westen, C. J. (2000). Remote sensing for natural disaster management. *International archives of photogrammetry and remote sensing*, 33(B7/4; PART 7), 1609-1617.
- 267. Velasquez, N., Quintero, F., Koya, S. R., Roy, T., & Mantilla, R. (2023). Snow-detonated floods: Assessment of the US midwest march 2019 event. *Journal of Hydrology: Regional Studies*, 47, 101387. https://doi.org/10.1016/j.ejrh.2023.101387
- 268. Vlodarchyk, B., Olivito, A., & Houser, C. (2019). Spatial and temporal variation of surf drownings in the Great lakes: 2010–17. *Journal of Coastal Research*, *35*(4), 794-804. https://doi.org/10.2112/JCOASTRES-D-18-00027.1
- 269. Vos, K., Splinter, K. D., Harley, M. D., Simmons, J. A., & Turner, I. L. (2019). CoastSat: A Google Earth Engine-enabled Python toolkit to extract shorelines from publicly available satellite imagery. *Environmental Modelling & Software*, *122*, 104528. https://doi.org/10.1016/j.envsoft.2019.104528
- 270. Walters, D. M., Leigh, D. S., Freeman, M. C., Freeman, B. J., & Pringle, C. M. (2003). Geomorphology and fish assemblages in a Piedmont river basin, USA. *Freshwater Biology*, 48(11), 1950-1970. https://doi.org/10.1046/j.1365-2427.2003.01137.x

- 271. Wang, L., Simonson, T. D., & Lyons, J. (1996). Accuracy and precision of selected stream habitat estimates. *North American Journal of Fisheries Management*, *16*(2), 340-347. https://doi.org/10.1577/1548-8675(1996)016%3C0340:AAPOSS%3E2.3.CO;2
- 272. Wang, B. H., Wang, D. B., Ali, Z. A., Ting Ting, B., & Wang, H. (2019). An overview of various kinds of wind effects on unmanned aerial vehicle. *Measurement and Control*, *52*(7-8), 731-739. https://doi.org/10.1177/0020294019847688
- 273. Wang, C., Du, P., Wu, H., Li, J., Zhao, C., & Zhu, H. (2021a). A cucumber leaf disease severity classification method based on the fusion of DeepLabV3+ and U-Net. *Computers and Electronics in Agriculture*, *189*, 106373. https://doi.org/10.1016/j.compag.2021.106373
- 274. Wang, P., Fan, E., & Wang, P. (2021b). Comparative analysis of image classification algorithms based on traditional machine learning and deep learning. *Pattern recognition letters*, *141*, 61-67. https://doi.org/10.1016/j.patrec.2020.07.042
- 275. Wang W., Lu, B., & Wu, C. (2025a) Cost-effective Drone Monitoring and Evaluating Toolkits for Stream Habitat Health: Development and Application.

https://doi.org/10.21203/rs.3.rs-6648262/v1

276. Wang, W., Lu, B., Li, Y., & Shi, W. (2025b). Descriptor: Coastal Aerial Imagery Dataset for Shoreline Segmentation (CAID). *IEEE Data Descriptions*.

https://doi.org/10.1109/IEEEDATA.2025.3599116

277. White, J. Y., & Walsh, C. J. (2020). Catchment-scale urbanization diminishes effects of habitat complexity on instream macroinvertebrate assemblages. *Ecological Applications*, *30*(8), e02199. https://doi.org/10.1002/eap.2199

- 278. Williams, R. A., Lizzadro-McPherson, D. J., & Meadows, G. (2025). Mapping Michigan's historical coastlines. *Journal of Great Lakes Research*, 102511. https://doi.org/10.1016/j.jglr.2025.102511
- 279. Wisconsin Department of Natural Resources, (2017). *Dane County color trout stream* map. https://p.widencdn.net/sbjjyw/Trout Dane color landscape
- 280. Wisconsin Department of Natural Resources, (2018). Guidelines for Assessing Fish Communities of Wadeable Streams in Wisconsin v2.0.

https://dnr.wi.gov/water/wsSWIMSDocument.ashx?documentSeqNo=159685968

281. Wisconsin Department of Natural Resources, (2019). *Trout Stream Management and Status Report of Black Earth Creek Watershed Dane County, Wisconsin 2019*. https://dnr.wisconsin.gov/sites/default/files/topic/Fishing/Reports_DaneBlackEarthCreek2019W atershedTrout.pdf

- 282. Woodget, A. S., Visser, F., Maddock, I. P., & Carbonneau, P. E. (2016). The accuracy and reliability of traditional surface flow type mapping: Is it time for a new method of characterizing physical river habitat?. *River Research and Applications*, *32*(9), 1902-1914. https://doi.org/10.1002/rra.3047
- 283. Woodget, A. S., Dietrich, J. T., & Wilson, R. T. (2019). Quantifying below-water fluvial geomorphic change: The implications of refraction correction, water surface elevations, and spatially variable error. *Remote Sensing*, *11*(20), 2415. https://doi.org/10.3390/rs11202415
 284. Wu, T. D., & Lee, M. T. (2007, July). Geological lineament and shoreline detection in SAR images. In *2007 IEEE International Geoscience and Remote Sensing Symposium* (pp. 520-523). IEEE. https://doi.org/10.1109/IGARSS.2007.4422845

- 285. Wulder, M. A., Hilker, T., White, J. C., Coops, N. C., Masek, J. G., Pflugmacher, D., & Crevier, Y. (2015). Virtual constellations for global terrestrial monitoring. *Remote Sensing of Environment*, 170, 62-76. https://doi.org/10.1016/j.rse.2015.09.001
- 286. Xu, J., Yan, S., Zou, Z. L., Liu, Z., Wang, Y., Chang, C. S., ... & You, Z. J. (2024). Flow characteristics of the rip current system adjacent to a coastal vertical structure for irregular waves. *Ocean Engineering*, *312*, 119128. https://doi.org/10.1016/j.oceaneng.2024.119128
 287. Yao, Y., Huang, X., Liu, J., Zheng, C., He, X., & Liu, C. (2015). Spatiotemporal variation of river temperature as a predictor of groundwater/surface-water interactions in an arid watershed in China. *Hydrogeology Journal*, *23*(5), 999-1007. https://doi.org/10.1007/s10040-015-1265-y
- 288. Yousef, A., Iftekharuddin, K. M., & Karim, M. A. (2014). Shoreline extraction from light detection and ranging digital elevation model data and aerial images. *Optical Engineering*, *53*(1), 011006-011006. https://doi.org/10.1117/1.OE.53.1.011006
- 289. Zacharioudaki, A., & Reeve, D. E. (2011). Shoreline evolution under climate change wave scenarios. *Climatic change*, 108(1-2), 73-105. https://doi.org/10.1007/s10584-010-0011-7
- 290. Zhang, T., Yang, X., Hu, S., & Su, F. (2013). Extraction of coastline in aquaculture coast from multispectral remote sensing images: Object-based region growing integrating edge detection. *Remote sensing*, *5*(9), 4470-4487. https://doi.org/10.3390/rs5094470
- 291. Zhang, Y., Huang, W., Liu, X., Zhang, C., Xu, G., & Wang, B. (2021). Rip current hazard at coastal recreational beaches in China. *Ocean & Coastal Management*, *210*, 105734. https://doi.org/10.1016/j.ocecoaman.2021.105734

- 292. Zhang, S., Xu, Q., Wang, H., Kang, Y., & Li, X. (2022). Automatic waterline extraction and topographic mapping of tidal flats from SAR images based on deep learning. *Geophysical Research Letters*, 49(2), e2021GL096007. https://doi.org/10.1029/2021GL096007
- 293. Zhao, J., Li, Y., Matgen, P., Pelich, R., Hostache, R., Wagner, W., & Chini, M. (2022). Urban-aware u-net for large-scale urban flood mapping using multitemporal sentinel-1 intensity and interferometric coherence. *IEEE Transactions on Geoscience and Remote Sensing*, 60, 1-21. https://doi.org/10.1109/TGRS.2022.3199036
- 294. Zheng, Y., Yang, T., Wang, N., Wan, X., Hu, C., Sun, L., & Yan, X. (2023). Quantifying hydrological-ecological response relationships based on zooplankton index of biotic integrity and comprehensive habitat quality index-A case study of typical rivers in Xi'an, China. *Science of The Total Environment*, 858, 159925. https://doi.org/10.1016/j.scitotenv.2022.159925
- 295. Zhu, H., Li, C., Zhang, L., & Shen, J. (2015). River channel extraction from SAR images by combining gray and morphological features. *Circuits, Systems, and Signal Processing*, *34*(7), 2271-2286. https://doi.org/10.1007/s00034-014-9922-2
- 296. Zhou, Q., Su, J., Leng, G., & Peng, J. (2019). The role of hazard and vulnerability in modulating economic damages of inland floods in the United States using a survey-based dataset. *Sustainability*, *11*(13), 3754. https://doi.org/10.3390/su11133754
- 297. Zhu, D., Qi, R., Hu, P., Su, Q., Qin, X., & Li, Z. (2022). YOLO-Rip: A modified lightweight network for Rip currents detection. *Frontiers in Marine Science*, *9*, 930478. https://doi.org/10.3389/fmars.2022.930478